RECENT ADVANCES IN INTRINSICALLY CONDUCTING POLYMERS AND COMPOSITES

EDITED BY: Bluma Guenther Soares, Sébastien Livi and Guilherme Mariz de Oliveira Barra

PUBLISHED IN: Frontiers in Materials

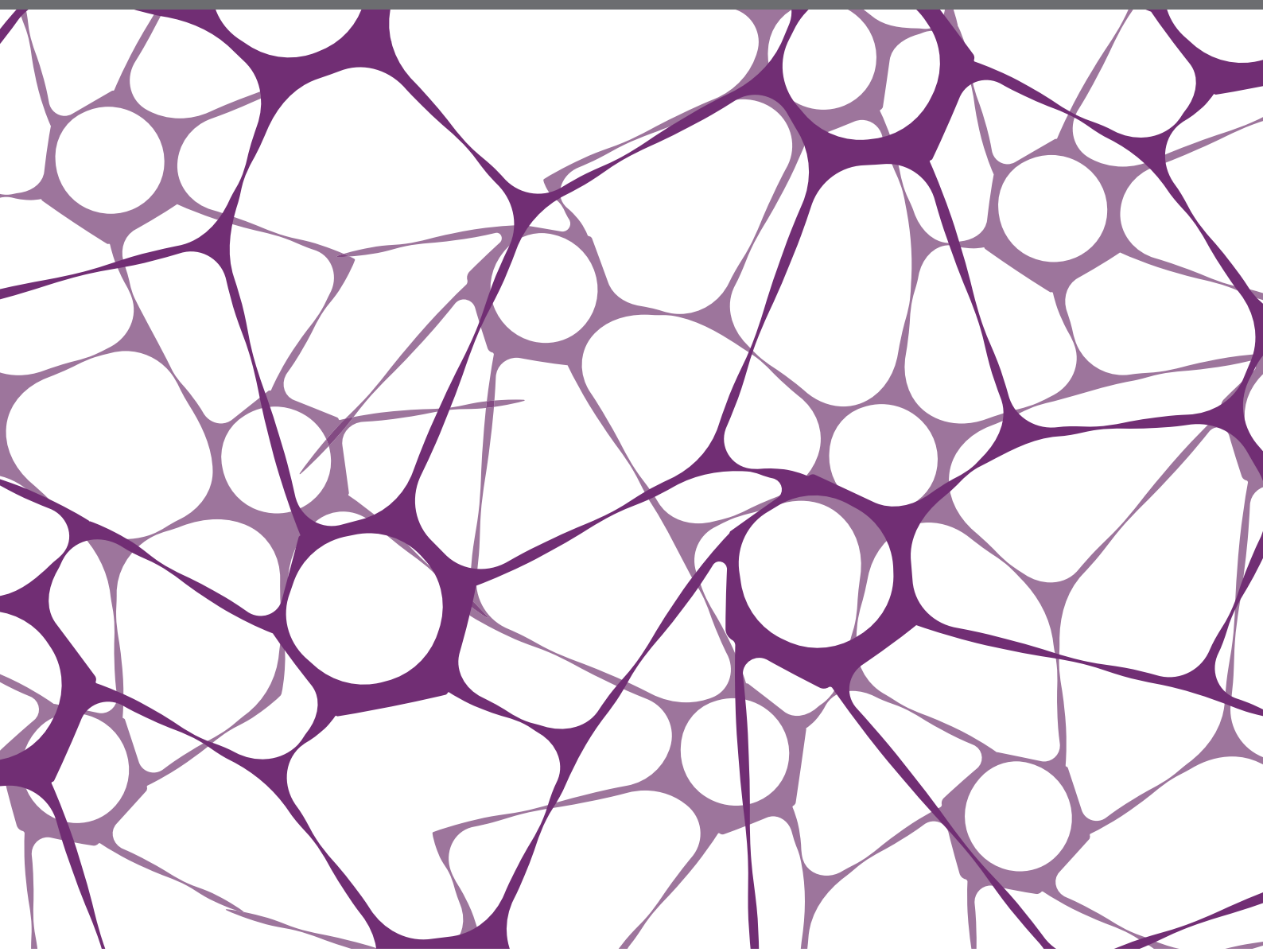

frontiers Research Topics

frontiers

Frontiers eBook Copyright Statement

The copyright in the text of individual articles in this eBook is the property of their respective authors or their respective institutions or funders. The copyright in graphics and images within each article may be subject to copyright of other parties. In both cases this is subject to a license granted to Frontiers.

The compilation of articles constituting this eBook is the property of Frontiers.

Each article within this eBook, and the eBook itself, are published under the most recent version of the Creative Commons CC-BY licence. The version current at the date of publication of this eBook is CC-BY 4.0. If the CC-BY licence is updated, the licence granted by Frontiers is automatically updated to the new version.

When exercising any right under the CC-BY licence, Frontiers must be attributed as the original publisher of the article or eBook, as applicable.

Authors have the responsibility of ensuring that any graphics or other materials which are the property of others may be included in the CC-BY licence, but this should be checked before relying on the CC-BY licence to reproduce those materials. Any copyright notices relating to those materials must be complied with.

Copyright and source acknowledgement notices may not be removed and must be displayed in any copy, derivative work or partial copy which includes the elements in question.

All copyright, and all rights therein, are protected by national and international copyright laws. The above represents a summary only. For further information please read Frontiers' Conditions for Website Use and Copyright Statement, and the applicable CC-BY licence.

ISSN 1664-8714
ISBN 978-2-88966-035-3
DOI 10.3389/978-2-88966-035-3

About Frontiers

Frontiers is more than just an open-access publisher of scholarly articles: it is a pioneering approach to the world of academia, radically improving the way scholarly research is managed. The grand vision of Frontiers is a world where all people have an equal opportunity to seek, share and generate knowledge. Frontiers provides immediate and permanent online open access to all its publications, but this alone is not enough to realize our grand goals.

Frontiers Journal Series

The Frontiers Journal Series is a multi-tier and interdisciplinary set of open-access, online journals, promising a paradigm shift from the current review, selection and dissemination processes in academic publishing. All Frontiers journals are driven by researchers for researchers; therefore, they constitute a service to the scholarly community. At the same time, the Frontiers Journal Series operates on a revolutionary invention, the tiered publishing system, initially addressing specific communities of scholars, and gradually climbing up to broader public understanding, thus serving the interests of the lay society, too.

Dedication to Quality

Each Frontiers article is a landmark of the highest quality, thanks to genuinely collaborative interactions between authors and review editors, who include some of the world's best academicians. Research must be certified by peers before entering a stream of knowledge that may eventually reach the public - and shape society; therefore, Frontiers only applies the most rigorous and unbiased reviews.
Frontiers revolutionizes research publishing by freely delivering the most outstanding research, evaluated with no bias from both the academic and social point of view. By applying the most advanced information technologies, Frontiers is catapulting scholarly publishing into a new generation.

What are Frontiers Research Topics?

Frontiers Research Topics are very popular trademarks of the Frontiers Journals Series: they are collections of at least ten articles, all centered on a particular subject. With their unique mix of varied contributions from Original Research to Review Articles, Frontiers Research Topics unify the most influential researchers, the latest key findings and historical advances in a hot research area! Find out more on how to host your own Frontiers Research Topic or contribute to one as an author by contacting the Frontiers Editorial Office: researchtopics@frontiersin.org

RECENT ADVANCES IN INTRINSICALLY CONDUCTING POLYMERS AND COMPOSITES

Topic Editors:
Bluma Guenther Soares, Federal University of Rio de Janeiro, Brazil
Sébastien Livi, Institut National des Sciences Appliquées de Lyon (INSA Lyon), France
Guilherme Mariz de Oliveira Barra, Federal University of Santa Catarina, Brazil

Citation: Soares, B. G., Livi, S., de Oliveira Barra, G. M., eds. (2020). Recent Advances in Intrinsically Conducting Polymers and Composites. Lausanne: Frontiers Media SA. doi: 10.3389/978-2-88966-035-3

Table of Contents

frontiers in Materials

ORIGINAL RESEARCH
published: 17 April 2019
doi: 10.3389/fmats.2019.00060

Regenerated Silk and Carbon Nanotubes Dough as Masterbatch for High Content Filled Nanocomposites

Luca Valentini[1]*, *Silvia Bittolo Bon*[1], *Manoj Tripathi*[2], *Alan Dalton*[2] and *Nicola M. Pugno*[3,4,5]*

[1] INSTM Research Unit, Civil and Environmental Engineering Department, University of Perugia, Terni, Italy, [2] Department of Mathematics and Physical Sciences, University of Sussex, Brighton, United Kingdom, [3] Laboratory of Bio-Inspired and Graphene Nanomechanics, Department of Civil, Environmental and Mechanical Engineering, University of Trento, Trento, Italy, [4] School of Engineering and Materials Science, Queen Mary University of London, London, United Kingdom, [5] Ket-Lab, Edoardo Amaldi Foundation, Rome, Italy

Regenerated silk (RS) is a natural polymer that results from the aggregation of liquid silk fibroin proteins. In this work, we observed that RS dispersed in aqueous solution undergoes a reversible solid/liquid transition by programmed heating/cooling cycles. Fourier transform infrared, atomic force microscopy imaging and Raman measurements of the RS reveal that the transition from random coil to β-sheet structures is involved in this liquid–solid transition. The reversible solid-liquid transition of silk fibroin was then found to be helpful to prepare polymer-like carbon nanotube (CNT) dispersions. We demonstrate that the gelation of RS makes the CNTs with the consistency of a dough with polymeric behavior. Such RS can disperse carbon nanotubes at high concentrations of tens of weight percent. Finally, such carbon nanotube dough has been used for the realization of rubber composites. With this method, we pave the way for handling nanopowders (e.g. CNTs or graphene related materials) with safety and reducing the filler volatility that is critical in polymer-processing.

Keywords: carbon nanotubes, regenerated silk, phase transitions, electrical conductivity, polymer composites

OPEN ACCESS

Edited by:
Yu Dong,
Curtin University, Australia

Reviewed by:
Francesca Lionetto,
University of Salento, Italy
Maria Conceição Paiva,
University of Minho, Portugal

***Correspondence:**
Luca Valentini
luca.valentini@unipg.it
Nicola M. Pugno
nicola.pugno@unitn.it

Specialty section:
This article was submitted to Polymeric and Composite Materials, a section of the journal Frontiers in Materials

Received: *12 November 2018*
Accepted: *25 March 2019*
Published: *17 April 2019*

Citation:
Valentini L, Bittolo Bon S, Tripathi M, Dalton A and Pugno NM (2019) Regenerated Silk and Carbon Nanotubes Dough as Masterbatch for High Content Filled Nanocomposites. Front. Mater. 6:60. doi: 10.3389/fmats.2019.00060

INTRODUCTION

Regenerated silk (RS) is a natural polymer made by the coagulation of silk fibroin that is a an aggregation of proteins with short and long chains; the combination of intermolecular interactions via hydrogen bonds between the chains leads to the formation of β-sheet structures that have a high crystalline local order. Increasing the fibroin concentration in a solution enhances the probability to generate chain interactions where the β-sheets form a stable gel transition. The dehydration of such crystalline structures results in an irreversible liquid-solid transition due to thermodynamic cross-linking of the β-structures that undergo gelation with time (Ayub et al., 1993; Hanawa et al., 1995; Kang et al., 2000; Wang et al., 2008). Some physical and/or chemical methods have been proposed to enhance the gelation kinetics of silk fibroin, including pH change, mechanical sonication and addition of salts (Matsumoto et al., 2006; Gong et al., 2012; Wu et al., 2012; Kapoor and Kundu, 2016). A reversible sol-gel transition of silk fibroin exposed to acidic or basic vapors and, more recently, in hydrogel-based silk fibroin have also been reported (Terry et al., 2004; Yin et al., 2017).

Liu et al. (2014) demonstrated the thixotropy (i.e., a time dependent shear thinning property) of silk fibroin via dissolution nanofibrils gel in alcohol and sodium chloride while Bai et al. (2014) also showed a reversible sol—gel transition by self-assembly of nanofibers into supramolecular

aggregations without altering the β-sheet contents. Numata et al. (2011) reported the gelation of the regenerated silk induced with ethanol and with a heterogeneous network structure made of a β-sheet and fibrillar structures.

The shape, dimension and the aspect ratios over 1,000 of carbon nanotubes (CNTs) with their ability to undergo large deformations without damage suggests that interesting parallels may be drawn with silk fibroin. However, attention turns to their behavior and potential processability in liquid suspension. There are a lot of experiments done with most common solvents to get stable dispersions of CNTs (Fukushima et al., 2003; Bergin et al., 2009; Davis et al., 2009); however, generally the most common solvents used, such as N-methyl-2-pyrrolidone, dimethylformamide, and 1,2-dichrolobenzene, can disperse only CNTs with specific size and dimension at low concentrations. Recently, Chiou et al. (2018) dispersed carbon nanotube powders in *m*-cresol at very high concentrations giving them a dough-like consistency. However, *m*-cresol is highly volatile, and the processing requires a controlled environment.

In this study we exploit the utilization of salts to dramatically reduce the gelation time of silk fibroin. The results demonstrate that regenerated silk drop solution can undergo liquid-solid transitions within a few min by thermal annealing. The proposed method induced a rapid gelation of CNTs that, when added to RS solution at high concentrations up to tens of weight percent, show a transition dough state that exhibit polymer-like and viscoelastic properties. Finally, as proofs of the concept, such polymer-like CNTs were used as masterbatch to realize a rubber composite.

MATERIALS AND METHODS

For the preparation of RS film, commercial *B. mori* silk cocoons were boiled for 1 h in distillated water solution of 0.025 wt % $NaHCO_3$, rinsing with distillated water every 30 min to remove the sericin. The degummed silk (i.e., 0.23 g) was then added to a $CaCl_2$ (i.e., 24 g)—water (i.e., 68 ml)—ethanol (i.e., 55 ml) solution and stirred 12 h at 40°C yielding an 1 wt % solution. NANOCYL® NC7000™ multi-walled carbon nanotube powder (average diameter 9.5 nm, average length 1.5 μm, volume resistivity 10^{-4} Ohm*cm) was used. In 1 ml of solution, 10 mg of CNTs up to 50 and 2 mg of regenerated silk were dispersed to yield, at maximum, a RS concentration of about 4 wt%. The liquid-solid transition was monitored by the optical density (OD) method, measuring the absorbance at wavelength 550 nm and temperature of 80°C at different times. Fourier transform infrared (FTIR) analysis was performed in a Jasco FTIR FT/IR-615 spectrometer, equipped with an ATR mode in the wave number range from 400 to 4,000 cm^{-1}. The spectra were deconvoluted by firstly smoothing the signal with a polynomial function with a 15-point Savitski—Golay smoothing function, subtracting a linear baseline and applying Gaussian deconvoluting curves by Origin 9 software. Rheological data for the RS/CNT dough were recorded on circular specimens (ca. 12 mm wide, and 0.13 mm thick) on an ARES rheometer (Rheometric Scientific). Frequency and strain sweeps, as well as constant strain amplitude, were performed at constant temperature to find the storage modulus (G′) and the loss modulus (G″) of RS and RS/CNT samples at different CNT concentrations. The electrical resistance of the RS/CNT solid dough was obtained with a Keithley 6517B electrometer/high resistance meter equipped with an 8009 test fixture, according to the ASTMD257 that is the worldwide laboratory standard for sensitive measurements. Briefly, the basic method used to determine the resistance is a two-step method: first a test voltage is applied to the sample and the subsequent current is measured; then, the test voltage value and measured current value are applied and the electrical resistance is calculated.

For the atomic force microscopy (AFM) and Raman characterization, dispersion of RS and RS/CNT was drop casted on silicon wafers and glass slides. The sample was heated at 80°C for 1 hour in air conditions. The solid samples were placed in AFM chamber which is an insulated box to minimize environmental noise and building vibration at room temperature. AFM instrument (Model: Bruker Dimension Icon) operated at intermittent contact mode using silicon cantilever (Model: ScanAsist). All the AFM images are produced as a function of time by keeping the other parameters (i.e., scan speed, scan size) constant.

Raman spectroscopy was carried out at room temperature by using 50X objective lens using LASER source of 532nm at 5mW and grating 2400 l/mm. The spectral range was analyzed between 200cm^{-1} to 3000cm^{-1}. The Raman spectra were recorded as a function of displacement (i.e. line map) and function of time (i.e. collection of spectra at single region at different time intervals).

For the realization of the polymer composite, an acrylonitrile butadiene rubber (NBR; KNB35), LEVAPREN 700 and vulcanizing agent LUPEROX® F40MF were used. Rubber compounds were prepared by dissolving separately 1.6 g of NBR, 3.1 g of LEVAPREN and 0.25 g of LUPEROX in chloroform and then mixing together with RS/CNTs dough with a DISPERMAT$^{(R)}$ and left to evaporate onto a Teflon mold until the complete evaporation of the solvent was achieved. Carbon nanotubes powder, for a comparison purpose, was sequentially added to the rubber by melt mixing (Banbury mixer) at about 100°C for 10 min. The vulcanizing agent was added just before the extraction of the composite to avoid any cross-linking effect. The composites prepared with both procedures were then vulcanized at 180°C for 5 min in a thermofluid-heated press.

Tensile properties were measured according to ASTM D 412 specifications, on an Instron dynamometer (Model 4301), at 25°C at a crosshead speed of 500 mm min^{-1}. At least five specimens of each sample type were tested. The samples were then cut into dumbbell specimens Die A with dimension of ∼140 × 25 × 2 mm.

RESULTS AND DISCUSSION

The liquid RS extracted from solution and a drop cast on silicon substrate at 80°C shows a liquid–solid transition (**Figure 1a**) that recovers the liquid state under cooling at 25°C within few minutes, which is lower than that of conventional silk-fibroin

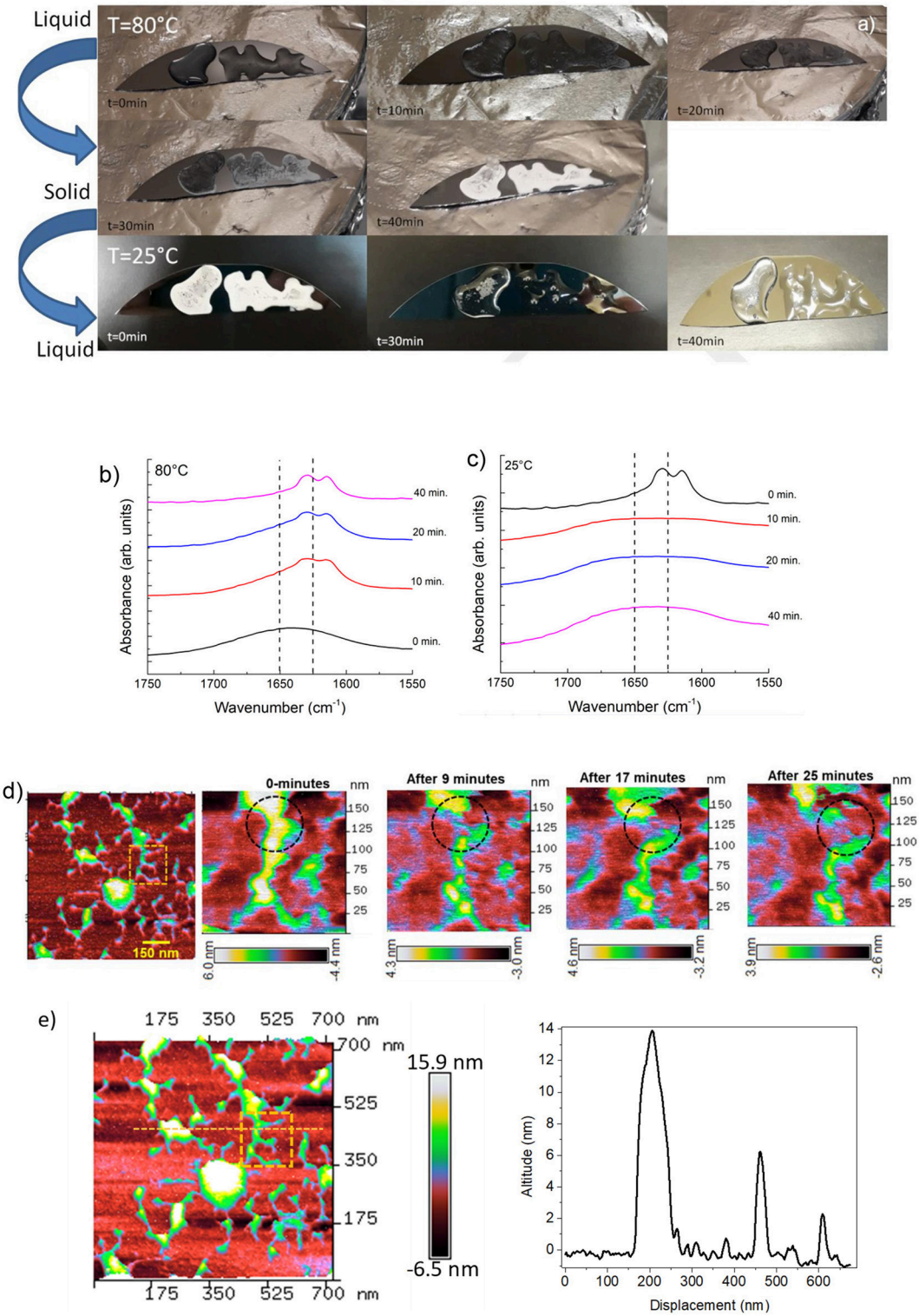

FIGURE 1 | (a) Photos showing the reversible liquid-solid transition observed along the heating/cooling time of RS. **(b)** ATR-FTIR spectra in the amide I region for RS liquid solution annealed at 80°C at different times. **(c)** ATR-FTIR spectra in the amide I region for RS solid phase cooled at room temperature at different times. **(d)** AFM topography of solid silk fibroin imaged at different time intervals at room temperature are showing dendritic structure of silk fibroin with several branches. The inset represents a peculiar region analyzed at different time intervals. AFM topography of a zoomed region analyzed up to 25 min; a transformation in the silk-fibroin structure is marked by dashed circle. The scale bar represents the degradation of the structure as a function of time. **(e)** AFM image of the dendritic fibroin network; the dashed line represent the topographic profile of different altitude of the fibroin structure.

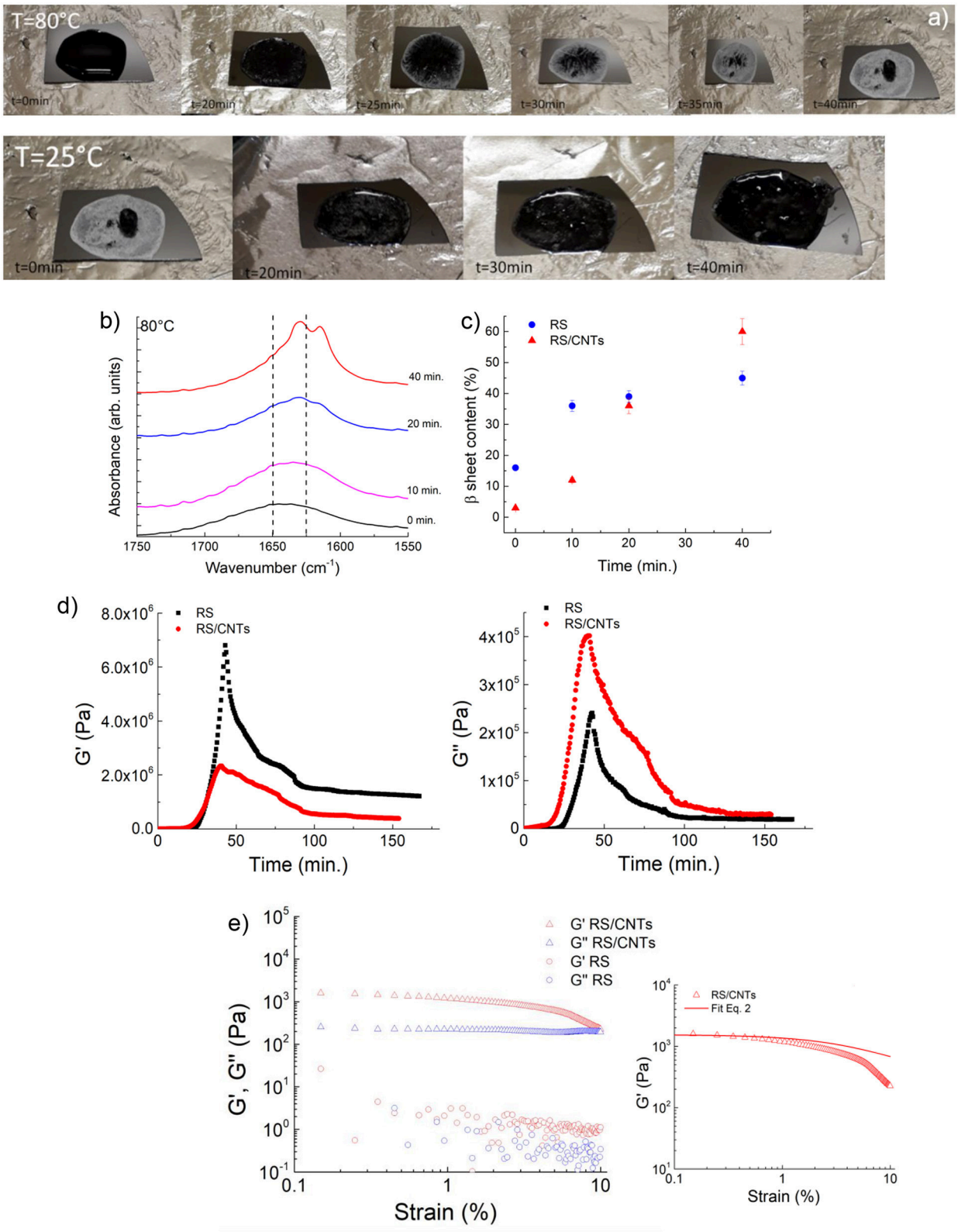

FIGURE 2 | (a) Photos showing the reversible liquid-solid transition observed along the heating/cooling time of RS/CNTs. **(b)** ATR-FTIR spectra in the amide I region for RS/CNTs liquid solution annealed at 80°C at different times. **(c)** Annealing time effect on β-sheet content at 80°C assessed by FTIR amide I band analysis for RS

(Continued)

FIGURE 2 | and RS/CNTs solutions. **(d)** Shear storage (G′) and loss (G″) moduli for RS 2 mg/ml and RS/CNTs dough with a CNT concentration of 50 mg/ml (i.e., 4 wt% RS) measured as a function of time during annealing at 80°C and cooling to 25°C. **(e)** Shear storage (G′) and loss (G″) moduli for RS 2 mg/ml and RS/CNTs dough with a CNT concentration of 50 mg/ml (i.e., 4 wt% RS), measured as a function of shear strain amplitude at 25°C. The plot on the right shows the fit of the storage modulus with Equation 2.

(usually a few weeks) (Matsumoto et al., 2006; Gong et al., 2012). The liquid-solid transition of fibroin results from the formation of physical cross-links made of a β-sheet that makes the optical aspect of the film more opaque. In its liquid state, fibroin is a hydrophobic molecule surrounded by ordered water. In this state, the ordered structure of the water hinders the fibroin aggregation but when the temperature increases, the positive entropic term overwhelms that of heat or enthalpy and local dehydration takes place, enhancing the hydrogen bonding between the chains (Connelly et al., 1964). Increasing the annealing time provides the increased chain interactions through dehydration of the system (Urry et al., 1997), and thus accelerates the solidification.

The RS also exhibits a transition from the solid to the liquid state by setting the substrate at room temperature (**Figure 1a**). Although silk fibroin contains a high content of β-sheet in the solid state, the return to the liquid phase may also imply the existence of metastable fibroin structures within the β-sheet fraction, likely those composed of silk fibroin and Ca^{2+} ions (Ling et al., 2016). Calcium ions can capture water molecules from the atmospheric and hence, the more calcium ion is in silk fibroin solution, the more water molecules, as a solvent, can be captured, resulting in liquid transition.

Changes in the structure of the RS were detected by FTIR analysis. ATR-FTIR spectra of the RS in the amide I region were measured at different times of annealing, as reported in **Figure 1b**. The β-sheet (crystalline) content was determined by the deconvolution of the amide I region and by estimating the ratio between the peak area in the wavenumber region of 1622–1637 cm^{-1}, which is the main absorbance region of β-sheet crystal in amide I (Hu et al., 2006), and the whole area of the amide I region comprising the peaks of the structural components, including turns and random coils. The dashed lines mark the adsorption bands at 1650 and 1625 cm^{-1}, which are characteristic of the random-coil and β-sheet structures of silk proteins, respectively, according to previous studies (Dong et al., 1990; Goormaghtigh et al., 1990; Mouro et al., 1997; Jung, 2000; Teramoto and Miyazawa, 2005; Tretinnikov and Tamada, 2001). The structure of RS shifted predominantly to a β-sheet structure by increasing the annealing time (**Figure 1b**), whereas random-coil structures are prevalent in the liquid state and vice-versa by cooling at 25°C (**Figure 1c**). The β-sheet content (calculated from the amide I bands over the other main components) in the liquid state was unexpectedly high (≈15%). Moreover, the β-sheet fraction increases with increasing the annealing time and was as high as 45% when the film was completely dry.

Figure 1d shows the images of single fibroin molecules obtained by AFM. The concentration of the RS sample was 1 wt %. According to Inoue et al. (2000), the silk fibroin molecule consists of a rodlike part with stringlike parts on each end of the rod. The observed size is 100 nm in width and 14 nm in height (**Figure 1e**). According to the ATR-FTIR analysis, the silk fibroin shows the disappearance of the dendritic structure at different time intervals at room temperature (**Figure 1d**).

The RS/CNT solution, which demonstrated a similar behavior (**Figure 2a**), showed a higher β-sheet content of about 60% once dried (**Figures 2b,c**). More indicative of such transition is the rheological behavior. In **Figure 2d**, the plots of storage (G′) and loss (G″) modulus vs. annealing/cooling cycles (increasing/decreasing values) are shown. According to the interpretation of the FTIR spectra both G′ and G″ increase with annealing time; interestingly both G′ and G″ are independent from the strain for the RS sample, instead they decrease with increasing the strain amplitude for the RS/CNTs sample (**Figure 2e**). For viscoelastic systems filled with rigid solids, this is known as the Payne effect (Payne, 1962). According to this theory, solid fillers may exist in chainlike formation or aggregates within the solid polymer. If there are attractive forces, the particles are held together in single agglomerates that behave like a rigid group under deformation. However, as the magnitude of the stress increases with increasing deformation, these groups will be broken down into smaller units and the elasticity of the material will change. Then, the number of connections N rescales as:

$$N = N_0[1 + (\gamma/\gamma_c)^{2m}]^{-1} \quad (1)$$

where, N_0 is the initial connection density, m is the network structure factor, γ and γ_c are the strain and the yield strain, respectively. This leads to the equation:

$$G' = G'_\infty + (G'_0 - G'_\infty)/[1 + (\gamma/\gamma_c)^{2m}] \quad (2)$$

where G'_0 or G'_∞ are the storage moduli at low or high strain, respectively. The best fit of the data (e.g. 0.53) reported in **Figure 2e** with Equation 2 results in a structure factor close to m = 0.5, which is typical for filled elastomers. From the rheological study, we can assume that the RS/CNTs sample behaves as a viscoelastic material.

RS can process CNTs up to tens of weight percent; the photos in **Figures 2a**, **3a** show the liquid CNT solution and its dough state as the annealing time in RS was increased. After drying at 80°C, a disk-shaped sample shrinks isotropically maintaining its shape, resulting in a stiff solid object that could be further handled (**Figure 3a**). Upon cooling, the dough-like state remains stable for at least 20 min (**Figures 2a**, **3a**). As reported in the FESEM images of **Figure 3b**, the CNTs are well-dispersed by the RS. From this analysis, we suggest that the interaction between silk fibroin and CNTs allows their dispersion.

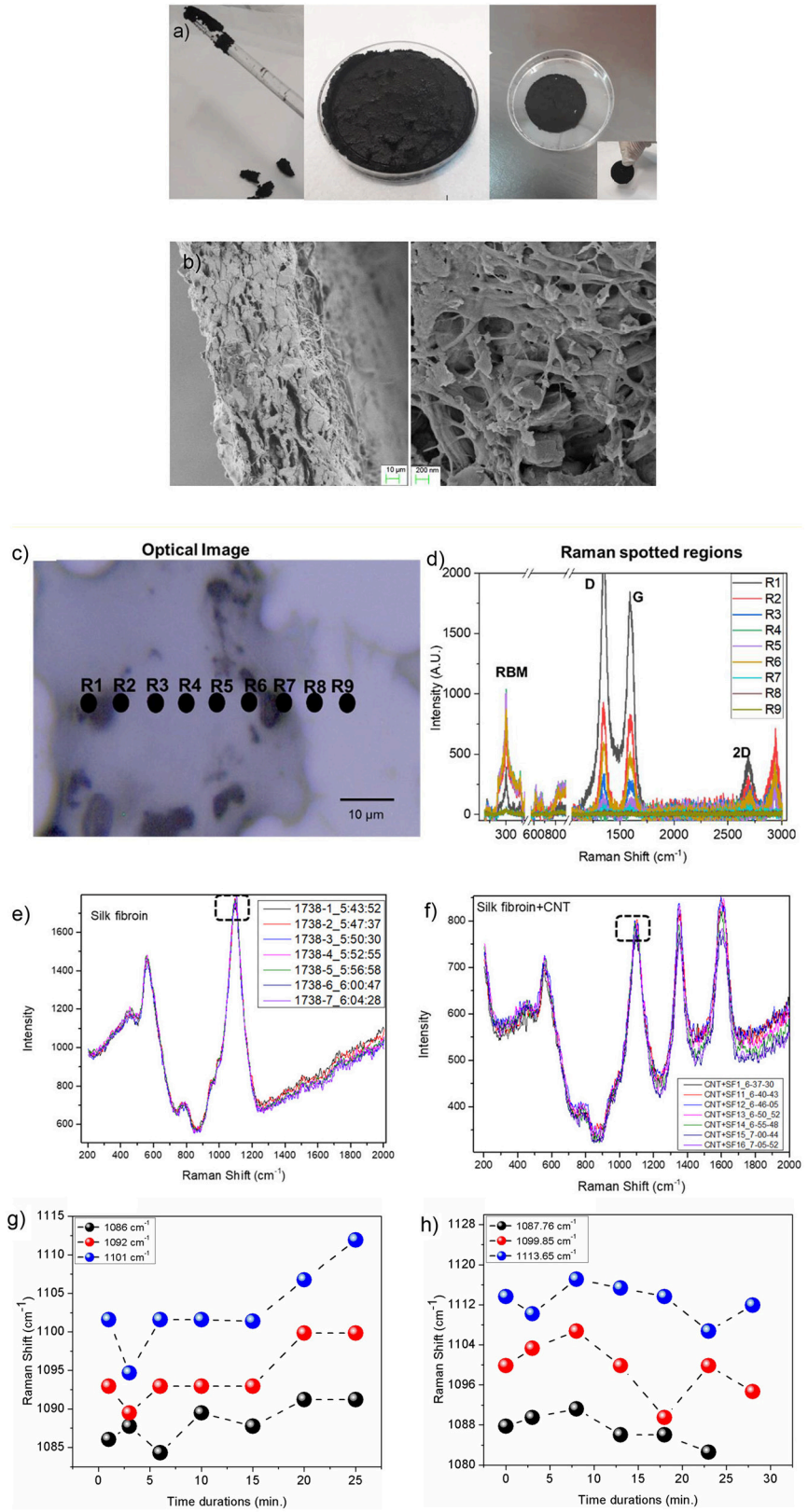

FIGURE 3 | (a) The CNTs in RS solution can be processed to obtain a dough. Once annealed, the RS/CNT dough shows a contraction and can be taken by hands as a freestanding solid sample. **(b)** Morphology of RS/CNTs dried sample in FESEM showing well separated CNTs after being processed in RS. **(c)** Optical image of

(Continued)

FIGURE 3 | RS/CNT showing accumulation of CNT (black regions). Regions marked with R1-R9 are localized spots of Raman spectra. **(d)** Raman spectrum range from 200–3,000 cm^{-1}, showing prominent peaks from CNT (RBM, D, G, and 2D), along with peaks from fibroin. Raman spectra of **(e)** RS and **(f)** RS/CNT as a function of time (min) over a glass substrate. Marked dashed rectangle in plots **(e,f)** are analyzed as a function of time. Variation of Raman shift (cm^{-1}) for peak positions 1,086, 1,092, and 1,101 cm^{-1} for RS **(g)** and at 1,087, 1099.85, and 1113.65 cm^{-1} for RS/CNT **(h)** monitored up to 24 and 28 min, respectively.

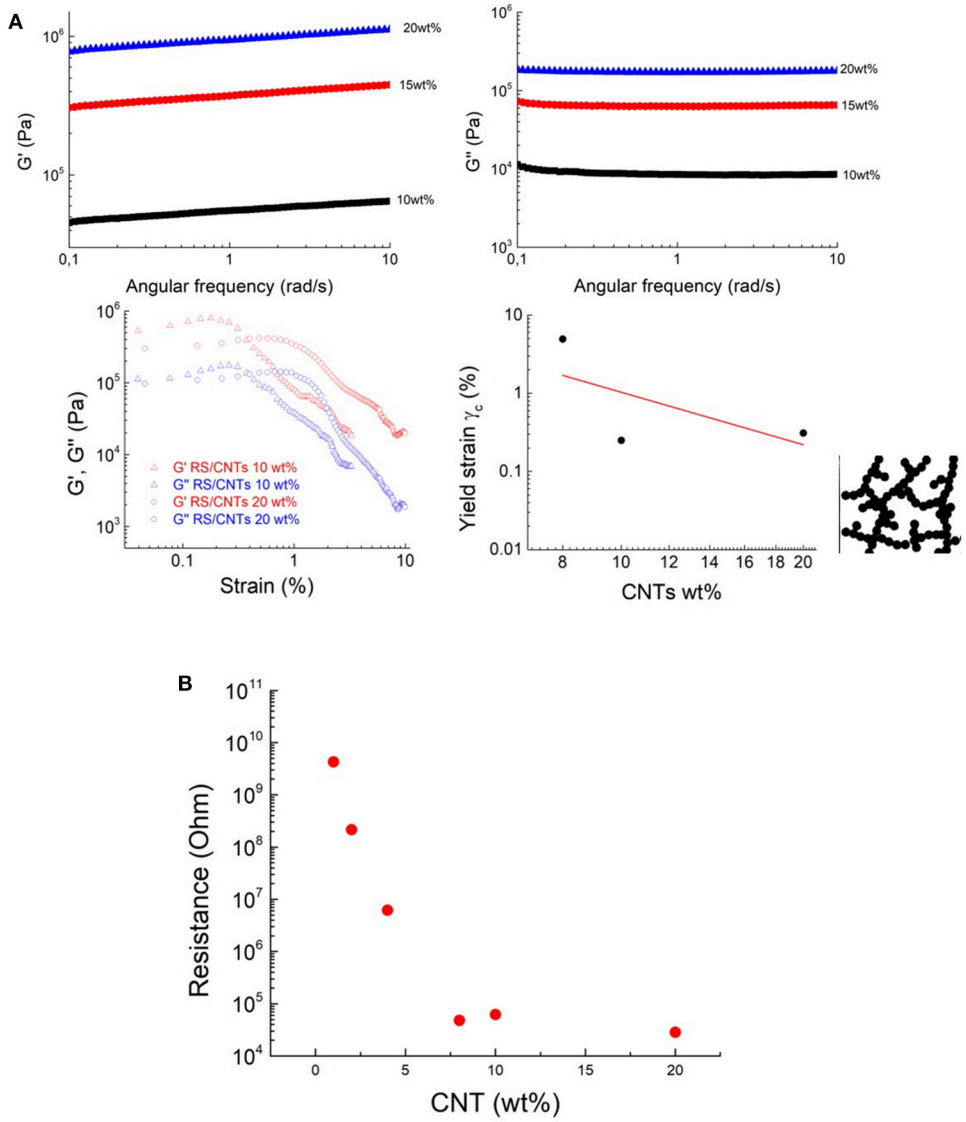

FIGURE 4 | The transition to dough-like state is characterized by an increase in a solid-like behavior, based on the results of **(A)** storage moduli (G′) and loss moduli (G") measurements. Shear storage (G′) and loss (G″) moduli RS/CNTs dough with different CNT concentrations, measured as a function of shear strain amplitude at 80°C. Yield strain plotted vs. CNT wt%. The line shows the best fit to Equation 3. Schematic structure of a fractal floc. The flocs are linked to each other. **(B)** Threshold decrease in the electrical resistance of the RS/CNT dough at different CNT concentrations.

In order to confirm this hypothesis, we reported the Raman characterization of RS and RS/CNT samples in **Figures 3c–h**. Raman spectra of the regions reported in **Figure 3c** show the typical Raman features of CNTs i.e., the so-called G-line that is a characteristic feature of the graphitic layers, the defective graphitic structure (D-line), the radial breathing mode (RBM) and the resonant 2D mode (Dresselhaus et al., 2005) (**Figure 3d**). **Figures 3e,g** show the Raman spectra of solid RS, analyzed as a function of time at room temperature. The spectra of **Figure 3e** are similar to those already published (Rousseau et al., 2004) and the assignment of the major bands observed around 600, 800, and 1100 cm^{-1} are based on published Raman results on silk, proteins, and polypeptides (Rousseau et al., 2004). The sub-peaks (**Figures S1–S3** in the Supplementary Material), due to the C-C

stretching vibration at around 1,103 cm^{-1} in the spectrum of the RS, show a blue-shift as a function of time that is associated with the β-sheet reduction, as suggested by Zheng et al. (1989). On the contrary, after addition of CNT in the RS (**Figures 3f,h**), the peak positions at 1,087, 1099.85, and 1113.65 cm^{-1}, show a red-shift as a function of time, illustrating a significant contribution from CNT.

The transition to solid state has also been confirmed by rheological, and viscoelastic properties. The transition to polymer-like state suggests that the nanotubes form a cohesive network in RS (Payne, 1962). After annealing, above 10 mg/mL, the CNT network is not free to flow, leading to a freestanding dough (**Figure 3a**). It becomes solid-like with increased storage modulus (**Figure 4A**). The loss modulus decreased more slowly than the storage modulus, giving the dough a sufficient level of viscous character for extrusion. In view of the similarity of our RS/CNTs dough with a viscoelastic medium, as reported in **Figure 2e**, the elastic properties of the samples were modeled by applying the scaling law:

$$\gamma_c \approx f^{-(1+d_B)*(3-d_N)} \quad (3)$$

which have been successfully demonstrated for polymer gels (Shih et al., 1990; Shaffer and Windle, 1992; Boland et al., 2016). These studies showed that both the storage modulus G′ and the limit of linearity of the strain γ (i.e., yield strain γ_c) exhibit a power-law with respect to particle concentration (f) that is $G' \approx f^{4.1}$ and $\gamma_c \approx f^{-2.1}$ (Sonntag and Russel, 1987; Buscall et al., 1988). Taking the γ_c values from **Figures 2e**, **4A** and plotting versus the CNT wt% in **Figure 4A**, we obtain the best fit with a power law with exponent −2.22. Such a value is consistent with the rheological model developed by Shaffer and Windle (1992), who considered the structure of a gel network as a collection of fractal flocs, which are closely packed throughout the sample whit d_N and d_B, indicating the fractal dimensions of the network and its backbone, respectively. They observed that in the strong-link regime, where there is an interfloc interaction, the elastic constant (i.e., G′) increases but the limit of linearity (i.e., γ_c) decreases with increasing particle concentration.

The higher CNT concentrations of this dough-like state are also accompanied by a threshold in the electrical properties. For example, the increase of the CNT concentration from ≈1wt% to ≈10wt% was accompanied by the onset of electrical conductivity (**Figure 4B**), which can be attributed to the start of a percolation threshold, through an interconnected pathway of nanotubes.

The dough state is of potential interest for polymer processing (De Gennes, 1979; Huang et al., 2012; De Volder et al., 2013). The dough can be added to the polymer matrices as masterbatch without handling powders, moreover, the dough state eliminates the use of solvents. **Figure 5** shows the mechanical results of the experiment, where rubber composite has been prepared by blending NBR with RS/CNTs dough. The nanocomposite was then vulcanized under a hot plate press at 180°C. At 10 wt% loading of CNTs in NBR, the toughness modulus of the RS/CNT composite increased by ≈16%, in comparison with a similar composite prepared with CNT powder (**Table 1**). Such preliminary findings suggest that RS/CNTs dough could be used for the processing of polymer nanocomposites.

CONCLUSIONS

In this study, the transition from solid to liquid state of RS was obtained by the addition of calcium chloride salts to water based silk fibroin solution. It was observed that the presence of salts stimulated the water absorption and this reaction led to a reversible transition. Moreover, the processing parameters including annealing time, allows the control of the molecular organization of silk fibroin in β-sheets structures. Such an inexpensive method to assemble silk in solid state was used for optimizing the dispersion of carbon nanotubes at high concentrations of tens of weight percent. The results show the advantage to use silk fibroin as a natural dispersant to obtain CNTs with the consistency of polymers. As a proof of concept, RS/CNT dough was used to prepare a polymer composite with improved deformability and toughness modulus, with respect to the composite prepared by the addition of CNT powder. Such findings pave the way the utilization of nanopowders dough as master batch in the processing of polymer composites and to overcome the problems of handling nanopowders in industrial implants including graphene and related materials.

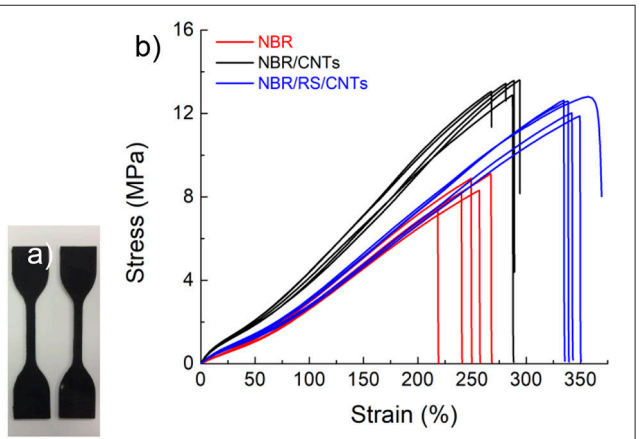

FIGURE 5 | (a) Polymer nanocomposite dumbbell specimens obtained by mixing RS/CNTs and NBR. **(b)** Mechanical characterization showing that the polymer composite prepared by mixing NBR with RS/CNT dough at its percolation threshold and CNT powder.

TABLE 1 | Polymer nanocomposites (e.g. 10 wt%) mechanical properties (i.e., elongation at break, tensile strength, stress at 50 and 100% of strain and toughness modulus).

Sample	Elongation at break (%)	Tensile strength (MPa)	Stress at 50% (MPa)	Stress at 100% (MPa)	Toughness modulus (MPa)
NBR	246 ± 10	8.35 ± 0.39	1.5 ± 0.1	3.8 ± 0.2	10.27 ± 0.24
NBR/CNTs	283 ± 18	13.30 ± 0.44	2.0 ± 0.1	7.8 ± 0.4	18.81 ± 0.31
NBR/RS/CNTs	344 ± 9	12.38 ± 0.49	1.5 ± 0.1	3.8 ± 0.2	21.29 ± 0.30

AUTHOR CONTRIBUTIONS

All authors listed have made a substantial, direct and intellectual contribution to the work, and approved it for publication. In particular SB contributed to the RS and composites realization. MT AFM imaging and its corresponding discussion. AD Raman data and its associated discussion and critical revision.

FUNDING

NP is supported by the European Commission under the Graphene Flagship Core 2 grant No. 785219 (WP14 Composites) and FET Proactive Neurofibres grant No. 732344 as well as by the Italian Ministry of Education, University and Research (MIUR) under the Departments of Excellence grant L.232/2016. LV is supported by the European Commission under the Graphene Flagship Core 2 grant No. 785219 (WP14 Composites) as well as by the Italian Ministry of Education, University and Research (MIUR) under the Departments of Excellence grant L.232/2016. MT is supported by University of Sussex strategic development fund.

SUPPLEMENTARY MATERIAL

The Supplementary Material for this article can be found online at: https://www.frontiersin.org/articles/10.3389/fmats.2019.00060/full#supplementary-material

REFERENCES

Ayub, Z. H., Arai, M., and Hirabayashi, K. (1993). Mechanism of the gelation of fibroin solution. *Biotechnol. Biochem.* 57, 1910–1912. doi: 10.1271/bbb.57.1910

Bai, S., Zhang, X., Lu, Q., Sheng, W., Liu, L., Dong, B., et al. (2014). Reversible hydrogel-solution system of silk with high beta-sheet content. *Biomacromolecules* 15, 3044–3051. doi: 10.1021/bm500662z

Bergin, S. D., Sun, Z., Rickard, D., Streich, P. V., Hamilton, J. P., and Coleman, J. N. (2009). Multicomponent solubility parameters for single-walled carbon nanotube-solvent mixtures. *ACS Nano* 3, 2340–2350. doi: 10.1021/nn900493u

Boland, C. S., Khan, U., Ryan, G., Barwich, S., Charifou, R., Harvey, A., et al. (2016). Sensitive electromechanical sensors using viscoelastic graphene-polymer nanocomposites. *Science* 354, 1257–1260. doi: 10.1126/science.aag2879

Buscall, R., Mills, P. D., Goodwin, J. W., and Lawson, D. (1988). Scaling behaviour of the rheology of aggregate networks formed from colloidal particles. *J. Chem. Soc. Faraday Trans.* 84, 4249–4260. doi: 10.1039/f19888404249

Chiou, K., Byun, S., Kim, J., and Huang, J. (2018). Additive-free carbon nanotube dispersions, pastes, gels, and doughs in cresols. *Proc. Natl. Acad. Sci. U.S.A.* 115, 5703–5708. doi: 10.1073/pnas.1800298115

Connelly, P. R., Aldape, R. A., Bruzzese, F. J., Chambers, S. P., Fitzgibbon, M. J., Fleming, M. A., et al. (1964). Enthalpy of hydrogen bond formation in a protein-ligand binding reaction. *Proc. Natl. Acad. Sci. U.S.A.* 9, 1964–1968.

Davis, V. A., Parra-Vasquez, A.N., Green, M. J., Rai, P. K., Behabtu, N., Prieto, V., et al. (2009). True solutions of single-walled carbon nanotubes for assembly into macroscopic materials. *Nat. Nanotechnol.* 4, 830–834. doi: 10.1038/nnano.2009.302

De Gennes, P. G. (1979). *Scaling Concepts of Polymer Physics.* Ithaca, NY, Cornell University Press.

De Volder, M. F., Tawfick, S. H., Baughman, R. H., and Hart, A. J. (2013). Carbon nanotubes: presentand future commercial applications. *Science.* 339, 535–539. doi: 10.1126/science.1222453

Dong, A., Huang, P., and Caughey, W. S. (1990). Protein secondary structures in water from second-derivative amide I infrared spectra. *Biochemistry.* 29, 3303–3308. doi: 10.1021/bi00465a022

Dresselhaus, M. S., Dresselhaus, G., Saito, R., and Jorio, A. (2005). Raman spectroscopy of carbon nanotubes. *Phys. Rep.* 409, 47–99. doi: 10.1016/j.physrep.2004.10.006

Fukushima, T., Kosaka, A., Ishimura, Y., Yamamoto, T., Takigawa, T., Ishii, N., et al. (2003). Molecular ordering of organic molten salts triggered by single-walled carbon nanotubes. *Science.* 300, 2072–2074. doi: 10.1126/science.1082289

Gong, Z., Yang, Y., Ren, Q., Chen, X., and Shao, Z. (2012). Injectable thixotropic hydrogel comprising regenerated silk fibroin and hydroxypropylcellulose. *Soft Matter.* 8, 2875–2883. doi: 10.1039/c2sm06984a

Goormaghtigh, E., Cabiaux, V., and Ruysschaert, J. M. (1990). Secondary structure and dosage of soluble and membrane proteins by attenuated total reflection Fourier-transform infrared spectroscopy on hydrated films. *J. Biochem.* 193, 409–420.

Hanawa, T., Watanabe, A., Tsuchiya, T., Ikoma, R., Hidaka, M., and Sugihara, M. (1995). New oral dosage form for elderly patients: preparation and characterization of silk fibroin gel. *Chem. Pharm. Bull.* 43, 284–288. doi: 10.1248/cpb.43.284

Hu, X., Kaplan, D., and Cebe, P. (2006). Determining Beta-Sheet Crystallinity in Fibrous Proteins by Thermal Analysis and Infrared Spectroscopy. *Macromolecules* 39, 6161–6170. doi: 10.1021/ma0610109

Huang, J. Q., Zhang, Q., Zhao, and, M. Q., and Wei, F. (2012). A review of the large-scale production of carbon nanotubes: the practice of nanoscale process engineering. *Chin. Sci. Bull.* 57, 157–166. doi: 10.1007/s11434-011-4879-z

Inoue, S.-I., Magoshi, J., Tanaka, T., Magoshi, Y., and Becker, M. (2000). Atomic force microscopy: bombyx mori silk fibroin molecules and their higher order structure. *J. Polymer Sci.* 38, 1436–1439. doi: 10.1002/(SICI)1099-0488(20000601)38:11&<1436::AID-POLB30&>3.0.CO;2-8

Jung, C. (2000). Insight into protein structure and protein–ligand recognition by Fourier transform infrared spectroscopy. *J. Mol. Recognit.* 13, 325–351. doi: 10.1002/1099-1352(200011/12)13:6&<325::AID-JMR507&>3.0.CO;2-C

Kang, G. D., Nahm, J. H., Park, J. S., Moon, J. Y., Cho, C. S., and Yeo, J. H. (2000). Effects of poloxamer on the gelation of silk fibroin. *Marcromol. Rapid Commun.* 21, 788–791. doi: 10.1002/1521-3927(20000701)21:11&<788::AID-MARC788&>3.0.CO;2-X

Kapoor, S., and Kundu, S. C. (2016). Silk protein-based hydrogels: promising advanced materials for biomedical applications. *Acta Biomater.* 31, 17–32. doi: 10.1016/j.actbio.2015.11.034

Ling, S., Zhang, Q., Kaplan, D. L., Omenetto, F., Buehler, M. J., and Qin, Z. (2016). Printing of stretchable silk membranes for strain measurements. *Lab Chip* 16, 2459–2466. doi: 10.1039/C6LC00519E

Liu, Y., Ling, S., Wang, S., Chen, X., and Shao, Z. (2014). Thixotropic silk nano fibril-based hydrogel with extracellular matrix-like structure. *Biomater. Sci.* 2, 1338–1342. doi: 10.1039/C4BM00214H

Matsumoto, A., Chen, J., Collette, A. L., Kim, U. J., Altman, G. H., and Cebe, P., et al. (2006). Mechanisms of silk fibroin sol-gel transitions. *J. Phys. Chem. B* 110, 21630–21638. doi: 10.1021/jp056350v

Mouro, C., Jung, C., Bondon, A., and Simonneaux, G. (1997). Comparative fourier transform infrared studies of the secondary structure and the co heme ligand environment in cytochrome p-450cam and cytochrome p-420cam. *Biochemistry* 36, 8125–8134. doi: 10.1021/bi9700173

Numata, K., Katashima, T., and Sakai, T. (2011). State of water, molecular structure, and cytotoxicity of silk hydrogels. *Biomacromolecules* 12, 2137–2144. doi: 10.1021/bm200221u

Payne, A. R. (1962). The dynamic properties of carbon black-loaded natural rubber vulcanizates. *Part I. J. Appl. Polym. Sci.* 6, 57–63. doi: 10.1002/app.1962.070061906

Rousseau, M. E., Lefèvre, T., Beaulieu, L., Asakura, T., and Pézolet, M. (2004). Study of protein conformation and orientation in silkworm and spider silk fibers using raman microspectroscopy. *Biomacromolecules* 5, 2247–2257. doi: 10.1021/bm049717v

Shaffer, M. S. P., and Windle, A. H. (1992). Analogies between polymer solutions and carbonnanotube dispersions. *Macromolecules* 32, 6864–6866. doi: 10.1021/ma990095t

Shih, W. H., Shih, W. Y., Kim, S. I. Liu, J., and Aksay, I. A. (1990). Scaling behavior of the elastic properties of colloidal gels. *Phys. Rev. A* 42, 4772–4779. doi: 10.1103/PhysRevA.42.4772

Sonntag, R. C., and Russel, W. B. (1987). Elastic properties of flocculated networks. *J. Colloid Interface Sci.* 116, 485–489. doi: 10.1016/0021-9797(87)90144-5

Teramoto, H., and Miyazawa, M. (2005). Molecular orientation behavior of silk sericin film as revealed by atr infrared spectroscopy. *Biomacromolecules* 6, 2049–2057. doi: 10.1021/bm0500547

Terry, A. E., Knight, D. P., Porter, D., and Vollrath , F. (2004). pH Induced changes in the rheology of silk fibroin solution from the middle division of bombyx mori silkworm. *Biomacromolecules* 5, 768–772. doi: 10.1021/bm034381v

Tretinnikov, O. N., and Tamada, Y. (2001). Influence of casting temperature on the near-surface structure and wettability of cast silk fibroin films. *Langmuir* 17, 7406–7413. doi: 10.1021/la010791y

Urry, D. W., Peng, S. Q., Xu, J., and McPherson, D. T. (1997). Modulation of reactivity in native chemical ligation through the use of thiol additives. *J. Am. Chem. Soc.* 19, 11161–11162.

Wang, X., Kluge, J. A., Leisk, G. G., and Kaplan, D. L. (2008). Sonication-induced gelation of silk fibroin for cellencapsulation. *Biomaterials* 29, 1054–1064. doi: 10.1016/j.biomaterials.2007.11.003

Wu, X., Hou, J., Li, M., Wang, J., Kaplan, D. L., and Lu, S. (2012). Sodium dodecyl sulfate-induced rapid gelation of silk fibroin. *Acta Biomater.* 8, 2185–2192. doi: 10.1016/j.actbio.2012.03.007

Yin, Z., Wu, F., Xing, T., Yadavalli, V. K., Kundu, S. C., and Lu, S. (2017). A silk fibroin hydrogel with reversible sol–gel transition. *RSC Adv.* 7, 24085–24096. doi: 10.1039/C7RA02682J

Zheng, S., Li, G., Yao, W., and Yu, T. (1989). Raman spectroscopic investigation of the denaturation process of silk fibroin. *Appl. Spectrosc.* 43, 1269–1272. doi: 10.1366/0003702894203525

Conflict of Interest Statement: The authors declare that the research was conducted in the absence of any commercial or financial relationships that could be construed as a potential conflict of interest.

Copyright © 2019 Valentini, Bittolo Bon, Tripathi, Dalton and Pugno. This is an open-access article distributed under the terms of the Creative Commons Attribution License (CC BY). The use, distribution or reproduction in other forums is permitted, provided the original author(s) and the copyright owner(s) are credited and that the original publication in this journal is cited, in accordance with accepted academic practice. No use, distribution or reproduction is permitted which does not comply with these terms.

frontiers in Materials

MINI REVIEW
published: 08 May 2019
doi: 10.3389/fmats.2019.00098

Advances in Conducting, Biodegradable and Biocompatible Copolymers for Biomedical Applications

*Aruã C. da Silva and Susana I. Córdoba de Torresi**

Instituto de Química, Universidade de São Paulo, São Paulo, Brazil

Electroactive biomaterials are a new generation of "smart" biomaterials based on intrinsically conducting polymers (ICP). Among them, poly(3,4-ethylenedioxythiophene) (PEDOT), polypyrrole (PPy) and polyaniline (PANI) are well known conducting polymers that present excellent electrical and optical properties emerging as main candidates for potential biomedical applications. Additionally, the biodegradability of biomaterials is very useful and desirable. In this context, biodegradable polymers based on polyesters, such as poly(*D,L*-lactic acid) (PDLLA), polycaprolactone (PCL), and poly(glycolic acid) (PGA) appear to be promising candidates because of their good biocompatibility and, as a consequence, they have been attracting attention as sustainable alternatives for applications in medicine. Weak molecular interaction with cells, biocompatibility, biodegradability, mechanics and topography are some of the main challenges for the use of conducting polymers as biomaterials. In order to improve their own biocompatibility, the main strategies are whether by doping with specific counter ions (biodopants) or chemically modifying the monomers with different molecules. Although conventional ICPs still present low or none biodegradability, there are relatively few examples of biodegradable electroactive polymers in the literature. Recently, novel approaches have been applied to solve the problem of lack of biodegradability of conducting polymers, mainly through (1) synthesis of a modified electroactive oligomers connected via degradable ester linkages creating block copolymers and (2) synthesis of modified electroactive and biodegradable macromonomers based on polyesters used in a second step copolymerization with conductive monomers. This mini-review focuses on developing trends, challenges and summarizes the recent advances on synthesis of conducting, biodegradable and biocompatible copolymers in terms of optimizing the chemical properties to improved response toward different cells, aiming biomedical applications.

Keywords: biodegradation, conducting copolymers, biomaterials, biocompatible, electroactive macromonomers

OPEN ACCESS

Edited by:
Guilherme Mariz de Oliveira Barra, Federal University of Santa Catarina, Brazil

Reviewed by:
John George Hardy, Lancaster University, United Kingdom
Walter Caseri, ETH Zürich, Switzerland

****Correspondence:***
Susana I. Córdoba de Torresi
storresi@iq.usp.br

Specialty section:
This article was submitted to Polymeric and Composite Materials, a section of the journal Frontiers in Materials

Received: *08 February 2019*
Accepted: *17 April 2019*
Published: *08 May 2019*

Citation:
da Silva AC and Córdoba de Torresi SI (2019) Advances in Conducting, Biodegradable and Biocompatible Copolymers for Biomedical Applications. Front. Mater. 6:98. doi: 10.3389/fmats.2019.00098

INTRODUCTION

Electrically active and/or responsive tissues includes skeletal muscle, brain, and heart and had been widely explored by interfacing metallic or semi-conductor electrodes to provide electrical stimulation (Tehovnik, 1996; Merrill et al., 2005). This effect plays important role in the cellular division, development, migration, signaling, muscle contraction and would healing, for electroresponsive cell types such as myoblasts, fibroblasts, osteoblasts, chick embryo dorsal root ganglia, and neural crest cells, therefore attracts attention on tissue engineering and regenerative medicine (Tandon et al., 2009; Ghasemi-Mobarakeh et al., 2011).

Intrinsically conducting polymers (ICPs) are already demonstrated suitable for substitution of traditional electrodes based on conductors or semi-conductors (e.g., gold, platinum or glassy carbon) in biological applications due to their soft interface and electrical properties (Owens and Malliaras, 2010). Among them poly-3,4-ethylenedioxythiophene (PEDOT), polypyrrole (PPy), and polyaniline (PANI) are well known conducting polymers that present excellent electrical and optical properties (Skotheim and Reynolds, 2007).

Biodegradable materials are present in a lot of different areas, such as agriculture, medicine, packaging (storage), food, among others (Lendlein and Sisson, 2011). The biodegradable properties are usually present in polymeric materials by the loss of bulk weight through the polymer chain breaking into small pieces by enzymes, living organisms, environmental conditions or simply by water molecules (Siracusa et al., 2008; Vroman and Tighzert, 2009; Lendlein and Sisson, 2011). For biomedical applications, biodegradability is highly desirable for devices which perform their function and automatically "disappear" from the body, either reabsorbed or eliminated (Ulery et al., 2011). For this purpose, the degradation products must be biocompatible with biological systems; so, they are obtained by monomers commonly present in the body. Among them, polyesters appear as good candidates and have been extensively applied as biomaterials (Nair and Laurencin, 2007). Nonetheless, polyglycolide (PGA) (Mooney et al., 1996; Moutos et al., 2007), polylactides (PLA, PLLA or PDLLA) (Yang et al., 2005a,b; Lasprilla et al., 2012; Shi et al., 2016) and polycaprolactones (PCL) (Kweon et al., 2003; Ghasemi-Mobarakeh et al., 2008) have been the most investigated due to the ease obtaining and good mechanical properties.

Recently, a new class has emerged as potential candidates on biomedical field, the biodegradable electrically conducting polymers (BECP), which allies enough conductivity (i.e., allow electrical stimulation) with biodegradable properties (Rivers et al., 2002). Nowadays, a huge number of applications require biomaterials which can interface with cells, tissues or biomolecules. The molecular events at the biointerface usually involves a complex matrix with water molecules, proteins, and ions (Kasemo and Lausmaa, 1994; Ploux et al., 2010; Timko et al., 2010). In this context, proteins can regulate the cell fate, even inside cells (regulated by genes expressions) or those secreted from cells in the extracellular matrix (ECM). This plays an important role in the interaction with biomaterials once their orientation and conformation supposed to be fundamental for biocompatibility (Stevens and George, 2005). To understand how the ICP/cell biointerface works, several studies have investigated the role of adsorbed ECM proteins, among them fibronectin (FN), laminin and fibrinogen, for supporting cell adhesion, migration, proliferation, differentiation, and other processes (Rief et al., 2000; Kotwal and Schmidt, 2001; Oberhauser et al., 2002; Kandel et al., 2014). Some important properties have been found to play an important role, such as protein conformation, surface charges, different dopants or oxidized/reduced state of ICP (Svennersten et al., 2009; Gelmi et al., 2010, 2013a,b; Nelea and Kaartinen, 2010; Persson et al., 2011).

In this context, the present mini-review focus on developing trends and challenges discussing the recent advances on: (1) synthesis of a modified electroactive oligomers connected via degradable ester linkages creating block copolymers (**Figure 1A**) and (2) synthesis of modified electroactive and biodegradable macromonomers based on polyesters used in a second step of copolymerization with conductive monomers (**Figure 1B**) for conducting and biodegradable biomaterials with suitable interfacial properties for biomedical applications.

ELECTROACTIVE AND BIODEGRADABLE OLIGOMERS FOR BLOCK COPOLYMERS

In the mid-1970s, Heeger et al. demonstrated that polyacetylene $(CH)_x$ could turns into highly conductive when doped with iodine (Shirakawa et al., 1977), which led the authors to win the Nobel Prize in chemistry in 2000. For the next decades several studies of polymeric films with metallic and semiconducting properties had been reported (Street and Clarke, 1981). They established the important role of linear π-conjugated systems on electronic properties and conjugated polymers have emerged as the best prototypes for the linear π-conjugated systems, such as polypyrrole and polythiophenes (Roncali, 1997). In this context, some well-defined oligomer synthesis based on pyrrole were developed in order to control the synthesis and the π-conjugated system. Groenendaal and colleagues were able to obtain controlled conditions for oligo(pyrrole-2,5-diyl) from 2 to 18 units (Groenendaal et al., 1995). In 1995 and 1997, Miller et al. (Hong and Miller, 1995) and Leclerc et al. (Donat-Bouillud et al., 1997), respectively, proposed the synthesis of π-conjugated oligomers based on thiophene groups linked to polyesters. Then, in 2002, Langer et al. (Zelikin et al., 2002) proposed, for biomedical purposes, the synthesis of carboxylic acid functionalized pyrrole monomers obtaining a functionalized polypyrrole named as "erodible conducting polymer," based on ionizable and/or hydrolysable groups that could promote its partial water solubilization. The carboxylic acid functionalized polypyrroles were not able to break the conjugated chain but partially solubilize it; therefore, the correct term should be a partially biodegradable conducting polymer.

With this purpose in mind, Schmidt et al. (Rivers et al., 2002) based on the idea of electrical properties of thiophenes and knowing that three pyrrole rings were enough to achieve π-conjugation, they were the first to demonstrate, by using modification of previous synthesis of π-conjugated oligomers

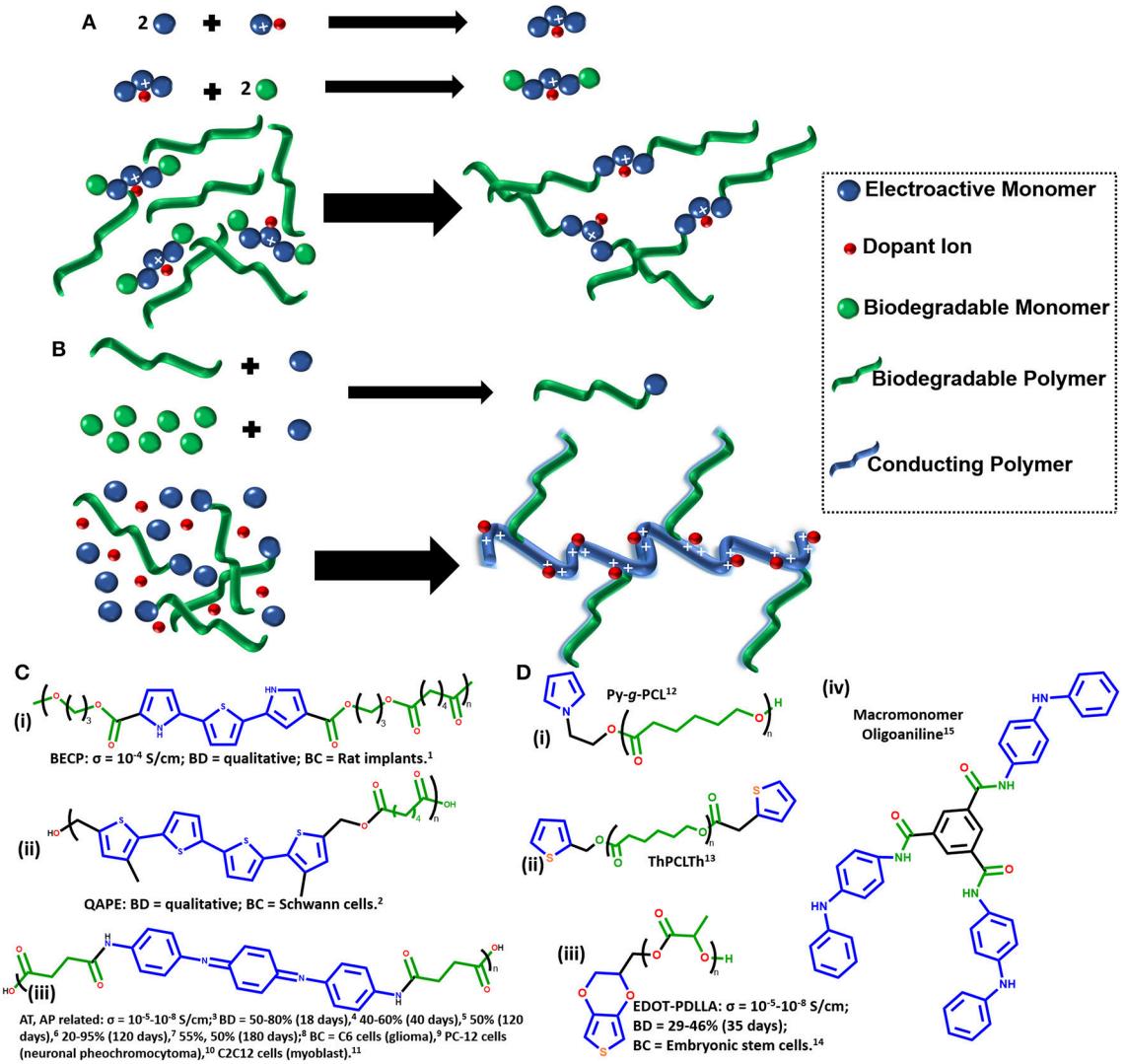

FIGURE 1 | (A) Schematic synthesis of electroactive oligomers and block copolymers. **(B)** Schematic synthesis of electroactive macromonomers and graft copolymers. **(C)** Chemical structure of electroactive and biodegradable oligomers. **(D)** Chemical structure of electroactive and biodegradable macromonomers. The σ is conductivity, BD is biodegradability and BC is biocompatibility. Blue color represents the conductive/electroactive molecules and green color represents the biodegradable molecules. The conductivity, biodegradability, and biocompatibility parameters are only reported for studies which aimed use the synthesized materials for biomedical applications. 1 (Rivers et al., 2002), 2 (Guimard et al., 2009), 3 (Ding et al., 2007; Huang et al., 2007, 2008; Guo et al., 2011d, 2012; Zhao et al., 2017), 4 (Zhao et al., 2017), 5 (Wang et al., 2015), 6 (Ding et al., 2007), 7 (Xie et al., 2015a), 8 (Huang et al., 2008), 9 (Huang et al., 2007), 10 (Huang et al., 2008), 11 (Xie et al., 2015a; Zhao et al., 2017), 12 (Mecerreyes et al., 2000, 2002), 13 (Türkan et al., 2011), 14 (da Silva et al., 2018a,b, 2019), 15 (Chao et al., 2007).

(Hong and Miller, 1995; Donat-Bouillud et al., 1997), the feasibility of creating the first BECP (**Figure 1Ci**) by using ester linkages (PLA) to achieve biodegradability and electrical conductivity based on three π-conjugated rings, a thiophene with two other pyrroles (Rivers et al., 2002). It was necessary to add a thiophene group in order to improve stability to the oligomer during synthesis (Rivers et al., 2002). Additionally, previous studies on macrophages activity using polyethylene revealed an important role of size and dose dependency, evidencing that small particles (0.24 μm) stimulated macrophages activity (Green et al., 2000; Ingram et al., 2004). Thus, Schmidt et al. (Rivers et al., 2002) assumed that the conducting oligomers could be easily removed *via* macrophages. However, the material was only possible to be doped with iodine vapor which could increase cytotoxicity. Trying to solve this problem, several years later the same group proposed the synthesis of 5,5‴-bis(hydroxymethyl)-3,3‴-dimethyl-2,2′:5′,2″:5″,2‴- quaterthiophene-*co*-adipic acid polyester (QAPE) (**Figure 1Cii**) as an electroactive oligothiophene unit (block of four thiophenes) with *in vitro* cytocompatibility studies for Schwann cells attested a non-cytotoxicity property (Guimard et al., 2009). Recently, Schmidt et al. (Hardy et al., 2014, 2015) reported electrochemically triggered biodegradable electroactive polymer oligoaniline-based materials for drug delivery.

Another remarkable synthesis of BECP was proposed by Wei et al. (Huang et al., 2007) in 2007, changing the electroactive

oligomer for an aniline pentamer (AP) (**Figure 1Ciii**) through ester linkages (based on PLA again) in a triblock copolymer called "PLA-*b*-AP-*b*-PLA." However, due to a molecular weight of ∼10 kDa, it did not present enough mechanical and plasticity properties for their practical applications. Thus, in the next year the same group proposed an improvement to the final properties of the biomaterial by adding multiblocks of PLA (M_w = 2.16 kDa) to get a higher molecular weight (M_w = 89.8 kDa) to the copolymer. Furthermore, it attended good solubility, mechanical properties and ease the processability, also keeping its own electroactivity, biodegradability and biocompatibility with *in vitro* experiments tested for PC-12 cells (Huang et al., 2008). Nonetheless, the cytotoxicity for the degradation products demonstrated in this study, where the aniline oligomers (AP) exhibited low cell viability for rat C6 cell line when compared to PLA and PLAAP, being ideal to use a low content of aniline oligomers(Huang et al., 2008). In parallel, Zhang et al. (Ding et al., 2007) proposed the polycondensation between carboxyl-capped aniline pentamer (CCAP) and hydroxyl-capped polyglycolide (PGA) by using N,N′-dicyclohexylcarbodiimide (DCC) as coupling reagent and tested its degradability (∼50% after 120 days) and electroactivity, but no cell experiments were performed.

In 2010, Albertsson et al. (Guo et al., 2010a) proposed the incorporation of amino-capped aniline trimer (ACAT), previously proposed by different research groups (Wei et al., 1996; Wang et al., 1998; Lu et al., 1999) and also the use of CCAP, both bonding to PLLA biodegradable chains but focused in different architectures of the biomaterials by using branched PLLAs. Then, the same group proposed the copolymerization of CCAP with linear and branched PCLs, obtained as a final product a linear and two different hyperbranched copolymers, also called "star-shape architecture" by themselves (Guo et al., 2010b). Later, poly(ethylene glycol) (PEG) was incorporated to the synthetic route in order to create hydrogels with conductive and biodegradable properties, based on acrylated PDLLA-PEG-PDLLA and aniline tetramer (AT), (Guo et al., 2011a) PCL-PEG-PCL with CCAP, (Guo et al., 2011b) and to improve the nondegradability of CS-*graft*-PANI hydrogels (Marcasuzaa et al., 2010) a CS-*graft*-AT was proposed by the same group (Guo et al., 2011c). After all the experience on synthesis with aniline oligomers and polyesters, the same group proposed a "universal two-step approach" for the synthesis of block copolymers oligoaniline-based, by using aniline dimer (AD) to obtain AT (Guo et al., 2011d). Then, by using the same approach, the size-tunable nanoparticles from the self-assembly coil-rod-coil triblock copolymers (Guo et al., 2011e) and the functionalization of PLA surface with AT to improve hydrophilicity were proposed (Guo et al., 2012).

In 2015, Ma et al. (Xie et al., 2015a) designed an electroactive degradable shape memory polymer network based on star-shaped, produced with PLA and ACAT as previously mentioned (Guo et al., 2010b), but now demonstrated their potential application for bone tissue engineering. Once conductive elastomers have been rarely reported in literature, the same group designed an AT-based electroconductive elastomer, which is a class of materials that mimic the mechanical properties of some specific tissues (Chen et al., 2015a) Their proposal led to high stretchability and low modulus material trying to simulate soft human tissues by using AT as rigid block, PEG and PLLA as soft ones. They investigated the molecular weight of PEG (1 to 6 kDa), amount of AT in the synthesis (3, 6, or 12% wt) and added end groups either cross-linked with trimethylolpropane (branched) or terminated with *n*-propanol (linear) (Chen et al., 2015a). Later, they designed a series of novel biocompatible biodegradable and electroactive polyurethane-urea (PUU) copolymers by combining the elastomeric property of polyurethane, conductive property of oligoaniline and the general good biodegradability and biocompatibility of PLLA (Chen et al., 2015b). Furthermore, it was investigated the effect of different molecular weight of PLLA (1500, 3500, or 8000 Da) on the final properties of the biomaterial (Chen et al., 2015b). Similar aniline oligomer-based biomaterials had been applied by the same research group for a wide range of applications, such as enhancement of myogenic differentiation of C2C12 myoblast cells, (Chen et al., 2015b; Wang et al., 2015; Xie et al., 2015a,b; Deng et al., 2016; Zhao et al., 2017) improve osteogenic differentiation from bone marrow derived mesenchymal stem cells (Li et al., 2016) and enhance myelin gene expression and neurotrophin secretion of Schwann cells (Wu et al., 2016).

Recently in the field of biomedical applications, Ma and colleagues had been substituting the conductive part of biomaterials for carbon nanotubes, avoiding aniline-based ones (Wu et al., 2017). It was already demonstrated that the conductivity of PANI and PANI-based material is strongly dependent on protonation (Cao et al., 1995; Stejskal et al., 2004). For biomedical applications, it supposed to have a deleterious effect when exposed to cells for a long period, either for biocompatibility or electrical stability (Meng et al., 2008; Green et al., 2012; Mawad et al., 2016). At this point, in 2017 Stevens et al. (Spicer et al., 2017) proposed a series of conjugated oligomers of EDOT as an interesting alternative to oligoanilines for tissue engineering.

ELECTROACTIVE AND BIODEGRADABLE MACROMONOMERS FOR GRAFT COPOLYMERS

Electroactive macromonomers can be defined as a reactive macromolecule which can be further electrochemically or chemically polymerized, due to electroactive functionalities on the chain, in order to obtain a copolymer. It is possible to copolymerize it with the same macromonomers, achieving "block copolymers structure," or by adding other individual monomers, grafting the macromonomer to other homopolymer chain, called "graft copolymers" (**Figure 1B**) (Yagci and Toppare, 2003).

Electroactive macromonomers are a very useful way to add new properties or functionalities to prepare block or graft copolymers. Usually the homopolymer presents completely different characteristics when compared to the copolymer. In this way, part of the interesting properties desired when adding electroactive macromonomers could be improved solubility, processability, biocompatibility, biodegradability,

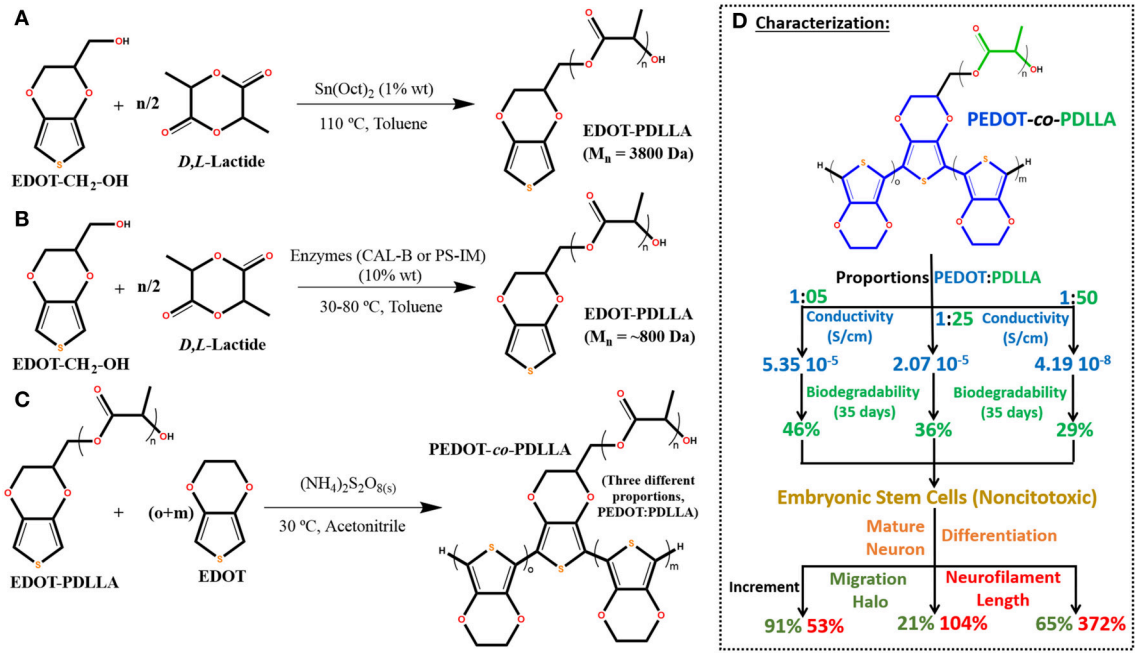

FIGURE 2 | Reactions of obtaining electroactive macromonomer of EDOT-PDLLA **(A)** via organometallic catalyst, **(B)** via enzymatic pathway and **(C)** "grafting through" copolymerization of PEDOT-*co*-PDLLA. **(D)** Summary of characterized properties for 1:05, 1:25, and 1:50 ratios (PEDOT:PDLLA) (da Silva et al., 2018a,b, 2019).

etc. However, it supposed to be aware that some functionalities on macromonomers can affect the π-electron density on conjugated backbone. It could either create a very stable conjugation which cannot be electropolymerized anymore or destabilize the macromonomer to degrade or promote side reactions instead the desired copolymer. An example of this is the addition of a oxadiazole group to oligothiophene chain, which are electron-withdrawing group, leading the thiophene trimers to do not electropolymerize and to promote an oxidative side reaction at high potentials that destroys the copolymer, whereas the thiophene pentamers can be electropolymerized (Fisyuk et al., 2005).

Toppare and Yagci have extensively worked with the "grafting through" method applied for electroactive macromonomers, mainly based on pyrrole and thiophene (Yagci and Toppare, 2003). Their approach was used to obtain ICPs with improved processability and mechanical properties, but focused on biosensing applications (Alkan et al., 1999; Kizilyar et al., 1999; Cirpan et al., 2001; Yagci and Toppare, 2003; Arica et al., 2005; Sahin et al., 2005; Uygun et al., 2010). There are a vast literature and excellent reviews on the grafting polymer chains for biointerfaces (Hackett et al., 2017), macromonomer techniques (Ito, 1998; Adachi and Tsukahara, 2015), functional materials (Strover et al., 2016), electroactive materials (Pron et al., 2010), biodegradable and electrically conducting polymers (Guo et al., 2013) and biomimetic conducting polymers (Hardy et al., 2013).

In 2000, Grande et al. (Mecerreyes et al., 2000) proposed the synthesis of novel pyrrole end-functional macromonomers prepared by ring-opening polymerization with ε-caprolactone (Py-*g*-PCL) (**Figure 1Di**). The aim of the work was not targeting the use for biomedical applications, but showed its versatility on copolymerizing with different polymers to change its final properties (Mecerreyes et al., 2002). In 2004, Catellani et al. (Dall'Acqua et al., 2004) proposed a intrinsically conductive cellulose-polypyrrole textile which they speculated could be useful from clothing to biomedical applications.

Recently, some of these graft copolymers based on electroactive macromonomer approach have been effectively proposed for biomedical field, mainly based on pyrrole (Domagala et al., 2014; Guo et al., 2017) aniline (**Figure 1Div**) (Chao et al., 2007; Peng et al., 2011) or thiophene groups,(Türkan et al., 2011) but most works are using the electroactive aniline-based oligomers previously discussed in this mini-review. Although some research groups propose new synthetic routes for novel copolymers and characterize the physical chemistry properties which could be useful in biomedical applications, studies of biocompatibility are not commonplace.

Regarding some of this issues, in 2018 our group proposed the synthesis for a novel electroactive macromonomer based on PDLLA with 3,4-ethylenedioxythiophene (EDOT) functionalized end group (**Figure 1Diii**) (da Silva et al., 2018a). Aiming biomedical applications, the proposed synthesis was performed either by using an organometallic catalyst (traditional method, with stannous octanoate) (**Figure 2A**) or by enzymatic pathway (two different lipases, CAL-B or PS-IM) (**Figure 2B**) to promote ring-opening polymerization of PLA. The organometallic catalyst builds up an electroactive macromonomer three times longer than the enzymatic ones.

Ozdemir et al. (Türkan et al., 2011) proposed a similar electroactive macromonomer with PCL and thiophene-capped (ThPCLTh) (**Figure 1Dii**) and reported the thiophene end groups could not react and polymerize. Thus, they copolymerized it with other conducting polymers (pyrrole and thiophene monomers) and no further cell experiments were performed to investigate the biocompatibility. Our study showed that the electroactive macromonomer of EDOT-PDLLA was able to electropolymerize at the same electrical potential of EDOT monomers, but no film formation was observed due to the soluble nature of EDOT-PDLLA in organic solvents, being able to produce only some non-conductive soluble oligomers (da Silva et al., 2018a).

Based on previous observations, we proposed by "grafting through" the electroactive macromonomer approach to synthesize copolymers of PEDOT-*co*-PDLLA in three different proportions (1:05, 1:25, and 1:50) (**Figures 2C,D**), leading to completely different final properties. The conductivity and biodegradability were characterized and noncytotoxic properties toward embryonic stem cells (**Figure 2D**) were found. Additionally, the copolymers presented an unexpected differentiation of the embryonic stem cells to mature neurons with migration halos and neurofilament lengths increased up to 65 and 370%, respectively, when compared to control (da Silva et al., 2018b).

In order to understand the different copolymer compositions, the nanoscale electrical properties of the films and the interaction with FN were characterized. It was observed that 1:50 copolymer films produced more uniform current dispersion (by Conductive-AFM) and the interface with different surface potential (negative interface, by Kelvin Probe Force Measurement) when compared to other copolymers. We speculate that it was related to a more homogeneously dispersed anionic doping on 1:50 during synthesis and film production. That nature of biointerface characteristics supposed to contribute for a higher FN affinity and stronger adsorption, 5 and 3 times stronger than for 1:05 and 1:25, respectively (da Silva et al., 2019).

CONCLUDING REMARKS AND OUTLOOK

Electroactive aniline-based oligomers have been extensively studied, and their toxicity is a limiting factor for biomedical applications. Proposals of new electroactive oligomers based on more stable and biocompatible electroactive monomers and/or oligomers may be interesting in this field. Additionally, another alternative may be the use of very low aniline-based oligomers content or to create new strategies to increase the biocompatibility.

The electroactive macromonomers emerge as a useful tool to obtain graft copolymers with conductivity and biodegradability properties. However, more studies are still necessary to apply that kind of biomaterials on cellular experiments, such as tissue engineering, biomedical devices, scaffold/templates, etc. It would provide great insights for the development of this area.

Another important remark is related to the fact that not only the synthesis of new materials is worth but also to go deeper in their characterization. Recently, important studies have been specifically looking to the biointerface of the materials with cells, whether by studying nanoscale properties or interactions with biomolecules, trying to understand what should be better for cell interfacing. Finally, the knowledge would lead us for smarter biomaterial designing in the future.

AUTHOR CONTRIBUTIONS

All authors listed have made a substantial, direct and intellectual contribution to the work, and approved it for publication.

ACKNOWLEDGMENTS

We gratefully acknowledge Brazilian agencies (São Paulo Research Foundation FAPESP, Proc. 2015/26308-7 and 2018/13492-2; the National Council for Scientific and Technological Development, CNPq; and Coordination of Improvement of Higher Level Personnel, CAPES) for their financial support. ACdS thanks FAPESP (Proc. 2014/09353-6, 2017/00705-5) for scholarships.

REFERENCES

Adachi, K., and Tsukahara, Y. (2015). *Encyclopedia of Polymeric Nanomaterials*. Heidelberg: Springer, 1167–1175.

Alkan, S., Toppare, L., Hepuzer, Y., and Yagci, Y. (1999). Block copolymers of thiophene-capped poly(methyl methacrylate) with pyrrole. *J. Polym. Sci. Part A Polym. Chem*. 37, 4218–4225. doi: 10.1002/(SICI)1099-0518(19991115)37:22<4218::AID-POLA22>3.0.CO;2-Z

Arica, M. Y., Bayramoglu, G., Arica, B., Yalçin, E., Ito, K., and Yagci, Y. (2005). Novel hydrogel membrane based on copoly(hydroxyethyl methacrylate/p-vinylbenzyl-poly(ethylene oxide)) for biomedical applications: properties and drug release characteristics. *Macromol. Biosci*. 5, 983–992. doi: 10.1002/mabi.200500091

Cao, Y., Qiu, J., and Smith, P. (1995). Effect of solvents and co-solvents on the processibility of polyaniline: I. solubility and conductivity studies. *Synth. Met*. 69, 187–190. doi: 10.1016/0379-6779(94)02412-R

Chao, D., Ma, X., Lu, X., Cui, L., Mao, H., Zhang, W., et al. (2007). Electroactive hyperbranched polyamide synthesized by oxidative coupling polymerization within an A2 + B3 Strategy. *Macromol. Chem. Phys*. 208, 658–664. doi: 10.1002/macp.200600571

Chen, J., Dong, R., Ge, J., Guo, B., and Ma, P. X. (2015b). Biocompatible, biodegradable, and electroactive polyurethane-urea elastomers with tunable hydrophilicity for skeletal muscle tissue engineering. *ACS Appl. Mater. Interfaces* 7, 28273–28285. doi: 10.1021/acsami.5b10829

Chen, J., Guo, B., Eyster, T. W., and Ma, P. X. (2015a). Super stretchable electroactive elastomer formation driven by aniline trimer self-assembly. *Chem. Mater*. 27, 5668–5677. doi: 10.1021/acs.chemmater.5b02086

Cirpan, A., Alkan, S., Toppare, L., David, G., and Yagci, Y. (2001). Synthesis and electroactivity of pyrrole end-functionalized poly(2-methyl-2-oxazoline). *Eur. Polym. J*. 37, 2225–2229. doi: 10.1016/S0014-3057(01)00103-3

da Silva, A. C., Augusto, T., Andrade, L. H., and Córdoba de Torresi, S. I. (2018a). One pot biocatalytic synthesis of a biodegradable electroactive macromonomer based on 3,4-ethylenedioxytiophene and poly(l -lactic acid). *Mater. Sci. Eng. C* 83, 35–43. doi: 10.1016/j.msec.2017.09.007

da Silva, A. C., Higgins, M. J., and Córdoba de Torresi, S. I. (2019). The effect of nanoscale surface electrical properties of partially biodegradable PEDOT-co-PDLLA conducting polymers on protein adhesion investigated by atomic force microscopy. *Mater. Sci. Eng. C.* 99, 468-478. doi: 10.1016/j.msec.2019.01.103

da Silva, A. C., Semeano, A. T. S., Dourado, A. H. B., Ulrich, H., and Cordoba de Torresi, S. I. (2018b). Novel conducting and biodegradable copolymers with noncytotoxic properties toward embryonic stem cells. *ACS Omega* 3, 5593–5604. doi: 10.1021/acsomega.8b00510

Dall'Acqua, L., Tonin, C., Peila, R., Ferrero, F., and Catellani, M. (2004). Performances and properties of intrinsic conductive cellulose-polypyrrole textiles. *Synth. Met.* 146, 213–221. doi: 10.1016/j.synthmet.2004.07.005

Deng, Z., Guo, Y., Zhao, X., Li, L., Dong, R., Guo, B., et al. (2016). Stretchable degradable and electroactive shape memory copolymers with tunable recovery temperature enhance myogenic differentiation. *Acta Biomater.* 46, 234–244. doi: 10.1016/j.actbio.2016.09.019

Ding, C., Wang, Y., and Zhang, S. (2007). Synthesis and characterization of degradable electrically conducting copolymer of aniline pentamer and polyglycolide. *Eur. Polym. J.* 43, 4244–4252. doi: 10.1016/j.eurpolymj.2007.07.032

Domagala, A., Maksymiak, M., Janeczek, H., Musiol, M., Turczyn, R., Ledwon, P., et al. (2014). Oligo-3-hydroxybutyrate functionalised pyrroles for preparation of biodegradable conductive polymers. *J. Mater. Sci.* 49, 5227–5236. doi: 10.1007/s10853-014-8241-0

Donat-Bouillud, A., Mazerolle, L., Gagnon, P., Goldenberg, L., Petty, M. C., and Leclerc, M. (1997). Synthesis, characterization, and processing of new electroactive and photoactive polyesters derived from oligothiophenes. *Chem. Mater.* 9, 2815–2821. doi: 10.1021/cm9701926

Fisyuk, A. S., Demadrille, R., Querner, C., Zagorska, M., Bleusec, J., and Pron, A. (2005). Mixed alkylthiophene-based heterocyclic polymers containing oxadiazole units via electrochemical polymerisation: spectroscopic, electrochemical and spectroelectrochemical properties. *New J. Chem.* 29:707. doi: 10.1039/b415587d

Gelmi, A., Higgins, M. J., and Wallace, G. G. (2010). Physical surface and electromechanical properties of doped polypyrrole biomaterials. *Biomaterials* 31, 1974–1983. doi: 10.1016/j.biomaterials.2009.11.040

Gelmi, A., Higgins, M. J., and Wallace, G. G. (2013a). Quantifying fibronectin adhesion with nanoscale spatial resolution on glycosaminoglycan doped polypyrrole using atomic force microscopy. *Biochim. Biophys. Acta Gen. Subj.* 1830, 4305–4313. doi: 10.1016/j.bbagen.2013.03.005

Gelmi, A., Higgins, M. J., and Wallace, G. G. (2013b). Resolving sub-molecular binding and electrical switching mechanisms of single proteins at electroactive conducting polymers. *Small* 9, 393–401. doi: 10.1002/smll.201201686

Ghasemi-Mobarakeh, L., Prabhakaran, M. P., Morshed, M., Nasr-Esfahani, M.-H., and Ramakrishna, S. (2008). Electrospun poly(ε-caprolactone)/gelatin nanofibrous scaffolds for nerve tissue engineering. *Biomaterials* 29, 4532–4539. doi: 10.1016/j.biomaterials.2008.08.007

Ghasemi-Mobarakeh, L., Prabhakaran, M. P., Morshed, M., Nasr-Esfahani, M. H., Baharvand, H., Kiani, S., et al. (2011). Application of conductive polymers, scaffolds and electrical stimulation for nerve tissue engineering. *J. Tissue Eng. Regen. Med.* 5, e17–e35. doi: 10.1002/term.383

Green, R. A., Hassarati, R. T., Bouchinet, L., Lee, C. S., Cheong, G. L., Yu, J. F., et al. (2012). Substrate dependent stability of conducting polymer coatings on medical electrodes. *Biomaterials* 33, 5875–5886. doi: 10.1016/j.biomaterials.2012.05.017

Green, T. R., Fisher, J., Matthews, J. B., Stone, M. H., and Ingham, E. (2000). Effect of size and dose on bone resorption activity of macrophages by *in vitro* clinically relevant ultra high molecular weight polyethylene particles. *J. Biomed. Mater. Res.* 53, 490–497. doi: 10.1002/1097-4636(200009)53:5<490::AID-JBM7>3.0.CO;2-7

Groenendaal, L., Peerlings, H. W. I., van Dongen, J. L. J., Havinga, E. E., Vekemans, J. A. J. M., and Meijer, E. W., et al. (1995). Well-defined oligo(pyrrole-2,5-diyl)s by the ullmann reaction. *Macromolecules* 28, 116–123. doi: 10.1021/ma00105a015

Guimard, N. K. E., Sessler, J. L., and Schmidt, C. E. (2009). Toward a biocompatible and biodegradable copolymer incorporating electroactive oligothiophene units. *Macromolecules* 42, 502–511. doi: 10.1021/ma8019859

Guo, B., Finne-Wistrand, A., and Albertsson, A.-C. (2010b). Enhanced electrical conductivity by macromolecular architecture: hyperbranched electroactive and degradable block copolymers based on poly(ε-caprolactone) and aniline pentamer. *Macromolecules* 43, 4472–4480. doi: 10.1021/ma100530k

Guo, B., Finne-Wistrand, A., and Albertsson, A.-C. (2011a). Degradable and electroactive hydrogels with tunable electrical conductivity and swelling behavior. *Chem. Mater.* 23, 1254–1262. doi: 10.1021/cm103498s

Guo, B., Finne-Wistrand, A., and Albertsson, A.-C. (2011b). Versatile functionalization of polyester hydrogels with electroactive aniline oligomers. *J. Polym. Sci. Part A Polym. Chem.* 49, 2097–2105. doi: 10.1002/pola.24643

Guo, B., Finne-Wistrand, A., and Albertsson, A.-C. (2011d). Universal two-step approach to degradable and electroactive block copolymers and networks from combined ring-opening polymerization and post-functionalization via oxidative coupling reactions. *Macromolecules* 44, 5227–5236. doi: 10.1021/ma2009595

Guo, B., Finne-Wistrand, A., and Albertsson, A.-C. (2011e). Simple route to size-tunable degradable and electroactive nanoparticles from the self-assembly of conducting coil-rod-coil triblock copolymers. *Chem. Mater.* 23, 4045–4055. doi: 10.1021/cm201782v

Guo, B., Finne-Wistrand, A., and Albertsson, A.-C. (2012). Electroactive hydrophilic polylactide surface by covalent modification with tetraaniline. *Macromolecules* 45, 652–659. doi: 10.1021/ma202508h

Guo, B., Finne-Wistrand, A., and Albertsson, A. C. (2010a). Molecular architecture of electroactive and biodegradable copolymers composed of polylactide and carboxyl-capped aniline trimer. *Biomacromolecules* 11, 855–863. doi: 10.1021/bm9011248

Guo, B., Finne-Wistrand, A., and Albertsson, A. C. (2011c). Facile synthesis of degradable and electrically conductive polysaccharide hydrogels. *Biomacromolecules* 12, 2601–2609. doi: 10.1021/bm200389t

Guo, B., Glavas, L., and Albertsson, A.-C. (2013). Biodegradable and electrically conducting polymers for biomedical applications. *Prog. Polym. Sci.* 38, 1263–1286. doi: 10.1016/j.progpolymsci.2013.06.003

Guo, H., Qiao, T., Jiang, S., Li, T., Song, P., Zhang, B., et al. (2017). Aligned poly (glycolide-lactide) fiber membranes with conducting polypyrrole. *Polym. Adv. Technol.* 28, 484–490. doi: 10.1002/pat.3912

Hackett, A. J., Malmström, J., and Travas-Sejdic, J. (2017). Functionalization of conducting polymers for biointerface applications. *Prog. Polym. Sci.* 70, 18–33. doi: 10.1016/j.progpolymsci.2017.03.004

Hardy, J. G., Amend, M. N., Geissler, S., Lynch, V. M., and Schmidt, C. E. (2015). Peptide-directed assembly of functional supramolecular polymers for biomedical applications: electroactive molecular tongue-twisters (oligoalanine-oligoaniline-oligoalanine) for electrochemically enhanced drug delivery. *J. Mater. Chem. B* 3, 5005–5009. doi: 10.1039/C5TB00106D

Hardy, J. G., Lee, J. Y., and Schmidt, C. E. (2013). Biomimetic conducting polymer-based tissue scaffolds. *Curr. Opin. Biotechnol.* 24, 847–854. doi: 10.1016/j.copbio.2013.03.011

Hardy, J. G., Mouser, D. J., Arroyo-Currás, N., Geissler, S., Chow, J. K., Nguy, L., et al. (2014). Biodegradable electroactive polymers for electrochemically-triggered drug delivery. *J. Mater. Chem. B* 2, 6809–6822. doi: 10.1039/C4TB00355A

Hong, Y., and Miller, L. L. (1995). An electrically conducting polyester that has isolated quatrathiophene units in the main chain. *Chem. Mater.* 7, 1999–2000. doi: 10.1021/cm00059a003

Huang, L., Hu, J., Lang, L., Wang, X., Zhang, P., Jing, X., et al. (2007). Synthesis and characterization of electroactive and biodegradable ABA block copolymer of polylactide and aniline pentamer. *Biomaterials* 28, 1741–1751. doi: 10.1016/j.biomaterials.2006.12.007

Huang, L., Zhuang, X., Hu, J., Lang, L., Zhang, P., Wang, Y., Huang, L., et al. (2008). Synthesis of biodegradable and electroactive multiblock polylactide and aniline pentamer copolymer for tissue engineering applications. *Biomacromolecules* 9, 850–858. doi: 10.1021/bm7011828

Ingram, J. H., Stone, M., Fisher, J., and Ingham, E. (2004). The influence of molecular weight, crosslinking and counterface roughness on TNF-alpha production by macrophages in response to ultra high molecular weight polyethylene particles. *Biomaterials* 25, 3511–3522. doi: 10.1016/j.biomaterials.2003.10.054

Ito, K. (1998). Polymeric design by macromonomer technique. *Prog. Polym. Sci.* 23, 581–620. doi: 10.1016/S0079-6700(97)00049-X

Kandel, J., Lee, H. S., Sobolewski, P., Tomczyk, N., Composto, R. J., and Eckmann, D. M. (2014). Chemically grafted fibronectin for use in QCM-D cell studies. *Biosens. Bioelectron*. 58, 249–257. doi: 10.1016/j.bios.2014.02.053

Kasemo, B., and Lausmaa, J. (1994). Material-tissue interfaces: the role of surface properties and processes. *Environ. Health Perspect*. 102, 41–45. doi: 10.1289/ehp.94102s541

Kizilyar, N., Akbulut, U., Toppare, L., Özden, M. Y., and Yagci, Y. (1999). Immobilization of invertase in conducting polypyrrole/polytetrahydrofuran graft polymer matrices. *Synth. Met*. 104, 45–50. doi: 10.1016/S0379-6779(99)00033-8

Kotwal, A., and Schmidt, C. E. (2001). Electrical stimulation alters protein adsorption and nerve cell interactions with electrically conducting biomaterials. *Biomaterials* 22, 1055–1064. doi: 10.1016/S0142-9612(00)00344-6

Kweon, H., Yoo, M. K., Park, I. K., Kim, T. H., Lee, H. C., Lee, H. S., et al. (2003). A novel degradable polycaprolactone networks for tissue engineering. *Biomaterials* 24, 801–808. doi: 10.1016/S0142-9612(02)00370-8

Lasprilla, A. J., Martinez, G. A., Lunelli, B. H., Jardini, A. L., and Filho, R. M. (2012). Poly-lactic acid synthesis for application in biomedical devices - a review. *Biotechnol. Adv*. 30, 321–328. doi: 10.1016/j.biotechadv.2011.06.019

Lendlein, A., and Sisson, A. (2011). *Handbook of Biodegradable Polymers*. (Weinheim: Wiley-VCH Verlag GmbH & Co. KGaA). doi: 10.1002/9783527635818

Li, L., Yu, M., Ma, P. X., and Guo, B. (2016). Electroactive degradable copolymers enhancing osteogenic differentiation from bone marrow derived mesenchymal stem cells. *J. Mater. Chem. B* 4, 471–481. doi: 10.1039/C5TB01899D

Lu, W., Sheng Meng, X., and Yuan Wang, Z. (1999). Electrochemical behavior of a new electroactive polyimide derived from aniline trimer. *J. Polym. Sci. Part A Polym. Chem*. 37, 4295–4301. doi: 10.1002/(SICI)1099-0518(19991201)37:23<4295::AID-POLA5>3.0.CO;2-X

Marcasuzaa, P., Reynaud, S., Ehrenfeld, F., Khoukh, A., and Desbrieres, J. (2010). Chitosan- graft -polyaniline-based hydrogels: elaboration and properties. *Biomacromolecules* 11, 1684–1691. doi: 10.1021/bm100379z

Mawad, D., Mansfield, C., Lauto, A., Perbellini, F., Nelson, G. W., Tonkin, J., et al. (2016). A conducting polymer with enhanced electronic stability applied in cardiac models. *Sci. Adv*. 2:e1601007. doi: 10.1126/sciadv.1601007

Mecerreyes, D., Pomposo, J. A., Bengoetxea, M., and Grande, H. (2000). Novel pyrrole end-functional macromonomers prepared by ring-opening and atom-transfer radical polymerizations. *Macromolecules* 33, 5846–5849. doi: 10.1021/ma0003046

Mecerreyes, D., Stevensb, R., Nguyen, C., Pomposo, J. A., Bengoetxea, M., Grande, H., et al. (2002). Synthesis and characterization of polypyrrole-graft-poly(ε-caprolactone) copolymers: new electrically conductive nanocomposites. *Synth. Met*. 126, 173–178. doi: 10.1016/S0379-6779(01)00503-3

Meng, S., Rouabhia, M., Shi, G., and Zhang, Z. (2008). Heparin dopant increases the electrical stability, cell adhesion, and growth of conducting polypyrrole/poly(L,L-lactide) composites. *J. Biomed. Mater. Res. Part A* 87, 332–344. doi: 10.1002/jbm.a.31735

Merrill, D. R., Bikson, M., and Jefferys, J. G. (2005). Electrical stimulation of excitable tissue: design of efficacious and safe protocols. *J. Neurosci. Methods* 141, 171–198. doi: 10.1016/j.jneumeth.2004.10.020

Mooney, D. J., Mazzoni, C. L., Breuer, C., McNamara, K., Hern, D., Vacanti, J. P., et al. (1996). Stabilized polyglycolic acid fibre-based tubes for tissue engineering. *Biomaterials* 17, 115–124. doi: 10.1016/0142-9612(96)85756-5

Moutos, F. T., Freed, L. E., and Guilak, F. (2007). A biomimetic three-dimensional woven composite scaffold for functional tissue engineering of cartilage. *Nat. Mater*. 6, 162–167. doi: 10.1038/nmat1822

Nair, L. S., and Laurencin, C. T. (2007). Biodegradable polymers as biomaterials. *Prog. Polym. Sci*. 32, 762–798. doi: 10.1016/j.progpolymsci.2007.05.017

Nelea, V., and Kaartinen, M. T. (2010). Periodic beaded-filament assembly of fibronectin on negatively charged surface. *J. Struct. Biol*. 170, 50–59. doi: 10.1016/j.jsb.2010.01.009

Oberhauser, A. F., Badilla-Fernandez, C., Carrion-Vazquez, M., and Fernandez, J. M. (2002). The mechanical hierarchies of fibronectin observed with single-molecule AFM. *J. Mol. Biol*. 319, 433–447. doi: 10.1016/S0022-2836(02)00306-6

Owens, R. M., and Malliaras, G. G. (2010). Organic electronics at the interface with biology. *MRS Bull*. 35, 449–456. doi: 10.1557/mrs2010.583

Peng, C.-W., Hsu, C.-H., Lin, K. H., Li, P.-G., Hsieh, M.-F., Wie, Y., et al. (2011). Electrochemical corrosion protection studies of aniline-capped aniline trimer-based electroactive polyurethane coatings. *Electrochim. Acta* 58, 614–620. doi: 10.1016/j.electacta.2011.10.002

Persson, K. M., Karlsson, R., Svennersten, K., Löffler, S., and Jager, E. W. (2011). Electronic control of cell detachment using a self-doped conducting polymer. *Adv. Mater*. 23, 4403–4408. doi: 10.1002/adma.201101724

Ploux, L., Ponche, A., and Anselme, K. (2010). Bacteria/material interfaces: role of the material and cell wall properties. *J. Adhes. Sci. Technol*. 24, 2165–2201. doi: 10.1163/016942410X511079

Pron, A., Gawrys, P., Zagorska, M., Djurado, D., and Demadrille, R. (2010). Electroactive materials for organic electronics: preparation strategies, structural aspects and characterization techniques. *Chem. Soc. Rev*. 39:2577. doi: 10.1039/b907999h

Rief, M., Gautel, M., and Gaub, H. E. (2000). "Unfolding Forces of Titin and Fibronectin Domains Directly Measured by AFM," in *Elastic Filaments of the Cell. Advances in Experimental Medicine and Biology, Vol. 481*, eds H. L. Granzier and G. H. Pollack (Boston, MA: Springer), 129–141. doi: 10.1007/978-1-4615-4267-4_8

Rivers, T. J., Hudson, T. W., and Schmidt, C. E. (2002). Synthesis of a novel, biodegradable electrically conducting polymer for biomedical applications. *Adv. Funct. Mater*. 12:33. doi: 10.1002/1616-3028(20020101)12:1<33::AID-ADFM33>3.0.CO;2-E

Roncali, J. (1997). Synthetic principles for bandgap control in linear π-conjugated systems. *Chem. Rev*. 97, 173–206. doi: 10.1021/cr950257t

Sahin, E., Camurlu, P., Toppare, L., Mercore, V. M., Cianga, I., Yag, Y., et al. (2005). Conducting copolymers of thiophene functionalized polystyrenes with thiophene. *J. Electroanal. Chem*. 579, 189–197. doi: 10.1016/j.jelechem.2005.01.017

Shi, K., Wang, Y. L., Qu, Y., Liao, J. F., Chu, B. Y., Zhang, H. P., Shi, K., et al (2016). Synthesis, characterization, and application of reversible PDLLA-PEG-PDLLA copolymer thermogels *in vitro* and *in vivo*. *Sci. Rep*. 6:19077. doi: 10.1038/srep19077

Shirakawa, H., Louis, E. J., MacDiarmid, A. G., Chiang, C. K., and Heeger, A. J. (1977). Synthesis of electrically conducting organic polymers: halogen derivatives of polyacetylene, (CH) x. *J. Chem. Soc. Chem. Commun*. 578–580. doi: 10.1039/c39770000578 Available online at: https://pubs.rsc.org/en/content/articlelanding/1977/c3/c39770000578#!divAbstract

Siracusa, V., Rocculi, P., Romani, S., and Rosa, M. D. (2008). Biodegradable polymers for food packaging: a review. *Trends Food Sci. Technol*. 19, 634–643. doi: 10.1016/j.tifs.2008.07.003

Skotheim, T. A., and Reynolds, J. (2007). *Handbook of Conducting Polymers, 2 Volume Set*. (Boca Raton: CRC Press). doi: 10.1201/9781420043594

Spicer, C. D., Booth, M. A., Mawad, D., Armgarth, A., Nielsen, C. B., and Stevens, M. M. (2017). Synthesis of hetero-bifunctional, end-capped oligo-EDOT derivatives. *Chem* 2, 125–138. doi: 10.1016/j.chempr.2016.12.003

Stejskal, J., Hlavatá, D., Holler, P., Trchová, M., Prokeš, J., Sapurina, I., et al. (2004). Polyaniline prepared in the presence of various acids: a conductivity study. *Polym. Int*. 53, 294–300. doi: 10.1002/pi.1406

Stevens, M. M., and George, J. H. (2005). Exploring and engineering the cell surface interface. *Science*. 310, 1135–1138. doi: 10.1126/science.1106587

Street, G. B., and Clarke, T. C. (1981). Conducting polymers: a review of recent work. *IBM J. Res. Dev*. 25, 51–57. doi: 10.1147/rd.251.0051

Strover, L. T., Malmström, J., and Travas-Sejdic, J. (2016). Graft copolymers with conducting polymer backbones: a versatile route to functional materials. *Chem. Rec*. 16, 393–418. doi: 10.1002/tcr.201500216

Svennersten, K., Bolin, M. H., Jager, E. W., Berggren, M., Richter-Dahlfors, A., Svennersten, K., et al. (2009). Electrochemical modulation of epithelia formation using conducting polymers. *Biomaterials* 30, 6257–6264. doi: 10.1016/j.biomaterials.2009.07.059

Tandon, N., Cannizzaro, C., Chao, P. H., Maidhof, R., Marsano, A., Au, H. T., et al. (2009). Electrical stimulation systems for cardiac tissue engineering. *Nat. Protoc*. 4, 155–173. doi: 10.1038/nprot.2008.183

Tehovnik, E. J. (1996). Electrical stimulation of neural tissue to evoke behavioral responses. *J. Neurosci. Methods* 65, 1–17. doi: 10.1016/0165-0270(95)00131-X

Timko, B. P., Cohen-Karni, T., Qing, Q., Tian, B., and Lieber, C. M. (2010). Design and implementation of functional nanoelectronic interfaces with biomolecules,

cells, and tissue using nanowire device arrays. *IEEE Trans. Nanotechnol.* 9, 269–280. doi: 10.1109/TNANO.2009.2031807

Türkan, A., Yilmaz, F., Küçük, A. Ç., and Özdemir, Y. (2011). One-pot two-step lipase-catalyzed synthesis of α,ω-thiophene-capped poly(ε-caprolactone) macromonomers and their use in electropolymerization. *Polym. Bull.* 67, 1483–1498. doi: 10.1007/s00289-011-0467-2

Ulery, B. D., Nair, L. S., and Laurencin, C. T. (2011). Biomedical applications of biodegradable polymers. *J. Polym. Sci. Part B Polym. Phys.* 49, 832–864. doi: 10.1002/polb.22259

Uygun, M., Tasdelen, M. A., and Yagci, Y. (2010). Influence of type of initiation on thiol–ene "click" chemistry. *Macromol. Chem. Phys.* 211, 103–110. doi: 10.1002/macp.200900442

Vroman, I., and Tighzert, L. (2009). Biodegradable polymers. *Materials* 2, 307–344. doi: 10.3390/ma2020307

Wang, L., Wu, Y., Guo, B., and Ma, P. X. (2015). Nanofiber yarn/hydrogel core-shell scaffolds mimicking native skeletal muscle tissue for guiding 3D myoblast alignment, elongation, and differentiation. *ACS Nano.* 9, 9167–9179. doi: 10.1021/acsnano.5b03644

Wang, Z., Y., Yang, C., Gao, J. P., Lin, J., and Meng, X. S. (1998). Electroactive polyimides derived from amino-terminated aniline trimer. *Macromolecules* 31, 2702–2704. doi: 10.1021/ma971782s

Wei, Y., Yang, C., and Ding, T. (1996). A one-step method to synthesize N,N′-bis(4′-aminophenyl)-1,4-quinonenediimine and its derivatives. *Tetrahedron Lett.* 37, 731–734. doi: 10.1016/0040-4039(95)02300-3

Wu, Y., Wang, L., Guo, B., and Ma, P. X. (2017). Interwoven aligned conductive nanofiber yarn/hydrogel composite scaffolds for engineered 3D cardiac anisotropy. *ACS Nano.* 11, 5646–5659. doi: 10.1021/acsnano.7b01062

Wu, Y., Wang, L., Guo, B., Shao, Y., and Ma, P. X. (2016). Electroactive biodegradable polyurethane significantly enhanced Schwann cells myelin gene expression and neurotrophin secretion for peripheral nerve tissue engineering. *Biomaterials* 87, 18–31. doi: 10.1016/j.biomaterials.2016.02.010

Xie, M., Wang, L., Ge, J., Guo, B., and Ma, P. X. (2015a). Strong electroactive biodegradable shape memory polymer networks based on star-shaped polylactide and aniline trimer for bone tissue engineering. *ACS Appl. Mater. Interfaces* 7, 6772–6781. doi: 10.1021/acsami.5b00191

Xie, M., Wang, L., Guo, B., Wang, Z., Chen, Y. E., and Ma, P. X. (2015b). Ductile electroactive biodegradable hyperbranched polylactide copolymers enhancing myoblast differentiation. *Biomaterials* 71, 158–167. doi: 10.1016/j.biomaterials.2015.08.042

Yagci, Y., and Toppare, L. (2003). Electroactive macromonomers based on pyrrole and thiophene: a versatile route to conducting block and graft polymers. *Polym. Int.* 52, 1573–1578. doi: 10.1002/pi.1341

Yang, F., Murugan, R., Wang, S., and Ramakrishna, S. (2005b). Electrospinning of nano/micro scale poly(l-lactic acid) aligned fibers and their potential in neural tissue engineering. *Biomaterials* 26, 2603–2610. doi: 10.1016/j.biomaterials.2004.06.051

Yang, J., Kim, D. H., Hendricks, J. L., Leach, M., Northey, R., and Martin, D. C. (2005a). Ordered surfactant-templated poly(3,4-ethylenedioxythiophene) (PEDOT) conducting polymer on microfabricated neural probes. *Acta Biomater.* 1, 125–136. doi: 10.1016/j.actbio.2004.09.006

Zelikin, A. N., Lynn, D. M., Farhadi, J., Martin, I., Shastri, V., and Langer, R. (2002). Erodible conducting polymers for potential biomedical applications. *Angew. Chemie Int. Ed.* 41, 141–144. doi: 10.1002/1521-3773(20020104)41:1<141::AID-ANIE141>3.0.CO;2-V

Zhao, X., Dong, R., Guo, B., and Ma, P. X. (2017). Dopamine-incorporated dual bioactive electroactive shape memory polyurethane elastomers with physiological shape recovery temperature, high stretchability, and enhanced c2c12 myogenic differentiation. *ACS Appl. Mater. Interfaces* 9, 29595–29611. doi: 10.1021/acsami.7b10583

Conflict of Interest Statement: The authors declare that the research was conducted in the absence of any commercial or financial relationships that could be construed as a potential conflict of interest.

Copyright © 2019 da Silva and Córdoba de Torresi. This is an open-access article distributed under the terms of the Creative Commons Attribution License (CC BY). The use, distribution or reproduction in other forums is permitted, provided the original author(s) and the copyright owner(s) are credited and that the original publication in this journal is cited, in accordance with accepted academic practice. No use, distribution or reproduction is permitted which does not comply with these terms.

frontiers in Materials

ORIGINAL RESEARCH
published: 06 June 2019
doi: 10.3389/fmats.2019.00131

Investigation of Polycarbazoles Thin Films Prepared by Electrochemical Oxidation of Synthesized Carbazole Derivatives

*Emmanuel Contal, Charmaké Moussa Sougueh, Sophie Lakard, Abdeslam Et Taouil, Claire Magnenet and Boris Lakard**

Institute UTINAM, UMR CNRS 6213, University of Bourgogne Franche-Comté, Besançon, France

Polycarbazole and its derivatives have advantages of good environmental stability, electrochromic properties and photoconductivity which have attracted considerable attention because of their potential industrial applications in electroluminescent applications, rechargeable batteries, and light emitting diodes. They have the possibility of different position substitution (carbon C_3-C_3' or N) that lead to different electropolymerization behaviors. However, the N position facilitates the grafting of various derivatives of interest and permits not to modify so much the radical cation formation during electropolymerization. In this paper, carbazole and its derivatives were electrochemically oxidized in acetonitrile solutions leading to the formation of thin polymer films. The morphological features and electrochemical properties of the as-formed polymer films were investigated in detail. Thanks to these experiments, the influence of the substitution on the properties of the polymer films was evidenced and discussed. In addition, fast electrochemistry experiments were carried out on platinum microelectrodes within 50–1,000 V/s scan speed range. Reactivity of carbazole derivatives radical cations and dimers was investigated through these experiments. Thermodynamic and kinetic information (e.g., redox standard potential, heterogeneous, and dimerization rate constants) was extracted after coupling with electrochemical simulations.

Keywords: electrochemistry, conducting polymers, carbazoles, reactivity, functionalization

OPEN ACCESS

Edited by:
Guilherme Mariz de Oliveira Barra, Federal University of Santa Catarina, Brazil

Reviewed by:
Johnny De Nardi Martins, Federal University of Santa Catarina, Brazil
Walter Caseri, ETH Zürich, Switzerland

****Correspondence:***
Boris Lakard
boris.lakard@univ-fcomte.fr

Specialty section:
This article was submitted to Polymeric and Composite Materials, a section of the journal Frontiers in Materials

Received: *19 March 2019*
Accepted: *20 May 2019*
Published: *06 June 2019*

Citation:
Contal E, Sougueh CM, Lakard S, Et Taouil A, Magnenet C and Lakard B (2019) Investigation of Polycarbazoles Thin Films Prepared by Electrochemical Oxidation of Synthesized Carbazole Derivatives. Front. Mater. 6:131. doi: 10.3389/fmats.2019.00131

INTRODUCTION

The discovery of organic conducting polymers in Shirakawa's laboratory in the early 1970s and the demonstration by MacDiarmid et al. of the semiconducting properties of polyacetylene (Shirakawa et al., 1977) paved the way for an intense research activity on these materials to exploit these conducting properties. Thus, over the last decades, other organic semiconducting polymers like polypyrrole, polyaniline, polythiophene, or polycarbazole have been gaining increasing interest, owing to their interesting physicochemical properties, for many different applications including flexible electronics (Savagatrup et al., 2014; Lee et al., 2018), optoelectronics (Ouyang et al., 2005; Akiyama et al., 2009; Cai et al., 2017), and energy storage devices (Mali et al., 2015; Bryan et al., 2016; Kausar, 2017).

Various methods have been used in the past for growing such conducting polymers including chemical oxidation (Huang et al., 2012), plasma polymerization (Yaguee et al., 2008), Langmuir-Blodgett technique (Park et al., 2003), or electrochemistry (Fonseca et al., 2017). Among these methods, electrochemical deposition is the most convenient and reliable method for growing conducting polymer thin films with controlled properties. Indeed, many physico-chemical properties [including conductivity (Patois et al., 2010), morphology and roughness (Patois et al., 2011) or wettability (Darmanin and Guittard, 2014)] of electrodeposited polymer films can be easily tuned by varying electrochemical conditions [such as solvent (Viau et al., 2014; Wojcik and Grzeszczuk, 2015), electrodeposition potential (Chmielewski et al., 2010), nature of the counter-anions (Atobe et al., 2006), temperature (Wojcik and Grzeszczuk, 2015), or pH (Peng et al., 2009)].

Carbazole is one of the aromatic heterocyclic organic compounds that could lead to the formation of a conducting polymer film by oxidation. Resulting carbazole-based conjugated polymer films can be used as components of sensors (Joshi et al., 2014; Vedarajan et al., 2014), batteries (Saraswathi et al., 1999), OLED (Grigalevicius et al., 2011; Srivastava and Chakrabarti, 2015), or electrochromic devices (Hu et al., 2013; Hsiao and Lin, 2016), mainly because of their electron-donating nature, high photoconductivity and strong fluorescence.

To tune properties of conducting polymers, it is possible to modify heterocyclic monomers by incorporation of functional groups with specific properties. Indeed, carbazole monomers have the possibility of substitution at N-position. Such chemical modification provides the opportunity to improve both the solubility and functionality of the resulting polymer. In addition, flexible side chains can cause steric hindrance and thereby provide a means to control the effective conjugation length.

Thus, chemical modifications to the carbazole monomers leading to N-substituted derivatives have already been done (Ambrose and Nelson, 1968; Ambrose et al., 1975; Chevrot et al., 1996; Wei et al., 2006). In particular, anodic electrochemical oxidation of carbazole and its N-substituted derivatives (N-methylcarbazole, N-ethylcarbazole, and N-isopropylcarbazole) were first studied by Ambrose and Nelson (1968); Ambrose et al. (1975). They investigated the reactivity of cation radicals formed from these substituted carbazoles using electrochemical and spectroscopic techniques and reported that their electrochemical oxidation leads to only 3,3′-bicarbazyls and not to 9,9′-bicarbazyls due to the fact that the 9-position is already occupied. The optical and electronic properties of undoped and doped electrodeposited poly(N-ethylcarbazole) thin layers were also characterized by Chevrot et al. (1996). In another study, Wei et al. have prepared high quality polymer films by anodic electro-oxidation of carbazole and its alkyl derivatives N-octylcarbazole, N-(6-bromohexyl)carbazole, and 1,6-bis(carbazolyl)hexane in boron trifluoride diethyl etherate (BFEE) or mixed electrolytes BFEE + $CHCl_3$ (Wei et al., 2006). However, among the various carbazole incorporated polymers, a central place is reserved to N-vinylcarbazole because it is easily synthesized and soluble in common organic solvents. Thus, the polymerization of N-vinylcarbazole in ethylenedichloride, acetone, benzene, and dioxane with cupric nitrate, ferric nitrate, and ceric ammonium nitrate catalysts was studied by Sarac and Bardavit (2004). Similarly, poly(N-vinylcarbazole) films were synthesized by electrochemical oxidation of N-vinylcarbazole in acetonitrile (Reyna-Gonzalez et al., 2006; Reyna-González et al., 2009). In this work, Reyna-Gonzalez et al. evidenced that modifying the acidity of the electrolyte leads to the deposition of polymer films with various properties in terms of chemical structure, morphology, conductivity, and optical properties. Such poly-(N-vinylcarbazole) films have been used as solar cells materials (Su et al., 2017), as sensing materials (Papez and Josowicz, 1994), or as light-emitting diode materials (Li et al., 2010; Cai et al., 2011).

Taking into account this literature, the present study aimed at preparing various N-substituted polycarbazole films by electrochemical oxidation using optimum electrodeposition conditions (in terms of solvent, supporting salt and monomer concentration) deduced from the study of carbazole electropolymerization. Then, the reactivity of carbazole derivatives radical cations and dimers was investigated through fast electrochemistry experiments to determine the influence of the substitution. Electrochemical properties and morphology of the various substituted polycarbazole films were also studied and compared.

MATERIALS AND METHODS

Reagents

Carbazole (Cz, 95%) and vinylcarbazole (CzV, 98%) were purchased from Sigma Aldrich. 9-ethyl-9H-carbazole (Cz1Me, 97%) was from TCI. Acetone (99.98%) and dimethylformamide (99.8%) were from Fisher Chemical. Lithium perchlorate, tetraethylammonium p-toluenesulfonate (TS), tetrabutylammonium hexafluorophosphate (TH), and tetrabutylammonium tetrafluoroborate (TBAB) were from Sigma-Aldrich.

All other chemical reagents used to prepare monomers were purchased from TCI or Sigma Aldrich and used as received unless otherwise stated. ^{1}H and ^{13}C NMR spectra were recorded on a Bruker AC 400 spectrometer. RMN spectra are given in **Supplementary Files**.

Synthesis

General Procedure to Alkylcarbazoles

KOH (2.50 g, 1.5 eq) and bromoalkane (45 mmol, 1.5 eq) were added at room temperature to a stirred solution of carbazole (5.00 g, 30 mmol) in acetone (30 mL). Then the reaction mixture was refluxed for 24 h. After cooling, water was added (30 mL) and the reaction mixture was neutralized with 0.1 M HCl solution. The solution was extracted with diethylether (3*50 mL). The combined organic layers were dried over sodium sulfate, filtered, and concentrated by rotary evaporation. The crude product was purified by chromatography (Dichloromethane/Cyclohexane 1/1 as eluent) to give the final compound.

9-butyl-9H-carbazole (Cz3Me)

According to the general procedure, 9-butylcarbazole was obtained as a white solid (5.45 g, 81%). ^{1}H NMR (400 MHz,

$CDCl_3$): δ (ppm) *8.12* (d, 2H, J = 7.6 Hz), 7.46 (d, 2H, J = 8.0 Hz), 7.24 (d, 2H, J = 6.4 Hz), 4.30 (t, 2H, J = 7.2 Hz), 1.85 (quint, 2H, J = 7.2 Hz), 1.40 (td, 2H, J = 7.6 Hz, J = 7.6 Hz), 0.95 (t, 2H, J = 7.2 Hz). ^{13}C NMR (100 MHz, $CDCl_3$): δ (ppm) 140.4, 125.5, 122.7, 120.3, 118.6, 108.6, 42.8, 31.1, 20.5, 13.9. Analyses were consistent to already published data (Petrov et al., 2013).

9-hexyl-9H-carbazole (Cz5Me)

According to the general procedure, 9-hexylcarbazole was obtained as a white solid (6.30 g, 84%). ^{1}H NMR (400 MHz, $CDCl_3$): δ (ppm) *8.07* (d, 2H, J = 7.6 Hz), 7.43 (m, 2H), 7.35 (d, 2H, J = 8 Hz), 7.20 (t, 2H, J = 7.2 Hz), 4.21 (t, 2H, J = 7.2 Hz), 1.80 (quint, 2H, J = 7.2 Hz), 1.35–1.21 (m, 6H), 0.85 (t, 2H, J = 7.2 Hz). ^{13}C NMR (100 MHz, $CDCl_3$): δ (ppm) 140.4, 125,5; 122,8; 120,3; 118,6; 108,6; 43,0; 31,6; 28,9; 26,9; 22,5; 14,0. Analyses were consistent to already published data (Petrov et al., 2013).

9-octyl-9H-carbazole (Cz7Me)

According to the general procedure, 9-octylcarbazole was obtained as a colorless oil (7.95 g, 94%). ^{1}H NMR (400 MHz, $CDCl_3$): δ (ppm) *8.10* (d, 2H, J = 7.6 Hz), 7.47 (m, 2H), 7.42 (d, 2H, J = 8.0 Hz), 7.23 (td, 2H, J = 7.2 Hz, J = 1.2 Hz), 4.30 (t, 2H, J = 7.2 Hz), 1.88 (quint, 2H, J = 7.2 Hz), 1.42–1.20 (m, 10H), 0.87 (t, 2H, J = 7.2 Hz). ^{13}C NMR (100 MHz, $CDCl_3$): δ (ppm) 140.4, 125.6, 122.8, 120.3, 118.7, 108.6, 43.1, 31.8, 29.4, 29.2, 29.0, 27.3, 22.6, 14.0. Analyses were consistent to already published data (Sathiyan and Sakthivel, 1993).

N-((Methoxycarbonyl)methyl)carbazole (CzE)

Carbazole (4.2 g, 30 mmol) was added at 0°C to a suspension of NaH (60% in oil, 2.0 g, 2 eq) in a dry THF/DMSO solution (80/40 mL). The mixture was stirred for 1 h and methyl bromoacetate was added (5.8 g, 1.5 eq). The reaction mixture was stirred overnight then quenched with water. The solution was extracted with diethylether (3*100 mL). The combined organic layers were dried over sodium sulfate, filtered and concentrated by rotary evaporation. The crude product was purified by chromatography (Dichloromethane/Cyclohexane 1/1 as eluent) to yield a white solid (4.37 g, 73%). ^{1}H NMR (400 MHz, $CDCl_3$): δ (ppm) *8.02* (d, 2H, J = 7.6 Hz), 7.40 (t, 2H, J = 8.0 Hz), 7.20 (m, 4H), 4.92 (s, 2H), 3.63 (s, 3H). ^{13}C NMR (100 MHz, $CDCl_3$): δ (ppm) 169.0, 140.5, 126.0, 123.2, 120.5, 119.7, 108.3, 52.5, 44.6. Analyses were consistent to already published data (Conn et al., 1993).

2-(9H-Carbazol-9-yl)acetic acid (CzA)

N-((Methoxycarbonyl)methyl)carbazole (1.08 g, 4.3 mmol) was dissolved in a THF/H_2O solution (5/5 mL). KOH (0.8 g, 3 eq) was added and the solution was stirred at room temperature overnight. Then THF was removed by evapory rotation and aqueous solution was acidified to pH =1 with 1M HCl solution. The precipitated compound was filtered, washed with cold water and dried under vacuum to yield a white solid (0.6 g, 56 %). ^{1}H NMR (400 MHz, $CDCl_3$): δ (ppm) *8.02* (d, 2H, J = 7.6 Hz), 7.40 (t, 2H, J = 8.0 Hz), 7.20 (m, 4H), 4.97 (s, 2H). ^{13}C NMR (100 MHz, $CDCl_3$): δ (ppm) 173.1, 140.4, 126.1, 123.3, 120.6, 119.9, 108.2, 44.1. Analyses were consistent to already published data (Zhang et al., 2014).

Electrochemistry

Electrodeposition of Cz and Its Derivatives

First, electrochemistry was used to study the electrochemical oxidation of the monomers on a platinum wire (area: 0.785 mm^2) using cyclic voltammetry technique (5 potential scans were done at 50 mV/s). Then, after optimization of the electrolyte composition, polycarbazole films were prepared using chronoamperometry technique (3 min of oxidation at the oxidation peak potential deduced from the corresponding cyclic voltammetry) on a Fluorine doped Tin Oxide (FTO) substrate (R = 80 V/square, area: 1.5 cm^2), before being extensively characterized.

The electrochemical activity of polyCz was also estimated by doing a cyclic voltammetry at a Pt electrode coated with a PCz film in the same electrolyte but in the absence of monomer. This electrode was rinsed in acetonitrile between the cycling in the solutions with monomers and those without.

All these electrochemical experiments were carried out at room temperature, with a VersaSTAT MC potentiostat/galvanostat from Princeton Applied Research, in a single-compartment cell with a three electrode set-up. This set-up employed a Saturated Calomel Electrode (SCE) as reference electrode, a platinum sheet as counter-electrode, and either a platinum wire or a FTO substrate as working electrode.

Fast Electrochemistry

Fast electrochemistry experiments were carried out using an AUTOLAB PGSTAT30 potentiostat equipped with SCAN250 and ADC10M modules. A classical three-electrode cell was used with platinum microelectrode (diameter 246 µm calibrated with ferrocene system) as working electrode, platinum wire as counter-electrode and Ag/AgCl reference electrode. The solution contained 1.5 mM of functionalized carbazole and 0.1 M of TBAB in acetonitrile. Electrochemical simulations were realized with DigiElch Pro software.

Characterization

SEM Microscopy

The surface morphology of the polycarbazole films was observed with a high-resolution Scanning Electron Microscope Quanta 450 W (from FEI) with an electron beam energy of 12.5 keV and a working distance of 9 mm. No metallization pre-treatment was needed since the samples were conductive.

Profilometry

Thickness and roughness of electrodeposited films were measured using a stylus-based mechanical probe profiler (Alpha-Step IQ, from KLA Tencor). Both thickness and roughness were obtained by moving this stylus perpendicularly to the film on a scan length of 3,000 µm at a scan speed of 50 µm.s^{-1}. Five measurements were achieved at different positions for each film.

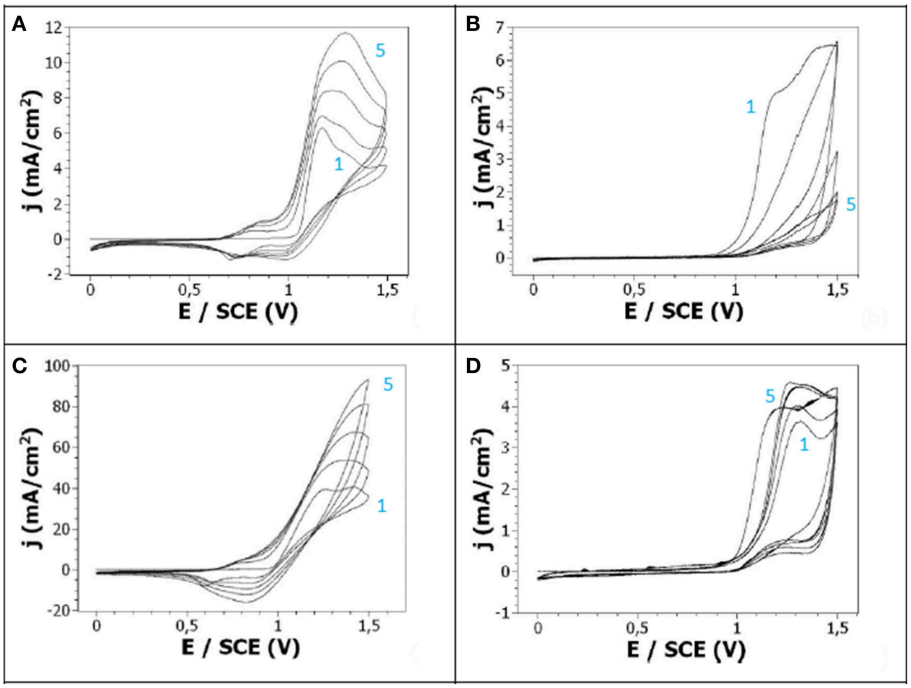

FIGURE 1 | Cyclic voltammetry at a Pt electrode of: **(A)** 10^{-2} M Cz + 0.1 M $LiClO_4$ in ACN, **(B)** 10^{-2} M Cz + 0.1 M $LiClO_4$ in DMF, **(C)** 10^{-1} M Cz + 0.1 M $LiClO_4$ in ACN, **(D)** 10^{-3} M Cz + 0.1 M $LiClO_4$ in ACN. Scan rate: 50 mV/s.

RESULTS

Electropolymerization of Carbazole at Pt Electrodes by Cyclic Voltammetry

Influence of the Solvent and Carbazole Concentration

The oxidation of 10^{-2} M carbazole was performed by cyclic voltammetry (CV) at Pt electrodes in 0.1 M $LiClO_4$ in acetonitrile (ACN) or dimethylformamide (DMF) solutions (**Figure 1**). The onset oxidation potentials of carbazole, leading to Cz radical cations, in $LiClO_4$/ACN and $LiClO_4$/DMF, appears at 1.05 and 0.95 V/SCE, respectively. The redox process of polycarbazole is observed in ACN since a polyCz oxidation peak and a polyCz reduction peak are clearly distinguishable at +0.8 and +0.7 V/SCE, respectively. After the first cycle, both Cz, and polyCz oxidation potential peak intensity increases and potentials shift toward higher values. The gradual increase of the reduction peak intensity with repeated scans indicates the progressive deposition of the polymer on the Pt surface. Moreover, the i_a/i_c ratio of the redox polyCz peaks is close to 1, indicating a good reversibility of the redox process.

This electrochemical behavior is consistent with the electropolymerization mechanism previously reported (Ambrose and Nelson, 1968). This mechanism begins with the oxidation of carbazole monomers leading to the formation of cation radicals in a one electron process. These cation radicals couple with each other or with a parent molecule leading to 3,3′-bicarbazyls. After that, the oxidation of the oligomers takes place leading progressively to the formation of a polycarbazole film at the electrode surface.

On the contrary, the redox process was not distinguishable when the cyclic voltammetry was performed in DMF, and the intensity of the Cz oxidation peak decreased upon repeated scans, both indicating that this solvent is less appropriate for this reaction than ACN. In addition, the film obtained by oxidation of Cz in DMF is very thin and copper-colored to the eye, contrary to the one obtained in ACN which is thicker and green-colored (**Figure 2**). This is in line with other studies which evidenced that acetonitrile was a better solvent than propylene carbonate and dichloromethane for the electropolymerization of Cz (Sarac et al., 2006).

The influence of the monomer concentration was then studied by comparing the cyclic voltammetry obtained from 10^{-2} M Cz in an acetonitrile solution (using 0.1 M $LiClO_4$ as supporting electrolyte) with the ones obtained from similar solutions containing Cz concentrated at 10^{-3} and 10^{-1} M (**Figures 1C,D**). Thus, the cyclic voltammetry obtained with 10^{-1} M Cz shows great similarities with the one obtained at 10^{-2} M, in particular a Cz oxidation peak beginning at +1.0 V/SCE whose intensity increases with repeated scans and potential shifts toward higher values, and two reversible redox peaks corresponding to the oxidation and reduction of the polyCz. On another side, the Cz oxidation peak was narrower at 10^{-2} M and its intensity was 10 times lower, both due to the lower monomer concentration. After this electrochemical oxidation, a thick green-colored film was obtained (**Figure 2**). On the contrary, the cyclic voltammetry obtained with 10^{-3} M Cz was very different from the ones obtained at 10^{-1} and 10^{-2} M since there was no increase with repeated scans of the Cz oxidation peak appearing at + 1.0 V/SCE

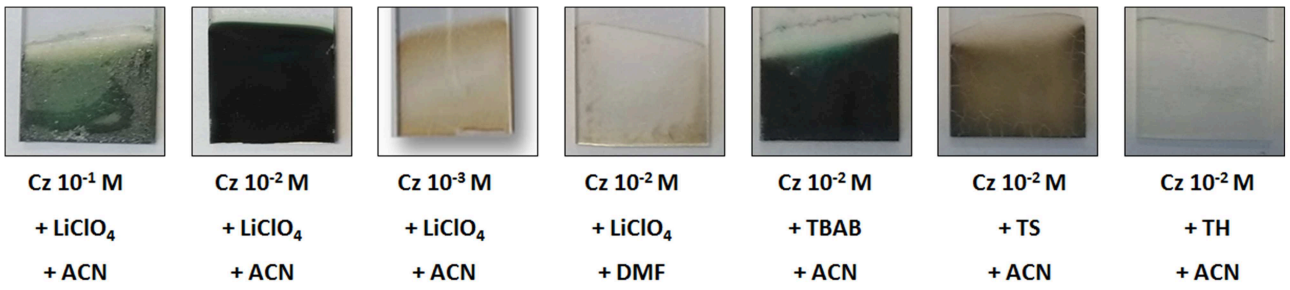

FIGURE 2 | Photographs of samples obtained by oxidation of carbazole at different concentrations and in electrolytes containing different solvents and supporting salts.

and no distinguishable redox peaks. Moreover, only a very thin pale yellow film is formed (**Figure 2**).

It can be deduced from these experiments that the best solvent for studying Cz electropolymerization is acetonitrile and the optimized monomer concentration is 10^{-2} M rather than 10^{-1} M since the PCz film obtained with 10^{-2} M Cz is more adherent and more uniform (**Figure 2**). In addition, the solubility of Cz into acetonitrile is more difficult in 0.1 M Cz.

Influence of the Supporting Salt

To determine the influence of the nature of the supporting salt, in particular the influence of its anions acting as dopants, on the electrochemical oxidation of carbazole, cyclic voltammograms were performed from an acetonitrile solution containing carbazole and one of the following salts: lithium perchlorate ($LiClO_4$), tetrabutylammonium tetrafluoroborate (TBAB), tetraethylammonium p-toluenesulfonate (TS), or tetrabutylammonium hexafluorophosphate (TH). These salts were chosen because they have different sizes, contain different anions, provide a good conductivity to the electrolyte and facilitate the dissolution of monomers in the electrolyte.

The cyclic voltammogramm obtained with TBAB salt (**Figure 3B**) presented similarities with the one previously obtained with $LiClO_4$ (**Figure 3A**). Indeed, the onset potentials of Cz in TBAB/ACN is located at + 1.1 V/SCE, the cyclic voltammetry shows an oxidation peak, the current intensity of this anodic peak increases with repeated scans and a reduction peak corresponding to redox processes is also visible. However, a lower maximum oxidation current density was obtained in TBAB/ACN (5 mA/cm^2, 5th cycle) than in $LiClO_4$/ACN (12 mA/cm^2, 5th cycle), as well as a lower maximum reduction current density (only −0.4 mA/cm^2 in TBAB/ACN compared to −1.2 mA/cm^2 in $LiClO_4$/ACN). The same general trends are observed in TS/ACN (**Figure 3C**) since an oxidation peak and a redox peak are also visible but with lower intensities than in $LiClO_4$/ACN films. This tends to indicate that the polymer film is thicker and the redox processes more reversible in $LiClO_4$/ACN. The behavior observed in the presence of TH salt was very different (**Figure 3D**). Indeed, the oxidation peak is less pronounced, the reduction peak is not distinguishable, and the intensity of the oxidation peak is very low. Thus, it can be assumed that the electropolymerization of Cz is far more difficult in TH/ACN than in $LiClO_4$/ACN and TS/ACN. This is confirmed by the pictures from the samples obtained by electro-oxidation of Cz on FTO electrodes (**Figure 2**) which show that a thick and homogeneous polyCz film is obtained in $LiClO_4$/ACN when less homogeneous films are obtained in TS/ACN and TBAB/ACN and no clearly visible film is obtained in TH/ACN.

The electrochemical activity of the polyCz films electrodeposited in the different electrolytes was also studied. To this aim, polyCz films were electrodeposited onto a Pt working electrode by cyclic voltammetry, then the Pt electrode with the polymer film attached was removed from the growth solution, and placed in a monomer-free solution of the solvent for post-polymerization voltammetric analysis. Since it is necessary to have enough salt to study the insertion/desinsertion of the anions in the PCz films, a concentration of 0.1 M in salt was chosen.

Whatever the nature of the supporting salt, post-polymerization CVs showed a peak separation that is expected for a reversible electron transfer process (Chen and Inganas, 1996) (**Figure 4**). However, the oxidation and reduction peaks are more pronounced when $LiClO_4$ was used. With this latter salt, the potential corresponding to the polyCz oxidation and reduction peaks is +1.3 and +1.05 V/SCE, respectively, during the 1st cycle (the potential shifted toward less anodic potentials with repeated scans). Moreover, the ratio of oxidation to reduction intensities remains constant around 2.25 with repeated scans which indicates that the doping/dedoping process happens even after a few scans. When TBAB is used as supporting electrolyte, the redox processes also take place as evidenced by the presence of the oxidation and reduction peaks at +1.35 and +0.95 V/SCE, respectively. Moreover, these peaks are present during the repeated scans (even if the reduction peak slowly decreases) indicating doping/dedoping process. When TS is used as supporting electrolyte, the redox processes again take place as proved by the presence of the oxidation and reduction peaks at +1.3 and +0.85 V/SCE, respectively, even if the oxidation peak is broader. The intensity of these peaks remains roughly constant with repeated scans indicating the doping/dedoping of the film by the p-toluenesulfonate anions. In the presence of TH salt, the oxidation and reduction peaks are also present but the current density is strongly lower than for the other salts indicating that the doping/dedoping process still goes on.

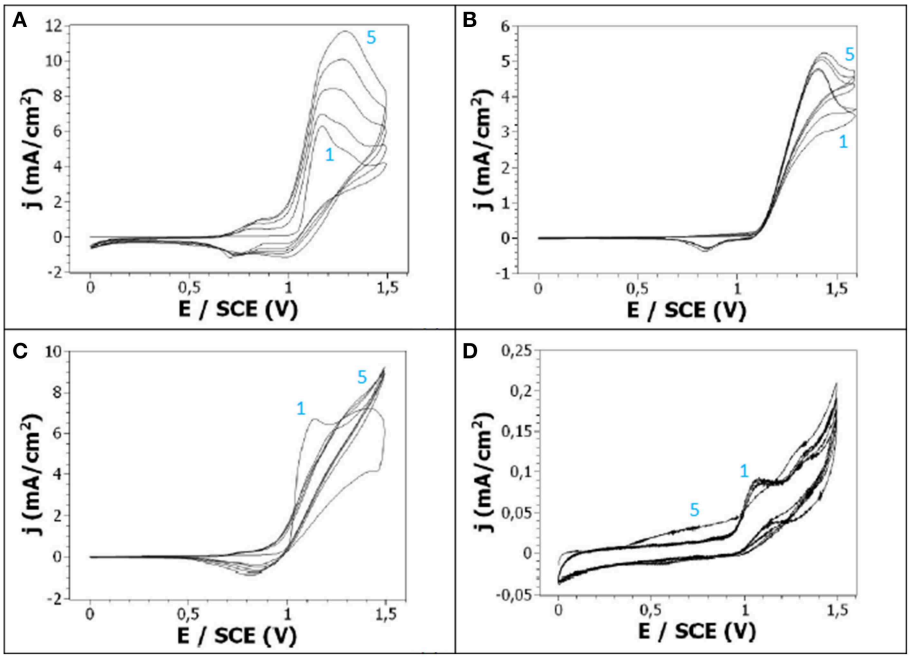

FIGURE 3 | Cyclic voltammetry of 10^{-2} M Cz in 0.1 M **(A)** $LiClO_4$/ACN, **(B)** TBAB/ACN, **(C)** TS/ACN, **(D)** TH/ACN. Scan rate: 50 mV/s.

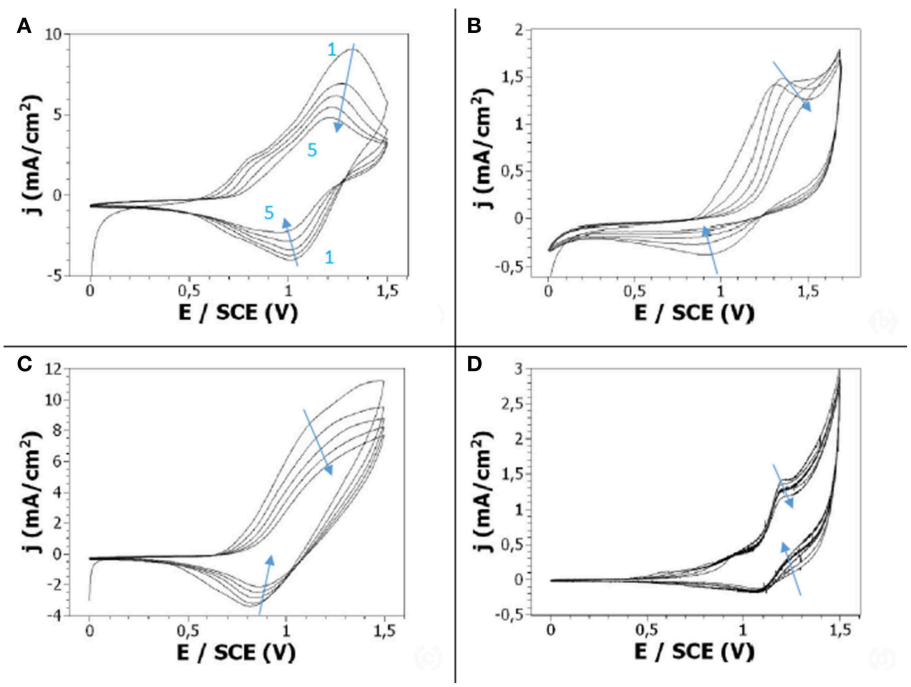

FIGURE 4 | Post-polymerization cyclic voltammetry of 10^{-2} M Cz in 0.1 M **(A)** $LiClO_4$/ACN, **(B)** TBAB/ACN, **(C)** TS/ACN, **(D)** TH/ACN. Scan rate: 50 mV/s.

To conclude, the study of the electropolymerization conditions (monomer concentration, nature of the solvent and nature of the supporting salt) recommends to work in acetonitrile solutions with lithium perchlorate and a carbazole concentration of 10^{-2} M. These optimized conditions will be used in the next part of this work dedicated to the electrochemical oxidation of N-substituted carbazole derivatives.

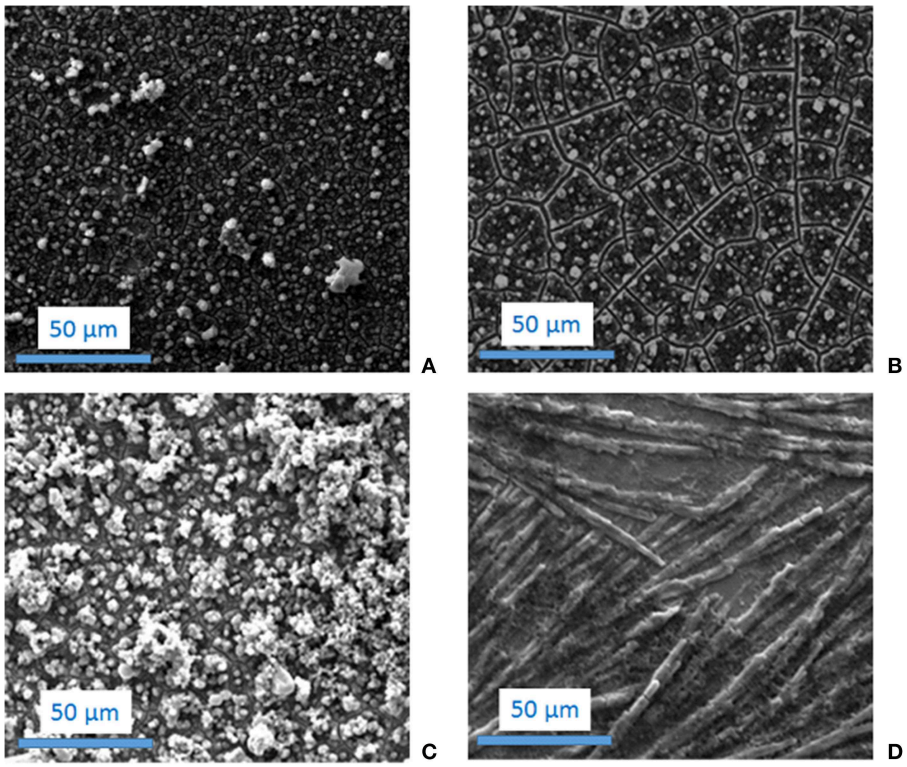

FIGURE 5 | SEM images of the films obtained by electrodeposition of 10^{-2} M: Cz **(A)**, CzA **(B)**, CzV **(C)** and CzE **(D)** in 0.1 M $LiClO_4$ + acetonitrile.

Characterization of the Polycz Obtained in the Optimized Conditions

The morphology of a polyCz film obtained from oxidation of 10^{-2} M Cz in an acetonitrile solution containing 0.1 M $LiClO_4$ was studied by SEM microscopy. The SEM image indicates that the overall surface of the polyCz film is homogeneous, the electrode being nearly completely covered by polymer (**Figure 5A**). Moreover, the film consists in small heaps electrodeposited onto the electrodes with bare domains between them. The shape of these small heaps is circular and the size of the structures varies from one to the other. Using profilometry measurements, the thickness of the polyCz films was estimated to 6–7 µm and its roughness to 0.05–0.09 µm.

N-substituted Carbazoles

9-alkylcarbazoles

In an attempt to obtain original thin solid polymer films by electrochemical oxidation of substituted carbazoles, different alkylcarbazoles were prepared by incorporation of alkyl chains at N-position. The alkyl chain length was varied to determine if this parameter has an influence on the oxidation of the modified carbazoles. The electrochemical parameters used to perform the electro-oxidation of the various N-alkylcarbazoles were those optimized in the first part of this work: a concentration of 10^{-2} M in monomer, 0.1 M $LiClO_4$ as supporting salt and acetonitrile as solvent. Thus, the anodic oxidation of 9-ethylcarbazole (Cz1Me), 9-butylcarbazole (Cz3Me), 9-hexylcarbazole (Cz5Me), and 9-octylcarbazole (Cz7Me) was performed by cyclic voltammetry at Pt electrodes, as shown in **Figure 6**. The onset oxidation potentials of these four alkylcarbazoles, leading to radical cations, appears at +1.0 V/SCE. A pronounced reduction peak is also observed for all carbazole derivatives at +0.7–0.8 V/SCE. Both the Cz oxidation peak and the corresponding reduction peak are observed during the successive scans. Another peak, whose intensity is very low, can be observed around +0.8 V/SCE. Concerning the intensity of the peaks, they are similar for all alkylcarbazoles but lower than for non-substituted carbazole (the intensity of the oxidation peak is around 6 mA/cm^2 for 9-alkylcarbazoles instead of 12 mA/cm^2 for Cz, and the reduction peak intensity was around −0.5 mA/cm^2 for 9-alkylcarbazoles instead of −1 mA/cm^2 for Cz). Moreover, there is no clear increase in redox currents during successive cycling which means that no adherent deposit is obtained on the electrode surface. This is confirmed visually as no polymer deposit is observed (with the naked eye or with a SEM microscope) on the substrates after electrochemical oxidation.

So, it is interesting to observe that carbazole and 9-alkylcarbazoles present a comparable electrochemical behavior but only carbazole leads to a polymer thin film on the working electrode. In addition, when the oxidation is performed by chronoamperometry, similar charge quantity is measured during the oxidation of Cz (368 mC/cm^2) and during the oxidation of Cz1Me (410 mC/cm^2), Cz3Me (367 mC/cm^2), Cz5Me

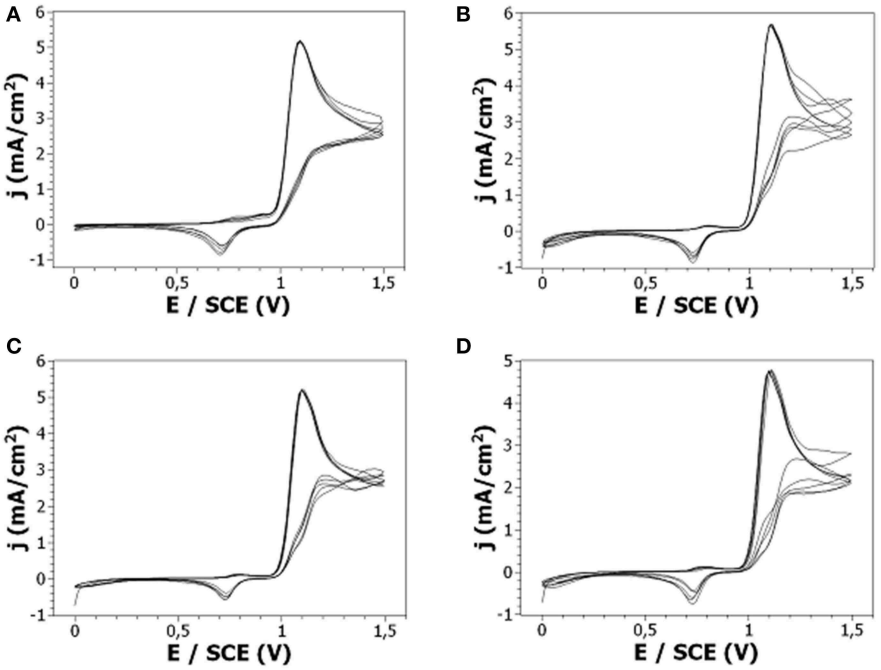

FIGURE 6 | Cyclic voltammetry at a Pt electrode of 10^{-2} M: **(A)** Cz1Me, **(B)** Cz3Me, **(C)** Cz5Me, **(D)** Cz7Me + 0.1 M $LiClO_4$ in ACN. Scan rate: 50 mV/s.

(369 mC/cm^2), and Cz7Me (376 mC/cm^2) indicating that the oxidation of these species takes place without particular difficulty for all of these monomers. In the review from Kapron and Lapkowski (2015) and in the pioneer works from Ambrose and Nelson (1968) dedicated to the electrochemistry of carbazoles, it is explained that the oxidation of Cz leads to the formation of the cation radical in a one electron process. As the cation radical is not stable, it tends to couple with another cation radical or a parent molecule (a loss of two protons accompanies this coupling) to form a more stable bicarbazyl (which can be either 3,3′-bicarbazyl, the main product, or 9,9′-bicarbazyl, the minor product). Then, the oxidation of the oligomers takes place (at a lower potential than the oxidation of the monomers) and the electropolymerization of Cz occurs. On the contrary, when the nitrogen atom is blocked by a substituent, the oxidation mainly leads to dimers but not to polymers. From our point of view, this difference of behavior between Cz and these substituted carbazoles may be due to the difference of stability of the cation radicals obtained by electro-oxidation of Cz and 9-alkylcarbazoles and their dimers. To validate our assumption, we performed fast electrochemistry experiments (**Figure 7**) since fast electrochemistry on such diffusive systems may be interesting in terms of kinetic and thermodynamic parameters extraction (e.g., redox standard potential, heterogeneous, and dimerization rate constants) as well as for mechanisms investigation (since it could give information about the reactivity of radical cations and dimers).

For 9-ethylcarbazole, signal reversibility was reached for scan rates above 50 V/s. The oxidation peak present at +1.25 V/Ag/AgCl is due to well-known monomer oxidation into radical cation which couples with another radical cation (dimerization) as it is unstable. This dimerization is accompanied by the loss of two protons. The scan rate being very fast, a non-negligible part of radical cations is reduced before total dimerization which leads to the small reduction peak. Electrochemical simulation enabled to estimate a dimerization rate constant of about $(4.25 \pm 0.75) \times 10^5$ $M^{-1}.s^{-1}$.

For 9-substituted carbazole with longer alkyl chains (i.e., 4, 6, and 8 carbons), electrochemical behavior is more complex. Indeed, oxidation peak is wider than expected and most importantly, two reduction peaks are observed at high scan rates (100 V/s). As previously described, electrochemical oxidation of 9-substituted carbazoles has been studied by Ambrose et al. at classical scan rates (i.e., a few hundreds of mV/s) leading to the mechanism previously described. Thus, the oxidation peak is due to classical oxidation/dimerization of substituted monomers. The reason that the peak is more important than the one expected for one-electron process is due to the fact that the obtained dimer is then oxidized into a radical cation dimer which is relatively stable. When shifting to reduction, the first peak shows the reduction of remaining radical cations (i.e., the ones which don't dimerize) into starting monomers. Dimerization rate constants are evaluated through this peak. The second peak is for reduction of radical cation dimer into neutral dimer. Thermodynamic and kinetic parameters extracted from electrochemical simulations are presented in **Table 1**. It is interesting to note that dimerization rate constant is very similar for 9- ethyl, butyl and hexyl carbazole as it keeps between 4.10^5 and 5.10^5 $M^{-1}.s^{-1}$ regardless of chain length. However, for 9-octyl carbazole the dimerization rate constant is more

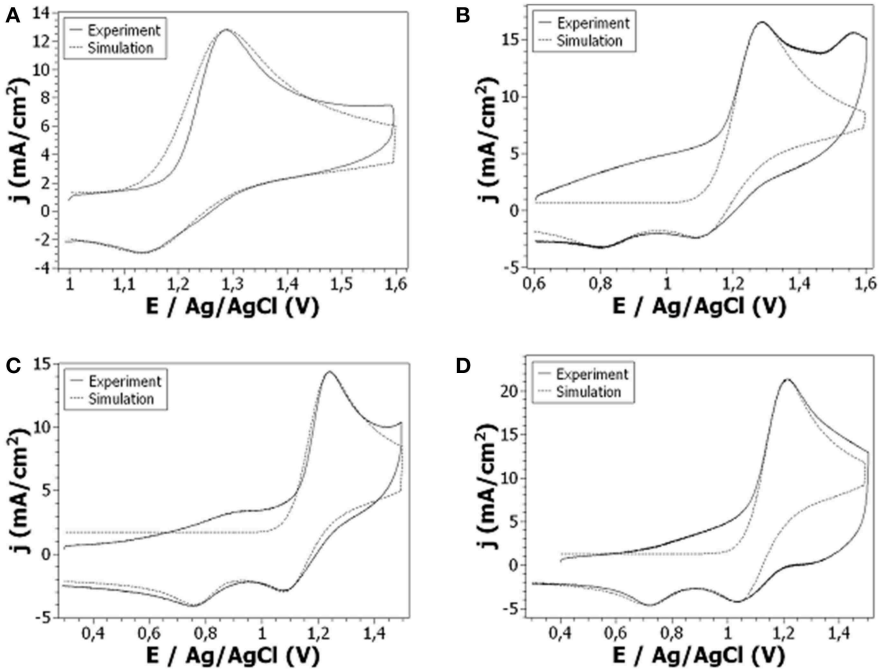

FIGURE 7 | Cyclic voltammetry at a Pt electrode of 10^{-2} M: **(A)** Cz1Me, **(B)** Cz3Me, **(C)** Cz5Me, **(D)** Cz7Me + 0.1 M $LiClO_4$ in ACN. Scan rate: 100 V/s.

TABLE 1 | Formal potential (E°), heterogeneous rate constant (k_s) and dimerization rate (k_{dim}) of Cz1Me, Cz3Me, Cz5Me, and Cz7Me deduced from fast electrochemistry experiments and corresponding simulations.

		E° (V/AgCl/Ag)	k_s (cm/s)	k_{dim} ($mol^{-1}.L.s^{-1}$)
Cz1Me	$Cz1Me^{+\circ} + e^- \rightleftharpoons Cz1Me$	1.21	0.055 ± 0.005	/
	$2\ Cz1Me^{+\circ} \rightarrow$ Dimer	/	/	$(4.25 \pm 0.75).10^5$
Cz3Me	$Cz3Me^{+\circ} + e^- \rightleftharpoons Cz3Me$	1.19	0.07 ± 0.01	/
	$2\ Cz3Me^{+\circ} \rightarrow$ Dimer	/	/	$(4.25 \pm 0.55).10^5$
	$Dimer^{+\circ} + e^- \rightleftharpoons$ Dimer	0.96	0.01	/
Cz5Me	$Cz5Me^{+\circ} + e^- \rightleftharpoons Cz5Me$	1.16	0.09 ± 0.01	/
	$2\ Cz5Me^{+\circ} \rightarrow$ Dimer	/	/	$(4.7 \pm 1.1).10^5$
	$Dimer^{+\circ} + e^- \rightleftharpoons$ Dimer	0.83 ± 0.01	0.07 ± 0.02	/
Cz7Me	$Cz7Me^{+\circ} + e^- \rightleftharpoons Cz7Me$	1.11 ± 0.02	0.085 ± 0.005	/
	$2\ Cz7Me^{+\circ} \rightarrow$ Dimer	/	/	$(2.0 \pm 0.5).10^5$
	$Dimer^{+\circ} + e^- \rightleftharpoons$ Dimer	0.815 ± 0.005	0.03	/

than twice smaller probably due to steric effects beginning to take place. Moreover, there is a tight relation between carbon chain length and redox standard potential of monomer/radical cation couples. Indeed, redox potential decreases with chain length meaning that the more the carbon chain is long, the more the substituted monomer is easily oxidized. Heterogeneous rate constant (k_s) also follows this trend as it increases with chain length (except for 9-hexyl and octyl carbazole for which it stays the same). This increase in k_s means a faster electron transfer and therefore an easier oxidation process.

The good stability of radical cation dimers from 9-alkyl substituted carbazoles can be an explanation for their non-deposition as the oxidized dimer does not polymerize very fast leading to short oligomer chains easily solubilized into the solution.

Other N-substituted Carbazoles

The oxidation of 10^{-2} M CzA and CzE was performed in 0.1 M $LiClO_4$ in acetonitrile at Pt electrodes. The onset oxidation potential of both carbazole derivatives is located at +1.1 V/SCE (**Figures 8A–C**). After the first cycle, both CzA and CzE oxidation potential peak intensity increases very slightly and the oxidation potential shifts toward slightly higher values. A reduction peak can also be observed at +0.8–0.9 V/SCE during the cathodic scan. A difference between the CVs of the 2 carbazole derivatives was the broadness of the oxidation

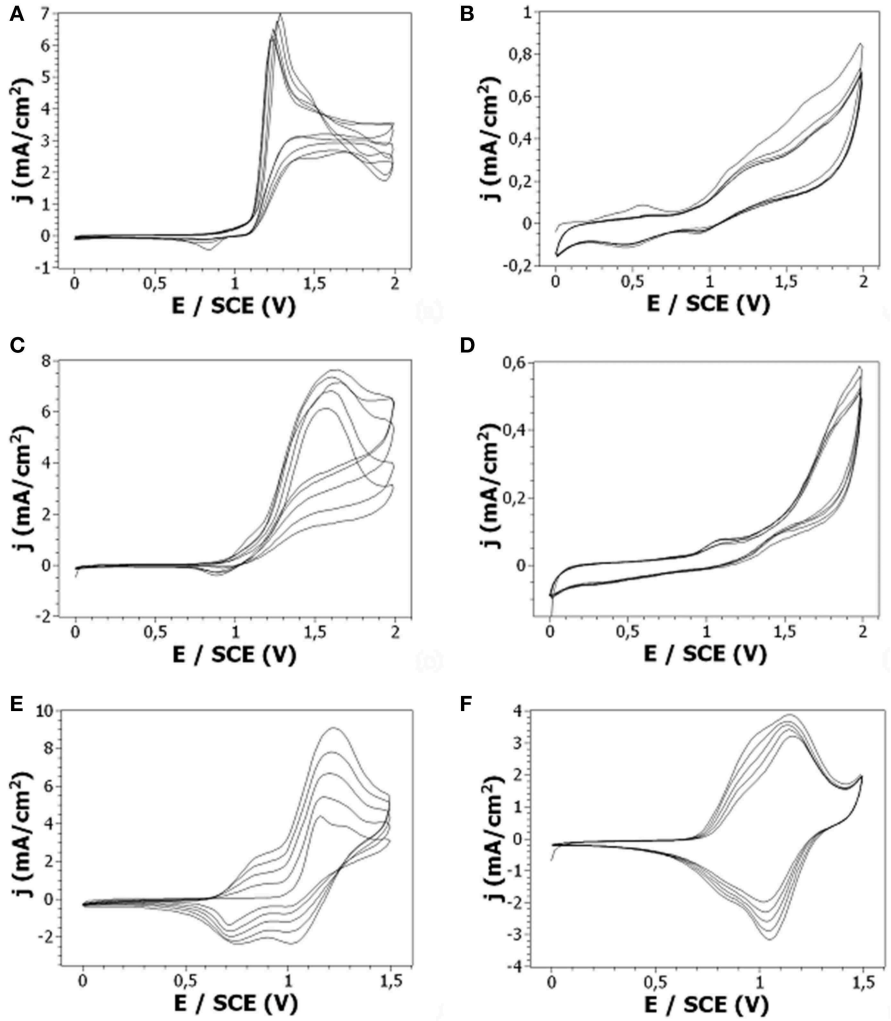

FIGURE 8 | CV **(A,C,E)** and post-polymerization CV **(B,D,F)** at a Pt electrode of 10^{-2} M: **(A,B)** CzE, **(C,D)** CzA, **(E-F)** CzV + 0.1 M $LiClO_4$ in ACN. Scan rate: 50 mV/s.

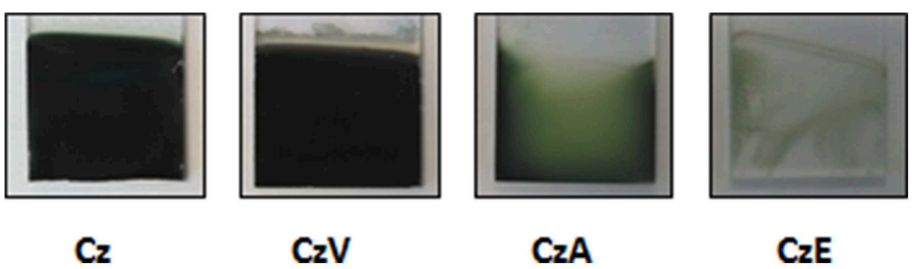

FIGURE 9 | Photographs of samples obtained by oxidation of 10^{-2} M Cz, CzV, CzA, and CzE in an acetonitrile solution (containing 0.1 M $LiClO_4$).

peak. Indeed, CzA leads to a broader oxidation peak than CzE indicating that more CzA monomers are oxidized (since the oxidation of CzA takes place over a wider potential range and with a comparable oxidation peak intensity). Moreover, looking at these 2 samples at the end of the potentiodynamic electrodeposition, it is clear than the oxidation of CzA results in a uniform green-colored film, when the oxidation of CzE results in a thin poor-quality film since only some parts of the substrate are coated (**Figure 9**).

Concerning CzV, the potentiodynamic electrodeposition on platinum displays an oxidation onset at +1.0 V/SCE (**Figure 8E**). Successive scans exhibit increasing anodic current peaks with corresponding cathodic peaks. More precisely, during the 1st scan, only an anodic peak can be observed, at +1.3 V/SCE,

which corresponds to the oxidation of the monomer into cation radicals leading to dimers. During the next scans, another peak is visible at +0.8 V/SCE which is due to the oxidation of oligomers. Hence, the anodic scans correspond to oxidation of the carbazole unit to give the carbazyl radical cation, which, upon cathodic scan, pairs up with another carbazyl moiety adjacent to it to form a dimer. Subsequent current increase (both anodic and cathodic) explains that the process is iterated to give dimers, trimers, oligomers on the working electrode. In addition, it can be noticed that when dimerization occurs, H^+ ions split-off and provoke the polymerization of CzV through its vinyl group. However, if the oxidation of the vinyl groups happens, there is no distinguishable additional oxidation peak. Indeed, the oxidation peak centered at +1.2 V/SCE is too broad to discriminate the oxidation of the nitrogen atom of CzV monomers and the oxidation of its vinyl group. Moreover, the attack of the protons on the vinyl group of the growing polymer causes cross-linking of the film through the vinyl groups as previously evidenced by Reyna-Gonzalez using SEM microscopy and FTIR spectroscopy (Reyna-Gonzalez et al., 2006), thus leading to a compact polymer film. Indeed, at the end of the potentiodynamic electrodeposition, a thick green polymer film is observed at the electrode surface (**Figure 9**) which appeared comparable to the polyCz film previously electrodeposited.

The determination of thermodynamic and kinetic parameters was possible by fast electrochemistry only for 9-alkylcarbazoles since oxidation of carbazole and its other derivatives (Cz, CzA, CzE, and CzV) leads to cation radicals whose stability was not high enough to allow thermodynamic and kinetic parameters extraction. Indeed, under our experimental conditions, it is not possible to estimate dimerization rate constants higher than 10^7 $M^{-1}.s^{-1}$ as cation radicals dimerize too fast, followed by rapid polymerization process leading to a thin conducting polymer film on the microelectrode surface which prevents from any further investigation.

The electrochemical activity of the films electrodeposited by oxidation of CzE, CzA, and CzV in $LiClO_4$ in acetonitrile was then studied at a Pt electrode by cyclic voltammetry in a monomer-free solution of the solvent. Thus, the post-polymerization CV of CzV shows a peak separation (**Figure 8F**) that is expected for a reversible electron transfer process and which was previously observed for polyCz (**Figure 4A**). More precisely, the potential of the oxidation peak, corresponding to the perchlorate anions insertion into the poly(9-vinylcarbazole) film, is located at +1.2 V/SCE, when the reduction peak, corresponding to the ejection of perchlorate anions from the film, is located at +1.05 V/SCE. Moreover, the ratio of oxidation to reduction intensities remains constant around 1.3–1.5 with repeated scans indicating that the doping/dedoping process occurs even after a few scans. On the contrary, the post-polymerization CVs of CzA and CzE don't show a well-defined peak separation (**Figures 8B,D**) even if it is noticeable than CzA leads to more distinguishable oxidation and reduction peaks than CzE (**Figure 8F**). In addition the current densities measured are far lower than those obtained during the post-polymerization of CzV. Thus, it seems that the films obtained by oxidation of CzE and CzA are weakly electroactive which means that the doping and dedoping of these films happens with difficulty.

The morphology of the films obtained by oxidation of these carbazole derivatives was then studied by SEM. The structure of the polyCzA is comparable to the one of PCz since it also consists in small circular heaps covering the whole surface of the substrate (**Figure 5B**). It can just be remarked that the size of the bare domains separating the globules is higher for polyCzA than for polyCz. The polyCzV films also contains globules but these globules agglomerate to form big aggregates composed of tens of globules [the same structure was already observed for polyCzV by Reyna-Gonzalez et al. (2006)]. It seems that the amount of polymer substance on the substrate is higher for polyCzV than for the other polymer materials (**Figure 5C**). Finally, the polyCzE film presents a very different and less uniform structure which doesn't consist in globules but in more extended shapes (**Figure 5D**). Using profilometry measurements, the thickness of the polyCzV films was estimated to 10–11 μm and its roughness to 0.4–0.6 μm indicating that these polymer films are thicker and have a higher roughness than polyCz films. On the contrary, polyCzA and polyCzE films are very thin (<1 μm) and have a roughness which is difficult to estimate since these electrodeposited films are not uniform.

CONCLUSION

The electropolymerization of carbazole was performed and the electrodeposition conditions were optimized. Thus, it was evidenced that it is better to perform the electro-oxidation of carbazole in acetonitrile solutions with perchlorate lithium and at a carbazole concentration of 10^{-2} M. Resulting polyCz film was thick, green-colored, and consists in globules covering the whole substrate and exhibiting a high electrochemical activity.

After organic synthesis of 9-alkylcarbazoles with various alkyl chain lengths, the same electrodeposition conditions were used in order to perform their electropolymerization. However, no deposit was observed at the electrode surface. Fast electrochemistry experiments allowed us to demonstrate that the high stability of resulting radical cation dimers is the explanation for their non-deposition as the oxidized dimers don't polymerize very fast leading to short oligomer chains.

On the contrary, for other carbazole derivatives, obtained by chemical grafting of acid, ester or vinyl groups on the N-position of carbazole, cation radicals are much less stable and polymerization process is more efficient leading to solid polymer films. The quality of these electrodeposited films varies from one compound to the other. Thus, the oxidation of Cz, CzA, and CzV leads to the formation of thick, uniform, green-colored films which are electroactive and present globules on the surface when the oxidation of CzE leads to a non-uniform film.

The carbazole N-substitution by various groups affects the radical cation stability, even if the functional group is not conjugated to the aromatic moiety. As a consequence, the quality of electrodeposited thin films is dependent of the N-substitution functional group.

The possible applications of the substituted polycarbazole films prepared in this work mainly concern the elaboration of chemical (bio)sensors and electrochromic devices. Indeed, the

fabrication of chemiresistors based on these polymer films can be envisaged since it is possible to tune their conductivity. Similarly, the presence of grafted ester and carboxyl groups open the way to the use of polymer films for anchoring biological molecules for biomedical applications. Also, the preparation of electrochromic devices can be envisaged since the color of the polymer films reversibly switches from white to green when changing the potential applied to the polymer-modified electrode.

DATA AVAILABILITY

The datasets generated for this study are available on request to the corresponding author.

AUTHOR CONTRIBUTIONS

EC performed the organic synthesis, CS, SL, CM, and AE performed the electrochemical experiments. BL performed SEM microscopy. All contributed to discussions and writing of the paper.

SUPPLEMENTARY MATERIAL

The Supplementary Material for this article can be found online at: https://www.frontiersin.org/articles/10.3389/fmats.2019.00131/full#supplementary-material

Figure S1 | ^{1}H and ^{13}C NMR spectra of synthesized carbazole monomers.

REFERENCES

Akiyama, T., Fukuyama, T., Sugawa, K., Yoneda, H., and Yamada, S. (2009). Photocurrent generation properties of electrochemically polymerized terthiophene-linked fullerene film. *Synth. Met*. 159, 965–968. doi: 10.1016/j.synthmet.2009.02.019

Ambrose, J. F., Carpenter, L. L., and Nelson, R. F. (1975). Electrochemical and spectroscopic properties of cation radicals (III. Reaction pathways of carbazolium radical ions). *J Electrochem. Soc*. 122, 876–893. doi: 10.1149/1.2134365

Ambrose, J. F., and Nelson, R. F. (1968). Anodic oxidation pathways of carbazoles (Carbazole, I., and N-substituted derivatives). *J Electrochem. Soc*. 115,1159–1163. doi: 10.1149/1.2410929

Atobe, M., Tsuji, H., Asami, R., and Fuchigami, T. (2006). A study on doping–undoping properties of polypyrrole films electropolymerized under ultrasonication electrochemical synthesis and engineering. *J. Electrochem. Soc*. 153, D10–D13. doi: 10.1149/1.2130664

Bryan, A. M., Santino, L. M., Lu, Y., Acharya, S., and D'Arcy, J. M. (2016). Conducting polymers for pseudocapacitive energy storage. *Chem. Mater*. 28, 5989–5998. doi: 10.1021/acs.chemmater.6b01762

Cai, M., Xiao, T., Chen, Y., Hellerich, E., Liu, R., Shinar, R., et al. (2011). Effect of molecular weight on the efficiency of poly(N-vinylcarbazole)-based polymer light-emitting diodes. *Appl. Phys. Lett*. 99:203302. doi: 10.1063/1.3659467

Cai, S., Wen, H., Wang, S., Niu, H., Wang, C., Jiang, X., et al. (2017). Electrochromic polymers electrochemically polymerized from 2, 5-dithienylpyrrole (DTP) with different triarylamine units: synthesis, characterization and opto electrochemical properties. *Electrochim. Acta* 228, 332–342. doi: 10.1016/j.electacta.2017.01.071

Chen, X., and Inganas, O. (1996). Three-step redox in polythiophenes: evidence from electrochemistry at an ultramicroelectrode. *J. Phys. Chem*. 100, 15202–15206. doi: 10.1021/jp.9601779

Chevrot, C., Ngbilo, E., Kham, K., and Sadki, S. (1996). Optical and electronic properties of undoped and doped poly(N-alkylcarbazole) thin layers. *Synth. Met*. 81, 201–204. doi: 10.1016/S0379-6779(96)03752-6

Chmielewski, M., Grzeszczuk, M., Kalenik, J., and Kpas-Suwara, A. (2010). Evaluation of the potential dependence of 2D-3D growth rates and structures of polypyrrole films in aqueous solutions of hexafluorates. *J. Electroanal. Chem*. 647 169–180. doi: 10.1016/j.jelechem.2010.06.006

Conn, M. M., Deslongchamps, G., de Mendoza, J., and Rebek Jr., J. (1993). Convergent functional groups. 13. High-affinity complexation of adenosine derivatives within induced binding pockets. *J. Am. Chem. Soc*. 115, 3548–3557. doi: 10.1021/ja00062a020

Darmanin, T., and Guittard, F. (2014). Wettability of conducting polymers: from superhydrophilicity to superoleohydrophobicity. *Prog. Polym. Sci*. 39, 656–682. doi: 10.1016/j.progpolymsci.2013.10.003

Fonseca, S. M., Moreira, T., Parola, A. J., Pinheiro, C., and Laia, C. A. T. (2017). PEDOT electrodeposition on oriented mesoporous silica templates for electrochromic devices. *Sol. Energy Mater. Sol. Cells* 159, 94–101. doi: 10.1016/j.solmat.2016.09.002

Grigalevicius, S., Zhang, B. H., Xie, Z. Y., Forster, M., and Scherf, U. (2011). Polycarbazole-based networks made by photo-crosslinking for hole transporting layers of OLED devices. *Org. Electron*. 12, 2253–2257. doi: 10.1016/j.orgel.2011.08.018

Hsiao, S. H., and Lin, S. W. (2016). Electrochemical synthesis of electrochromic polycarbazole films from N-phenyl-3,6-bis(N-carbazolyl)carbazoles. *Polym. Chem*. 7, 198–211. doi: 10.1039/C5PY01407G

Hu, B., Lv, X. J., Sun, J. W., Bian, G. F., Ouyang, M., Fu, Z. Y., et al. (2013). Effects on the electrochemical and electrochromic properties of 3,6 linked polycarbazole derivative by the introduction of different acceptor groups and copolymerization. *Org. Electron*. 14, 1521–1530. doi: 10.1016/j.orgel.2013.03.024

Huang, Z. H., Hu, S. C., Zhang, N., Chen, X. L., Chen, D., Jin, Q., et al. (2012). Effect of volume ratio of acetonitrile to water on the morphology and property of polypyrrole prepared by chemical oxidation method. *Polym. Eng. Sci*. 52, 1600–1605. doi: 10.1002/pen.23101

Joshi, N., Saxena, V., Singh, A., Koiry, S. P., Debnath, A. K., Chehimi, M. M., et al. (2014). Flexible H_2S sensor based on gold modified polycarbazole films. *Sens. Actuators B* 200, 227–234. doi: 10.1016/j.snb.2014.04.041

Kapron, K. and Lapkowski, M. (2015). Carbazole electrochemistry: a short review. *Sol. St. Electrochem*. 19, 2601–2610. doi: 10.1007/s10008-015-2973-x

Kausar, A. (2017). Overview on conducting polymer in energy storage and energy conversion. *J. Macromol. Sci. A*. 54, 640–653. doi: 10.1080/10601325.2017.1317210

Lee, Y., Zhou, H., and Lee, T. W. (2018). One-dimensional conjugated polymer nanomaterials for flexible and stretchable electronics. *J. Mater. Chem*. 14, 3538–3550. doi: 10.1039/C7TC05927B

Li, A. Y., Li, Y. Y., Cai, W. Z., Zhou, G. J., Chen, Z., Wu, H. B., et al. (2010). Realization of highly efficient white polymer light-emitting devices via interfacial energy transfer from poly(N-vinylcarbazole). *Org. Electron*. 11, 529–534. doi: 10.1016/j.orgel.2009.12.008

Mali, S. P., Gosavi, S. A., Inamdar, A. S., Chougale, U. M., and Fulari, V. J. (2015). Synthesis and characterizations of chemically and electrochemically polymerized polyaniline thin films for energy storage. *Adv. Sci. Lett*. 21, 2534–2538. doi: 10.1166/asl.2015.6414

Ouyang, J., Chu, C. W., Chen, F. C., Xu, Q., and Yang, Y. (2005). High-conductivity poly(3,4-ethylenedioxythiophene):poly(styrene sulfonate) film and its application in polymer optoelectronic devices. *Adv. Funct. Mater*. 15, 203–208. doi: 10.1002/adfm.200400016

Papez, V., and Josowicz, M. (1994). Electrochemical preparation and study of poly(N-vinylcarbazole) as a sensing layer for propylamine vapor. *J. Electroanal. Chem*. 365, 139–150. doi: 10.1016/0022-0728(93)02979-R

Park, Y. H., Kim, S. J., and Lee, J. Y. (2003). Preparation and characterization of electroconductive polypyrrole copolymer Langmuir-Blodgett films. *Thin Solid Films* 425, 233–238. doi: 10.1016/S0040-6090(02)01123-9

Patois, T., Lakard, B., Martin, N., and Fievet, P. (2010). Effect of various parameters on the conductivity of free standing electrosynthesized polypyrrole films. *Synth. Met*. 160, 2180–2185. doi: 10.1016/j.synthmet.2010.08.005

Patois, T., Lakard, B., Monney, S., Roizard, X., and Fievet, P. (2011). Characterization of the surface properties of polypyrrole films. Influence of the electrodeposition parameters. *Synth. Met.* 161, 2498–2505. doi: 10.1016/j.synthmet.2011.10.003

Peng, X. Y., Luan, F., Liu, X. X., Diamond, D., and Lau, K. T. (2009). pH-controlled morphological structure of polyaniline during electrochemical deposition. *Electrochim. Acta* 54, 6172–6177. doi: 10.1016/j.electacta.2009.05.075

Petrov, R. R., Knight, L., Chen, S. R., Wager-Miller, J., Mc Daniel, S. W., Diaz, F., et al. (2013). Mastering tricyclic ring systems for desirable functional cannabinoid activity. *Eur. J. Med. Chem.* 69, 881–907. doi: 10.1016/j.ejmech.2013.09.038

Reyna-Gonzalez, J. M., Aguilar-Martinez, M., Bautista-Martinez, J. A., Rivera, E., Gonzalez, I., and Roquero, P. (2006). Influence of the acidity level on the electropolymerization of N-vinylcarbazole: electrochemical study and characterization of poly(3,6-N-vinylcarbazole). *Polymer* 47, 6664–6672. doi: 10.1016/j.polymer.2006.07.023

Reyna-González, J. M., Roquero, P., and E., Rivera E (2009). A comparative investigation between poly(N-vinylcarbazole) and poly(3,6-Nvinylcarbazole): spectroscopy, conductivity, thermal and optical properties. *Des. Monomers Polym.* 12, 233–245. doi: 10.1163/156855509X436058

Sarac, A. S., Ates, M., and Parlak, E. A. (2006). Electrolyte and solvent effects of electrocoated polycarbazole thin films on carbon fiber microelectrodes. *J. Appl. Electrochem.* 36, 889–898. doi: 10.1007/s10800-006-9145-8

Sarac, A. S., and Bardavit, Y. (2004). N-vinylcarbazole-styrene free radical polymerization and electrochemical and chemical oxidation of P(NVCz-co-sty) and P(NVCz-co-AN): cyclic voltammetric, spectroscopic (FTIR) and conductometric study. *Int. J. Polym. Mater.* 53, 185–200. doi: 10.1080/00914030490267609

Saraswathi, R., Gerard, M., and Malhotra, B. D. (1999). Characteristics of aqueous polycarbazole batteries. *J. Appl. Polym. Sci.* 74, 145-—50. doi: 10.1002/(SICI)1097-4628(19991003)74:1%3C145::AID-APP18%3E3.0.CO;2-C

Sathiyan, G., and Sakthivel, P. (1993). A multibranched carbazole linked triazine based fluorescent molecule for the selective detection of picric acid. *RSC Adv.* 6, 106705–106715. doi: 10.1039/C6RA22632A

Savagatrup, S., Printz, A. D., O'Connor, T. F., Zaretski, A. V., and Lipomi, D. J. (2014). Molecularly stretchable electronics. *Chem. Mater.* 26, 3028–3041. doi: 10.1021/cm501021v

Shirakawa, H., Louis, E. J., MacDiarmid, A. G., Chiang, C. K., and Heeger, A. J. (1977). Synthesis of electrically conducting organic polymers: halogen derivatives of polyacetylene, $(CH)_x$. *J. Chem. Soc. Chem. Commun.* 1977, 578–580. doi: 10.1039/c39770000578

Srivastava, A., and Chakrabarti, P. (2015). An organic Schottky diode (OSD) based on a-silicon/polycarbazole contact. *Synth. Met.* 207, 96–101. doi: 10.1016/j.synthmet.2015.05.024

Su, P. Y., Huang, L. B., Liu, J. M., Chen, Y. F., Xiao, L. M., Kuang, D. B., et al. (2017). A multifunctional poly-N-vinylcarbazole interlayer in perovskite solar cells for high stability and efficiency: a test with new triazatruxene-based hole transporting materials. *J. Mater. Chem. A* 5, 1913–1918. doi: 10.1039/C6TA09314K

Vedarajan, R., Hosono, Y., and Matsumi, N. (2014). pi-Conjugated polycarbazole-boron complex as a colorimetric fluoride ion sensor. *Sol. Stat. Ion.* 262, 795–800. doi: 10.1016/j.ssi.2013.09.062

Viau, L., Hihn, J. Y., Lakard, S., Moutarlier, V., Flaud, V., and Lakard, B. (2014). Full characterization of polypyrrole thin films electrosynthesized in room temperature ionic liquid, water or acetonitrile. *Electrochim. Acta* 137, 298–310. doi: 10.1016/j.electacta.2014.05.143

Wei, Z., Xu, J., Nie, G., Du, Y., and Pu, S. (2006). Low-potential electrochemical polymerization of carbazole and its alkyl derivatives. *J. Electroanal. Chem.* 589, 112–119. doi: 10.1016/j.jelechem.2006.01.023

Wojcik, K., and Grzeszczuk, M. (2015). Surface morphology of thin polypyrrole films electrodeposited along aqueous electrolyte-organic liquid interface. Influence of temperature and solvent. *J. Sol. State Electrochem.* 19, 1293–1300. doi: 10.1007/s10008-015-2750-x

Yaguee, J. L., Agulo, N., and Borros, S. (2008). Plasma polymerization of polypyrrole-like films on nanostructured surfaces. *Plasma Proces. Polym.* 5, 433–443. doi: 10.1002/ppap.200700139

Zhang, T., Wang, J., Zhou, M., Ma, L., Yin, G., Chen, G., et al. (2014). Influence of polyhedral oligomeric silsesquioxanes (POSS) on blue light-emitting materials for OLED. *Tetrahedron* 70, 2478–2486. doi: 10.1016/j.tet.2013.11.082

Conflict of Interest Statement: The authors declare that the research was conducted in the absence of any commercial or financial relationships that could be construed as a potential conflict of interest.

Copyright © 2019 Contal, Sougueh, Lakard, Et Taouil, Magnenet and Lakard. This is an open-access article distributed under the terms of the Creative Commons Attribution License (CC BY). The use, distribution or reproduction in other forums is permitted, provided the original author(s) and the copyright owner(s) are credited and that the original publication in this journal is cited, in accordance with accepted academic practice. No use, distribution or reproduction is permitted which does not comply with these terms.

frontiers in Materials

ORIGINAL RESEARCH
published: 10 July 2019
doi: 10.3389/fmats.2019.00156

Conducting Materials Based on Epoxy/Graphene Nanoplatelet Composites With Microwave Absorbing Properties: Effect of the Processing Conditions and Ionic Liquid

Adriana A. Silva[1], Raiany Stein[2], Daniela Campos[1], Tamara Indrusiak[3,4], Bluma G. Soares[2,3]* and Guilherme M. O. Barra[5]*

[1] Escola de Química, Universidade Federal do Rio de Janeiro, Rio de Janeiro, Brazil, [2] Instituto de Macromoléculas, Universidade Federal do Rio de Janeiro, Rio de Janeiro, Brazil, [3] PEMM-COPPE, Universidade Federal do Rio de Janeiro, Rio de Janeiro, Brazil, [4] Brazilian Army Technological Center, Rio de Janeiro, Brazil, [5] Departamento de Engenharia Mecânica, Universidade Federal de Santa Catarina, Florianopolis, Brazil

OPEN ACCESS

Edited by:
Andrea Dorigato,
University of Trento, Italy

Reviewed by:
Veronique Michaud,
École Polytechnique Fédérale de Lausanne, Switzerland
Dongyan Liu,
Institute of Metals Research (CAS), China

***Correspondence:**
Adriana A. Silva
anjosadriana@eq.ufrj.br
Bluma G. Soares
bluma@metalmat.ufrj.br

Specialty section:
This article was submitted to Polymeric and Composite Materials, a section of the journal Frontiers in Materials

Received: 19 April 2019
Accepted: 18 June 2019
Published: 10 July 2019

Citation:
Silva AA, Stein R, Campos D, Indrusiak T, Soares BG and Barra GMO (2019) Conducting Materials Based on Epoxy/Graphene Nanoplatelet Composites With Microwave Absorbing Properties: Effect of the Processing Conditions and Ionic Liquid. Front. Mater. 6:156. doi: 10.3389/fmats.2019.00156

Conducting composite materials based on epoxy matrix loaded with graphene nanoplatelets (GNP) were prepared by different procedures using ultrasonication. The dispersions of GNP in a mixture of epoxy/methyl-tetrahydrophthalic anhydride without solvent, resulted in composites with better conductivity, higher storage modulus and higher glass transition temperature than those prepared with solvent assisted procedure, indicating better filler dispersion. The non-covalent functionalization of GNP with the ionic liquid, 1-butyl-3-methyl-imidazolium bis(trifluorosulfonyl) imide (bmim.TFSI) contributed for an increase of the modulus for the systems containing low amount of filler. The electrical conductivity was not influenced by the presence of ionic liquid. Nevertheless, the micro-wave absorption effectiveness in the frequency range of 8-12 GHz (X-band frequency) was improved by the presence of IL mainly for the composites containing 0.9 and 1.5 vol.% of filler. All systems were characterized by low viscosity, comparable to that of neat epoxy resin, thus making easier their application on the development of coatings, conducting adhesives, etc.

Keywords: epoxy resin, graphene nanoplatelets, ionic liquid, electrical conductivity, micro-wave absorption property

INTRODUCTION

Epoxy resins have been widely used as thermosetting matrices for composites and nanocomposites due to their excellent mechanical, thermal and adhesion properties. However, their insulating nature contributes for accumulating static charges during service, which may be dangerous in some situations. Blending epoxy resins with nanoscale carbon-based fillers is considered a promising approach for developing multi-functional thermosetting materials with outstanding mechanical performance and electrical properties, thus enlarging their field of applications as antistatic coatings, conducting adhesives, sensors, electromagnetic interference shielding materials

for electronic devices, etc. Among these fillers, carbon nanotubes (CNT) are nowadays the most studied conductive filler for this purpose, due to their high thermal and electrical conductivity, as well as high aspect ratio, thus contributing for the development of new conducting composites with low percolation threshold, i.e., low amount of filler to attain good level of conductivity for specific purposes (Ma et al., 2010; Sahoo et al., 2010). As the main drawbacks, CNT is still expensive and also induces significant increase in viscosity of the epoxy dispersion, which limits the amount of filler that can be compounded.

Recently, graphene nanoplatelets (GNP) appeared as an alternative for producing conducting polymeric materials due to their excellent thermal, mechanical and electrical properties. GNP consists of few stacked graphene layers, easily obtained by exfoliation of low cost and available natural graphite, being less expensive than CNT. Moreover, the viscosity of epoxy/GNP dispersions is usually lower than that observed for epoxy/CNT dispersions (Martin-Gallego et al., 2013). The superior physico-mechanical performance, better processability and increasing availability of expanded graphite (EG) and graphene nanoplatelets (GNP) led to a large research effort in the last decade related to GNP-based composites (Liu et al., 2018). Several reports describe the superior toughness (Tang et al., 2013; Kang et al., 2017; Chakraborty et al., 2018; Hashim and Jumahat, 2019), reinforcement (Yasmin et al., 2006; Chatterjee et al., 2012) and thermal properties (Prolongo et al., 2014) of epoxy nanocomposites loaded with different amounts of GNP. This filler also promotes an increase of electrical conductivity. However, the values are usually lower than those observed for CNT-based nanocomposites (Martin-Gallego et al., 2013; Yue et al., 2014). This behavior may be attributed to the great tendency of GNP to agglomerate due to the strong Van der Waals forces and π-π interactions between the graphene sheets, which are favored by its planar structure. Therefore, the preparation and exfoliation of GNP commonly involves the treatment with strong acids, which introduces some defects on the electron π conjugation along the graphene surface and negatively affects its intrinsic conductivity. Thus, a great strategy in this field is to find appropriate conditions to promote better dispersion of GNP within a polymer matrix without disturbing the conjugated structure. This can be achieved by employing appropriate mixing conditions and/or the non-covalent functionalization of GNP. Some works in the literature reported the use of sonication (Corcione and Maffezzoli, 2013; Monti et al., 2013) ball milling procedure (Guo and Chen, 2014) and high shear laminar flow using three roll-mill (Ma et al., 2010; Prolongo et al., 2013), among others.

The use of room temperature ionic liquids has been recently considered as another approach to disperse carbon-based nanomaterials due to the favorable cation-π interactions between the carbon surface and ILs. This strategy has been successfully used in epoxy/CNT systems (Throckmorton et al., 2013; Lopes Pereira and Soares, 2016; Sanes et al., 2016; Soares et al., 2016), and also with some epoxy/GNP networks. For example, Zhang and Park (2019) modified GNP previously treated with atmosphere-pressure plasma with 1-ethyl-3-methylimidazolium chloride (emim.Cl) and obtained epoxy/GNP nanocomposites with improved thermal conductivity and storage modulus, when compared to those produced with non-functionalized GNP. Hameed et al. (2018) used 40% of 1-butyl-3-methylimidazolium chloride (bmim.Cl) in epoxy resin loaded with different amounts of GNP in order to produce flexible epoxy networks. They observed lower conductivity values when compared with epoxy/IL system. Dermani et al. (2018) also employed bmim.Cl in epoxy formulations modified with graphene oxide nanosheets and observed a significant increase on storage modulus and glass transition temperature. Kowsary and Mohammed (2016) prepared reduced graphene oxide covalently modified with magnetic imidazolium-based ionic liquid and used it as filler in epoxy resin. They obtained composites with good microwave absorbing properties. Throckmorton et al. dispersed GNP in a mixture of epoxy and 1-ethyl-3-methylimidazolium dicyanamide (emim.DCN) using three roll-mill (Throckmorton et al., 2013; Throckmorton and Palmese, 2015) and obtained compositions with outstanding electrical conductivity. In this case, IL exerted the role of curing agent. Guo et al. (2009) studied the effect of bmim.PF_6 on the curing behavior of epoxy/graphite composites cured with Jeffamine D230, an aliphatic amine. However, no mention regarding the electrical properties was made. Liu et al. (2013) dispersed GNP with 1-aminopropyl-3-butylimidazolium hexafluorophosphate and used in epoxy system cured with methyl-tetrahydrophthalic anhydride (MTHPA). They observed a better dispersion of GNP with IL and an improvement of modulus. However, the electrical properties were not discussed.

The development of sophisticated electronic equipments and communication devices also originates a type of invisible pollution, known as electromagnetic interference, which can affect the efficient operation of other electronic devices. Therefore, studies involving the development of materials with enhanced electromagnetic interference shielding effectiveness (EMI SE) have increased in interest in several fields of telecommunications and other civil applications. Moreover, such materials find enormous interest in the military research involved on the stealth technology. Conducting composites based on carbon materials have been widely employed as microwave absorbing materials, because of their light-weight and cost-effective characteristics, as well as the ability of being used in different forms as film, plaques or even coatings (Thomassin et al., 2013; Sankaran et al., 2018; Wang et al., 2018). The success of these materials is derived of the ability of the conducting particles dispersed inside a certain polymer matrix in interacting with the electromagnetic wave in the microwave frequency range thus absorbing or reflecting the radiation. There are a lot of publications in the literature related to this theme. Most of them discuss the effectiveness of carbon black- and carbon nanotube as the filler for the development of carbon-based composites with these characteristics. The interest related to epoxy/GNP networks also increased in the last decade due to the several advantages of using GNP as conducting filler, such as, low cost, high surface area and high intrinsic conductivity. Liang et al. (2009) used graphene-based sheets in epoxy matrix and obtained composites with around 21 dB shielding efficiency in the X-band frequency range, when 15 wt.% of filler was employed. Kowsary and Mohammed (2016) obtained a maximum of reflection loss

(attenuation of the EM radiation) of 25 dB at 8.62 GHz by using epoxy composite containing 40 wt.% of reduced graphene oxide covalently modified with ionic liquid bearing magnetic anion. Chhetri et al. (2016) prepared graphene oxide non-covalently functionalized with sulfanilic acid azocromotrop followed by reduction with hydrazine. The epoxy composite containing 0.5 wt.% of the modified RGO presented a EMI SE of 226 dB at a frequency of around 2 GHz.

The aim of the work was to investigate the processing conditions for dispersing commercial GNP within the epoxy matrix cured with anhydride and how these conditions affected the electrical conductivity. This work also highlights the influence of the imidazolium-based ionic liquid on the electrical conductivity, thermal properties and microwave absorbing properties of the corresponding epoxy composites. For this purpose, 1-butyl-3-methyl imidazolium bis(trifluormethylsulfonyl) imide (bmim.TFSI) was chosen as the ionic liquid because of its high thermal stability, good ionic conductivity and hydrophobicity when compared with other ionic liquids, thus improving the miscibility with epoxy systems (Herath et al., 2011).

EXPERIMENTAL SECTION

Materials

Epoxy resin, diglycidyl ether of bisphenol A (DGEBA) (MC 130) (epoxide equivalent weight = 185–192; density = 1.25; viscosity = 12.5 Pa.s) was purchased from Turlock, China and commercialized by Epoxyfiber, Brazil. Methyl-tetrahydrophthalic anhydride (MTHPA) used as hardener (density = 1.20; viscosity = 40-70 mPa.s) and benzyldimethylamine used as accelerator was fabricated by DDChem, Italy, and commercialized by EpoxyFiber, Brazil. Graphene nanoplatelet (GNP) (trade name = xGnP-M-5) (average particle diameter = 5 mm; average thickness = 7 nm; density = 2.17 g/cm^3; surface area =130 m^2/g) was purchased from XG Sciences, Lansing. 1-butyl-3-methyl-imidazolium bis(trifluormethylsulfonyl)imide as the ionic liquid (bmim.TFSI) was purchased from Sigma-Aldrich.

Preparation of Nanocomposites

The studies involving the methodology for the dispersion of GNP into epoxy matrix were performed without ionic liquid. The filler was dispersed in the ER using two different procedures: (Method A) the filler was dispersed in a mixture containing ER and acetone (2:1 by weight) under sonication at 135 W for 15 min, with ice bath to avoid heating of the medium. This operation was repeated four times with intervals of 5 min, to ensure good dispersion. After this step, the solvent was removed under vacuum, the MTHPA as the hardener (80 phr related to the resin) and the catalyst (1 phr) were added and the mixture was poured into silicon molds and cured using the following curing protocol: 2 h at 80°C, 2 h at 120°C, and 1 h at 130°C; (Method B) the filler was dispersed in a mixture containing ER and MTHPA (100:80). The medium was sonicated using similar conditions as in the Method A. Then, the mixture was submitted to vacuum to remove some bubbles. After that, 1 phr of the catalyst was added and the mixture was poured into silicon molds and cured with similar protocol as that mentioned before. The amount of the filler was designed as vol. %. The conversion from wt.% to vol.% was performed by using the density values of each component in the blend.

For the studies related to the effect of ionic liquid on the main properties of the ER/GNP nanocomposites, the GNP was previously modified with different ILs by grinding both components in a mortar for about 20 min. Afterwards, the resulting black paste was dispersed in a mixture of ER/MTHPA using Method B (without acetone).

Characterization

Scanning electron microscopy was performed on a TESCAN (Vega 3 model) at 20 kV. The samples were fractured and coated with thin layer of gold before analysis.

The AC electrical conductivity (σ_{AC}) was measured in a frequency range from 0.1 Hz to 10 MHz using a Solartron SI 1260 gain phase analyzer interfaced to a Solartron 1296 dielectric interface. The measurements were made at 25°C, using electrodes with 25 mm diameter and oscillating voltage of 100 mV. Samples of 1 mm thickness were prepared.

Microwave absorbing properties of the composites were measured at a X-band frequency range (8.2–12.4 GHz) using a network analyzer N530L PNA-L from Agilent, equipped with rectangular waveguide. In order to evaluate the reflection loss, a configuration consisting of metal plate fixed to the sample holder was used. This configuration enables measuring only the reflection parameter. A decreasing of this reflection corresponds to the absorbed radiation (Chen et al., 2004). Samples with 2 mm thickness were employed.

Rheological measurements were carried out with a strain controlled rotational rheometer (DHR, TA Instruments) at 25°C. Nanocomposites samples were loaded between 25 mm parallel plates. They were squeezed into disks ∼1 mm thick by slowly lowering the upper plate. The measurements were performed in oscillatory mode in the frequency range from 0.1 to100 rad/s and strain of 0.1%.

Dynamic-mechanical analysis (DMA) was performed in a DMA Q800 from TA Instruments Inc, operating at frequency of 1 Hz, strain of 0.1 % and a heating rate of 3°C/min from 25 to 200°C. Single-cantilever clamp was used in samples with 17 × 12 × 2.5 mm dimensions. The glass transition temperature was taken from the maximum of tan delta peak.

RESULTS AND DISCUSSION

Effect of the Processing Conditions

Two different methodologies were employed to disperse GNP within the epoxy matrix: method A (solvent-assisted procedure) and method B (non-solvent procedure). For method B, it was taken the advantage of the low viscosity of the anhydride-based curing agent, which allows efficient dispersion of the filler in the ER/MTHPA system using ultrasonication, without the solvent assistance. Moreover, the low reactivity of the hardener enables safe dispersion of GNP without premature cure, as the curing only occurs with the addition of the catalyst. **Figure 1** shows the dependence of AC electrical conductivity (σ_{AC}) vs. frequency

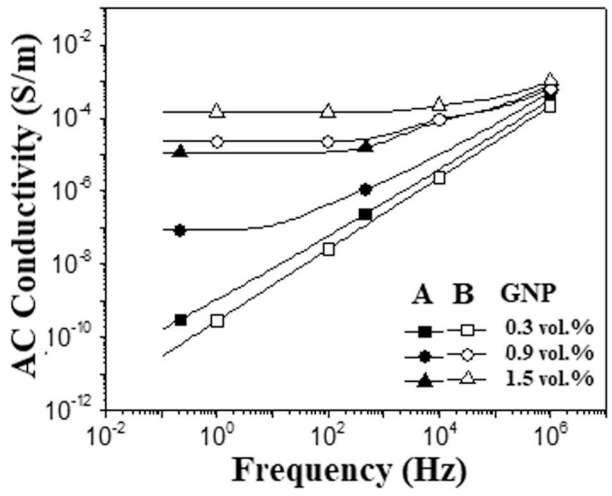

FIGURE 1 | AC electrical conductivity vs. frequency for ER/GNP composites as a function of the dispersion procedure and GNP content (A, method A; B, method B).

for the ER/GNP composites prepared by the two different procedures. The composites loaded with 0.55 wt% (0.3 vol.%) of GNP presented a linear dependence of the σ_{AC} with frequency, which is typical of an insulating material. The amount of GNP was too low to allow the formation of a conducting pathway.

Increasing the amount of filler increased the conductivity at low frequency region. The composites with higher amount of filler (0.9 and 1.5 vol %) also presented a DC conductivity plateau at low frequency, which was shifted toward higher frequencies as the amount of filler increased, suggesting the formation of a conductive network. The increase of σ_{AC} beyond a certain frequency indicated that the conducting process turned back to the non-ohmic way (frequency dependent) which is characterized by a hopping-tunneling effect between GNP particles separated by the polymer layer. The composite prepared by method B, loaded with 0.9 vol.% of GNP, displayed σ_{AC} values around three orders of magnitude higher than that prepared by the solvent-assisted procedure (method A). This result suggests that the anhydride used as hardener interacts with GNP and favors the de-agglomeration of the GNP stacks. The better dispersion of GNP endows the GNP particles to touch each other, increasing the conductivity.

The conductivity values found in the present work, prepared by method B, were comparable or even superior to those reported in the literature, as indicated in **Table 1**. Although a comparative study for this system is not reliable due to different nature of the GNP, as well as different hardeners and processing conditions, the present study highlights the effectiveness of the non-solvent processing methodology to achieve good GNP dispersion. These results are interesting for the technological, economical and environmental point of view because it does not use solvent during processing, which also eliminate the solvent withdrawal step under vacuum for several hours or days performing the curing process.

The effect of the processing methodology on the dynamic-mechanical properties of ER/GNP composites was evaluated in terms of storage modulus (E') and tan delta, whose data are summarized in **Table 2**.

The GNP-based composites prepared by both techniques displayed higher E' values than that obtained for the neat epoxy network, except the composite loaded with 0.3 vol.% of GNP and prepared by solvent-assisted method, which presented similar E' value. These results confirm the reinforcing effect of GNP as filler for epoxy network. Similar behavior has been reported in the literature (Saurin et al., 2014). The E' of composites prepared by method A increased as the amount of GNP in the composites increased. Regarding those composites prepared by Method B, the addition of as low as 0.3 vol.% of GNP was enough to increase the modulus in both glassy and rubbery region. Also the addition of 1.5 vol.% of GNP resulted in significant improvement of E' in the glassy region, confirming the better GNP dispersion and higher reinforcing action of the filler by using the non-solvent technique. The glass transition temperature was superior to the neat epoxy network, the difference being more significant for the composites prepared by Method B. For this series, the higher value was obtained by using 0.9 vol.% of GNP. These results can be attributed to the improved interfacial interaction between filler-matrix, probably due to a good interaction between anhydride and GNP during the processing step. Increasing the GNP amount decreased the Tg probably because the formation of GNP aggregates in this higher concentration, which favor the presence of free volume at the filler-matrix interface and a better polymer chain mobility.

The effect of the dispersion methodology on the morphology of ER/GNP composites was evaluated by SEM micrograph, as illustrated in **Figure 2**. The micrographs of the composites prepared by Method A or B are similar, with rough surface. However, it is possible to observe in the samples prepared by method A the presence of agglomerated structures in higher extent, mainly for the samples with higher GNP content (**Figure 2c**).

Effect of Ionic Liquid as Dispersing Agent for GNP

To improve the dispersion of GNP within the epoxy matrix, the filler was previously treated with bmim.TFSI as the ionic liquid to promote a physical interaction between them and facilitate the debundling of the graphene sheets from GNP stacks. The effect of the ionic liquid on the processability of the ER/GNP dispersions was evaluated in terms of complex viscosity (η^*). For this study, the Method B was adopted. Therefore, the measurements were performed in GNP dispersion in the ER/MTHPA mixture. **Figure 3** illustrates the dependence of η^* with frequency for the ER and the corresponding dispersions loaded with 1.5 and 3.0 vol.% of GNP (2.7 and 5.3 wt.%). All systems presented a Newtonian behavior, i.e., the viscosity practically did not change with the frequency. The η^* values of the dispersions were quite similar as that found for neat ER, except that corresponding to the ER/MTHMA dispersion with 3.0 vol.% of GNP/IL, which displayed an increase in viscosity. This behavior suggests some

TABLE 1 | Comparative results of electrical conductivity of epoxy/GNP composites.

GNP amount	Curing agent	Observations	Conductivity (S/m)	References
2 wt.%	triethylenetetramine	Sonication with acetone	10^{-7}	Jovic et al., 2008
2 vol.%	Isophorone diamine		10^{-8}	Corcione and Maffezzoli, 2013
0.63 vol.%	polyamide	Sonication with ethanol	10^{-6}	Zheng et al., 2019
2 wt.%	Methyl-hexahydrophthalic anhydride	Fast dispersion method/sonication without solvent	10^{-4}	Li et al., 2017a
4 wt.%	amine	sonication	10^{-5}	Yue et al., 2014
1.5 vol.%	MTHPA	sonication without solvent	10^{-4}	This work

TABLE 2 | Dynamic-mechanical properties of ER/GNP composites as a function of the processing methodology.

GNP (vol.%)	E' at 25°C (GPa)		E' at 200°C (GPa)		Glass transition temperature (°C)	
	A	B	A	B	A	B
0	1.7		0.013		118	
0.3	1.6	2.0	0.009	0.019	131	142
0.9	1.8	1.8	0.011	0.013	134	141
1.5	2.2	2.7	0.018	0.018	132	133

A, Method A (solvent-assisted method); B, Method B (non-solvent method).

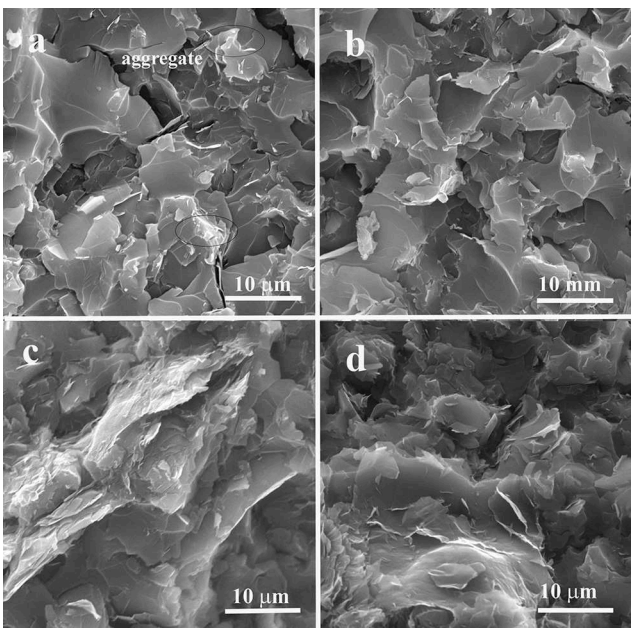

FIGURE 2 | SEM micrographs of ER/GNP loaded with 0.9 vol.% dispersed by **(a)** Method A and **(b)** Method B with 1.5 vol.% of GNP dispersed by **(c)** Method A and **(d)** Method B.

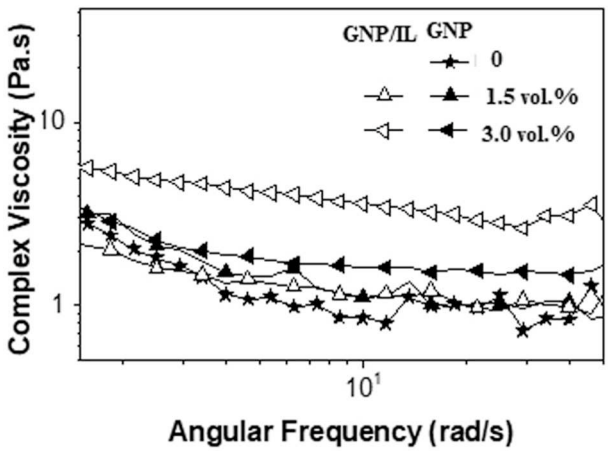

FIGURE 3 | Dependence of complex viscosity with frequency for the neat ER and the corresponding ER/MTHPA dispersions loaded with 1.5 and 3.0 vol.% of GNP or GNP/IL.

TABLE 3 | AC electrical conductivity of epoxy-based composites loaded with different amounts of GNP.

GNP content (vol.%)	AC electrical conductivity at 1 Hz (S/m)	
	Without IL	With 2.2 vol.% of IL
0.3	$2.7\ (\pm0.1) \times 10^{-10}$	$6.0\ (\pm0.6) \times 10^{-10}$
0.9	$2.0\ (\pm1.2) \times 10^{-5}$	$9.0\ (\pm2.9) \times 10^{-6}$
1.5	$1.6\ (\pm1.0) \times 10^{-4}$	$3.2\ (\pm3.0) \times 10^{-5}$
3.0	$1.0\ (\pm0.1) \times 10^{-4}$	$1.0\ (\pm0.9) \times 10^{-4}$

improvement of filler-matrix interaction imparted by the IL at the interface. Nevertheless, all dispersions presented low viscosity values due to the presence of the anhydride, which is interesting for processing purpose.

The σ_{AC} values of the composites loaded with GNP and GNP/IL are summarized in **Table 3**, as a function of the GNP content. The values were an average of at least three measurements. Both systems presented a significant transition from an insulator into a semiconductor when the amount of filler increased from 0.3 to 0.9 vol.%. Beyond this concentration,

TABLE 4 | Dynamic-mechanical parameters of ER/GNP composites as a function of the GNP content and the presence of ionic liquid.

GNP content (vol.%)	Storage modulus at 25°C (GPa)		Storage modulus at 190 °C (GPa)		Glass transition temperature (°C)	
	A	B	A	B	A	B
0	1.7		0.011		118	
0.3	2.0	2.0	0.019	0.010	142	126
0.9	1.8	2.3	0.013	0.014	141	129
1.5	2.7	2.6	0.018	0.050	133	146
3.0	2.7	2.3	0.020	0.014	128	132

A, without ionic liquid; B, with 2.2 vol.% of ionic liquid.

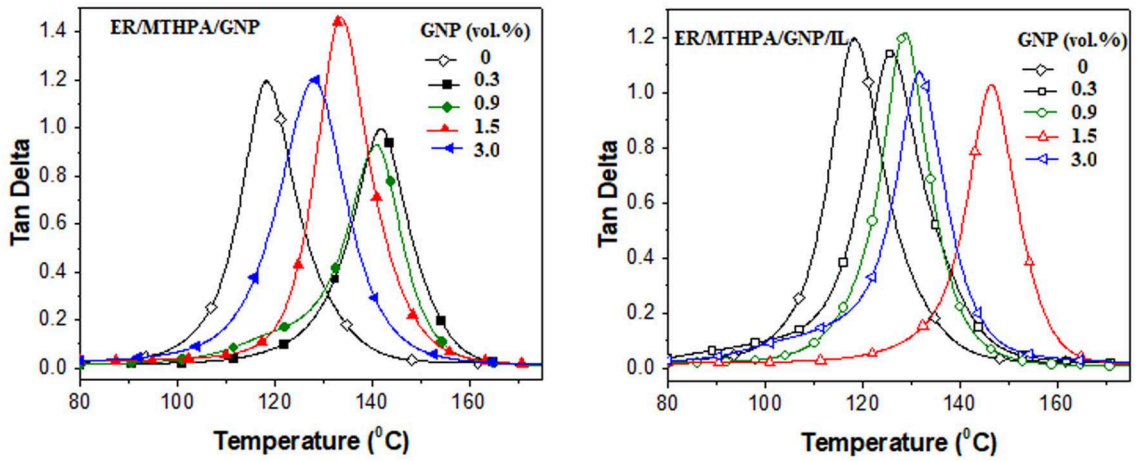

FIGURE 4 | Effect of ionic liquid and GNP content on the Tan delta of ER/GNP composites.

the conductivity slightly increased, probably because of the aggregation of the filler. Similar behavior was reported by Min et al. (2013) for epoxy/GNP composites using similar hardener. The authors observed an increase of the conductivity value at low frequency from the composite loaded with 0.9 vol.% of GNP to that containing 2.7 vol.% of GNP of about one order of magnitude (from 10^{-8} to 10^{-7} S/cm) (Min et al., 2013). Other studies reported that after around 1 vol.% of GNP the conductivity did not change (Yue et al., 2014; Zheng et al., 2019) or even decreased with higher amount of GNP (Yousefi et al., 2013; Li et al., 2017b). According to Zheng et al. (2019) the decrease in the conductivity of the composites with larger GNP loading may be explained by the agglomeration of GNP.

Contrarily to the behavior usually reported for epoxy/CNT functionalized with ionic liquids, the functionalization of GNP with ionic liquid did not exert great influence on the conductivity value of the epoxy-based composites. In fact, a slight decrease of the conductivity was observed with the addition of IL. Zhang and Park (2019) observed an increase of the conductivity of epoxy matrix cured with aromatic amine by using plasma-induced expanded graphite functionalized with 1-ethyl-3-methyl imidazolium chloride.

The different behavior observed in the present work may be due to the different nature of the GNP as well as the different hardener used to cure the epoxy matrix. One can suggest that the exfoliation of GNP by the IL is a difficult process due to the Van der Waals forces between the graphene sheets, which should be stronger than in the case of CNT due to the planar structure of the sheets, providing more contact points between the sheets. Moreover, the IL at the GNP surface may form a thin insulating layer that prevents direct contact between the conducting filler particles. Xu et al. (2014) observed similar behavior in polypropylene-based composites loaded with carbon nanotube functionalized with imidazolium-type ionic liquid.

The effect of the ionic liquid on the dynamic-mechanical properties of ER/GNP composites was summarized in **Table 4**, as a function of the GNP content. The dependence of the Tan delta with the temperature was also illustrated in **Figure 4**. The E' values of the composites prepared with GNP/IL increased as the amount of filler increased until 1.5 vol.% of filler. Increasing the amount of filler decreased the modulus, probably due some agglomeration of the filler at this concentration (Chhetri et al., 2017). It is interesting to observe that the system loaded with 0.9 vol.% of GNP/IL presented significantly higher E' value than that containing GNP, suggesting a better dispersion of the filler within the epoxy matrix thus forming higher surface area. Moreover, the ionic liquid at the GNP surface should act as an interfacial agent, improving the interfacial adhesion between filler and matrix. The

glass transition temperature was taken as the temperature at the maximum of the tan delta peak. All systems presented higher Tg than the neat epoxy network. Regarding the systems loaded with non-functionalized GNP, the Tg values are higher with low amount of filler (until 0.9 vol.%) and decrease as the amount of filler increase, because of the filler agglomeration phenomenon that occurs with higher filler loading. The formation of aggregates contributes for the presence of free volume at the interface, thus increasing the chain mobility. The decrease of Tg with higher amount of GNP was also reported by Zaman et al. (2011). Regarding the composites loaded with GNP/IL, the Tg increased with the increasing the amount of filler, reaching the maximum value of 146°C at a concentration of GNP corresponding to 1.5 vol.%. After this point, the Tg decreased due to the presence of aggregates. The higher Tg value for the composite loaded with 1.5 vol.% of GNP/IL suggests a good interfacial adhesion between filler and epoxy, thus reducing the mobility of the epoxy chains around the GNP sheet.

Micro-Wave Absorption Property

The effect of ionic liquid on the reflection loss in the X-band frequency range for the ER/GNP composites with a thickness of 2 mm is illustrated in **Figure 5**. The curves present three minimum reflection loss, that, is, maximum of electromagnetic radiation attenuation. For the composites prepared with non-functionalized GNP, the RL is low for the composite containing 0.3 vol.% of GNP and increased when the amount of GNP increased to 0.9 vol.%. After this point, the RL decreased, which can be attributed to an increase of the conductivity. The mobile charge carriers in higher extent interact with EM radiation, thus increasing the reflection phenomenon, higher than absorption. The higher RL value was observed for the composite containing 0.9 vol.%, at 8.75 GHz with RL value of 11.7 dB. The functionalization of the GNP with ionic liquid resulted in composites with higher RL. For the system loaded with 0.3 vol.% of GNP/IL, the minimum RL value was observed at 11.7 GHz with a RL value of 6.9 dB, whereas for the composite containing 0.9 vol.% of GNP/IL, minimum RL values of dB = 9 and 10 dB were observed at−12 and−13 dB, respectively. The composite containing 1.5 vol% presented the better radiation attenuation and this phenomenon corresponded to a frequency of 8.7 GHz. At this point, a RL value of 13.5 dB was obtained, which corresponds to an absorption efficiency of around 96%. These results indicated that the presence of 2.2 vol.% of IL in these composites contributed for a better electromagnetic radiation attenuation, although the conductivity was not varied. This phenomenon may be related to the dispersion of the GNP sheets in the composite. The presence of the IL at the GNP surface provided a better dispersion of the filler. Therefore, the possibility of the interaction of the radiation with the GNP platelets is increased, thus contributing for a better microwave absorption property.

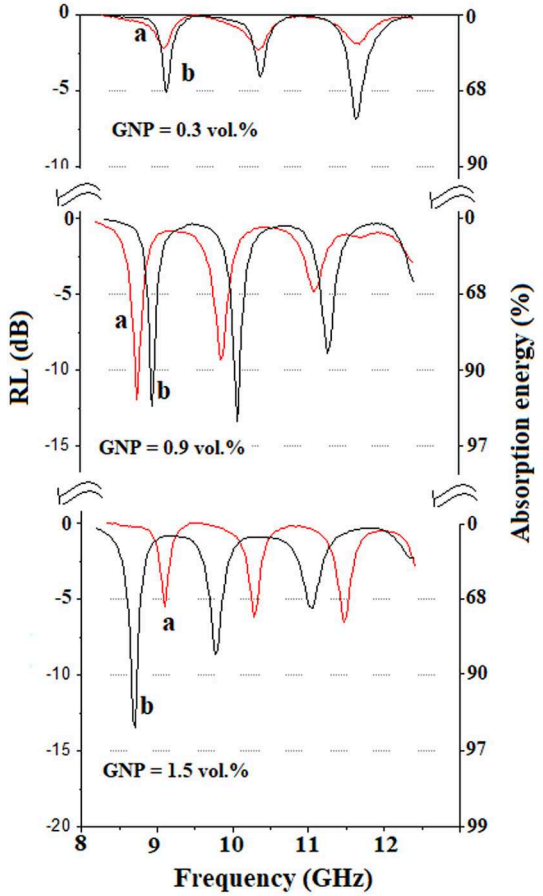

FIGURE 5 | Reflection loss in the X-band frequency range for the ER/GNP composites with thickness of 2 mm (a; red line) = GNP; (b; black line) = GNP/IL.

CONCLUSION

Conducting composites based on epoxy matrix containing different proportions of GNP or GNP non-covalently functionalized with bmim.TFSI as the ionic liquid were prepared in this study. The ER/GNP composites were prepared by two different methodologies: solvent assisted and non-solvent procedure, and cured with MTHPA. The later methodology resulted in higher conductivity values and outstanding storage modulus and glass transition temperature. The functionalization of GNP with 2.2 vol.% of ionic liquid resulted in composites with increased storage modulus when lower amount of GNP/IL was used. Finally, the presence of ionic liquid resulted in better micro-wave absorption properties, which may explained by the better dispersion of the filler. The present work highlights the influence of the ionic liquid as dispersing agent for GNP and opens new possibilities of developing profitable micro-wave absorbing epoxy networks with low viscosity, thus enlarging the field of application, mainly as coating and adhesives.

DATA AVAILABILITY

All datasets generated for this study are included in the manuscript and/or the supplementary files.

AUTHOR CONTRIBUTIONS

RS and DC are undergraduate students of the University, and develop a research project of scientific initiation, and were responsible for preparing the samples for the characterization of the composites. TI contributed with the measurements and interpretation of the absorption analysis of electromagnetic radiation. GB, who has experience in conducting polymers, collaborated in the interpretation of the phenomena of electric conduction of composite materials. BS with extensive experience in composite materials and conductive polymers contributed to the characterization of the mechanical and conductive properties of the research systems. AS contributed to the interpretation of the mechanical and thermal properties of the composite materials with nanofillers.

FUNDING

This work was sponsored in part by Coordenação de Aperfeiçoamento de Pessoal de Nível Superior – Brasil (CAPES) – Finance code 001; Conselho Nacional de Desenvolvimento Científico e Tecnológico – CNPq (Grant number 303457/2013-9), and Fundação de Amparo à Pesquisa do Estado do Rio de Janeiro – FAPERJ (Grant number E-26/201.183/2014).

REFERENCES

Chakraborty, S., Chakraborty, A. K., Barbezat, M., and Terrasi, G. P. (2018). Interfacial interaction and the fracture toughness (K_{IC}) trends in epoxy nanocomposites filled with functionalized graphene-based fillers. *Polym. Compos.* 39, E2356–E2369. doi: 10.1002/pc.24675

Chatterjee, S., Wang, J. W., Kuo, W. S., Tai, N. H., Salzmann, C., Li, W. L., et al. (2012). Mechanical reinforcement and thermal conductivity in expanded graphene nanoplatelets reinforced epoxy composites. *Chem. Phys. Lett.* 531, 6–10. doi: 10.1016/j.cplett.2012.02.006

Chen, L. F., Ong, C. K., Neo, C. P., Varadan, V. V., and Varadan, V. K. (2004). *Microwave Electronics: Measurements and Materials Characterization*. West Sussex: John Wiley & Sons.

Chhetri, S., Adak, N. C., Samanta, P., Murmu, N. C., and Kuila, T. (2017). Functionalized reduced graphene oxide/epoxy composites with enhanced mechanical properties and thermal stability. *Polym. Test.* 63, 1–11. doi: 10.1016/j.polymertesting.2017.08.005.

Chhetri, S., Samanta, P., Murmu, N. C., Srivastava, S. K., and Kuila, T. (2016). Electromagnetic interference shielding and thermal properties of non-covalently functionalized reduced graphene oxide/epoxy composites. *AIMS Mater. Sci.* 4, 61–74. doi: 10.3934/matersci.2017.1.61.

Corcione, C. E., and Maffezzoli, A. (2013). Transport properties of graphite/epoxy composites: thermal, permeability and dielectric characterization. *Polym. Test.* 32, 880–888. doi: 10.1016/j.polymertesting.2013.03.023

Dermani, A. K., Kowsari, E., Ramezanzadeh, B., and Amini, R. (2018). Screening the effect of graphene oxide nanosheets functionalization with ionic liquid on the mechanical properties of an epoxy coating. *Prog. Org. Coat.* 122, 255–262. doi: 10.1016/j.porgcoat.2018.06.003

Guo, B., Wan, J., Lei, Y., and Jia, D. (2009). Curing behaviour of epoxy resin/graphite composites containing ionic liquid. *J. Phys. D Appl. Phys.* 42, 145307–145315. doi: 10.1088/0022-3727/42/14/145307

Guo, W., and Chen, G. (2014). Fabrication of grapheme/epoxy resin composites with much enhanced thermal conductivity via Ball milling technique. *J. Appl. Polym. Sci.* 131, 40565–40569. doi: 10.1002/app.40565

Hameed, N., Dumée, L. F., Allioux, F. M., Reghat, M., Church, J. S., Naebe, M., et al. (2018). Graphene based room temperature fexible nanocomposites from permanently cross-linked networks. *Nat. Sci. Rep.* 8, 2803-2811. doi: 10.1038/s41598-018-21114-5

Hashim, U. R., and Jumahat, A. (2019). Improved tensile and fracture toughness properties of graphene nanoplatelets filled epoxy polymer via solvent compounding shear milling method. *Mater. Res. Express* 6, 2053–2071. doi: 10.1088/2053-1591/aaeaf0.

Herath, M. B., Hickman, T., Creager, S. E., and DesMarteau, D. D. (2011). A new fluorinated anion for room-temperature ionic liquids. *J. Fluorine Chem.* 132, 52–56. doi: 10.1016/j.jfluchem.2010.11.005

Jovic, N., Dudi,é, D., Montone, A., Antisari, M. V., Mitri,é, M., and Djokovié, V. (2008). Temperature dependence of the electrical conductivity of epoxy/expanded graphite nanosheet composites. *Scripta Mater.* 58, 846–849. doi: 10.1016/j.scriptamat.2007.12.041

Kang, W. S., Rhee, K. Y., and Park, S. J. (2017). Influence of surface energetic of graphene oxide on fracture toughness of epoxy nanocomposites. *Composites Part B.* 114, 175–183. doi: 10.1016/j.compositesb.2017.01.032

Kowsary, E., and Mohammed, M. (2016). Synthesis of reduced and functional graphene oxide with magnetic ionic liquid and its application as an electromagnetic-absorbing coating. *Compos. Sci. Technol.* 126, 106–114. doi: 10.1016/j.compscitech.2016.02.019

Li, A., Zhang, C., and Zhang, Y. F. (2017a). Graphene nanosheets-filled epoxy composites prepared by a fast dispersion method. *J. Appl. Polym. Sci.* 134, 45152–45159. doi: 10.1002/app.45152

Li, Y., Zhang, H., Porwal, H., Huang, Z., Bilotti, E., and Peijs, T. (2017b). Mechanical, electrical and thermal properties of in-situ exfoliated graphene/epoxy nanocomposites. *Composites Part B* 95, 229–236. doi: 10.1016/j.compositesa.2017.01.007

Liang, J., Wang, Y., Huang, Y., Ma, Y., Liu, Z., Cai, J., et al. (2009). Electromagnetic interference shielding of graphene/epoxy composites. *Carbon* 47, 922–925. doi: 10.1016/j.carbon.2008.12.038.

Liu, S., Chevali, V. S., Xu, Z., Hui, D., and Wang, H. (2018). A review of extending performance of epoxy resins using carbon nanomaterials. *Composites Part B* 136, 197–214. doi: 10.1016/j.compositesb.2017.08.0201359-8368

Liu, Y. E., He, C. E., Peng, R., Tang, W., and Yang, Y. (2013). Ionic liquid assisted dispersion of reduced graphene oxide in epoxy composites with improved mechanical properties. *Adv. Mater. Res.* 738, 56–60. doi: 10.4028/www.scientific.net/AMR.738.56

Lopes Pereira, E. C., and Soares, B. G. (2016). Conducting epoxy networks modified with non-covalently functionalized multi-walled carbon nanotube with imidazolium-based ionic liquid. *J. Appl. Polym. Sci*. 133, 43976–43977. doi: 10.1002/app.43976

Ma, P. C., Siddiqui, N., Marom, G., and Kim, J. K. (2010). Dispersion and functionalization of carbon nanotubes for polymer-based nanocomposites: a review. *Composites Part A* 41, 1345–1367. doi: 10.1016/j.compositesa.2010.07.003

Martin-Gallego, M., Bernal, M. M., Hernandez, M., Verdejo, R., and Lopez-Manchado, M. A. (2013). Comparison of filler percolation and mechanical properties in graphene and carbon nanotubes filled epoxy nanocomposites. *Eur. Polym. J.* 49, 1347–1353. doi: 10.1016/j.eurpolymj.2013.02.033

Min, C., Yu, D., Cao, J., Wang, G., and Feng, L. (2013). A graphite nanoplatelet/epoxy composite with high dielectric constant and high thermal conductivity. *Carbon* 55, 116–125. doi: 10.1016/j.carbon.2012.12.017

Monti, M., Rallini, M., Puglia, D., Peponi, L., Torre, L., and Kenny, J. M. (2013). Morphology and electrical properties of graphene-epoxy nanocomposites obtained by different solvent assisted processing methods. *Composites Part A* 46, 166–172. doi: 10.1016/j.compositesa.2012.11.005

Prolongo, S. G., Jimenez-Suarez, A., Moriche, R., and Ureña, A. (2013). In situ processing of epoxy composites reinforced with graphene nanoplatelets. *Compos. Sci. Technol.* 86, 185–191. doi: 10.1016/j.compscitech.2013.06.020

Prolongo, S. G., Jiménez-Suárez, A., Moriche, R., and Ureña, A. (2014). Graphene nanoplatelets thickness and lateral size influence on the morphology and behavior of epoxy composites. *Eur. Polym. J.* 53, 292–301. doi: 10.1016/j.eurpolymj.2014.01.019

Sahoo, N. G., Rana, S., Cho, J. W., Li, L., and Chan, S. H. (2010). Polymer nanocomposites based on functionalized carbon nanotubes. *Prog. Polym. Sci.* 35, 837–867. doi: 10.1016/j.progpolymsci.2010.03.002

Sanes, J., Saurín, N., Carrión, F. J., Ojados, G., and Bermúdez, M. D. (2016). Synergy between single-walled carbon nanotubes and ionic liquids in epoxy resin nanocomposites. *Composites Part B* 105, 149–159. doi: 10.1016/j.compositesb.2016.08.044

Sankaran, S., Deshmukh, K., Ahamed, M. B., and Pasha, S. K. K. (2018). Recent advances in electromagnetic interference shielding properties of metal and carbon filler reinforced flexible polymer compsites: a review. *Composites Part A*. 114, 49–71. doi: 10.1016/j.compositesa.2018.08.006

Saurin, N., Sanes, J., and Bermudez, M. D. (2014). Effect of graphene and ionic liquid additives on the tribological performance of epoxy resin. *Tribol. Lett.* 56, 133–142. doi: 10.1007/s11249-014-0392-2.

Soares, B. G., Riany, N., Silva, A. A., Barra, G. M. O., and Livi, S. (2016). Dual-role of phosphonium – based ionic liquid in epoxy/MWCNT systems: Electric, rheological behavior and electromagnetic interference shielding effectiveness. *Eur. Polym. J.* 84, 77–88. doi: 10.1016/j.eurpolymj.2016.09.016

Tang, L. C., Wan, Y. J., Yan, D., Pei, Y. B., Zhao, L., Li, Y. B., et al. (2013). The effect of graphene dispersion on the mechanical properties of graphene/epoxy nanocomposites. *Carbon* 60, 16–27. doi: 10.1016/j.carbon.2013.03.050

Thomassin, J. M., Jérôme, C., Pardoen, T., Bailly, C., Huynen, I., and Detrembleur, C. (2013). Polymer/carbon based composites as electromagnetic interference (EMI) shielding materials. *Mater. Sci. Eng. R*, 74, 211–232. doi: 10.1016/j.mser.2013.06.001

Throckmorton, J., and Palmese, G. (2015). Direct preparation of few layer graphene epoxy nanocomposites from untreated flake graphite. *Appl. Mater. Interfaces* 7, 14870–14877. doi: 10.1021/acsami.5b03465

Throckmorton, J. A., Watters, A. L., Geng, X., and Palmese, G. R. (2013). Room temperature ionic liquids for epoxy nanocomposite synthesis: direct dispersion and cure. *Compos. Sci, Technol.* 86, 38–44. doi: 10.1016/j.compscitech.2013.06.016

Wang, C., Murugadoss, V., Kong, J., He, Z., Mai, X., Shao, Q., et al. (2018). Overview of carbon nanostructures and nanocomposites for electromagnetic wave shielding. *Carbon* 140, 696–733. doi: 10.1016/j.carbon.2018.09.006

Xu, P., Gui, H., Hu, Y., Bahader, A., and Ding, Y. (2014). Dielectric properties of polypropylene-based nanocomposites with ionic liquid-functionalized multiwalled carbon nanotubes. *J. Electron. Mater.* 43, 2754–2758. doi: 10.1007/s11664-014-3195-1

Yasmin, A., Luo, J. J., and Daniel, I. M. (2006). Processing of expanded graphite reinforced polymer nanocomposites. *Compos. Sci. Technol.* 66, 1182–1189. doi: 10.1016/j.compscitech.2005.10.014

Yousefi, N., Lin, X., Zheng, Q., Shen, X., Pothnis, J. R., Jia, J., et al. (2013). Simultaneous in situ reduction, self-alignment and covalent bonding in graphene oxide/epoxy composites. *Carbon* 59, 406–417. doi: 10.1016/j.carbon.2013.03.034

Yue, L., Pircheragui, G., Monemian, S. A., and Manas-Zloczower, I. (2014). Epoxy composites with carbon nanotubes and graphene nanoplatelets – dispersion and synergy effects. *Carbon* 78, 268–278. doi: 10.1016/j.carbon.2014.07.003

Zaman, I., Phan, T. T., Kuan, H. C., Meng, Q., La, L. T. B., Luong, L., et al. (2011). Epoxy/graphene platelets nanocomposites with two levels of interface strength. *Polymer* 52, 1603–1611. doi: 10.1016/j.polymer.2011.02.003

Zhang, Y., and Park, S. (2019). Imidazolium-optimized conductive interfaces in multilayer graphene nanoplatelet/epoxy composites for thermal management applications and electroactive devices. *Polymer* 168, 53–60. doi: 10.1016/j.polymer.2019.01.086

Zheng, W., Chen, W. G., Zhao, Q., Ren, S. X., and Fu, Y. Q. (2019). Interfacial structures and mechanisms for strengthening and enhanced conductivity of graphene/epoxy nanocomposites. *Polymer* 163, 171–177. doi: 10.1016/j.polymer.2018.12.055

Conflict of Interest Statement: The authors declare that the research was conducted in the absence of any commercial or financial relationships that could be construed as a potential conflict of interest.

Copyright © 2019 Silva, Stein, Campos, Indrusiak, Soares and Barra. This is an open-access article distributed under the terms of the Creative Commons Attribution License (CC BY). The use, distribution or reproduction in other forums is permitted, provided the original author(s) and the copyright owner(s) are credited and that the original publication in this journal is cited, in accordance with accepted academic practice. No use, distribution or reproduction is permitted which does not comply with these terms.

frontiers in Materials

ORIGINAL RESEARCH
published: 09 August 2019
doi: 10.3389/fmats.2019.00191

Double Percolation of Melt-Mixed PS/PBAT Blends Loaded With Carbon Nanotube: Effect of Molding Temperature and the Non-covalent Functionalization of the Filler by Ionic Liquid

Jéssica P. Soares da Silva[1], *Bluma G. Soares*[1,2]*, *Adriana A. Silva*[3] *and Sebastien Livi*[4]

[1] Instituto de Macromoléculas, Universidade Federal do Rio de Janeiro, Rio de Janeiro, Brazil, [2] PEMM-COPPE, Universidade Federal do Rio de Janeiro, Rio de Janeiro, Brazil, [3] Escola de Química, Universidade Federal do Rio de Janeiro, Rio de Janeiro, Brazil, [4] CNRS, UMR 5223, Ingenierie des Materiaux Polymeres, INSA Lyon, Villeurbanne, France

OPEN ACCESS

Edited by:
Andrea Dorigato, University of Trento, Italy

Reviewed by:
Liqing Wei, United States Forest Service (USDA), United States
Arup R. Bhattacharyya, Indian Institute of Technology Bombay, India

***Correspondence:**
Bluma G. Soares
bluma@metalmat.ufrj.br

Specialty section:
This article was submitted to Polymeric and Composite Materials, a section of the journal Frontiers in Materials

Received: *20 March 2019*
Accepted: *24 July 2019*
Published: *09 August 2019*

Citation:
Soares da Silva JP, Soares BG, Silva AA and Livi S (2019) Double Percolation of Melt-Mixed PS/PBAT Blends Loaded With Carbon Nanotube: Effect of Molding Temperature and the Non-covalent Functionalization of the Filler by Ionic Liquid. Front. Mater. 6:191. doi: 10.3389/fmats.2019.00191

Polystyrene/poly(butylene adipate-co-terephthalate) (PS/PBAT) composites loaded with different amounts of carbon nanotube (CNT) were prepared by melt mixing followed by compression molding at different temperatures. The effect of the non-covalent functionalization of CNT with the ionic liquid (IL), trihexyl(tetra decyl)-phosphonium bis-triflimide on the electrical and rheological properties of the composites with co-continuous morphology was investigated. The AC electrical conductivity of the composites loaded with 0.16 wt.% of pristine CNT jumped from 10^{-7} to 10^{-3} S/m by increasing the molding temperature from 180 to 200°C. Moreover, conductivity as high as 0.8 S/m was achieved in composite containing 0.66 wt.% of CNT. The outstanding electrical performance was attributed to the double percolation and the selective localization of CNT within PBAT phase. The functionalization with IL resulted in an increase of the conductivity for composites containing low amount of filler. IL-functionalized CNT resulted in a decrease of the melt viscosity and storage modulus due to the plasticizing effect of IL. However, for the system containing IL/CNT = 5:1 wt.%, the modulus increased significantly due to the formation of the percolated networked structure of the filler within the polymer matrix.

Keywords: ionic liquid, electric conductivity, polymer blend, carbon nanotube, rheology, biodegradable polymer

INTRODUCTION

Blending a thermoplastic polymer with conductive filler using melt processing approach is by far one of the cheapest and most technically viable alternatives to producing conductive composites. These materials have been attracted enormous interest for several decades due to the possibility of developing processable materials with controlled electrical conductivity for applications in important industrial sectors, as antistatic, electrostatic charge dissipating materials, as well as, electromagnetic interference shielding and micro-wave absorbing materials. The electrical properties of these materials can be improved by appropriate choice of the polymer matrix,

processing conditions, as well as the nature of the conductive filler. In this context, carbon nanotubes (CNT) have been focus of increasing interest due to their unique mechanical, electrical and thermal properties (Spitalsky et al., 2010). Furthermore, their large aspect ratio contributes to the corresponding composites achieving high conductivity level with lower proportion of the filler. CNT-loaded thermoplastics can be obtained by different techniques, including solution process, dispersion in polymers in the latex form, *in situ* polymerization and melt mixing procedure. The last one has been considered the most versatile for technological and industrial purposes because of its low cost, being easily scalable using conventional processing equipments (Lim et al., 2010; Rios-Fachal et al., 2013; Soares da Silva et al., 2017).

In order to achieve lower percolation threshold in the polymer matrix, the CNT must be uniformly and properly dispersed to form the conducting pathway. However, the dispersion of CNT in thermoplastic matrices through melt mixing approach is somewhat difficult due to the strong tendency of CNT to agglomerate in bundles and ropes. To overcome these drawbacks, several approaches have been considered in the literature. Some of them involve some modification in the melt-mixing protocol, including processing time and temperature (Tambe et al., 2013). Non-covalent modification of CNT with organic compounds and polymers also contributes for an improved dispersion of CNT within a polymer matrix, without deteriorating the electrical properties of CNT (Sahoo et al., 2010; Roy et al., 2012). For example, Bhattacharyya et al. encapsulated single walled carbon nanotube (SWCNT) with styrene-maleic anhydride copolymer and used in blends with polyamide 12 (Bhattacharyya et al., 2007). The authors achieved good filler dispersion but a decrease of electrical conductivity due to the formation of a polymer layer surrounding the CNT, thus avoiding contact each other. Other organic molecules as sodium salt of 6-aminohexanoic acid (Bose et al., 2008, 2009) and 1-pyrene-carboxaldehyde (Poyekar et al., 2015a) were employed to modify CNT in order to improve the dispersion in thermoplastic matrices. In these cases, a significant enhancement in electrical conductivity was observed by using both modifier agents. Considering similar strategy for dispersing CNT within polymeric matrices, the use of ionic liquids as surface modifiers for CNTs appeared as an innovative approach for dispersing CNT in polymeric matrices without destroying the conjugation at the surface, responsible for the conductivity. Some reports deals with the treatment of CNT with imidazolium-based ionic liquids to improve the dispersion of CNT in some thermoplastic matrices as well as, the filler-matrix interaction (Bellayer et al., 2005; Zhao et al., 2012; Sharma et al., 2014; Chen et al., 2015; Soares, 2018). Recently, alkyl phosphonium-based ionic liquids was also considered for assisting the CNT dispersion in polystyrene (PS) matrix (Soares da Silva et al., 2017), as well as polypropylene (PP)/polyamide12 (PA12) (Lopes Pereira et al., 2019) and PS/ethylene-vinyl acetate copolymer (EVA) (Soares et al., 2018) blends. A significant increase in conductivity by several orders of magnitude was observed for PS/CNT composites using the trihexyl (tetradecyl) phosphoniumbistriflimide (Soares da Silva et al., 2017).

The lowering of the percolation threshold was also achieved using heterogeneous polymer blends as matrices due to the uneven distribution of the filler in these phases (Sumita et al., 1991). By choosing a blend composition whose phase containing the percolated conductive filler is continuous or a blend with co-continuous structure, the amount of required conductive filler for attaining the insulator-conducting transition (percolation threshold) is usually lower that that employed in single polymer matrix. This phenomenon is known as double percolation and has been reported for several CNT-loaded thermoplastic binary blends, including acrylonitrile-butadiene-styrene (ABS) copolymers with PA6 (Poyekar et al., 2014, 2015a,b), ABS/ polycarbonate (PC) (Xiong et al., 2013), poly(L-lactide) (PLA)/(EVA) (Shi et al., 2013), PS/PP (Hwang et al., 2012), PS/PE (Patra et al., 2015), PS/polyvinylidene fluoride (PVDF) (Ren et al., 2017), PS/EVA (Soares et al., 2018), and PS/PLA (Nasti et al., 2016).

PS is a versatile and inexpensive commodity polymer with good mechanical properties, optical transparency, and processability, being chosen by several researchers as a matrix for the development of melt-mixing conductive composites (Zeimaran et al., 2015; Kausar et al., 2017) loaded with carbon—based fillers as carbon black (Soares et al., 1995, 1998, 2016), expanded graphite (Goyal et al., 2009), graphene (Bai et al., 2018), and carbon nanotube (Lim et al., 2010; Rios-Fachal et al., 2013; Soares da Silva et al., 2017). This thermoplastic is well known by its non-biodegradability. Therefore, blending PS with biodegradable polymers constitutes a promising strategy for rendering better biodegradability to the corresponding blend. These semi-biodegradable blends are known to degrade by a process known as biodisintegration, where the non-biodegradable phase is transformed in very small pieces due to the biodegradation of the other phase (Sarasa et al., 2009). Semi-biodegradable PS blends involving PLA were reported in the literature (Nasti et al., 2016; Kaseem and Ko, 2017; Gu et al., 2018). However, to the best of the authors' knowledge, no studies regarding PS/poly (butylene adipate-co-terephthalate) (PBAT) blends and the corresponding conductive composites have been found in the accessible literature.

PBAT, a fully biodegradable aliphatic-aromatic copolyester originated from petrochemical resources, is a flexible and low modulus copolymer. Therefore, the PS/PBAT blends should combine the toughness and biodegradability imparted by PBAT and the stiffness originated from PS. Furthermore, the corresponding blend and composites are cost-effective as compared with pure biodegradable polymer. Adding CNT in biodegradable or semi-biodegradable polymer blends enlarges the field of application of these materials in electro-electronic industries and packages with dissipating electrostatic charge characteristics and microwave absorbing or electromagnetic shielding properties.

Based on the profitable results reported with heterogeneous blends loaded with CNT, the motivation of the present work is to extent this approach to a semi-biodegradable PS/PBAT blends. The present work highlights the superior conductivity levels achieved by using low amount of CNT, <1 wt.%, in these PS/PBAT blends with co-continuous morphology. The

effect of the compression molding temperature and the non-covalent functionalization of CNT with Trihexyl(tetradecyl)-phosphoniumbistriflimide (Ph-TFSI) as the ionic liquid on the electrical properties of these composites was also discussed. The morphology and rheological properties of these systems were also discussed in details.

EXPERIMENTAL SECTION

Materials

Poly (butylene adipate-co-terephthalate) (PBAT) (density = 1.26 g.cm^{-3}; molar mass = 79,550 g.mol^{-1}; glass transition temperature = −33°C) produced by BASF (Germany) under the trade name of Ecoflex was purchased by OEKO Bioplasticos, Brazil. Polystyrene (PS) was fabricated by companhia de Estireno do Brasil (melt flow index was determined according ASTM D1238 as 6.13 g/10 min at 200°C/2.16 Kg) Trihexyl(tetradecyl)-phosphoniumbistriflimide (Ph-TFSI) as the ionic liquid (density = 1.07 g cm^{-1})was kindly supplied by Cytec Inc. MWCNT(NC7000) was kindly supplied by Nanocyl (average diameter = 9.5 nm; average length = 1.5 μm; carbon purity = 90%; surface area = 250–300 m^2/g; density = 1.67 g cm^{-1}).

Composite Preparation

PS and PBAT were previously dried overnight at 70°C. CNT was first dispersed in ionic liquid (Ph-TFSI) in a mortar for about 20 min, obtaining a black paste. The mixtures were performed by introducing all blend components into the W50 EHT internal mixer of a Brabender Plastograph equipped with roller rotors. The blends were compounded at 170°C for 10 min at 60 rpm. The CNT-based composites were prepared under the same processing conditions, by adding the CNT or the IL-CNT paste together with the polymer components. After this step, the materials were milled and compression-molded at 180 or 200°C and 6 MPa for 5 min and immediately cooled at the same pressure.

Characterization

A Physica MRC 302 rheometer from Anton Paar was employed to measure the rheological properties. The measurements in oscillatory mode were made using parallel plates with 25 mm diameter and a gap of 1.0 mm; 200°C; frequency range from 0.1 to 100 Hz and amplitude of 0.1 %, which is within the linear viscoelastic region.

Scanning electron microscopy was performed on a TESCAN (Vega 3 model) at 15 kV. The samples were cryogenically fractured and treated with aqueous solution of NaOH (5 wt.%) in order to selectively extract the PBAT phase. Then, the surface was coated with thin layer of gold before analysis.

The AC electrical conductivity (σ_{AC}) was measured in a frequency range from 0.1 Hz to 10 MHz using a Solartron SI 1260 gain phase analyzer interfaced to a Solartron 1296 dielectric interface. The measurements were made at 25°C, using electrodes with 25 mm diameter and oscillating voltage of 5 V. Samples of 1 mm thickness were prepared by compression molding at 180°C or 200°C.

Transmission electron microscopy was obtained using a Tecnai Spirit from Fei Company, operating at 120 kV, localized at the Centro Nacional de Bioimagens—CENABIO/UFRJ (Brazil). The samples were cut using a Leyca ultracryomicrotome equipped with diamond knife. Samples with thickness about 60–90 nm were obtained.

RESULTS AND DISCUSSION

Rheology

Rheology is an important way for characterizing the microstructure of a nanocomposite due to the great dependence of the main viscoelastic properties of the nanocomposites in the melt state on the filler dispersion state and filler-matrix interaction. The dependence of the complex viscosity, η*, with frequency for PS, PBAT, and the neat blend is illustrated in **Figure 1**. PBAT presented lower η* than PS at low frequency and a greater Newtonian behavior. The blend presented intermediary viscosity at low frequency, and a higher shear thinning effect, resulting in lower viscosity than the pure components at higher frequency.

The effect of pristine CNT (pCNT) and the IL-modified CNT (IL-CNT) on the η* of the composites is illustrated in **Figure 2**. The main rheological parameters are also summarized in **Table 1**. In both loaded systems, the viscosity at lower frequencies increased as the amount of the filler increased. However, for composites containing lower amount of pCNT (up to 0.33%), the viscosity values were lower than that observed for the neat PS/PBAT blend. This behavior was even more pronounced for the composites containing IL-CNT. Similar feature was also reported by Lin et al in their studies involving PP/CNT nanocomposites and was attributed to the increase of the free volume around the CNT due to a better dispersion state of the filler (Lin et al., 2015). The free volume acts as a lubricant during the molecular chain flowing. The effect is more pronounced for the composites

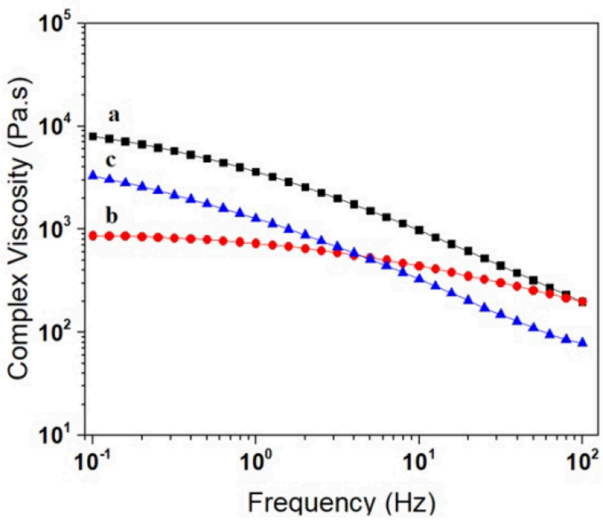

FIGURE 1 | Complex viscosity vs. frequency for **(a)** PS, **(b)** PBAT, and the **(c)** PS/PBAT = 50:50 wt.% blend.

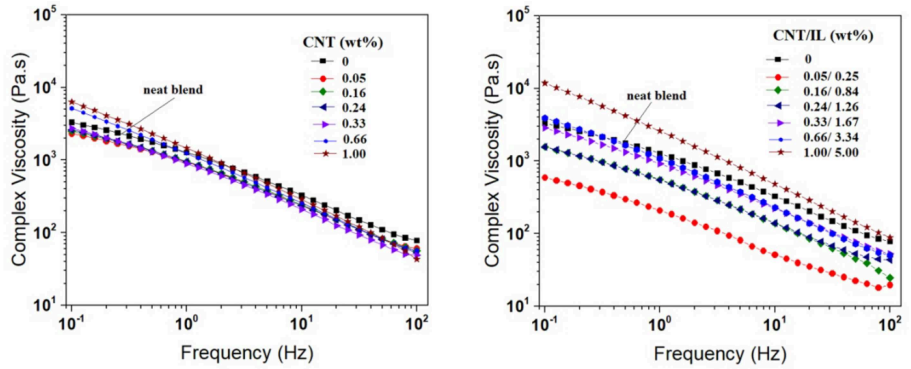

FIGURE 2 | Complex viscosity vs. frequency for the PS/PBAT composites as a function of the filler content.

TABLE 1 | Main rheological parameters of PS/PBAT composites as a function of the filler content.

Filler content	η*at 1 Hz (Pa.s)		G' at 0.1 Hz (Pa)		Frequency at G' = G" (Hz)		G' slope at low frequency	
(wt.%)	pCNT	IL-CNT	pCNT	IL-CNT	pCNT	IL-CNT	pCNT	IL-CNT
0	3,340		785		1.45		0.55	
0.05	2,300	600	570	180			0.55	0.51
0.16	2,500	1,560	750	500	1.10	1.08	0.52	0.48
0.24	2,600	1,560	840	560	0.90	0.89	0.49	0.50
0.33	2,700	2,880	970	1,100	0.58	0.58	0.46	0.46
0.66	5,150	3,900	2,450	1,690	–	–	0.36	0.39
1.00	6,300	11,900	3,050	5,850	–	–	0.31	0.30

loaded with IL-CNT due to the plasticizing/lubricating role of the IL at the filler-matrix interface, as also observed in other studies (Zhao et al., 2012). Composites containing higher amount of filler (0.66 or 1.0 wt.%) displayed η* values higher than that observed for the neat blend at low frequency and a greater shear thinning effect, which can be related to the formation of a percolated three-dimensional structure of the filer in the polymer matrix. The nanocomposite loaded with 1 wt.% of IL-CNT presented the highest η* value in all frequency range studied, in spite of the higher proportion of IL. This behavior may be attributed to the formation of the filler network in higher extent due to the filler-filler interaction imparted by the IL at the CNT surface.

The dependence of the storage modulus with frequency also provides important information regarding the formation of the percolated structure. **Figure 3** illustrates the G' plots vs. frequency for the composites containing different amounts of filler (pCNT or IL-CNT). The storage modulus increased as the amount of pCNT increased and the slope of the G' vs. frequency curve in the low frequency region significantly deviated from a typical terminal behavior (see **Table 1**) for the composites containing higher amount of filler, suggesting the development of a three dimensional networked structure formed by the interconnected CNT. This structure is also responsible for the higher conductivity. The composite containing 1 wt.% of IL-CNT displayed significantly higher G' value in all frequency range studied suggesting the formation of a percolated filler network in higher extent (Pötschke et al., 2004). This result suggests that the IL helps on debundling of the CNT thus facilitating the network formation.

The dependence of G' and G" with the frequency is illustrated in **Figure 4** for the PS/PBAT composites with 0.33 and 1% of pCNT or IL-CNT. Both storage modulus (G') and loss modulus (G") increases with increasing in frequency. At low frequency, the composite loaded with 0.33 wt.% of filler exhibited G" > G', which is characteristic of liquid-like behavior. At a specific frequency (cross-over frequency) G' and G" values are similar and after this frequency, G' > G", indicating the transition to solid-like behavior. The effect of the CNT content on the frequency corresponding to the G'/G" cross-over point is also summarized in **Table 1**. This point (G' = G") shifted toward lower frequencies as the amount of filler increased, confirming the formation of the three dimensional network structure. The composites containing 0.66 or 1 wt.% of filler presented G' > G" in all frequency range studied, suggesting pseudo solid-like behavior, due to the development of the network formed by the CNT.

The plot related to the phase angle δ against the absolute value of the complex modulus |G*|, known as van Gurp-Palmen plot, is usually employed in the literature to estimate the rheological percolation (Pötschke et al., 2004). The deviation of the δ value from 90° in the low |G*| region suggests the elastic response of polymer chains. **Figure 5** illustrates the van Gurp-Palmen plots for the composites loaded with pCNT and

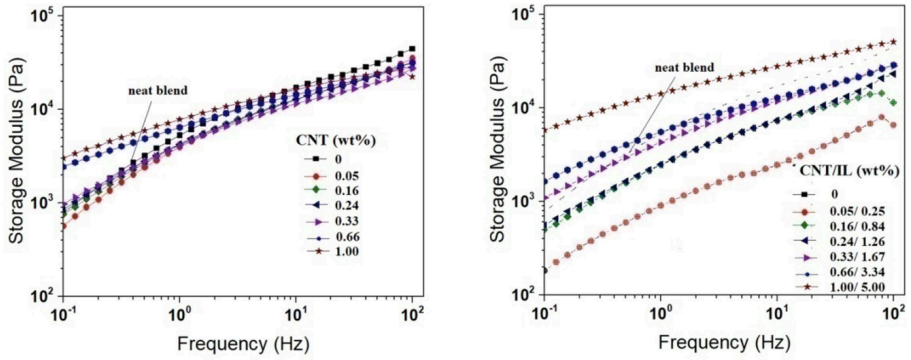

FIGURE 3 | Storage modulus vs. frequency for the PS/PBAT composites as a function of the filler content.

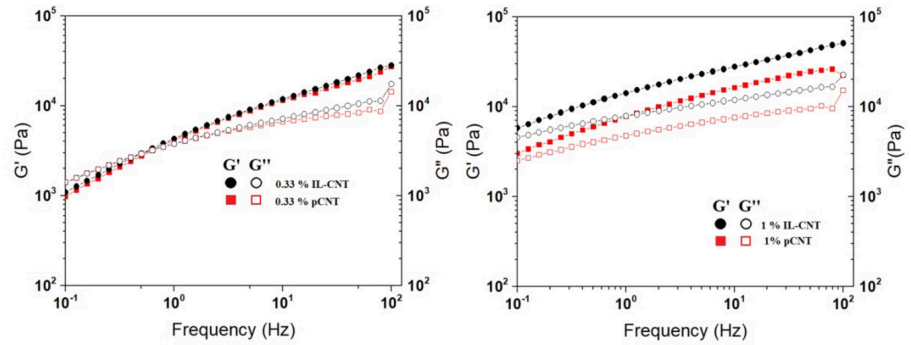

FIGURE 4 | G' and G" vs. frequency of PS/PBAT loaded with 0.33 and 1.0 % of CNT.

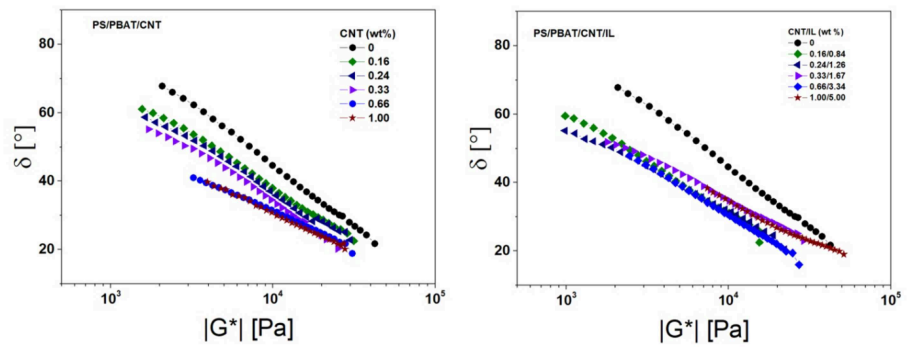

FIGURE 5 | Van Gurp-Palmen plot for the PS/PBAT composites as a function of the filler content Morphology.

IL-CNT. For a similar |G*|, the neat PS/PBAT blend displayed the highest phase angle indicating a flow behavior. As the amount of pCNT increased, the deviation of the low range |G*| values to lower phase angle was observed indicating an increase of the contribution of the CNT entanglement. In this context, the composite containing 0.16 wt.% of pCNT presented a great deviation when compared to the neat blend, indicating the rheological percolation. This value is comparable with that observed for the electrical percolation threshold. The same amount of IL-CNT (0.16 wt.%) presented a higher deviation from the phase angle of 90°, indicating the formation of the network structure. These behaviors are in agreement with those observed from electrical conductivity.

The SEM micrographs of PS/PBAT blends and the composites containing 0.66 wt.% of CNT of IL-CNT are shown in **Figure 6**, as a function of the molding temperature. The micrographs were taken from the surfaces that were previously treated with NaOH solution in order to degrade

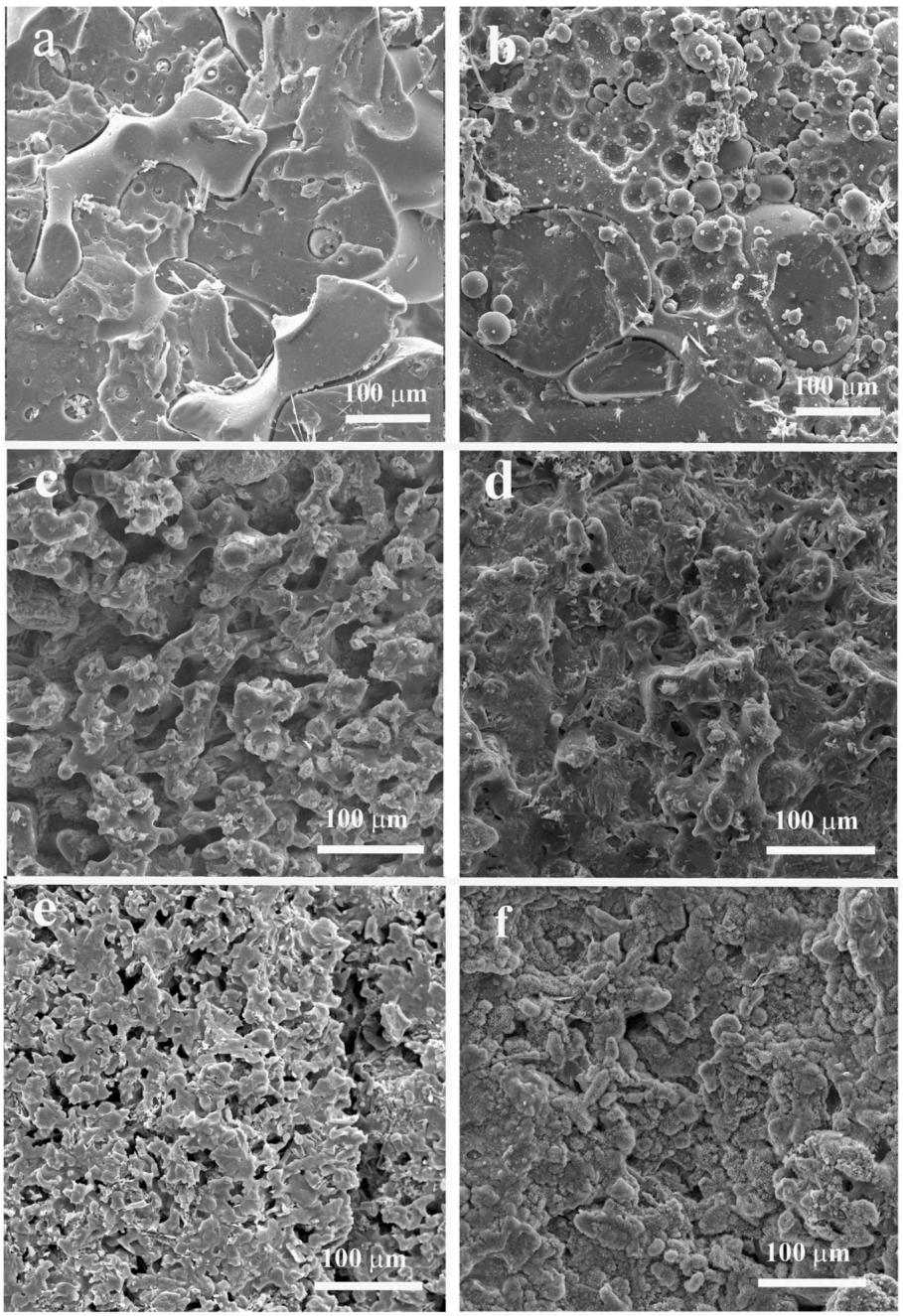

FIGURE 6 | SEM micrographs of PS/PBAT blends with **(a,b)** 0% of filler, **(c,d)** 0.66% of pCNT, and **(e,f)** 0.66% of IL-CNT, compression molded at 180°C (left column) and 200°C (right column).

the PBAT phase. Although the PAT phase could not be completely extracted by this method, the gross phase separated morphology with co-continuous structure can be observed for the neat blend compression molded at 180°C (**Figure 6a**). The neat blend compression molded at higher temperature displayed a sea-island type morphology characterized by large PBAT domains (**Figure 6b**). The presence of CNT resulted in finer co-continuous morphology, which can be attributed to the change in the viscosity ratio between the blend components, as also reported in other CNT—loaded heterogeneous blends (Gao et al., 2017; Soares et al., 2018). The co-continuous structure is more difficult to observe for the blend compression-molded at 200°C. The presence of IL-CNT also changes the morphology of the systems suggesting a compatibilizing action of this (Ph-TFSI) -based ionic liquid. The sample compression molded at 180°C displayed a finer

morphology when compared to that of the composite loaded with pCNT.

The filler dispersion in the composites was investigated by TEM microscopy. **Figure 7** compares the TEM images of the composites loaded with 0.66% wt.% of pCNT and IL-CNT, and compression molded at 200°C. In both systems, the CNT seems to be well dispersed within the polymeric matrix. It is possible to observe even several tubes completely debundled in both systems, indicating that the dispersion of CNT in the PS/PBAT was effective, without needing the assistance of the IL.

Electrical Conductivity

The AC electrical conductivity (σ_{AC}) at 1 Hz for the PS/PBAT composites with different compositions and loaded with 0.66 wt.% of CNT are summarized in **Table 2**. The σ_{AC} values of the blends were superior to that observed for the single PS/CNT composite due to the contribution of double percolation and the preferential localization of CNT within the percolated PBAT phase.

The composite with a composition of PS/PBAT = 50:50 wt.% presented the highest σ_{AC} value probably due to the higher degree of co-continuity at this composition.

Evidence for the preferential localization of CNT within the PBAT phase was testified from selective extraction of the PS phase using acetone. After extracting the PS phase, the solvent remained colorless indicating that the CNT was mainly localized in the non-extracted PBAT phase.

Selective localization of CNT in a given phase or at the interface of PS/PBAT blend was predicted from wetting coefficient (ω_a) (Equation 1), determined by measuring the interfacial energy ($\gamma_{A/B}$) between two components, as shown in Equation (2).

$$\omega_a = \frac{\gamma_{PS/CNT} - \gamma_{PBAT/CNT}}{\gamma_{PS/PBAT}} \quad (1)$$

$$\gamma_{A/B} = \gamma_A + \gamma_B - 4\left[\frac{\gamma_A^d \gamma_B^d}{\gamma_A^d + \gamma_B^d} + \frac{\gamma_A^p \gamma_B^p}{\gamma_A^p + \gamma_B^p}\right] \quad (2)$$

The surface energy of the blend components is listed in **Table 3**.

If $\omega_a > 1$, the filler is expected to be located in the PBAT phase; if $\omega_a < -1$, the preferential localization of the filler should be in the PS phase. From thermodynamic calculations, the value of ω_a was found to be −1.5, indicating a preferential localization in the PS phase. The thermodynamic prediction does not agree with the experimental results. The selective localization of the filler is also governed by other kinetic parameters as well as the viscosity of the blend component. PBAT presented lower viscosity than PS and melts first, favoring the encapsulation of CNT in this phase.

The PS/PBAT (50:50 wt.%) blend was chosen for studies involving the effect of filler content, compression-molded temperature and the non-covalent functionalization of CNT by ionic liquid. **Figure 8** illustrates the dependence of the (σ_{AC}) with the frequency for the composites loaded with different amounts of pristine CNT (pCNT) and compression molded at two different temperatures: 180°C and 200°C. The composite containing 0.05 % of CNT and compression molded at 180°C displayed σ_{AC} value around 10^{-10} S/m at low frequency. Increasing the molding temperature increased the (σ_{AC}) in two orders of magnitude, reaching values around 10^{-8} S/m. In both cases, the conductivity became frequency dependent at a certain frequency, indicating the electrical conduction through hopping process. Increasing the amount of filler, the conductivity

TABLE 2 | σ_{AC} of PS/PBAT blends with different compositions and loaded with 0.66 wt.% of CNT.

Blend components (wt.%)		(σ_{AC}) (S/m)
PS	**PBAT**	
100	0	8×10^{-6}
70	30	4×10^{-4}
50	50	5×10^{-3}
30	70	2×10^{-4}

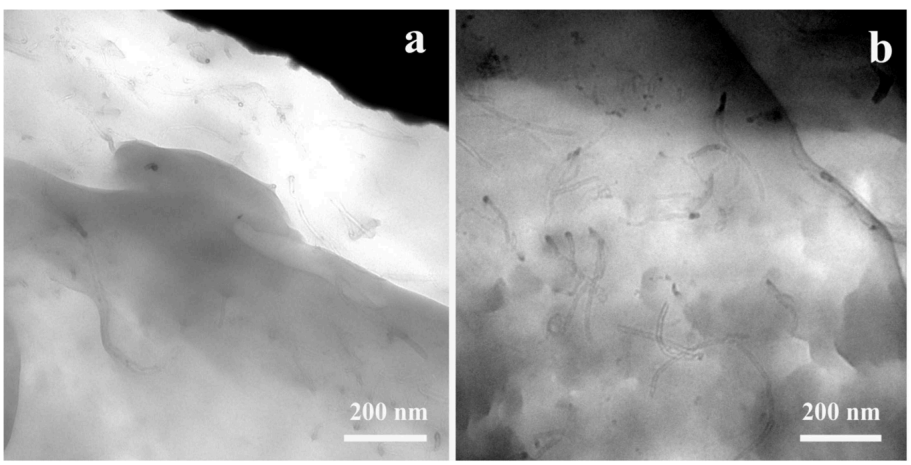

FIGURE 7 | TEM micrographs of PS/PBAT composites containing 0.66% of **(a)** pCNT and **(b)** IL-CNT, and molded at 200°C.

increased and became frequency independent, characterizing a conductive material. The percolation threshold may be estimated in between 0.05 and 0.16 % of CNT, which is considerably lower than some other studies reported in the literature for several heterogeneous polymer blends loaded with CNT and prepared by melt mixing. **Table 4** compares the conductivity of different CNT-loaded thermoplastic systems, where it is possible to observe the superior conductivity values for the system studied in the present work, with lower amount of CNT. This behavior highlights the influence of the nature of the polymer matrix to attain high conductivity levels with low amount of CNT.

The filler localized in the PBAT phase tends to flocculate during compression molding at higher temperatures and forms the conductive network. This phenomenon was also reported in others studies and suggests that the polymer composite containing conductive particles is not a thermodynamic equilibrium system, whose the formation of the conductive network is temperature and time dependent (Zhang et al., 2006).

The effect of the non-covalent functionalization of CNT by ionic liquid on the electrical conductivity of PS/PBAT blend molded at different temperatures is illustrated in **Figure 9**. At low filler content, the conductivity of the composites loaded with IL-CNT were higher, indicating that the presence of IL contributes for the debundling of the CNT, thus improving the formation of the conducting network with lower amount of filler, i.e., lower percolation threshold. As the amount of IL-CNT increased, the conductivity values of the composites were lower than those loaded with pristine CNT. As the IL/CNT ratio was kept as 5:1, increasing the amount of filler also increased the proportion of IL. The IL in higher proportion should wrap the CNT thus forming a layer between the tubes that affects the contact each other and formation of the conducting network. Although, this is not a usual behavior for polymer composites loaded with IL-CNT, some examples in the literature also reported a decrease of conductivity by using the IL modified CNT (Sharma et al., 2014; Xu et al., 2014).

CONCLUSION

PS/PBAT (50:50 wt.%) blend with co-continuous structure was loaded with different amounts of CNT to prepare conductive composites with AC electrical conductivity as high as 0.8 S/m with 1 wt.% of CNT. The CNT was preferentially localized within the PBAT phase. Although it is not the thermodynamically favored phase, the lower viscosity of this component favors the localization of the filler. The co-continuous morphology and the selective localization of the filler account for the superior electrical properties. The increasing of molding temperature also contributed for a significant improvement of the electrical conductivity. The functionalization of the CNT with ionic liquid resulted in an increase of the conductivity for composites loaded with low amount of CNT, also resulting in lower percolation threshold. Higher proportion of the functionalized CNT did not result in outstanding electrical conductivity probably due to the

TABLE 3 | Surface energies of the blend component.

Materials	γ^d (mN/m)	γ^p (mN/m)	γ (mN/m)	References
PS	21.64	6.1	27.74	Rohini and Bose, 2014
PBAT	45	3	48	Livi et al., 2016
CNT	17.6	10.2	27.8	Barber et al., 2004

γ^d, dispersive part; γ^d, polar part; γ, total surface energy.

TABLE 4 | Conductivity values of CNT-thermoplastic systems prepared by melt mixing.

Polymer matrix	CNT (%)	Conductivity (S/m)	References
PA6/ABS (50:50)	5	10^{-7}	Poyekar et al., 2014
PLA/PCL (50:50)	1	2×10^{-4}	Huang et al., 2014
PC/PVDF (60:40)	1	10^{-5}	Biswas et al., 2015
PP/PA6 (80:20)	4	4×10^{-5}	Zhang et al., 2009
PLA/PBAT (60:40)	2	10^{-5}	Urquijo et al., 2017
PS/EVA (70:30)	1	0.5	Soares et al., 2018
PS/PBAT (50:50)	1	1.0	This work

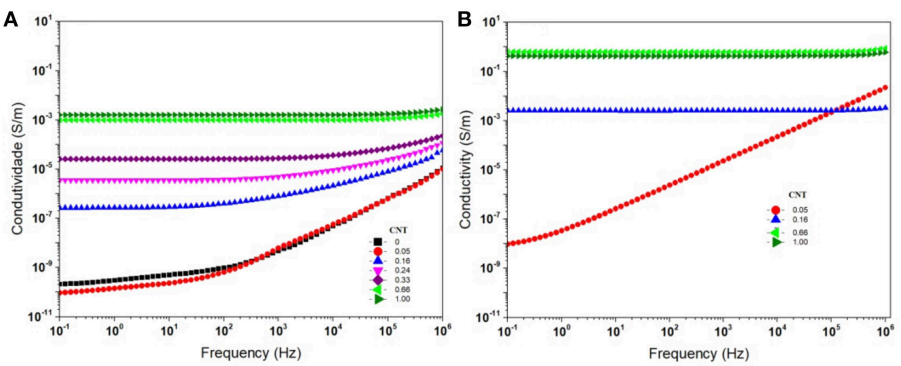

FIGURE 8 | AC conductivity of PS/PBAT composites as a function of the pCNT content. Systems compression molded at 180°C **(A)** and at 200°C **(B)**.

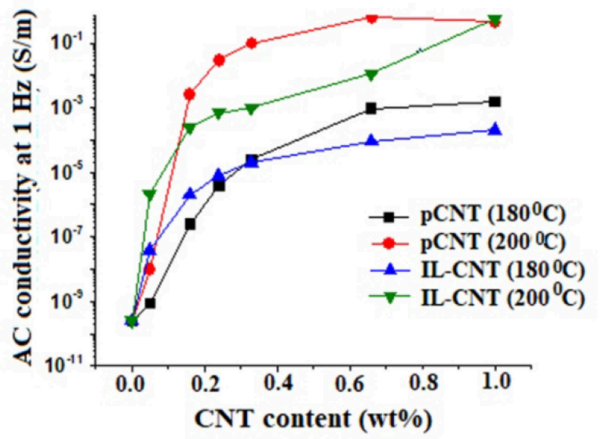

FIGURE 9 | AC conductivity at 1 Hz of PS/PBAT composites as a function of pCNT or IL-CNT content and molding temperature.

formation of an insulating layer of IL (in higher proportion) that wraps the CNT, thus avoiding the conductive contact.

The co-continuous morphology of the blends became thinner with the presence of the filler, due to changes in the viscosity ratio between the blend components.

The composites filled with IL-functionalized CNT displayed significantly lower viscosity in the melt state due to the plasticizing/lubricating effect of the IL at the filler-matrix interface. However, for higher amount of filler, the presence of IL resulted in significant increase of viscosity and G', mainly in the low frequency region due to the formation of a percolated networked structure formed by the well dispersed IL-CNT. The present works confirms the possibility of attaining good conductivity levels with the addition of low amount of filler, by appropriate choice of the polymer system and processing conditions.

DATA AVAILABILITY

All datasets generated for this study are included in the manuscript and/or the supplementary files.

AUTHOR CONTRIBUTIONS

JS prepared all samples and discussed. AS was involved in all micrograph characterization. SL participated in the discussion of the results. BS was responsible for writing, discussing and organizing all manuscript, and provide all support in the laboratory for the experimental part of the manuscript. All authors contributed to manuscript revision, read and approved the submitted version.

FUNDING

This work was sponsored in part by Coordenação de Aperfeiçoamento de Pessoal de Nível Superior – Brasil (CAPES) – Financecode 001, Conselho Nacional de Desenvolvimento Científico e Tecnológico – CNPq (Grant number 303457/2013-9), and Fundação de Amparo à Pesquisa do Estado do Rio de Janeiro – FAPERJ (Grant number E-26/201.183/2014).

REFERENCES

Bai, L., Sharma, R., Cheng, X., and Macosko, C. W. (2018). Kinetic control of graphene localization in co-continuous polymer blends via melt compounding. *Langmuir* 34, 1073–1083. doi: 10.1021/acs.langmuir.7b03085

Barber, A. H., Cohen, S. R., and Wagner, H. D. (2004). Static and dynamic wetting measurements of single carbon nanotubes. *Phys. Rev. Lett.* 92:186103. doi: 10.1103/PhysRevLett.92.186103

Bellayer,. S., Gilman, J. W., Eidelman, N., Bourbigot, S., Flambard, X., Fox, D. M., et al. (2005). Preparation of homogeneously dispersed multiwalled carbon nanotube/polystyrene nanocomposites via melt extrusion using trialkyl imidazolium compatibilizer. *Adv. Funct. Mater.* 15, 910–916. doi: 10.1002/adfm.200400441

Bhattacharyya, A. R., Bose, S., Kulkarni, A. R., Pötschke, P., Häussler, L., Fischer, D., et al. (2007). Styrene maleic anhydride copolymer mediated dispersion of single wall carbon nanotubes in polyamide 12: crystallization behavior and morphology. *J. Appl. Polym. Sci.* 106, 345–353. doi: 10.1002/app.26680

Biswas, S., Kar, G. P., and Bose, S. (2015). Tailor-made distribution of nanoparticles in blend structure toward outstanding electromagnetic interference shielding. *ACS Appl. Mater. Interface* 7, 25448–25463. doi: 10.1021/acsami.5b08333

Bose, S., Bhattacharyya, A. R., Khare, R. A., Kulkarni, A. R., and Pötschke, P. (2008). Specific interactions and reactive coupling induced dispersion of multiwall carbon nanotubes in co-continuous polyamide6/ionomer blends. *Macromol. Symp.* 263, 11–20. doi: 10.1002/masy.200850302

Bose, S., Bhattacharyya, A. R., Kulkarni, A. R., and Pötschke, P. (2009). Electrical, rheological, and morphological studies in co-continuous blends of polyamide 6 and acrylonitrile-butadiene-styrene with multiwall carbon nanotubes prepared by melt-blending. *Compos. Sci. Technol.* 69, 365–372. doi: 10.1016/j.compscitech.2008.10.024

Chen, G. X., Zhang, S., Zhou, Z., and Li, Q. (2015). Dielectric properties of poly(vinylidene fluoride) composites based on bucky gels of carbon nanotubes with ionic liquids. *Polym. Compos.* 36, 94–101. doi: 10.1002/pc.22917

Gao, T., Li, Y. Y., Bao, R. Y., Liu, Z. Y., Xie, B. H., and Yang, M. B. (2017). Tailoring co-continuous like morphology in blends with highly asymmetric compositon by MWCNTs: Towards biodegradable high-performance electrical conductive poly(l-lactide)/poly(3-hydroxybutyrate-co-4-hydroxybutyrate) blends. *Compos. Sci. Technol.* 152, 111–119. doi: 10.1016/j.compscitech.2017.09.014

Goyal, R. K., Jagadale, P. A., and Mulik, U. P. (2009). Thermal, mechanical and dielectric properties of polystyrene/espanded graphite nanocomposites. *J. Appl. Polym. Sci.* 111, 2071–2077. doi: 10.1002/app.29042

Gu, L., Nessim, E. E., and Macosko, W. (2018). Reactive compatibilization of poly(lactic acid)/polystyrene blends and its application to preparation of hierarchically porous poly(lactic acid). *Polymer* 134, 104–116. doi: 10.1016/j.polymer.2017.11.054

Huang, J., Mao, C., Zhu, Y., Jiang, W., and Yang, X. (2014). Control of carbon nanotubes at the interface of a co-continuous immiscible polymer blend to fabricate conductive composites with ultralow percolation thresholds. *Carbon* 73, 267–274. doi: 10.1016/j.carbon.2014.02.063

Hwang, T. Y., Yoo, Y., and Lee, J. W. (2012). Electrical conductivity, phase behavior, and rheology of polypropylene/polystyrene blends with multi-walled carbon nanotube. *Rheol. Acta* 51, 623–636. doi: 10.1007/s00397-012-0630-1

Kaseem, M., and Ko, Y. G. (2017). Melt flow behavior and processability of polylactic acid /polystyrene (PLA/PS) polymer blends. *J. Polym. Environ.* 25, 994–998. doi: 10.1007/s10924-016-0873-5

Kausar, A., Ahmad, S., and Salamn, S. M. (2017). Effectiveness of polystyrene/carbon nanotube composit in electromagnetic interference shielding materials: a review. *Polym. Plast. Technol. Eng.* 56, 1027–1042. doi: 10.1080/03602559.2016.1266367

Lim, G. O., Min, K. T., and Kim, G. H. (2010). Effect of cooling rate on the surface resistivity of polymer/multi-walled carbon nanotube nanocomposites. *Polym. Eng. Sci.* 50, 290–294. doi: 10.1002/pen.21537

Lin, X., Tian, J. W., Hu, P. H., Ambardekar, R., Thompson, G., Dang, Z. M., et al. (2015). Improved dielectric performance of polypropylene/multiwalled carbon nanotube nanocomposites by solid-phase orientation. *J. Appl. Polym. Sci.* 132:42893. doi: 10.1002/app.42893

Livi, S., Lins, L. C., Sar, G., Gerard, J. F., and Duchet-Rumeau, J. (2016). Supercritical CO2- ionic liquids: a successful wedding to prepare biopolymer foams. *ACS Sustainable Chem. Eng.* 4, 461–470. doi: 10.1021/acssuschemeng.5b00969

Lopes Pereira, E. C., Soares, B. G., Silva, A. A., Farias da Silva, J. M., Barra, G. M. O., and Livi, S. (2019). Conductive heterogeneous blend composites of PP/PA12 filled with ionic liquids treated-CNT. *Polym. Test.* 74, 187–195. doi: 10.1016/j.polymertesting.2019.01.003

Nasti, G., Gentile, G., Cerruti, P., Carfagna, C., and Ambrogi, V. (2016). Double percolation of multiwalled carbon nanotubes in polystyrene/polylactic acid blends. *Polymer* 99, 193–203. doi: 10.1016/j.polymer.2016.06.058

Patra,. R., Suin, S., Mandal, D., and Khatua, B. B. (2015). Reduction of percolation threshold of multiwall carbon nanotube (MWCNT) in polystyrene (PS)/low-density polyethylene (LDPE)/MWCNT nanocomposites: and eco-friendly approach. *Polym. Compos.* 36, 1574–1583. doi: 10.1002/pc.23065

Pötschke, P., Abdel-Goad, M., Alig, I., Dudkin, S., and Lellinger, D. (2004). Rheological and dielectrical characterization of melt mixed polycarbonate-multiwalled carbon nanotube composites. *Polymer* 45, 8863–8870. doi: 10.1016/j.polymer.2004.10.040

Poyekar, A. V., Bhattacharyya, A. R., Khare, R. A., Panwar, A. S., Simon, G. P., Dhar, S., et al. (2015b). Dispersion, migration, and "network-like" structure formation of multiwall carbon nanotubes in co-continuous, binary immiscible blends of polyamide6 and acrylonitrile-butadiene-styrene copolymer during simultaneous melt-mixing. *Polym Eng. Sci.* 55, 443–456. doi: 10.1002/pen.23904

Poyekar, A. V., Bhattacharyya, A. R., Panwar, A. S., and Simon, G. P. (2015a). Evolution of phase morphology and "network-like" structure of multiwall carbon nanotubes in binary polymer blends during melt-mixing. *Polym Eng. Sci.* 55:429. doi: 10.1002/pen.23897

Poyekar, A. V., Bhattacharyya, A. R., Panwar, A. S., Simon, G. P., and Sutar, D. S. (2014). Influence of noncovalent modification on dispersion state of multiwalled carbon nanotubes in melt-mixed immiscible blends. *ACS Appl. Mater. Interface* 6, 11054–11067. doi: 10.1021/am501737z

Ren, L., Zha, J. W., Li, R. K. Y., Shi, C. Y., and Dang, Z. M. (2017). Co-continuous structural polystyrene /poly(vinylidene fluoride) nanocomposites with high dielectric constant and magnetic properties. *Compos. Commun.* 4, 24–32. doi: 10.1016/j.coco.2017.03.004

Rios-Fachal, M., Gracia-Fernandez, C., Lopez-Beceiro, J., Gomez-Barreiro, S., Tarrío-Saavedra, J., Ponton, A., et al. (2013). Effect of nanotubes on the thermal stability of polystyrene. *J. Therm. Anal. Calorim.* 113, 481–487. doi: 10.1007/s10973-013-3160-x

Rohini, R., and Bose, S. (2014). Electromagnetic interference shielding materials derived from gelation of multiwall carbon nanotubes in polystyrene/poly(methyl methacrylate) blends. *ACS Appl. Mater. Interface* 6, 11302–11310. doi: 10.1021/am502641h

Roy, N., Sengupta, R., and Bhowmick, A. K. (2012). Modifications of carbon for polymer composites and nanocomposites. *Prog. Polym. Sci.* 37, 781–819. doi: 10.1016/j.progpolymsci.2012.02.002

Sahoo, N. G., Rana, S., Cho, J. W., Li, L., and Chan, S. H. (2010). Polymer nanocomposites based on functionalized carbon nanotubes. *Prog. Polym. Sci.* 35, 837–867. doi: 10.1016/j.progpolymsci.2010.03.002

Sarasa, J., Gracia, J. M., and Javierre, C. (2009). Study of the biodisintegration of a bioplastic material waste. *Bioresour Technol.* 100, 3764–3768. doi: 10.1016/j.biortech.2008.11.049

Sharma, M., Sharma, S., Abraham, J., Thomas, S., Madras, G., and Bose, S. (2014). Flexible EMI shielding materials derived by melt blending PVDF and ionic liquid modified MWNTs. *Mater. Res. Express* 1:035003. doi: 10.1088/2053-1591/1/3/035003

Shi, Y. Y., Yang, J. H., Huang, T., Zhang, N., Chen, C., and Wang, Y. (2013). Selective localization of carbon nanotubes at the interface of poly(L-lactide)/ethylene-co-vinyl acetate resulting in lowered electrical resistivity. *Composites B* 55, 463–469. doi: 10.1016/j.compositesb.2013.07.012

Soares da Silva, J. P., Soares, B. G., Livi, S., and Barra, G. M. O. (2017). Phosphonium-based ionic liquid as dispersing agent for MWCNT in melt-mixing polystyrene blends: rheology, electrical properties and EMI shielding effectiveness. *Mater. Chem. Phys.* 189, 162–168. doi: 10.1016/j.matchemphys.2016.12.073

Soares, B. G. (2018). Ionic liquid: a smart approach for developing conducting polymer composites. A review. *J. Mol. Liquids* 262, 8–18. doi: 10.1016/j.molliq.2018.04.049

Soares, B. G., Calheiros, L. F., Silva, A. A., Indrusiak, T., Barra, G. M. O., and Livi, S. (2018). Conducting melt blending of polystyrene and EVA copolymer with carbon nanotube assisted by phosphonium-based ionic liquid. *J. Appl. Polym. Sci.* 135:45564. doi: 10.1002/app.45564

Soares, B. G., Gamboa, K. M. N., Ferreira, A. J. B., Ueti, E., and Camargo, S. S. Jr. (1998). Effect of the mold temperature on the electrical properties of carbon black-loaded polystyrene/SB block copolymer blends. *J. Appl. Polym. Sci.* 69, 825–833. doi: 10.1002/(SICI)1097-4628(19980725)69:4<825::AID-APP22>3.0.CO;2-M

Soares, B. G., Gubbels, F., Jérôme, R., Teyssié, P., Vanlthem, E., and Deltour, R. (1995). Electrical conductivity in carbon black-loaded polystyrene-polyisoprene blends. Selective localization of carbon black at the interface. *Polym. Bull.* 35, 223–228. doi: 10.1007/BF00312918

Soares, B. G., Touchaleaume, F., Calheiros, L. F., and Barra, G. M. O. (2016). Effect of double percolation on the electrical properties and electromagnetic interference shielding effectiveness of carbon black-loaded polystyrene/ethylene vinyl acetate copolymer blends. *J. Appl. Polym. Sci.* 133:43013. doi: 10.1002/app.43013

Spitalsky, Z., Tasis, D., Papagelis, K., and Galiotis, C. (2010). Carbon nanotube-polymer composites: chemistry, processing, mechanical and electrical properties. *Prog. Polym. Sci.* 35, 357–401. doi: 10.1016/j.progpolymsci.2009.09.003

Sumita, M., Sakata, K., Asai, S., Miyasaka, K., and Nakagawa, H. (1991). Dispersion of fillers and the electrical conductivity of polymer blends filled with carbon black. *Polym. Bull.* 25, 265–271. doi: 10.1007/BF00310802

Tambe, P. B., Bhattacharyya, A. R., and Kulkarni, A. R. (2013). The influence of melt-mixing process conditions on electrical conductivity of polypropylene/multiwall carbon nanotubes composites. *J. Appl. Polym. Sci.* 127, 1017–1026. doi: 10.1002/app.37889

Urquijo, J., Aranburu, N., Dagréou, S., Guerrica-Echevarria, G., and Eguiazábal, J. I. (2017). CNT-induced morphology and its effect on properties in PLA/PBAT-based nanocomposites. *Eur. Polym. J.* 93, 545–555. doi: 10.1016/j.eurpolymj.2017.06.035

Xiong, Z. Y., Wang, L., Sun, Y., Guo, Z. X., and Yu, J. (2013). Migration of MWCNTs during melt preparation of ABS/PC/MWCNT conductive composites via PC/MWCNT master batch approach. *Polymer* 54, 447–455. doi: 10.1016/j.polymer.2012.11.044

Xu, P., Gui, H., Hu, Y., Bahader, A., and Ding, Y. (2014). Dielectric properties of polypropylene-based nanocomposites with ionic liquid-functionalized multiwalled carbon nanotubes. *J. Electronic Mater.* 43, 2754–2758. doi: 10.1007/s11664-014-3195-1

Zeimaran, E., Akbarivakilabadi, A., and Majumder, M. (2015). "Polystyrene Carbon nanotube composites," in *Handbook of Polymer Nanocomposites. Processing, Performance and Application, Vol. 10*, eds K. K. Kar, J. K. Pandey, and S. Rana (Berlin; Heidelberg: Springer-Verlag), 213.

Zhang, C., Wang, P., Ma, C., Wu, G., and Sumita, M. (2006). Temperature and time dependence of conductive network formation: dynamic percolation and percolation time. *Polymer* 47, 466–473. doi: 10.1016/j.polymer.2005.11.053

Zhang, L., Wan, C., and Zhang, Y. (2009). Morphology and electrical properties of polyamide 6/polypropylene/multi-walled carbon nanotubes composites. *Compos. Sci. Technol.* 69, 2212–2217. doi: 10.1016/j.compscitech.2009.06.005

Zhao, L., Li, Y., Cao, X., You, J., and Dong, W. (2012). Multifunctional role of an ionic liquid in melt-blended poly(methyl methacrylate)/multi-walled carbon nanotube nanocomposites. *Nanotechnology* 23:255702. doi: 10.1088/0957-4484/23/25/255702

Conflict of Interest Statement: The authors declare that the research was conducted in the absence of any commercial or financial relationships that could be construed as a potential conflict of interest.

Copyright © 2019 Soares da Silva, Soares, Silva and Livi. This is an open-access article distributed under the terms of the Creative Commons Attribution License (CC BY). The use, distribution or reproduction in other forums is permitted, provided the original author(s) and the copyright owner(s) are credited and that the original publication in this journal is cited, in accordance with accepted academic practice. No use, distribution or reproduction is permitted which does not comply with these terms.

frontiers in Materials

ORIGINAL RESEARCH
published: 13 August 2019
doi: 10.3389/fmats.2019.00193

Comparative Study of the Structure and Properties of Poly(Vinylidene Fluoride)/Montmorillonite-Polypyrrole Nanocomposites Prepared by Electrospinning and Solution Casting

Vinicius de M. Schiefferdecker[1], *Guilherme M. O. Barra*[2], *Silvia D. A. S. Ramôa*[2] *and Claudia Merlini*[1,2]*

[1] Material Engineering Special Coordinating, Universidade Federal de Santa Catarina, Blumenau, Brazil, [2] Department of Mechanical Engineering, Universidade Federal de Santa Catarina, Florianópolis, Brazil

OPEN ACCESS

Edited by:
Yu Dong,
Curtin University, Australia

Reviewed by:
Xiaowen Qi,
Yanshan University, China
Dongyan Liu,
Institute of Metals Research (CAS), China

***Correspondence:**
Claudia Merlini
claudia.merlini@ufsc.br

Specialty section:
This article was submitted to Polymeric and Composite Materials, a section of the journal Frontiers in Materials

Received: 19 March 2019
Accepted: 25 July 2019
Published: 13 August 2019

Citation:
Schiefferdecker VM, Barra GMO, Ramôa SDAS and Merlini C (2019) Comparative Study of the Structure and Properties of Poly(Vinylidene Fluoride)/Montmorillonite-Polypyrrole Nanocomposites Prepared by Electrospinning and Solution Casting. Front. Mater. 6:193. doi: 10.3389/fmats.2019.00193

In this work, non-woven mats of poly(vinylidene fluoride; PVDF) containing different weight fractions (2.5, 5, 10, and 12.5 wt%) of a nanostructured conductive additive based on montmorillonite—dodecylbenzenesulfonic acid—doped polypyrrole (Mt-PPy.DBSA) have been prepared by electrospinning. The effect of Mt-PPy.DBSA content on the properties of PVDF solution, mats morphology, thermo-mechanical, and electrical properties was investigated. Polymorphism of PVDF/Mt-PPy.DBSA mats was investigated by Fourier Transform Infrared (FTIR) spectroscopy. Moreover, the electromagnetic interference shielding effectiveness (EMI SE) and EMI attenuation mechanism was investigated. In order to perform a comparative study, nanocomposites with the same weight fraction of Mt-PPy.DBSA was also prepared by solution casting. The PVDF/Mt-PPy.DBSA mats display fibers with smaller diameters than neat PVDF, due to the increment in the ionic conductivity of the solution. The incorporation of the Mt-PPy.DBSA additive slightly improved electrical conductivity of the mats and they behave like as an electrically insulating material (10^{-14} S cm^{-1}), due to their porosity, that prevents the formation of a conducting network. Furthermore, the EMI SE of electrospun mats is practically null, indicating that they are almost transparent to magnetic waves. On the other hand, nanocomposites fabricated by solution casting display superior electrical conductivity (10^{-2} S cm^{-1}) and EMI SE reached values of −5 dB.

Keywords: conductive nanocomposites, intrinsically conductive polymers, polypyrrole, montmorillonite, electrospun mats, shielding effectiveness

INTRODUCTION

There is a strong scientific and technological interest for producing conductive polymer composites (CPC's) due to the wide design flexibility and properties that can be obtained by combining different materials. Moreover, CPC's can display both the advantages of organic polymers, such as lightweight, flexible and easily moldable, and functionality of conductive additives, especially the

electrical conductivity (Kim et al., 2003; Das et al., 2009; Lakshmi et al., 2009; Pirvu et al., 2011; Qin and Brosseau, 2012; Yan et al., 2012; Luzio et al., 2014; Merlini et al., 2017; Ramoa et al., 2018; Ram et al., 2019).

Intrinsically conducting polymers (ICP's), such as polypyrrole (PPy) and polyaniline (PANI), have been used as conductive filler to produce CPC's (Moučka et al., 2011; Jin et al., 2016; Merlini et al., 2017; Ramoa et al., 2018). Considerable efforts have been made in order to improve the dispersion of ICP's into the matrix and to reduce the amount of the filler necessary to achieve high values of electrical conductivity. Works in literature have reported that the synthesis of PPy into layered inorganic host material, such as, montmorillonite (Mt), results in nanostructured conductive filler of Mt/PPy, with an intercalative or exfoliated structure, large surface area, and high electrical conductivity (Moučka et al., 2011; Jin et al., 2016; Merlini et al., 2017; Ramoa et al., 2018). The chemical *in situ* polymerization has been the most studied method for the production of Mt/PPy nanostructured conductive filler. This technique consists of inserting PPy into Mt layers through the chemical *in situ* polymerization of pyrrole (Py) in the presence of Mt suspension, using an oxidant. da Silva Ramôa et al. (2015) investigated the effect of the anionic and cationic surfactants used in the pyrrole polymerization, in the morphology and properties of Mt-PPy. The authors concluded that the Mt acts as a template for the Py polymerization, inducing a greater orientation of the PPy chains between the clay layers. Moreover, the anionic surfactants (as DBSA) promoted the intercalation and partial exfoliation of the clay. In this context, the use of nanostructured conductive filler based on Mt-PPy.DBSA can be a strategy to improve the filler dispersion and the electrical conductivity of CPCs, when compared to neat PPy (Ramoa et al., 2018).

Among possible applications of electrically conductive polymer composites containing nanostructured conductive filler, studies in the literature (da Silva Ramôa, 2015; Vargas et al., 2018) have demonstrated the potential for electromagnetic shielding applications (Ramoa et al., 2018). Nowadays, due to the increasing usability of electronic devices in commercial and military setting, electromagnetic interference has become a serious environmental problem (Idris et al., 2015; Liu et al., 2015; Ni et al., 2015; Ramoa et al., 2018). Most of CPC's used as attenuating materials have been processed from conventional manufacturing methods, such as, solution casting or polymer melting procedure, in order to form a conducting network of particles into the matrix (Al-Saleh et al., 2011; Ramoa et al., 2013; Merlini, 2014). However, recent works have been demonstrated the potential of using composite nanofibers for EMI (Im et al., 2009). Among the approaches reported to fabricate non-woven fibrous mat for EMI SE applications, electrospinning can be considered a simple, cheap, and versatile technique (Li and Xia, 2004; Greiner and Wendorff, 2007; Agarwal et al., 2009; Long et al., 2011; Luzio et al., 2014; Ni et al., 2015; Obaid et al., 2016; Liao et al., 2018; Qiao et al., 2018). Basically it is used a syringe filled with the desired polymeric solution where a high electric potential is applied to overcome the surface tension of the fluid, in order to expel it already as fiber (Agarwal et al., 2013; Luzio et al., 2014; Nthumbi et al., 2017; Ji et al., 2018). The nanofiber formation undergoes three stages: (i) stretching and development of a rectilinear jet; (ii) deformation jet with looping and spiraling trajectories, and (iii) fiber solidification with evaporation of solvents resulting fiber solidification deposited in a collector (Reneker and Fong, 2006; Liao et al., 2018).

The electrospinning of polymer composites using ICPs, such as, polypyrrole and polyaniline, is a approach extensively used, in order to provide new functionalities to the mats. The main challenge in the development of electrospun mats is to achieve a good dispersion of conductive additive in order to obtain defect-free fibers (Merlini et al., 2014, 2016). The use of conductive additive also increases the solution charge density and viscosity and usually makes difficult to prepare the electrospun mats. Moreover, great effort has been made to develop mats based on ICP with the good electrical conductivity, since the amount of filer, type of conductive filler, type of dopant and surfactant, chemical compatibility between the components, and porous structure affect the electrical behavior (Yanilmaz and Sarac, 2014). In this context, in our previous work (Merlini et al., 2018), it was investigated the effect Mt-PPy.DBSA, and neat PPy.DBSA on the properties of TPU mats. The TPU/MMT-PPy.DBSA mats exhibited more uniform fibers, and higher mechanical properties, and electrical conductivity than found for TPU/PPy.DBSA.

Relatively few publications on electrospun mats based on conductive nanocomposites for EMI SE applications have been reported in the literature. Jin et al. (2012) have studied the EMI SE of nanocomposites fibers made from polyacrylonitrile (PAN) containing carbon nanotubes (CNTs) and a magnetic nanoparticle of cobalt ferrite ($CoFe_2O_4$), fabricated by electrospinning. The mat with 5 wt% of CNTs and 10 wt% of $CoFe_2O_4$ (PAN/5CNT-10$CoFe_2O_4$) displayed an EMI SE varying from −0.4 to −0.5 dB over the frequency range of 8–12 GHz. In other work, reported by Im et al. (2009), electrospun fibers embedded fluorinated carbon black (CB) were heat-treated and the electrical conductivity of carbon composite reached ∼38 S cm^{-1}, and a high EMI shielding efficiency was obtained (−50 dB), over a frequency range from 800 MHz to 8.5 GHz. It is important to highlight that works reporting comparative analysis of the values of conductivity, morphology and EMI SE still limited, making it necessary to develop studies with this approach.

Considering this framework, in this study electrospun mats of PVDF/Mt-PPy.DBSA were fabricated and its structure, properties, and EMI SE were evaluated as a function of the conductive filler amount. The use of Mt.PPy.DBSA instead of neat PPy can be a strategy to ensure homogenous distribution of the conductive filler and to produce homogeneous fibers. The development of electrospun fibers can improve the surface area that could allow a better interaction with the electromagnetic wave, however, morphology, electrical conductivity, and thickness must to be evaluated. To the best of our knowledge, in the open scientific literature were not found studies that report the fabrication of electrospun mats containing nanostructured conductive additive of montmorillonite/polypyrrole (Mt-PPy), and evaluation of potential for EMI SE applications. For comparison purposes, membranes containing different concentration of Mt-PPy.DBSA were also produced by solution

casting process. In this study, Poly(vinylidene fluoride) (PVDF) were used as a matrix because of its piezoelectric/pyroelectric (β crystal phase), coupled with superior mechanical properties and easy processability (Sarvi et al., 2013; Merlini et al., 2014).

EXPERIMENTAL

Materials

In this study, the poly (vinylidene fluoride) (PVDF), Solef® 6,010 was provided by Solvay. According to the manufacturer, the PVDF displays density of 1.74 g.cm^{-3}, glass transition temperature of −40°C and melting temperature ranging from 170 to 175°C. It was used pyrrole (Py) monomer (Aldrich 98%) with molar mass of 67.09 g.mol^{-1}. The montmorillonite (Mt), Sodium bentonite (Na^+Mt), (VULGEL CN 45) of high purity was produced by *Aliança Latina Indústrias and Comércio Ltda*, with pH of 5.5 and electrical conductivity of 10^{-6} S cm^{-1}. The chemical composition of dry Mt is: SiO_2 (64.75%), Al_2O_3 (17.90%), Fe_2O_3 (3.55%), MgO (3.00%), Na_2O (2.35%), CaO (0.60%), TiO_2 (0.40%), and K_2O (0.15). Iron (III) chloride hexahydrate ($FeCl_3{\cdot}6H_2O$) analytical grade (270.3 g.mol^{-1}) (Vetec) Dodecilbenzenesulfonic acid (DBSA) (Aldrich) with molar mass of 326.54 g.mol^{-1}, acetone and dimethylformamide (DMF), with analytical purity degree (P.A.), from VETEC, were used as provided.

Mt-PPy.DBSA Synthesis

The synthesis of nanostructured conductive additive (Mt-PPy.DBSA) was performed through *in situ* oxidative polymerization, following the procedure described by da Silva Ramôa (2015). Firstly 2.5 g of clay were mixed in 250 mL of distilled water containing 7.15 g of DBSA (0.0219 mol), which represents a molar ratio surfactant/pirrol (DBSA/Py) of 1:5. This suspension was stirred for 2 h under magnetic stirring at room temperature, further, it was scattered in an ultrasonic processor (Sonics VCX 750) with 35% power (263 W). Then, 125 mL of aqueous solution containing 0.2541 mol of $FeCl_3.6H_2O$ were added in a oxidant/Py molar ratio of 2.3:1 to the dispersion of Mt, under stirring. After 15 min, 50 mL of aqueous solution containing Py (0.1103 mol) were dropwise into the dispersion. The reaction was carried out for 1 h under magnetic stirring at room temperature. At the end of 24 h resting, the nanostructured conductive additive was filtered and washed several times with distilled water and dried in a vacuum oven at 60°C, up to constant mass.

Preparation of Electrospun Mats

The preparation procedure for electrospun mats of PVDF/Mt-PPy.DBSA were based on the method described by Merlini et al. (2014, 2015). Firstly, a determined amount of PVDF was dissolved in DMF by magnetic stirring in a thermostatic bath for 2 h at 70°C. Once the temperature downs back to 25°C (room temperature), acetone was added under stirring in order to decrease the viscosity of the solution (proportion of DMF/acetone−3:1 by weight). The solution (with a PVDF concentration of 20 wt%) was magnetic stirred for 1 h. The nanostructured conductive additive at various weight concentrations (2.5, 5, 10, and 12.5 wt%) was added into the solution and maintained under magnetic stirring for 15 min, and after, sonicated with an ultrasonic probe for 5 min. The suspensions were electrospun through a 10 mL syringe, with a needle with an internal diameter of 0.66 mm, coupled with a syringe pump (Instor Apparatus). The metallic collector was covered with an aluminum sheet and grounded, while the positive pole was connected to the syringe. The power supply used to generate the electric field has direct current up to 30 kV (Instor Apparatus). The PVDF/Mt-PPy.DBSA solution was electrospun by using a flow rate of 2.5 mL h^{-1}, a voltage of 17.5 kV and needle-to-collector distance of 30 cm, according to the process parameters used by Merlini (2014) to electrospun mats of PVDF/PPy.DBSA. The electrospinning was carried out in an environment with around 20°C and 50% of humidity. The samples have been named as PVDF/Mt-PPy.DBSA [*x*], where *x* represents weight amount of conductive additive in the mat.

Preparation of Membranes by Solution Casting

In order to perform a comparative study, dense membranes with the same concentrations of additive were developed by casting process. The suspensions were prepared following the same procedure as the one for electrospinning process. The suspensions were deposited on a Petri dish and then they were placed in an oven under vacuum, at 70°C for 15 h. In the end of the process, the Petri dishes were withdrawals of the oven, and the membrane carefully removed.

Characterizations

To analyse the viscosity of the solutions used in both processes, a vertical laboratory rotating viscosimeter HAAKE™ VISCOTESTER™ 550—DC 10 was used. In each measure, the shear rate was of 0.46 s^{-1}. Once the viscosity depends on the temperature, all measures were performed at 25°C.

The ionic conductivity of the solutions were performed with controlled temperature from 24 to 27°C in a conductivity meter model mCA150 by MS TECNOPON.

Micrographs of nanostructured conductive additive were obtained using a field emission scanning electron microscope (FESEM), Jeol JSM−6701F. The morphology of the electrospun mats and membranes produced by solution casting were analyzed using a Scanning Electron Microscope (SEM) (Jeol, model JSM-6390LV), with source of electrons of tungsten and secondary electron detector. Membranes produced by solution were previously fractured in nitrogen. The samples were fixed with double carbon tape in a sample holder, covered with gold and analyzed under an accelerating voltage of 10 or 15 kV. From the SEM images, the fiber average diameter was measured by using ImageJ free software.

Dynamic mechanical thermal analysis (DMTA) were carried out on a DMA Q-800 (TA Scientific) under the tensile mode on rectangular specimens with a 6.4 mm width and 30 mm length. The analysis were performed from −100 to 130°C at a heating rate of 3°C min^{-1}, by using a frequency of 1 Hz, and a peak-to-peak displacement of 64 mm.

The Fourier Transform Infrared (FT-IR) spectra were obtained on a Bruker spectrometer (model TENSOR 27) equipped with an attenuated total reflectance probe (ATR). The spectra were obtained in wavenumbers from 1,600 to 600 cm^{-1}, by accumulation of 32 scans, with a resolution of 4 cm^{-1}.

The electrical conductivity of Mt-PPy.DBSA and high-conductivity membranes was measured using the four-probe standard method with a Keithley 6220 current source to apply the current and a Keithley Model 6517A electrometer to measure the potential difference. The electrical conductivity (σ) (S cm^{-1}) was determined by Equation (1), where, I is the electric current (A), V is the electrical potential difference (V), and w is the sample thickness (cm).

$$\sigma = \frac{I}{V}\frac{\ln 2}{\pi}\frac{1}{w} \quad (1)$$

The PVDF and low-conductivity mats measurements (with values from 10^{-7} to 10^{-17} S cm^{-1}) were performed using a Keithley 6517A electrometer connected to a Keithley 8009 test fixture, on circular specimens of 90 mm of diameter, and the electrical resistivity was calculated by Equation (2):

$$\rho = \frac{\frac{(d+g)^2\pi}{4}}{w}\frac{V}{I} = \frac{1}{\sigma} \quad (2)$$

where, d is the sample support's diameter (cm) and *g* is the distance between sample support and the security ring of the equipment (cm). The electrical conductivity (S cm^{-1}) can be defined as the inverse of the resistivity.

Electromagnetic interference shielding effectiveness (EMI SE) characterization in the X-band frequency range (from 8.2 to 12.4 GHz) were carried out in an Agilent Technology PNA series network analyzer (N5230C Agi-lent PNA-L, Santa Clara, CA) and a standard rectangular waveguide. From complex scattering parameters that correspond to reflection (S_{11}^*) and transmission (S_{21}^*), were calculated the EMI SE, reflected energy (SE_R), transmitted energy (SE_T), and absorbed energy (SE_A) (Ramoa et al., 2018). EMI SE measurements were performed on rectangular samples with 10 mm width, 23 mm length, and thickness of 0.15 mm for electrospun mats and 0.15 and 0.25 mm for membranes by solution casting.

RESULTS AND DISCUSSIONS

During electrospinning process, solution properties can affect the final morphology of fibers and the performance of the process. Viscosity parameter, affects the stretching of charged jet, wherein too high viscosity prevents polymer motion under the electric field (Yanilmaz and Sarac, 2014). The ionic conductivity has a significant influence on Taylor cone formation and on fiber diameter (Merlini, 2014). From **Figure 1** it is possible to note that both properties—viscosity and ionic conductivity—increased with the nanostructured conductor additive loading. The Mt/PPy.DBSA is a nanoadditive, which presents a layered structure with nanometric thickness. When the Py is synthetized among Mt layers, a partial exfoliation occurs, and the PPy particles stand among the layers (micrograph shown in **Figure 2**), resulting in an additive with higher surface area (3.52 m^2 g^{-1}) (Vargas et al., 2018), if compared to the neat PPy, without the presence of the clay (2.06 m^2 g^{-1}) (Vargas et al., 2018). The large surface area of Mt-PPy.DBSA provides a better dispersion and interaction with the PVDF matrix, however resulting in greater restriction of the polymer chains mobility. As a result, lower amount of Mt-PPy.DBSA (12.5 wt%) can be incorporated into the solution when compared to neat PPy.DBSA (23 wt%) (Merlini et al., 2014). The increment in ionic conductivity can be related to the high electrical conductivity of the additive (8.16 $\pm$ 0.32) $\times$ 10^2 S cm^{-1}, to the presence of organic modifier and ions Na^+ located between Mt layers (Merlini et al., 2018) and the presence of DBSA surfactant used during *in situ* polymerization.

SEM micrographs of neat PVDF and PVDF/Mt-PPy.DBSA mats containing different amounts of Mt-PPy.DBSA fabricated

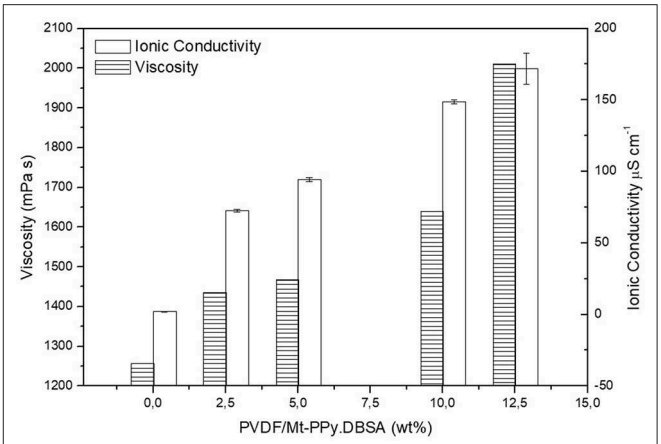

FIGURE 1 | Viscosity (left axis) and ionic conductivity (right axis) of the solution containing different amount of Mt-PPy.DBSA.

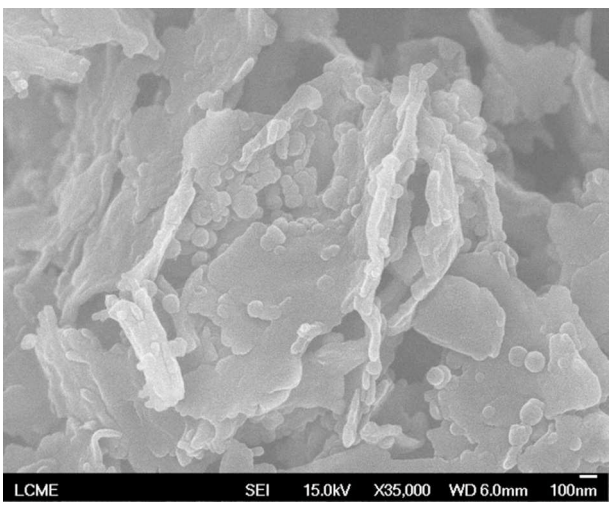

FIGURE 2 | FESEM micrograph of nanostructured conductive additive of Mt-PPy.DBSA.

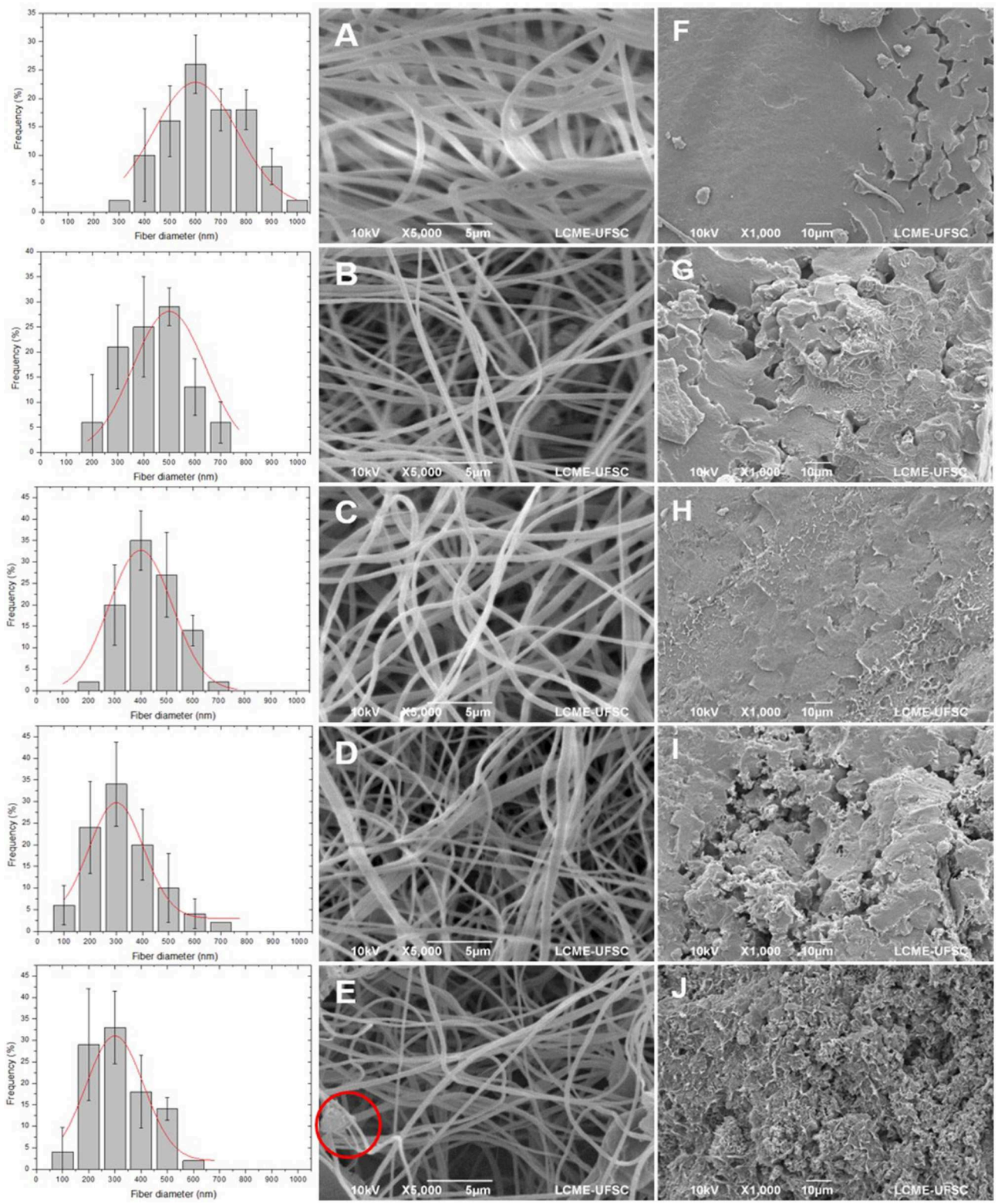

FIGURE 3 | SEM micrographs of the electrospun mats (middle) and membranes fabricated by solution casting (right): **(A,F)** PVDF, **(B,G)** PVDF/Mt-PPy.DBSA [2.5], **(C,H)** PVDF/Mt-PPy.DBSA [5], **(D,I)** PVDF/Mt-PPy.DBSA [10], **(E,J)** PVDF/Mt-PPy.DBSA [12.5]. The histograms are also reported.

by electrospinning and solution casting process are shown at **Figure 3**. Histograms with the diameter distribution of randomly oriented fibers measured by ImageJ free software are also presented. The electrospun PVDF mat (**Figure 3A**), as already reported by Merlini et al. (2015), has a three-dimensional network structure with randomly oriented fibers, with a mean diameter of 642 ± 153 nm. From the micrographs of mats containing different filler contents (**Figures 3B–E**), it is possible to notice that the morphology is quite similar, however, for all mats, fibers diameter were modified with addition of the additive. The fibers became thinner (seen by the graphics of diameter size distribution at the column on the left) and, as the concentration of filler increased (to 12.5 wt%). Usually, it has been reported in the literature that the increase of solution viscosity, result in fibers with larger diameters, due to the greater difficulty to eject the polymer solution from the needle (Merlini et al., 2015). However, in this work, the increase of the ionic conductivity also occurred, which may have strongly influenced the results, since the ionic transport is accelerated/reinforced by the electric current, inducing a greater stretching of the fibers during the process. As reported by Merlini et al. (2018) under the electrical field, by increasing the charge density, high elongation forces are imposed on the solution jet, resulting in thinner fibers and also, the production of beads-free fibers. Moreover, agglomerates outside of the fibers (highlighted at the image) can be seen in the mats with 12.5 wt% of filler, due to the higher amount of Mt-PPy.DBSA in the solution, which hampers the dispersion and distribution of the additive particles.

Figures 3F–J, show the micrographs of all nanocomposites containing 0.0, 2.5, 5.0, 10.0, and 12.5 wt% of Mt-PPy.DBSA developed by solution casting process. A completely different morphology is observed, if compared to electrospinning mats, with a dense structure and low pores density. It is evident that with the increase of additive concentration, the sample microstructure became rougher, generating more and more porosity due to the formation of agglomerates.

The storage modulus curves (E′) loss factor (Tan δ) as a function of the temperature for the electrospun mats and membranes fabricated by solution casting of neat PVDF and PVDF/Mt-PPy.DBSA are shown in **Figures 4A–D**. It is important to highlight the decrease of E′ (**Figures 4A,B**) with the increase of temperature, due to the softening of the polymeric chains. Virtually throughout the temperature range for electrospun mats (**Figure 4A**), E′ values of PVDF are slightly higher than those found to PVDF/Mt-PPy.DBSA mats. This effect can be attributed to the presence of Mt-PPy.DBSA agglomerates, in the electrospun fibers that induce defects in the structure, reducing the storage modulus. However, this variation, caused by the increase of the additive concentration, is very low comparing with the difference between the storage modulus values for the electrospun mats and dense membranes. The last one (**Figure 4B**) displays storage modulus from 2,000 MPa up to almost 3,000 MPa, which is around 100 times higher than the electrospun mats values. This behavior can be related to a denser microstructure of membranes prepared by solution casting (**Figures 3F–J**), when compared to those electrospun mats, which have high porosity, and flexibility. Furthermore, membranes fabricated by solution casting display an opposite behavior when compared to the electrospun mats, for which the modulus increases with the increase of the filler amount, over the entire temperature range. This performance can be explained due to the mechanical reinforcement caused by the conductive additive that display partially exfoliated layers. The behavior obtained in this work for PVDF/Mt-PPy.DBSA is consistent with those reported in the literature for TPU/Mt-PPy.DBSA. Merlini et al. (2018) reported very low mechanical properties for TPU/Mt-PPy.DBSA electrospun mats when compared to nanocomposites prepared by melting process, in the study reported by da Silva Ramôa (2015).

From the loss tangent curves (Tan δ) it is possible to see the peak related to the glass transition temperature (T_g) at around −55°C for electrospun mats (**Figure 4C**) and −46°C for membranes fabricated by solution casting (**Figure 4D**). The lower T_g values for electrospun mats indicates that the electrospinning can induce to a higher molecular organization, reducing the secondary bonds strength between polymer molecules. Therefore, lower energy is required to achieve molecular movement of amorphous phase. Moreover, T_g values are not influenced by the amount of the filler in both nanocomposites, but the intensity of the peak related to the glass transition temperature reduces significantly as the concentration of Mt-PPy.DBSA in the membrane increases. A second peak at superior temperatures to 70°C corresponds to the relaxation process associated with molecular motions of crystalline fraction (Merlini, 2014), and are affected by the presence of Mt-PPy.DBSA.

FTIR spectra of Mt-PPy.DBSA, PVDF, and PVDF/Mt-PPy.DBSA are shown at **Figures 5A,B**. According to previous studies of da Silva Ramôa (2015), Mt presents a broad band at 995 cm^{-1}, which is assigned to the stretching of Si-O-Si groups (da Silva Ramôa, 2015). However, in the spectra of Mt-PPy.DBSA the intensity of the bands associated to the mode of vibration of Si-O-Si groups decreased, indicating the presence of PPy on Mt. The spectrum of Mt-PPy.DBSA exhibits absorption bands at 1,511 and 1,414 cm^{-1}, that correspond to the stretching vibrations of C-C and C-N groups of the pyrrole ring. Absorption band at 1,264 cm^{-1} is assigned to the deformation in the plane of C-H or C-N bonds, while at 1,110 cm^{-1} represents deformation in the plane of C-H bonds. Furthermore, deformations at the vibrational plane of N^+H_2 (formed in doped PPy) entail absorption band at 1,080 cm^{-1} whereas, bands at 988 and 953 cm^{-1} are related to the vibrational deformation in and out of the C-H bonds plane of pyrrole ring.

PVDF has a polymorphic structure, and can present different crystalline structures depending on its processing conditions: as alpha (α), beta (β), gamma (γ), and delta (δ) (Zheng et al., 2007). From the PVDF spectra of electrospun mats and membranes fabricated by solution casting it is possible to note that they display bands assigned to various crystalline phases. Electrospun mats display bands at 1,401 and 876 cm^{-1} (amorphous phase bands) corresponding to the C-F vibrational stretching and the 1,177 cm^{-1} band is attributed to the C-C bonds (Kim et al., 2011;

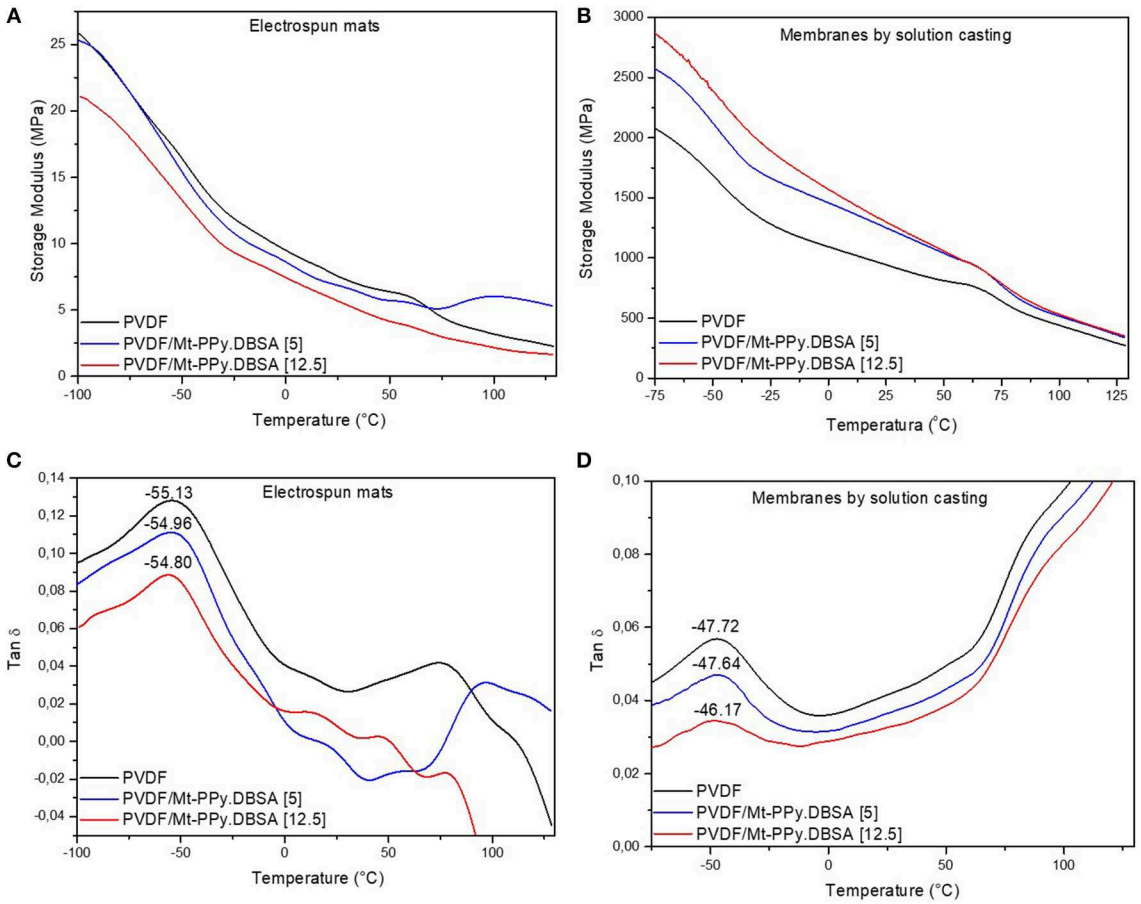

FIGURE 4 | DMTA traces **(A,B)** storage modulus and loss factor **(C,D)** of electrospun mats and membranes fabricated by solution casting.

Merlini, 2014). In addition to, bands at 1,275, 1,071, and 839 cm^{-1} are associated to the β phase (Gregorio and Borges, 2008; Merlini, 2014). In membranes produced by solution casting, characteristic bands of amorphous phase were observed at 1,402, 876, and 1,168 cm^{-1} (and bands associated to the β phase at 1,071 and 834 cm^{-1}, similar to those of the electrospun mats (Gregorio and Borges, 2008; Kim et al., 2011; Merlini et al., 2014). Moreover, bands at 660 and 1,231 cm^{-1} are related, respectively, to α and γ phase (Yu and Cebe, 2009; Wu et al., 2011). The electrospun fibers mats spectrum showed predominance of β phases (which offers the piezoelectric properties), if compared to the solution casting dense membranes spectrum. This result suggests that electrospinning could induced the formation of the β piezoelectric phase in the PVDF mats. The FTIR spectra of PVDF/Mt-PPy.DBSA shows absorption bands similar to those of neat PVDF, however, membranes produced by casting with 12.5 wt% of filler presents a stronger band at 1,546 cm^{-1}, related to the pyrrole ring vibration.

Figure 6 shows the variation of electrical conductivity (σ) (Scm^{-1}) as a function of Mt-PPy.DBSA concentration for membranes fabricated by solution casting and electrospun mats. It can be observed that the electrical conductivity of dense membranes increases sharply from 3.93×10^{-15} to 0.36 S cm^{-1} with Mt-PPy.DBSA contents from 0 to 12.5 wt%, respectively. However, the electrical conductivity obtained for electrospun mats did not show a significant growth with the increment of Mt-PPy.DBSA concentration, ranging from 7.06×10^{-18} S cm^{-1} (raw PVDF) up to 6.13×10^{-14} S cm^{-1} for the PVDF with 12.5 wt% of additive. This behavior can be explained by the morphology, that displays a fibrous and highly porous structure (shown at **Figure 3)** as well as the fact that the nanostructured conductive additive is encapsulated within the fibers, preventing conductive paths formation.

Table 1 shows electrical conductivity of electrospun mats with different composition. The electrical conductivity values obtained in this work are significantly lower than those reported in the literature, however, usually significantly high amount of conducting polymer are used to achieve these elevated values. As can be seen in **Table 1**, electrospun mats can display different ranges of conductivities depending on several factors, as for example, types of polymers, additives, and other chemicals (solvents, dopants, oxidizing agents, etc.), ratios between the components, compactness, and homogeneity of the mats. According to the review work reported by Yanilmaz and Sarac (2014), after investigating several studies, it was reported that the high porosity of fibrous mat structure limits the contact of

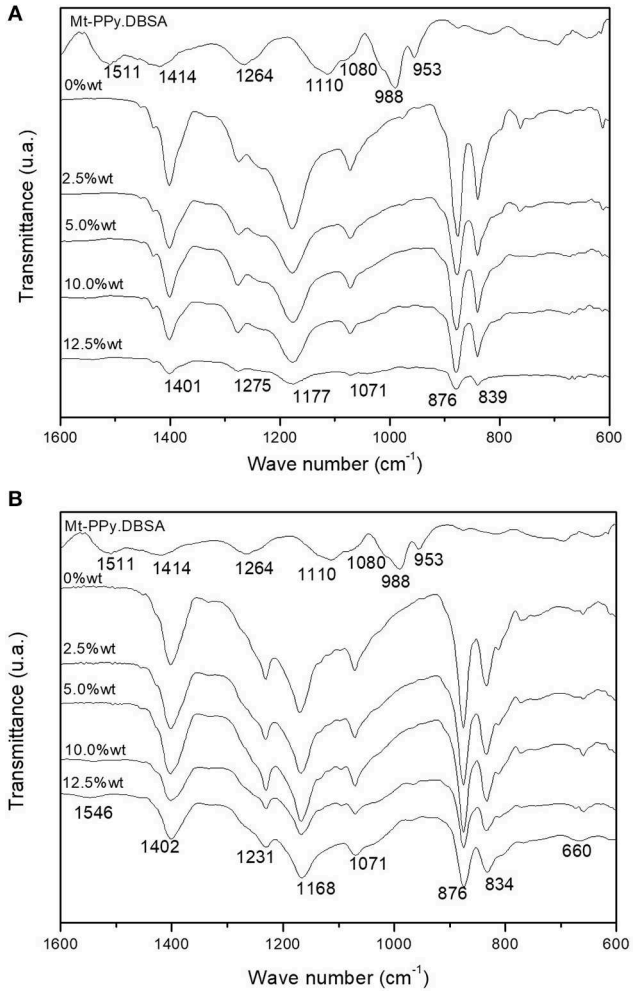

FIGURE 5 | FTIR spectra of PVDF and PVDF/Mt-PPy.DBSA (2.5, 5.0, 10.0, and 12.5 wt%) for **(A)** electrospun mats and **(B)** membranes by solution casting.

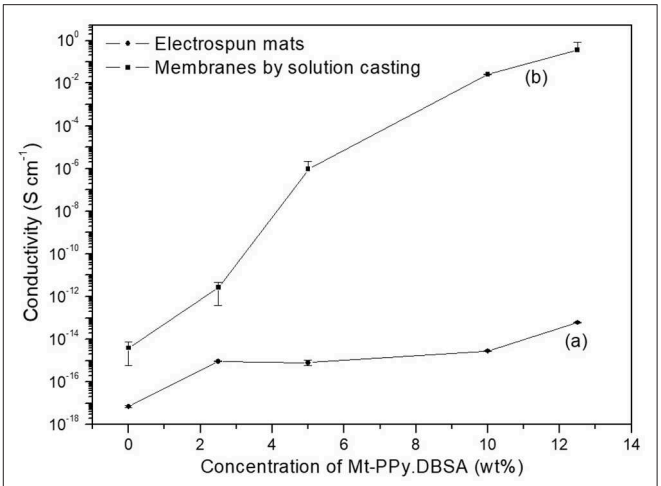

FIGURE 6 | Electrical conductivity of **(A)** electrospun mats and **(B)** membranes fabricated by solution casting.

TABLE 1 | Electrical conductivity for different conductive electrospun mats.

Electrospun mats	Filler content (%wt)	Conductivity (S cm^{-1})	References
PVDF/PANI.DBSA	3	1.4×10^{-14}	Merlini et al., 2016
	13	1.1×10^{-14}	
	23	6.7×10^{-12}	
PVDF/PANI/MWCNT	5	1.7×10^{-12}	Sarvi et al., 2013
	10	4.1×10^{-12}	
PEO(1.5 wt%)/PPy(SO3H)-DEHS	50	3.5×10^{-4}	Chronakis et al., 2006
PEO(2.5 wt%)/PPy(SO3H)-DEHS	37.5	1.1×10^{-4}	
PA6/PANI.DBSA	25	6.2×10^{-7}	Hong and Kang, 2006
PVP/PEDOT:PSS	5	2.3×10^{-12}	Choi et al., 2010

conductive segments, and high level of conductivity required for many applications may not be achieved.

The EMI SE can be defined as the attenuation of electromagnetic waves performed by the shielding material (Merlini et al., 2017). The total EMI SE is described as a sum of three EMI attenuation mechanisms: reflection loss (SE_R); absorption (SE_A) and multiple internal reflection loss at the material interface (SE_M). According to Ramoa et al. (2018) SE_M cannot be measured as separated factor; therefore, they were disregard in this study (Im et al., 2010; Al-Saleh et al., 2011).

In order to investigate the contribution of reflection and absorption to the total EMI SE of the composites, Transmittance (T) and Reflectance (R) powers were calculated through the scattering parameters. That represent the reflection S_{11} (S_{22}) and transmission $S_{12}(S_{21})$ coefficients, from the vector network analyzer, as described by Equations (3) and (4) (Al-Saleh et al., 2011; Ramoa et al., 2013, 2018; Vargas et al., 2018).

$$T = |E_T/E_I|^2 = |S_{12}|^2 (= |S_{21}|^2) \quad (3)$$

$$R = |E_R/E_I|^2 = |S_{11}|^2 (= |S_{22}|^2) \quad (4)$$

The absorbed coefficient (A), as product of incident (I), transmitted (T) and reflected (R) waves, was calculated according to Equation (5), considering 1 (Merlini et al., 2017).

$$A = I - T - R \quad (5)$$

Herewith, the total EMI average, absorption loss (SE_A) and reflection loss (SE_R) were calculated on

the basis of transmittance (T) and reflectance (R) coefficients, according to Equations (6–8) (Al-Saleh et al., 2011; Ramoa et al., 2013, 2018; Vargas et al., 2018).

$$EMI\ SE = SE_R + SE_A = 10log\, I/(I-R) + 10log\,(I-R)/T = 10log\, I/T \quad (6)$$

$$SE_R = 10log\, I/(I-R) \quad (7)$$

$$SE_A = 10log\,(I-R)/T \quad (8)$$

Figure 7 shows the EMI SE of investigated electrospun mats and dense membranes as a function of weight fraction of Mt-PPy.DBSA filler, over the frequency range of 8.2–12.4 GHz. It is possible to note that EMI SE of electrospun mats is practically null (lower than −2dB), indicating that they are almost transparent to magnetic waves, even with higher concentration of additive (12.5 wt%). This behavior was not expected since works in the literature have demonstrated the potential use of electrospun mats for electromagnetic shielding applications, especially due to the high surface area to interact with the radiation (Im et al., 2010). However, Im et al. (2010) reported a great EMI SE of −42 dB to MWCNT embedded PANI/PEO-based fibers, when a very high amount of fluorinated MWCNTs (120 wt%) were embedded in the PANI/PEO fibers. The low EMI SE of PVDF/Mt-PPy.DBSA electrospun mats can be explained by the low values of electrical conductivity of the mats, as reported previously, as well as the low amount of Mt-PPy.DBSA incorporated into the fibers. The electrical conductivity has been shown to be a critical factor in the development of electromagnetic radiation attenuating materials and required conductivity levels are $>10^2$ S m^{-1} for electromagnetic shielding applications (Sudha et al., 2009). Moreover, these mats display lower thickness (0.15 mm) when compared to conventional nanocomposites used for EMI SE (2 mm). According to the literature (Vargas et al., 2018), EMI SE is significantly influenced by the nanocomposites thickness. Vargas et al. (2018) reported that, by increasing thickness of PU/Mt-PPy.DBSA nanocomposites from 2 to 8 mm, the EMI SE increases from −20.8 to −60.3 dB, when 25 wt% of Mt-PPy.DBSA.

It is possible to note that the EMI SE of membranes produced by solution casting (**Figure 7B**) is quite similar to those values reported for electrospun mats, even that the electrical conductivity of these membranes are superior to those of electrospun mats. This behavior can be associated to the low thickness (0.15 mm), which allows the transmission of the wave through the material. In order to analyze the effect of the thickness, thicker membranes (0.25 mm) were produced by solution casting. For these membranes (**Figure 7C**) the EMI SE increased with the Mt-PPy.DBSA loading, indicating that a better interaction of the conductive filler with the radiation. For membranes with lower filler content, the EMI SE values varied over the frequency range, but became almost independent of frequency with the increase of Mt-PPy.DBSA amount. This behavior can be explained due to the reduction of the material skin depth with increasing filler content into the nanocomposites (Al-Hartomy et al., 2011; Choudhary and Gupt, 2011; Ramoa et al., 2018). It is important to highlight that was not possible to fabricate electrospun mats with thickness higher than 0.15 mm.

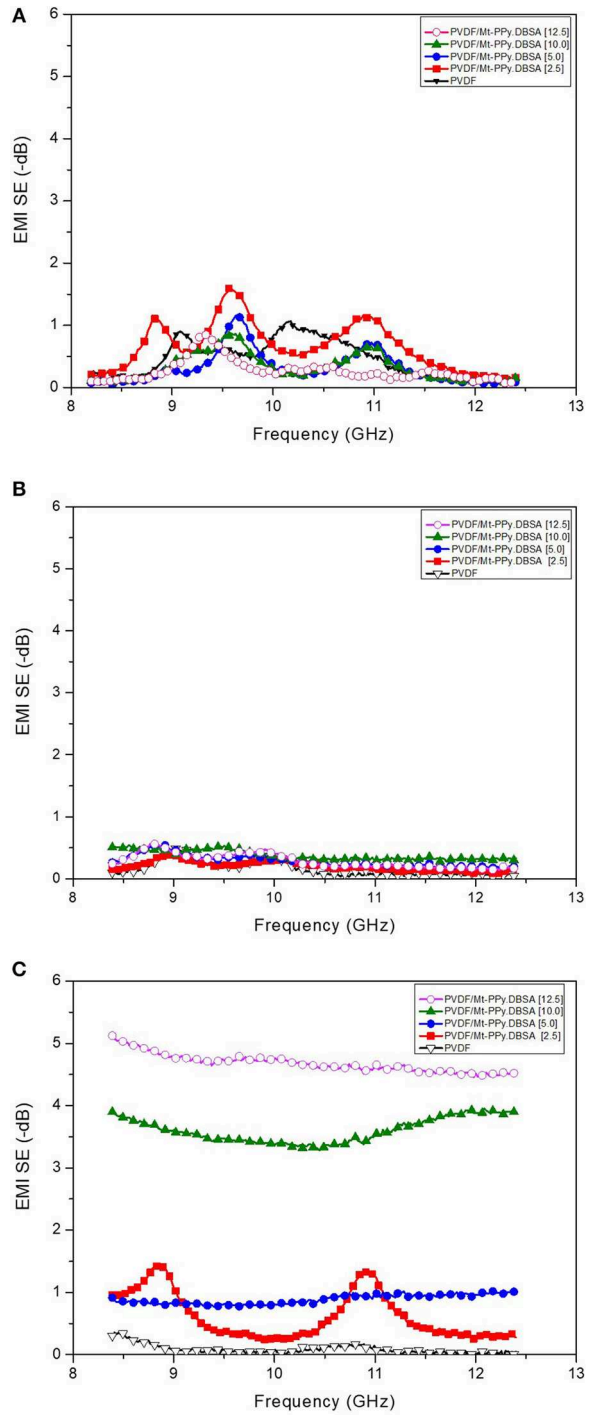

FIGURE 7 | EMI SE in the X-band frequency range for **(A)** electrospun mats of PVDF/Mt-PPy.DBSA and **(B,C)** membranes of PVDF/Mt-PPy.DBSA fabricated by solution casting process with thickness of 0.15 mm and 0.25 mm, respectively.

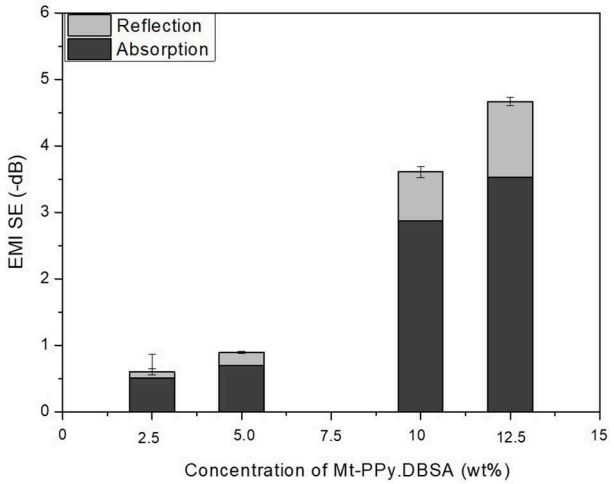

FIGURE 8 | Effect of conductive filler content on the total EMI SE average, absorption loss (SEA) and reflection loss (SER) of PVDF/Mt-PPy.DBSA membranes by solution casting with a thickness average of 0.25 mm.

The contribution of reflection and absorption in the total EMI SE for thicker membranes produced by solution casting is reported at **Figure 8**. The results are expressed as average values in the frequency range of 8.2–12.4 GHz. It is possible to note that the shielding by reflection and absorption contribute to the total electromagnetic shielding and the contribution of both mechanism increases with the filler loading, resulting in higher EMI SE. The SE_A becomes the main EMI shielding mechanism, similar to the results reported by Vargas et al. (2018) for nanocomposites containing Mt-PPy.DBSA.

CONCLUSIONS

Non-woven mats of PVDF containing different weight fractions of Mt-PPy.DBSA were successfully obtained by electrospinning. The fibers diameter of electrospun mats decreased with the increase of additive loading, due to a higher elongation imposed to the solution caused by the higher ionic conductivity. Mats produced by electrospinning display the piezoelectric phase, indicating effectiveness of this process to produce β phase. Electrospun mats behave as insulating material with electrical conductivity ranging from 10^{-18} to 10^{-14} S cm^{-1} due to the highly porous structure and encapsulation of the filler. Moreover, they did not achieve a satisfactory EMI SE due to the low electrical conductivity and thickness. However, membranes produced by solution casting, showed superior mechanical properties, electrical conductivity (10^{-2} S cm^{-1}) and those with higher thickness achieve to EMI SE of −5 dB with 12.5 wt% Mt-PPy.DBSA. The values obtained for both systems remains below to that required for commercial application (−20 dB), indicating that is necessary to expand the studies related to shielding efficiency, in order to conclude if these materials are feasible for this application.

DATA AVAILABILITY

All datasets generated for this study are included in the manuscript and/or the supplementary files.

AUTHOR CONTRIBUTIONS

SR performed the synthesis of the additives. VS fabricated the electrospun mats and dense membranes, performed the characterizations and wrote the article. CM assisted in writing of the manuscript and discussion of results. GB conducted the discussion of results. All authors reviewed the final manuscript.

ACKNOWLEDGMENTS

The authors acknowledge the financial support of Conselho Nacional de Desenvolvimento Científico e Tecnológico (Process: 406286/2018-3), Coordenação de Aperfeiçoamento de Pessoal de Ensino Superior (CAPES), and Fundação de Amparo à Pesquisa e Inovação do Estado de Santa Catarina (FAPESC). In addition, we extend our sincere gratitude to the Central Electronic Microscopy Laboratory, Federal University of Santa Catarina (LCME-UFSC).

REFERENCES

Agarwal, S., Greimer, A., and Wendorff, J. H. (2009). Electrospinning of manmade and biopolymer nanofibers - progress in techniques, materials, and applications. *Adv. Funct. Mater.* 19, 2863–2879. doi: 10.1002/adfm.200900591

Agarwal, S., Greiner, A., and Wendorff, J. H. (2013). Functional materials by electrospinning of polymers. *Prog. Polym. Sci.* 38, 963–991. doi: 10.1016/j.progpolymsci.2013.02.001

Al-Hartomy, O. A., Al-Salamy, F., Al-Ghamdi, A. A., Abdel Fatah, M., Dishovsky, N., and El-Tantawy, F. (2011). Influence of graphite nanosheets on the structure and properties of PVC-based nanocomposites. *J. Appl. Polym. Sci.* 120, 3628–3634. doi: 10.1002/app.33547

Al-Saleh, M. H., Gelves, G. A., and Sundararaj, U. (2011). Copper nanowire/polystyrene nanocomposites: lower percolation threshold and higher EMI shielding. *Compos. Part A Appl. Sci. Manuf.* 42, 92–97. doi: 10.1016/j.compositesa.2010.10.003

Choi, J., Lee, J., Choi, J., Jung, D., and Shim, S. E. (2010). Electrospun PEDOT:PSS/PVP nanofibers as the chemiresistor in chemical vapour sensing. *Synth. Met.* 160, 1415–1421. doi: 10.1016/j.synthmet.2010.04.021

Choudhary, V., and Gupt, A. (2011). "Polymer/carbon nanotube nanocomposites," in *Carbon Nanotubes - Polymer Nanocomposites*, ed S. Yellampalli (Delhi: InTech), 65–90.

Chronakis, I. S., Grapenson, S., and Jakob, A. (2006). Conductive polypyrrole nanofibers via electrospinning: electrical and morphological properties. *Polymer* 47, 1597–1603. doi: 10.1016/j.polymer.2006.01.032

Das, N. C., Liu, Y., Yang, K., Peng, W., Maiti, S., and Wang, H. (2009). Single-walled carbon nanotube/poly(methyl methacrylate) composites for electromagnetic interference shielding. *Polym. Eng. Sci.* 49, 1627–1634. doi: 10.1002/pen.21384

da Silva Ramôa, S. D. A., Barra, G. M. O., Merlini, C., Schreiner, W. H., Livi, S., Soares, B. G., et al. (2015). Production of montmorillonite/polypyrrole nanocomposites through *in situ* oxidative polymerization of pyrrole: effect of

anionic and cationic surfactants on structure and properties. *Appl. Clay Sci.* 104, 160–167. doi: 10.1016/j.clay.2014.11.026

da Silva Ramôa, S. D. A. (2015). Síntese, caracterização e avaliação da utilização de aditivo condutor nanoestruturado à base de montmorilonita/polipirrol em matriz de poliuretano termoplástico para aplicação em blindagem eletromagnética. (Doctoral's thesis). Federal University of Santa Catarina, Florianópolis, Brazil.

Gregorio, R., and Borges, D. S. (2008). Effect of crystallization rate on the formation of the polymorphs of solution cast poly(vinylidene fluoride). *Polymer* 49, 4009–4016. doi: 10.1016/j.polymer.2008.07.010

Greiner, A., and Wendorff, J. H. (2007). Electrospinning: a fascinating method for the preparation of ultrathin fibers. *Angew. Chem. Int. Ed.* 46, 5670–5703. doi: 10.1002/anie.200604646

Hong, K. H., and Kang, T. J. (2006). Polyaniline-nylon 6 composite nanowires prepared by emulsion polymerization and electrospinning process. *J. Appl. Polym. Sci.* 99, 1277–1286. doi: 10.1002/app.22654

Idris, F. M., Hashim, M., Ibrahim, I. R., Ismail, I., Abbas, Z., Nazlan, R., et al. (2015). Recent developments of smart electromagnetic absorbers based polymer-composites at gigahertz frequencies. *J. Magn. Magn. Mater.* 405, 197–208. doi: 10.1016/j.jmmm.2015.12.070

Im, J. S., Kim, J. G., Lee, S.-H., and Lee, Y.-S. (2010). Enhanced adhesion and dispersion of carbon nanotube in PANI/PEO electrospun fibers for shielding effectiveness of electromagnetic interference. *Colloids Surfaces A Physicochem. Eng. Asp.* 364, 151–157. doi: 10.1016/j.colsurfa.2010.05.015

Im, J. S., Kim, J. G., and Lee, Y.-S. (2009). Fluorination effects of carbon black additives for electrical properties and EMI shielding efficiency by improved dispersion and adhesion. *Carbon* 47, 2640–2647. doi: 10.1016/j.carbon.2009.05.017

Ji, H., Zhao, R., Zhang, N., Jin, C., Lu, X., and Wang, C. (2018). Lightweight and flexible electrospun polymer nanofiber/metal nanoparticle hybrid membrane for high-performance electromagnetic interference shielding. *NPG Asia Mater.* 10, 749–760. doi: 10.1038/s41427-018-0070-1

Jin, J., Song, J., Deng, S., and Li, G. (2016). Synthesis and microwave absorbing characteristics of flake-like polypyrrole filled composites in X-band. *Polym. Compos.* 37, 1137–1142. doi: 10.1002/pc.23209

Jin, X., Ni, Q.-Q., Fu, Y., Zhang, L., and Natsuki, T. (2012). Electrospun nanocomposite polyacrylonitrile fibers containing carbon nanotubes and cobalt ferrite. *Polym. Compos.* 33, 317–323. doi: 10.1002/pc.21251

Kim, H. K., Kim, M. S., Song, K., Park, Y. H., Kim, S. H., Joo, J., et al. (2003). EMI shielding intrinsically conducting polymer/PET textile composites. *Synth. Met.* 135–136, 105–106. doi: 10.1016/S0379-6779(02)00876-7

Kim, Y. J., Ahn, C. H., Lee, M. B., and Choi, M. S. (2011). Characteristics of electrospun PVDF/SiO2 composite nanofiber membranes as polymer electrolyte. *Mater. Chem. Phys.* 127, 137–142. doi: 10.1016/j.matchemphys.2011.01.046

Lakshmi, K., John, H., Mathew, K. T., Joseph, R., and George, K. E. (2009). Microwave absorption, reflection and EMI shielding of PU-PANI composite. *Acta Mater.* 57, 371–375. doi: 10.1016/j.actamat.2008.09.018

Li, D., and Xia, Y. (2004). Electrospinning of nanofibers: reinventing the wheel? *Adv. Mater.* 16, 1151–1170. doi: 10.1002/adma.200400719

Liao, Y., Loh, C. H., Tian, M., Wang, R., and Fane, A. G. (2018). Progress in electrospun polymeric nanofibrous membranes for water treatment: fabrication, modification and applications. *Prog. Polym. Sci.* 77, 69–94. doi: 10.1016/j.progpolymsci.2017.10.003

Liu, P., Huang, Y., and Zhang, X. (2015). Synthesis, characterization and excellent electromagnetic wave absorption properties of graphene@CoFe2O4@polyaniline nanocomposites. *Synth. Met.* 201, 76–81. doi: 10.1016/j.synthmet.2015.01.022

Long, Y. Z., Li, M. M., Gu, C., Wan, M., Duvail, J. L., Liu, Z., et al. (2011). Recent advances in synthesis, physical properties and applications of conducting polymer nanotubes and nanofibers. *Prog. Polym. Sci.* 36, 1415–1442. doi: 10.1016/j.progpolymsci.2011.04.001

Luzio, A., Canesi, E. V., Bertarelli, C., and Caironi, M. (2014). Electrospun polymer fibers for electronic applications. *Materials* 7, 906–947. doi: 10.3390/ma7020906

Merlini, C. (2014). *Desenvolvimento de membranas eletrofiadas de poli (fluoreto de vinilideno) com polipirrol para aplicação em sensores de compressão* (Doctoral's thesis). Federal University of Santa Catarina, Florianópolis, Brazil.

Merlini, C., Barra, G. M. O., Medeiros Araujo, T., and Pegoretti, A. (2014). Electrically pressure sensitive poly(vinylidene fluoride)/polypyrrole electrospun mats. *RSC Adv.* 4, 15749–15758. doi: 10.1039/C4RA01058B

Merlini, C., Contri, G., de Oliveira Barra, G. M., da Silva Ramôa, S. D. A., Soares, B. G., D'Ávila, M., et al. (2015). Electrically conductive polyaniline-coated electrospun poly(vinylidene fluoride) mats. *Front. Mater.* 2:14. doi: 10.3389/fmats.2015.00014

Merlini, C., Pegoretti, A., Araujo, T. M., Ramoa, S. D. A. S., Schreiner, W. H., and De Oliveira Barra, G. M. (2016). Electrospinning of doped and undoped-polyaniline/poly(vinylidene fluoride) blends. *Synth. Met.* 213, 34–41. doi: 10.1016/j.synthmet.2015.12.024

Merlini, C., Pegoretti, A., Vargas, P. C., Cunha, T. F., da Ramôa, S. D. A. S., Soares, B. G., et al. (2017). Electromagnetic interference shielding effectiveness of composites based on polyurethane derived from castor oil and nanostructured carbon fillers. *Polym. Compos.* 37, 1137–1142. doi: 10.1002/pc.24501

Merlini, C., Silveira, A., Ramôa, S. D. A. S., Soares, B. G., Alavarse, A. C., Bonvent, J. J., et al. (2018). A comparative study of aligned and random electrospun mats of thermoplastic polyurethane and conductive additives based on polypyrrole. *Polym. Test.* 70, 486–497. doi: 10.1016/j.polymertesting.2018.08.002

Moučka, R., Mravčáková, M., Vilčáková, J., Omastová, M., and Sáha, P. (2011). Electromagnetic absorption efficiency of polypropylene/montmorillonite/polypyrrole nanocomposites. *Mater. Des.* 32, 2006–2011. doi: 10.1016/j.matdes.2010.11.064

Ni, Q.-Q., Xia, H., Jin, X., and Liu, F. (2015). "Application of electrospun nanofibers in electromagnetic interference shielding," in *Electrospun Nanofibers for Energy and Environmental Applications*, eds J. David, B. Lockwood, Ding, and J. Yu (Ueda: Springer), 518.

Nthumbi, R. M., Adelodun, A. A., and Ngila, J. C. (2017). Electrospun and functionalized PVDF/PAN composite for the removal of trace metals in contaminated water. *Phys. Chem. Earth* 100, 225–235. doi: 10.1016/j.pce.2016.08.007

Obaid, M., Mohamed, H. O., Yasin, A. S., Fadali, O. A., Khalil, K. A., Kim, T., et al. (2016). A novel strategy for enhancing the electrospun PVDF support layer of thin-film composite forward osmosis membranes. *RSC Adv.* 6, 102762–102772. doi: 10.1039/C6RA18153H

Pirvu, C., Manole, C. C., Stoian, A. B., and Demetrescu, I. (2011). Understanding of electrochemical and structural changes of polypyrrole/polyethylene glycol composite films in aqueous solution. *Electrochim. Acta* 56, 9893–9903. doi: 10.1016/j.electacta.2011.08.061

Qiao, J., Liu, J., Liu, W., Wang, F., Zhang, X., Xu, D., et al. (2018). Self-assembled ZnO/Co hybrid nanotubes prepared by electrospinning for lightweight and high-performance electromagnetic wave absorption. *ACS Appl. Nano Mater.* 1, 5297–5306. doi: 10.1021/acsanm.8b01303

Qin, F., and Brosseau, C. (2012). A review and analysis of microwave absorption in polymer composites filled with carbonaceous particles. *J. Appl. Phys.* 111:061301. doi: 10.1063/1.3688435

Ram, R., Rahaman, M., and Khastgir, D. (2019). "Electromagnetic interference (EMI) shielding effectiveness (SE) of polymer-carbon composites," in *Carbon-Containing Polymer Composites,* eds M. Rahaman, D. Khastgir, and A. Aldalbahi (Singapore: Springer), 339–368. doi: 10.1007/978-981-13-2688-2_10

Ramoa, S. D. A. S., Merlini, C., Soares, B. G., Barra, G. M. O., Pegoretti, A., and Livi, S. (2018). Electromagnetic interference shielding effectiveness and microwave absorption properties of thermoplastic polyurethane/montmorillonite-polypyrrole nanocomposites. *Polym. Adv. Technol.* 29, 1377–1384. doi: 10.1002/pat.4249

Ramoa, S. D. A. S., Soares, B. G., Oliveira, R. V., de Oliveira, M. G., Cossa, M., and Barra, G. M. O. (2013). Electrical, rheological and electromagnetic interference shielding properties of thermoplastic polyurethane/carbon nanotube composites. *Polym. Int.* 62, 1477–1484. doi: 10.1002/pi.4446

Reneker, D. H., and Fong, H. (2006). "Polymeric nanofibers: introduction," in *Polymeric Nanofibers* (Washington, DC: American Chemical Society), 1–6. doi: 10.1021/bk-2006-0918.ch001

Sarvi, A., Chimello, V., Silva, A. B., Bretas, R. E. S., and Sundararaj, U. (2013). Coaxial electrospun nanofibers of poly(vinylidene fluoride)/polyaniline filled with multi-walled carbon nanotubes. *Polym. Compos.* 35, 1198–1203. doi: 10.1002/pc.22768

Sudha, J. D., Radhakrishnan Nair, P., Reena, V. L., Prasanth, R., and Sivakala, S. (2009). Development of electromagnetic shielding materials from the conductive blends of polyaniline and polyaniline-clay nanocomposite-EVA: preparation and properties. *Compos. Sci. Technol.* 69, 358–364. doi: 10.1016/j.compscitech.2008.10.026

Vargas, P. C., Merlinia, C., Ramôaa, S. D. A., da, S., Arenharta, R., Barra, G. M. de, O., et al. (2018). Conductive composites based on polyurethane and nanostructured conductive filler of montmorillonite/polypyrrole for electromagnetic shielding applications. *Mater. Res.* 21:e20180014. doi: 10.1590/1980-5373-mr-2018-0014

Wu, N., Cao, Q., Wang, X., and Chen, Q. (2011). Study of a novel porous gel polymer electrolyte based on TPU/PVdF by electrospinning technique. *Solid State Ionics* 203, 42–46. doi: 10.1016/j.ssi.2011.08.020

Yan, D.-X., Ren, P.-G., Pang, H., Li, Z.-M., Fu, Q., and Yang, M.-B. (2012). Efficient electromagnetic interference shielding of lightweight graphene/polystyrene composite. *J. Mater. Chem.* 22:18772. doi: 10.1039/c2jm32692b

Yanilmaz, M., and Sarac, A. S. (2014). A review: effect of conductive polymers on the conductivities of electrospun mats. *Text. Res. J.* 84, 1325–1342. doi: 10.1177/0040517513495943

Yu, L., and Cebe, P. (2009). Crystal polymorphism in electrospun composite nanofibers of poly(vinylidene fluoride) with nanoclay. *Polymer* 50, 2133–2141. doi: 10.1016/j.polymer.2009.03.003

Zheng, J., He, A., Li, J., and Han, C. C. (2007). Polymorphism control of poly(vinylidene fluoride) through electrospinning. *Macromol. Rapid Commun.* 28, 2159–2162. doi: 10.1002/marc.200700544

Conflict of Interest Statement: The authors declare that the research was conducted in the absence of any commercial or financial relationships that could be construed as a potential conflict of interest.

Copyright © 2019 Schiefferdecker, Barra, Ramôa and Merlini. This is an open-access article distributed under the terms of the Creative Commons Attribution License (CC BY). The use, distribution or reproduction in other forums is permitted, provided the original author(s) and the copyright owner(s) are credited and that the original publication in this journal is cited, in accordance with accepted academic practice. No use, distribution or reproduction is permitted which does not comply with these terms.

frontiers in Materials

ORIGINAL RESEARCH
published: 16 August 2019
doi: 10.3389/fmats.2019.00189

Pressure Sensibility of Conductive Rubber Based on NBR- and Polypyrrole-Designed Materials

*Débora França[1], Ana Cláudia Rebessi[1], Fernanda Ferraz Camilo[2], Fernando G. Souza Jr.[3] and Roselena Faez[1]**

[1] Laboratório de Materiais Poliméricos e Biossorventes, Universidade Federal de São Carlos, Araras, Brazil, [2] Laboratório de Materiais Híbridos, Universidade Federal de São Paulo, Diadema, Brazil, [3] Instituto de Macromoléculas Professora Eloisa Mano, Universidade Federal do Rio de Janeiro, Rio de Janeiro, Brazil

Conductive rubbers combine features such as elasticity and electrical conductivities. Here, we developed an elastic conductive material based on nitrile rubber (NBR) and polypyrrole (PPy) by melt processing. PPy was also synthesized in three different media as silver (PPy-Ag), organomontmorillonite (PPy-OMt), and silver-organomontmorillonite (PPy-Ag-OMt) before mixture with NBR. Chemical structure, morphology, and stress–strain properties were evaluated. Pressure sensibility was evaluated in the range of 0–67 MPa during 10 cycles. During the compression and expansion processes, the electrical conductivity changes from high to low values and the difference of loading and unloading cycles demonstrates the repeatability and low hysteresis. The organomontmorillonite clay improves the homogeneity of particles into the matrix, and based on SEM images, the dispersity follows the sequence PPy-OMt, PPy-Ag-OMt, and PPy-Ag-OMt. This behavior affects the electrical conductivity and mechanical and electromechanical properties. The higher elastic modulus for composites compared to neat NBR is assigned to the reinforcing effect of the fillers. NBR/PPy-Ag-OMt (5 wt.%) is the best material in the absolute value of Scomp (46.3%/MPa) and the Scomp/hysteresis ratio (8.5%). In spite of different formulations displaying the best performance on the evaluated criteria (highest absolute conductivity, the highest percentage change in conductivity, lowest hysteresis, and lack of sample disruption), we can suggest that a lower amount of conducting particles benefits the reticulation process (as observed by the gel fraction values). Additionally, the possibility of using mechanical processing to obtain large-scale pressure sensor materials is without a doubt the most important outcome of this research area.

Keywords: conducting polymer, conductive rubber, melt processing, montmorillonite, silver

OPEN ACCESS

Edited by:
Guilherme Mariz de Oliveira Barra, Federal University of Santa Catarina, Brazil

Reviewed by:
Rafael Guntzel Arenhart, Federal University of Santa Catarina, Brazil
Marcos Akira D'Avila, Campinas State University, Brazil
Chayan Das, Visvesvaraya National Institute of Technology, India

***Correspondence:**
Roselena Faez
faez@ufscar.br

Specialty section:
This article was submitted to Polymeric and Composite Materials, a section of the journal Frontiers in Materials

Received: *19 March 2019*
Accepted: *24 July 2019*
Published: *16 August 2019*

Citation:
França D, Rebessi AC, Camilo FF, Souza FG Jr and Faez R (2019) Pressure Sensibility of Conductive Rubber Based on NBR- and Polypyrrole-Designed Materials. Front. Mater. 6:189. doi: 10.3389/fmats.2019.00189

INTRODUCTION

Pressure sensors are quite interesting materials to be used in areas such as medical and computer science (Job et al., 2003; Rosa et al., 2019). Conductive rubber is a composite material of an elastomeric matrix and conductive particles as a dispersed phase. Typically, the conductive particles are carbon composites and/or intrinsically conducting polymers (ICP) (Ali and Abo-Hashem, 1997; Cho et al., 1998; Sombatsompop et al., 2000; Das et al., 2002; Knite et al., 2004; Bing et al., 2010). This last class has attracted the attention of a wide academic and technological

field since they combine electrical properties, similar to metals, and mechanical properties and processability inherent to conventional polymers (Mattoso, 1996; Job et al., 2003; Swart et al., 2017; Sethi et al., 2018; Rosa et al., 2019). The addition of ICP in elastomers can combine the electrical and mechanical properties of these two classes of polymer in one (Hussain et al., 2001; Soto-Oviedo et al., 2006; Tran et al., 2018), allowing its application on technological fields such as pressure sensors, electric wires and cables coating, electrical contacts, carpet with antistatic properties, and others (Mravčáková et al., 2006; Bing et al., 2010). The electrical conductivity of conductive rubber depends on factors such as the nature of the elastomeric matrix and the type, size, structure, surface, and dispersion of the conductive particles as well as the test conditions, such as temperature and pressure (Ali and Abo-Hashem, 1997; Sombatsompop et al., 2000; Job et al., 2003; Bing et al., 2010). The conductor path is created by the different sizes and shapes of conducting particles homogeneously distributed and closer to each other (Hussain et al., 2001; Rosa et al., 2019). At the percolation threshold, the contact between the particles produces a conductive network that can be improved during the compression. From this phenomenon, the resistivity of the material reduces and its conductivity increases (Sombatsompop et al., 2000; Hussain et al., 2001; Job et al., 2003; Bing et al., 2010). However, elastomers–ICP composites still have challenges with the elastomeric cross-linking process (Prudêncio et al., 2014). Then, the use of an inorganic matrix [e.g., organomontmorillonite clay (OMt)] as a template for ICP synthesis is interesting to improve the compatibility of the conductive polymer and the elastomeric matrix, affording a material with superior mechanical properties (Baldissera and Ferreira, 2017). In addition, ICP produced in a confined environment, such as clays, produces a material with superior polymer chain organization and, consequently, higher electrical conductivity and thermal stability, which enables melt processing without degradation and/or electrical properties loss (Mravčáková et al., 2006; Soto-Oviedo et al., 2006; Rosa et al., 2019). Furthermore, the combination of silver nanoparticles with ICP improves the conductivity of the polymer (Wei et al., 2010) and opens the opportunity to use humidity and chemoreceptive sensors (Jlassi et al., 2013). The aim of this work was to prove the hypothesis that the insertion of fillers such as polypyrrole (PPy)-Ag, PPy-OMt, and PPy-Ag-OMt improves the processability and the conductive, thermal, and mechanical properties required for a pressure sensor.

EXPERIMENTAL

Chemicals

Pyrrole (Aldrich, P.A.), ammonium persulfate (APS; Aldrich, P.A.), cetyltrimethylammonium bromide (CTAB; Aldrich, P.A.), silver nitrate ($AgNO_3$; Aldrich, P.A.), sodium dodecyl sulfate (SDS; Aldrich, P.A.), sulfur (Aldrich, P.A.), stearic acid (Synth, P.A.), 2-mercaptobenzothiazole (MBTS-Fluka, PA), and zinc oxide (Synth, PA) were used as received. Bentonit Union (Brazilian trademark) provided montmorillonite clay. Organic-modified montmorillonite clay with ammonium quaternary salt (CTAB) in a weight ratio of salt:clay 1:1 (nominated OMt) was prepared as described in the literature (Fontana et al., 2013). Nitriflex SA, Brazil, provided nitrile rubber (NBR) with 30–34% acrylonitrile.

Preparation of PPy Composites (PPy-OMt; PPy-Ag; and PPy-Ag-OMt)

Polypyrrole (PPy) composites were prepared according to the previous work of França et al. (2017). Briefly, cationic (CTAB) and anionic (SDS) surfactants were dissolved in 100 ml of ultrapure water at a molar ratio of 1:5. Afterward, CTAB/SDS was added to the OMt dispersion (mass proportion of 1:1, PPy : OMt) and stirred for 2 h. Pyrrole (0.35 ml; 5.0 mmol) and APS (1.14 g; 5.0 mmol) were then added to the previous solution. The polymerization proceeded under magnetic stirring for 24 h. It was named PPy-OMt. For PPy-Ag-OMt composites, we used the same procedure, except for the silver nitrate ($AgNO_3$) (0.85 g; 5.0 mmol) used as an oxidant instead of the APS (França et al., 2017). For PPy-Ag, the same procedure for PPy-Ag-OMt was used except for the OMt absence. All samples were isolated by vacuum filtration using 0.22 μm hydrophilic PVDF membranes, washed several times with ultrapure water, and dried in a desiccator containing P_2O_5.

Preparation of NBR/PPy Composites

Conductive rubber containing PPy composites in a proportion of 5, 10, and 15 wt.% were mechanically mixed in a Haake Torque Rheometer mixer chamber with roller rotors. First, NBR was kept in the chamber for 2 min for mastication process, followed by the addition of the PPy composites at 150°C and 70 rpm for an additional 4 min, totaling 6 min of mixing. Secondly, at 100°C and 50 rpm, the vulcanizing agents were added in sequence: 5 wt.% of ZnO, 3 wt.% of stearic acid, 2 wt.% of sulfur, and 1 wt.% of MBT. Then, the material was passed under a roll mill and pressed under 6 tons in a hot press at 160°C for 10 min to complete the curing reaction.

Characterization

The fracture morphology images of the NBR/PPy composites containing 10 wt.% were taken in a field emission scanning electron microscope SEM-FEG JEOL (model JSM6701F) at 500× and 5,000× magnification using BS and SE detectors. Stress–strain behavior was performed according to DIN53504 Standard (DIN 53504, Germany, 1975) in a universal testing machine EMIC DL 2000 with a speed of 200 mm min^{-1}. The compression sensitivity test was conducted according to the method developed by Souza et al. (2005). The test was performed using a Keithley electrometer 6517A connected to the sample compartment and coupled to an Instron machine (Model 5569) using 10 cycles. The parameters of the experiment were as follows: a maximum force of 10,000 N, a test speed of 2 mm s^{-1}, and a maximum pressure of 62.70 MPa.

In order to better understand the cross-linking behavior of the elastomers, the soluble fraction (SF) and gel fraction (GF) were determined. Samples were soaked in methylethylketone (MEK) for 8 days. The difference between the swelled and dried samples was used to determine the SF and GF.

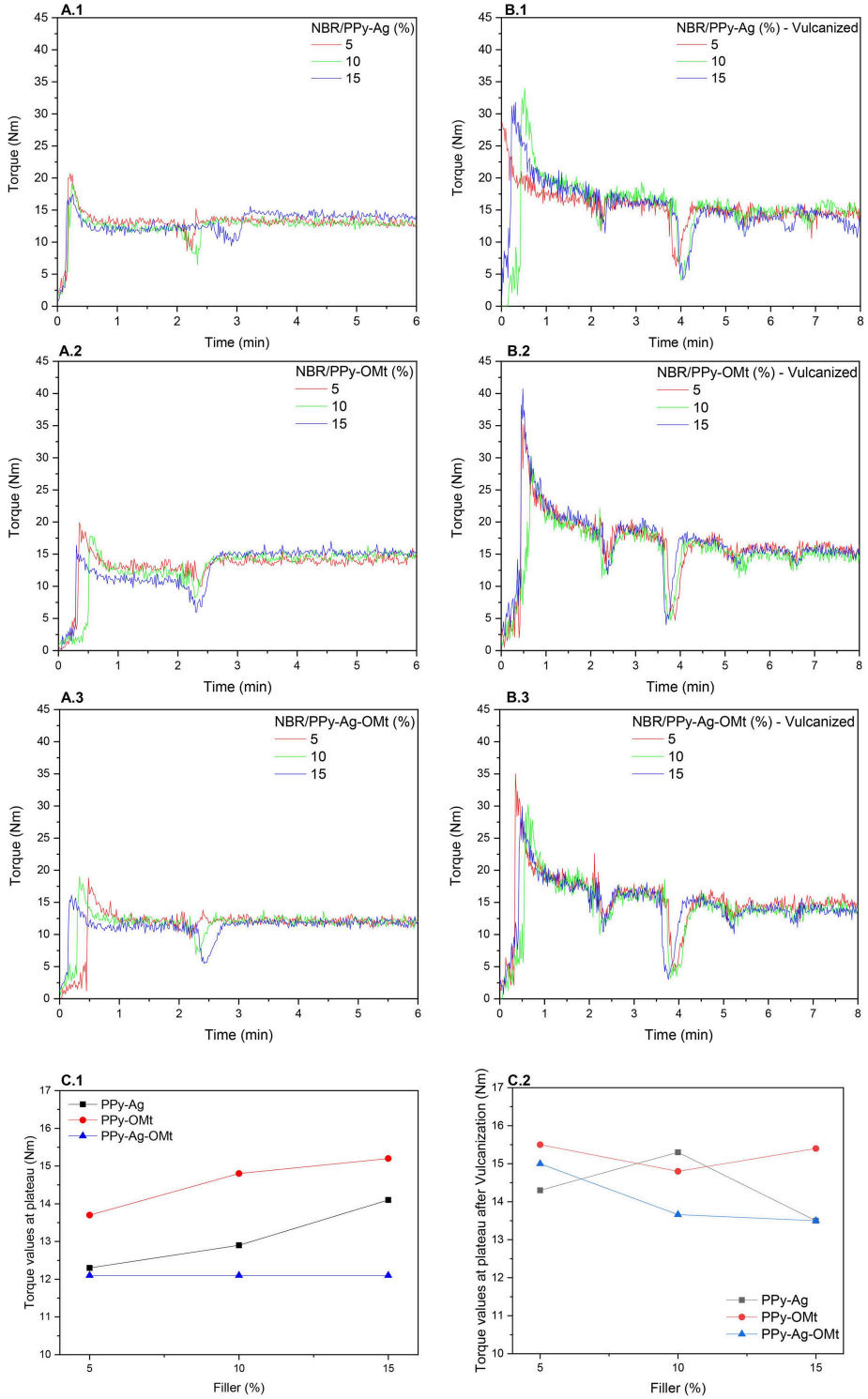

FIGURE 1 | Torque curves of NBR/PPy composites. **(A.1–A.3)** Components mixing curves; **(B.1–B.3)** NBR/PPy composites combined with the vulcanizing system; and **(C.1,C.2)** torque values at the plateau vs. PPy composite loadings.

RESULTS AND DISCUSSION

Figure 1 shows the torque curves of the NBR/PPy composite mixing (**Figure 1A**), NBR/PPy composites combined with the vulcanizing system (**Figure 1B**), and torque values at the plateau vs. PPy composite loadings (**Figure 1C**). From torque curves, we can follow the mixing behavior of the components of the mixture independent of the PPy composite types. At the beginning of

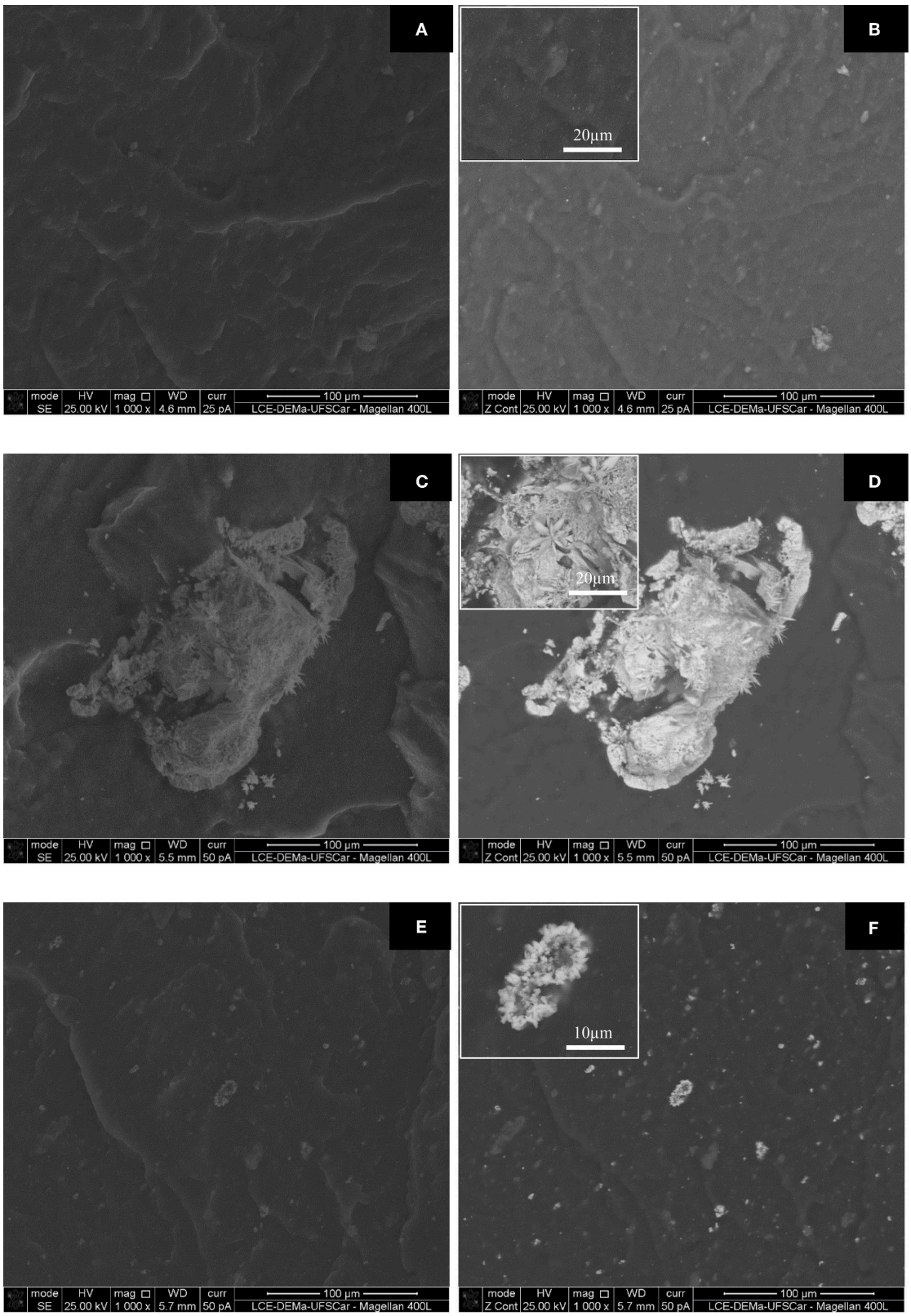

FIGURE 2 | SEM fracture morphology of NBR with 10 wt.% of **(A,B)** PPy-OMt, **(C,D)** PPy-Ag, and **(E,F)** PPy-Ag-OMt. **(A,C,E)** are images of secondary electrons and **(B,D,F)** are images of backscattered electrons.

the mixture, the increase of the torque (∼30 s) is assigned to the NBR addition in the chamber followed by a torque decrease due to the mastication process. After 2 min, a torque decrease shown as a peak is attributed to the chamber opening to add PPy composites, and the mixing process continued until reaching a plateau (6 min). The torque curves of the NBR/PPy composites during the insertion of the vulcanizing system (**Figure 1B**) shows four peaks at ∼30, 60, 150, 300, and 390 s assigned, respectively, to the addition of the ZnO, stearic acid, sulfur, and MBT. After the whole vulcanizing system was inserted, the process continued for 90 s to guarantee that no reticulation reaction started to occur inside the mixing chamber. The reticulation only occurred during the molding at 160°C in the hot press (6 tons for 10 min). **Figures 1C.1, C.2** compare the torque values at the plateau for the different PPy composites before and after vulcanization, respectively. The sequence of torque values, independently of the filler amount, is NBR/PPy-OMt > NBR/PPy-Ag > NBR/PPy-Ag-OMt. Higher torque values at the plateau represent a harder mixture and imply better interaction among the components, mainly the aggregation of the filler into the matrix. Also, we observe the influence of the amount of filler for PPy-OMt, which corroborated the hypothesis of better interaction of the filler with NBR (Thomas and Maria, 2017). PPy-Ag shows intermediate performance with a slight increase for superior filler loading; PPy-Ag-OMt displays no influence of the filler amount. Besides, no significant differences of the torque values at the plateau for composites after the addition of vulcanizing system were observed (**Figure 1C.2**).

Figure 2 shows the fracture morphology of the NBR/PPy-OMt, NBR/PPy-Ag, and NBR/PPy-Ag-OMt, all of them with 10 wt.% of PPy composite. A backscattered electron (BSE) detector (**Figures 2B,D,F**) was used in order to show the difference in contrast over the SEM images. Brighter BSE images are shown for material prepared with an element with a high atomic number. In this way, the dispersity of nanosilver particles can be identified as well as the inorganic material dispersed

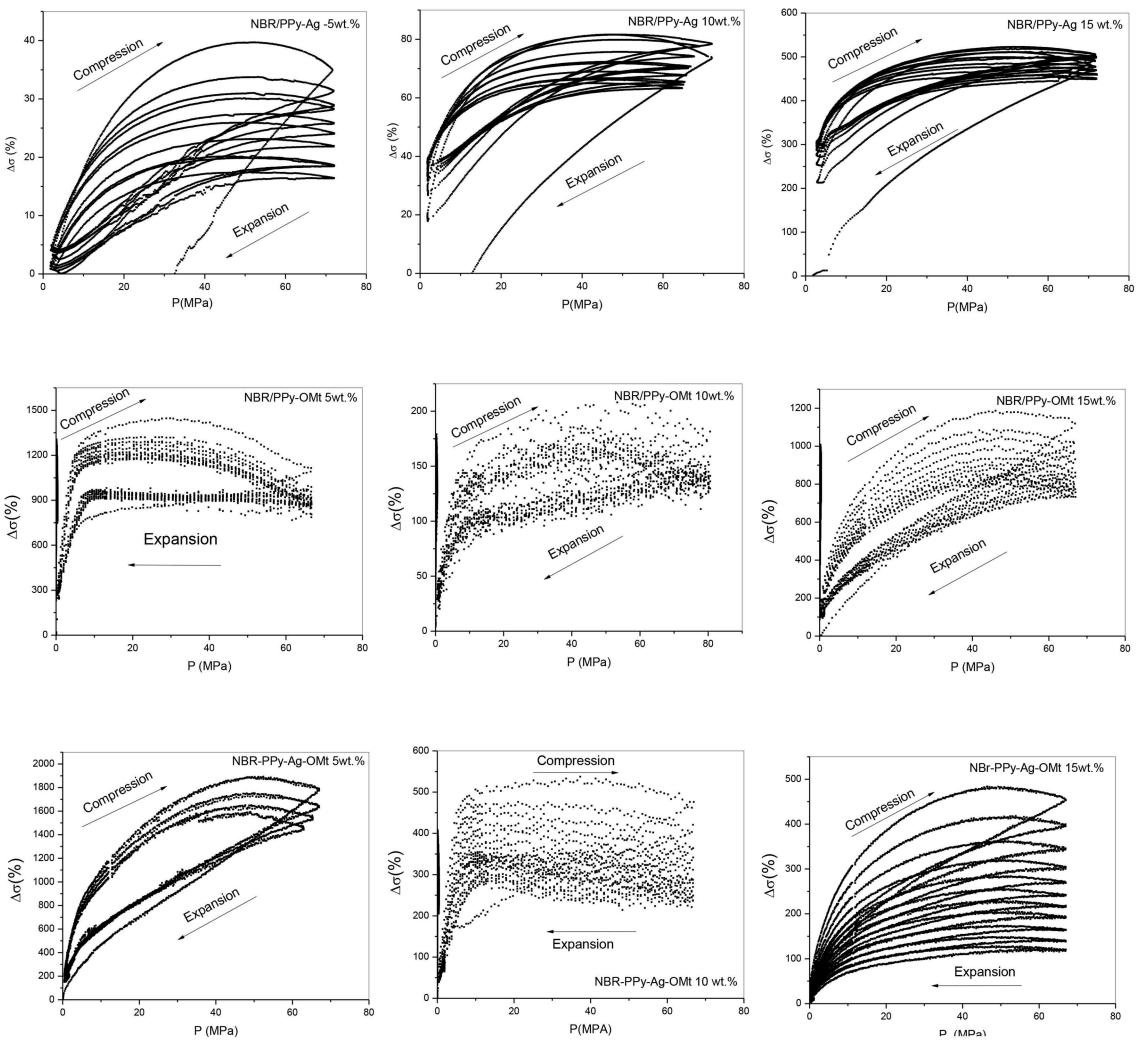

FIGURE 3 | Compression–expansion curves of NBR-PPy-Ag, NBR-PPy-OMt, and NBR-PPy-Ag-OMt.

TABLE 1 | Electrical conductivity, elastic modulus, maximum stress, maximum strain, and gel fraction of NBR/PPy-OMt, NBR/PPy-Ag, and NBR/PPy-Ag-OMt conductive rubbers.

Sample (wt.%)		Conductivity $\times 10^{-6}$ (S cm^{-1})	Elastic module [E(MPa)]	Tension at break [σ(MPa)]	Deformation at rupture [ε (%)]	GF (%)
NBR pure		—	1.8 ± 0.20	4.60 ± 0.40	443 ± 42	92
NBR/PPy-OMt	5	0.040 ± 0.022	2.50 ± 0.08	5.54 ± 0.73	412 ± 13	98
	10	0.50 ± 0.32	2.82 ± 0.35	7.22 ± 1.06	430 ± 50	97
	15	6.60 ± 0.88	3.65 ± 0.53	9.39 ± 0.75	453 ± 50	96
NBR/PPy-Ag	5	10.00 ± 1.50	2.32 ± 0.19	5.35 ± 1.19	425 ± 63	92
	10	14.30 ± 1.60	1.81 ± 0.80	4.85 ± 0.67	457 ± 67	86
	15	33.00 ± 2.30	2.38 ± 0.62	3.52 ± 1.42	607 ± 126	86
NBR/PPy-Ag-OMt	5	1.30 ± 0.65	1.83 ± 0.16	5.04 ± 0.52	431 ± 56	97
	10	7.70 ± 2.80	2.47 ± 0.25	4.86 ± 0.77	450 ± 55	95
	15	12.50 ± 2.60	1.51 ± 0.43	6.03 ± 0.44	791 ± 175	89

TABLE 2 | Electromechanical properties.

Sample-wt.%	Δσ (%) @ Pmax/2 (%)	S_{Comp} (%/Mpa) @ Pmax/2	Hysteresis (%) @ Pmax/2
NBR/PPyAg-5	20.0 ± 2.9	0.6 ± 0.1	13.0 ± 2.7
NBR/PPyAg-10	71.9 ± 5.8	2.1 ± 0.2	8.9 ± 6.6
NBR/PPyAg-15	484.8 ± 20.5	13.9 ± 0.6	45.9 ± 9.8
NBR/PPyOMt-5	1,252.6 ± 81.9	35.8 ± 2.3	342.1 ± 68.3
NBR/PPyOMt-10	173.7 ± 14.5	5.0 ± 0.4	60.9 ± 6.4
NBR/PPyOMt-15	983.5 ± 96.9	28.1 ± 2.8	254.3 ± 53.2
NBR/PPyAgOMt-5	1,621.8 ± 91.7	46.3 ± 2.6	559.6 ± 56.1
NBR/PPyAgOMt-10	419.9 ± 55.8	12.0 ± 1.6	155.4 ± 33.0
NBR/PPyAgOMt-15	321.0 ± 72.5	9.2 ± 2.1	170.6 ± 33.2

on the elastomeric matrix. Inserted images at **Figures 2B,D,F** are at high magnifications to show the morphology of the particles into de NBR. Conductive rubbers with 5 and 15 wt.% of PPy composite displayed similar morphology and are not shown here. We observe a high dispersity and homogeneity of PPy-OMt particles into an NBR with a smooth surface. The morphology reflected the torque results since the homogeneous morphology aspect is related to a good interparticle interaction among components (**Figures 2A,B**). The morphologies of NBR/PPy-Ag and NBR/PPy-Ag-OMt (**Figures 2C–F**, respectively) were analyzed as a function of the presence of Ag nanoparticles and OMt. We also observe higher homogeneity but small clusters dispersed in the matrix. According to the BSE images (**Figures 2D,F**) we assigned the white images to the Ag in which the particles are clumped in the pointed stars shape. This morphology is quite interesting since the agglomerations improve the performance of the material during the compression-expanded cycles due to the particle–particle contact (**Figure 3**; Souza et al., 2005; Thomas and Maria, 2017). It is interesting to note the decrease of the particle size and also the improvement of the dispersion and homogeneity of the particle into the NBR rubber matrix comparing PPy-Ag and PPy-Ag-OMt composites.

Table 1 shows the electrical conductivity and mechanical properties of the NBR composites. The electrical conductivity values are in the order of 10^{-6} to 10^{-8} S cm^{-1}, which characterizes semiconducting material. The sequence of the conductivity of the material is due to the presence of the nanosilver, i.e., NBR/PPy-OMt < NBR/PPy-Ag-OMt < NBR/PPy-Ag. This behavior is in accordance with the value of neat particle conductivity (França et al., 2017) and the contact between the dispersed particles in the NBR matrix. Mechanical properties depicted as elastic modulus, tension, and deformation at break show discrepant values according to the amount and type of the conducting particles. Elastic modulus represents the rigidity or stiffness of a material. Compared to the neat NBR, we observed higher elastic modulus for composites, corroborating the reinforcing effect of the filler on the elastomeric matrix. NBR/PPy-OMt show higher values and increase with the filler content. However, in NBR/PPy-Ag and NBR/PPy-Ag-OMt, besides the lower values, no linearity is observed according to the filler amount. This behavior is assigned to the GF values. GF measures the degree of the reticulation of the material, and lower values are due to the solubilization of the elastomer not cross-linked. Since the reticulation is lower, the module also decreases. The tensile strength at break is higher for PPy-OMt, but Ag particles decrease the strength. This behavior can be assigned to the agglomeration of the particles that generate points of fragility in the material. Both properties, module and strength, corroborate with the largest deformation of PPy-Ag and PPy-Ag-OMt composites.

Figure 3 shows the expansion–compression cycles and **Table 2** shows the electromechanical properties of NBR/PPy-Ag, NBR/PPy-OMt, and NBR/PPy-Ag-OMt. In order to correlate the data sets supplied by the Instron machine and the electrometer, a method was followed as summarized: The percentage variation of the sample conductivity ($\Delta\sigma$) is calculated in accordance with Equation (1).

$$\Delta\sigma = \frac{100x(R^{-1} - R_0^{-1})}{R_0^{-1}} \quad (1)$$

Experimental data obtained during compression (loading) and expansion (unloading) are treated separately. The average hysteresis ($\bar{h}$) is calculated in accordance with Equation (2).

$$\overline{h} = \sum_{j=1}^{n} \frac{(\Delta\sigma_{c(j)} - \Delta\sigma_{d(j)})}{n} \quad (2)$$

where n is the number of compression and expansion cycles and $\Delta\sigma_{c(j)}$ and $\Delta\sigma_{d(j)}$ represent the percentage variation of the sample conductivity obtained during the jth compression and expansion cycles, respectively. $\Delta\sigma_{c(j)}$ and $\Delta\sigma_{d(j)}$ are taken at the half of the maximum applied pressure. The compression sensitivity (*Scomp*) can be defined as shown in Equation (3).

$$\text{Scomp} = \left(\frac{\Delta\sigma}{\Delta P}\right) \quad (3)$$

and can be computed for each data pair ($\Delta\sigma$ vs. P) during compression and expansion cycles. Finally, the average *Scomp* can be calculated as shown in Equation (4).

$$\overline{\text{Scomp}} = \sum_{j=1}^{n} \frac{\left(\Delta\sigma_{(j)} P_{(j)}\right)}{n} \quad (4)$$

For NBR/PPy-Ag materials, as PPy-Ag content is increased, the higher is the compression sensitivity. By increasing content, the contact between the particles is improved, and as these particles are large in size and the dispersity is lower (as observed in SEM images), a higher concentration is necessary to have contact and, consequently, conductivity. The linearity was not observed for NBR/PPy-OMt and NBR/PPy-Ag-OMt. Both material composites with 5 wt.% PPy-OMt or PPy-Ag-OMt showed higher Scomp (35.8 and 46.3%/MPa, respectively), besides higher hysteresis. However, comparing the relative percentage of Scomp/hysteresis values of 10.5% and 8.5%, it is found that NBR/PPy-Ag-OMt (5 wt.%) is the best material in terms of absolute value of Scomp and Scomp/hysteresis ratio. In spite of the different formulations displayed and the best performance on the evaluated criteria (highest absolute conductivity, the highest percentage change in conductivity, lowest hysteresis, and lack of sample disruption), we can suggest that a lower amount of conducting particles benefits the reticulation process (as observed by the GF values). Also, considering the 16 vol.% general concentration of particles to achieve the percolation threshold, the materials we prepared are below this value and can contribute to particle contact during expansion–compression cycles (Schueler et al., 1997). Besides, the clay improved the dispersion of the particles in the NBR, which helps to decrease the necessary amount of filler to the performance of the material. The properties of the conductive rubbers can be influenced by the amount of filler used, in the way it interacts with the matrix and with the other filler particles. Song (2017) compared micro- and nanofillers used as reinforcement and emphasized how organic modifications, coupling agents, and better dispersion control techniques influence the interaction between the rubber matrix and the fillers as we observed in our work.

CONCLUSION

Conductive rubber based on NBR added with PPy composites has shown interesting properties to be applied in the pressure sensor. Among the samples, NBR/PPy-Ag 15 wt.% was highlighted because of the highest volume conductivity and lower hysteresis attained. On the other hand, the NBR/PPy-Ag-OMt 5% proved to be the best material in terms of absolute value of Scomp and the Scomp/hysteresis ratio. These results were related to morphological aspects, where the particles are shown to be dispersed, and the amount and the type of filler played an important role to the connected–disconnected system between particles that could happen during the compression–expansion cycles.

DATA AVAILABILITY

All datasets generated for this study are included in the manuscript and/or the supplementary files.

AUTHOR CONTRIBUTIONS

DF and AR performed the materials preparation and the structural, morphological, stress-strain, and conductivities measurements. RF was involved in planning and supervised the work. FC was involved in planning and PPy-Ag synthesis. FS performed the pressure sensibility measurements. RF and FS interpreted the pressure sensibility results. DF and RF processed the experimental data, performed the analysis, drafted the manuscript, and designed the figures. All authors discussed the results and commented on the manuscript.

ACKNOWLEDGMENTS

Thanks to FAPESP (07/50742-2, 08/57706-4, and 11/23742-7) for financial support. RF and FC are CNPq researchers.

REFERENCES

Ali, M. H., and Abo-Hashem, A. (1997). The percolation concept and the electrical conductivity of carbon black-polymer composites. 3. Crystalline chloroprene rubber mixed with FEF carbon black. *J. Mater. Process. Tech.* 68, 168–171. doi: 10.1016/S0924-0136(96)00023-4

Baldissera, A. F., and Ferreira, C. A. (2017). "Clay-based conducting polymer nanocomposites," in *Conducting Polymer Hybrids*, eds V. Kumar, S. Kalia, and H. C. Swart (Cham: Springer International Publishing), 143–163.

Bing, G., Lan, Q., and Biao, W. (2010). Study on pressure and temperature characteristics of sensitive rubber composite. *Adv. Mat. Res.* 143–144, 134–138. doi: 10.4028/www.scientific.net/amr.143-144.134

Cho, M. S., Choi, H. J., and To, K. (1998). Effect of ionic pendent groups on a polyaniline-based electrorheological fluid. *Macromol. Rapid Commun.* 19, 271–273. doi: 10.1002/marc.1998.030190601

Das, N. C., Chaki, T. K., and Khastgir, D. (2002). Effect of axial stretching on electrical resistivity of short carbon fibre and carbon black filled conductive rubber composites. *Polym. Int.* 51, 156–163. doi: 10.1002/pi.811

Fontana, J. P., Camilo, F. F., Bizeto, M. A., and Faez, R. (2013). Evaluation of the role of an ionic liquid as organophilization agent into montmorillonite for NBR rubber nanocomposite production. *Appl. Clay Sci.* 83–84, 203–209. doi: 10.1016/j.clay.2013.09.002

França, D., Rebessi, A. C., Rubinger, C. P. L., Ribeiro, G. M., Camilo, F. F., and Faez, R. (2017). Structural and conductivity relationship of binary and ternary composites of polypyrrole, montmorillonite and silver. *J. Nanosci. Nanotechnol.* 17, 9203–9210. doi: 10.1166/jnn.2017.14302

Hussain, M., Choa, Y.-H., and Niihara, K. (2001). Fabrication process and electrical behavior of novel pressure-sensitive composites. *Compos. Part A: Appl. Sci. Manuf.* 32, 1689–1696. doi: 10.1016/S1359-835X(01)00035-5

Jlassi, K., Singh, A., Aswal, D. K., Losno, R., Benna-Zayani, M., and Chehimi, M. M. (2013). Novel, ternary clay/polypyrrole/silver hybrid materials through *in situ* photopolymerization. *Colloids Surf. Physicochem. Eng. Asp.* 439, 193–199. doi: 10.1016/j.colsurfa.2013.04.005

Job, A. E., Oliveira, F. A., Alves, N., Giacometti, J. A., and Mattoso, L. H. C. (2003). Conductive composites of natural rubber and carbon black for pressure sensors. *Synth. Met.* 135–136, 99–100. doi: 10.1016/S0379-6779(02)00866-4

Knite, M., Teteris, V., Kiploka, A., and Kaupuzs, J. (2004). Polyisoprene-carbon black nanocomposites as tensile strain and pressure sensor materials. *Sens. Actuators Phys.* 110, 142–149. doi: 10.1016/j.sna.2003.08.006

Mattoso, L. H. C. (1996). Polianilinas: síntese, estrutura e propriedades. *Quím. Nova* 19, 388–399.

Mravčáková, M., Boukerma, K., Omastová, M., and Chehimi, M. M. (2006). Montmorillonite/polypyrrole nanocomposites. The effect of organic modification of clay on the chemical and electrical properties. *Mater. Sci. Eng. C* 26, 306–313. doi: 10.1016/j.msec.2005.10.044

Prudêncio, L., Camilo, F. F., and Faez, R. (2014). Ionic liquids as plasticizers in nitrile rubber/polyaniline blends. *Quím. Nova* 37, 618–623. doi: 10.5935/0100-4042.20140103

Rosa, B. D. S., Merlini, C., Livi, S., and de Oliveira Barra, G. M. (2019). Development of poly(butylene adipate-co-terephthalate) filled with montmorillonite-polypyrrole for pressure sensor applications. *Mat. Res.* 22:e20180541. doi: 10.1590/1980-5373-mr-2018-0541

Schueler, R., Petermann, J., Schulte, K., and Wentzel, H.-P. (1997). Agglomeration and electrical percolation behavior of carbon black dispersed in epoxy resin. *J. Appl. Polym. Sci.* 63, 1741–1746. doi: 10.1002/(sici)1097-4628(19970328)63:13<1741::aid-app5>3.3.co;2-s

Sethi, D., Ram, R., and Khastgir, D. (2018). Analysis of electrical and dynamic mechanical response of conductive elastomeric composites subjected to cyclic deformations and temperature. *Polym. Compos.* 39, 3912–3923. doi: 10.1002/pc.24429

Sombatsompop, N., Intawong, N. T., and Intawong, N. S. (2000). Novel sensing device for pressure measurement in molten polymer systems. *Polym. Test.* 19, 579–589. doi: 10.1016/S0142-9418(99)00028-8

Song, K. (2017). "Micro- and nano-fillers used in the rubber industry," in *Woodhead Publishing Series in Composites Science and Engineering, Progress in Rubber Nanocomposites,* eds S. Thomas and H. J. Maria (Woodhead Publishing), 41–80.

Soto-Oviedo, M. A., Araújo, O. A., Faez, R., Rezende, M. C., and De Paoli, M. A. (2006). Antistatic coating and electromagnetic shielding properties of a hybrid material based on polyaniline/organoclay nanocomposite and EPDM rubber. *Synth. Met.* 156, 1249–1255. doi: 10.1016/j.synthmet.2006.09.003

Souza, F. G. Jr., Michel, R. C., and Soares, B. G. (2005). A methodology for studying the dependence of electrical resistivity with pressure in conducting composites. *Polym. Test.* 24, 998–1004. doi: 10.1016/j.polymertesting.2005.08.001

Swart, H. C., Kumar, V., and Kalia, S. (2017). *Conducting Polymer Hybrids.* Cham: Springer International Publishing.

Thomas, S., and Maria, H. J. (eds.) (2017). *Progress in Rubber Nanocomposites, 3rd Edn*. New York, NY: Elsevier; Oxford University.

Tran, X. T., Park, S. S., Hussain, M., and Kim, H. T. (2018). Electroconductive and catalytic performance of polypyrrole/montmorillonite/silver composites synthesized through *in situ* oxidative polymerization. *J. Appl. Polym. Sci.* 135, 1–10. doi: 10.1002/app.45986

Wei, Y., Li, L., Yang, X., Pan, G., Yan, G., and Yu, X. (2010). One-step UV-induced synthesis of polypyrrole/Ag nanocomposites at the water/ionic liquid interface. *Nanoscale Res. Lett.* 5, 433–437. doi: 10.1007/s11671-009-9501-9

Conflict of Interest Statement: The authors declare that the research was conducted in the absence of any commercial or financial relationships that could be construed as a potential conflict of interest.

Copyright © 2019 França, Rebessi, Camilo, Souza and Faez. This is an open-access article distributed under the terms of the Creative Commons Attribution License (CC BY). The use, distribution or reproduction in other forums is permitted, provided the original author(s) and the copyright owner(s) are credited and that the original publication in this journal is cited, in accordance with accepted academic practice. No use, distribution or reproduction is permitted which does not comply with these terms.

frontiers in Materials

ORIGINAL RESEARCH
published: 27 September 2019
doi: 10.3389/fmats.2019.00234

Influence of Protonic Ionic Liquid on the Dispersion of Carbon Nanotube in PLA/EVA Blends and Blend Compatibilization

Elaine Cristina Lopes Pereira[1]*, *Maria Eduarda C. Fernandes da Silva*[1], *Ketly Pontes*[2] and *Bluma Guenther Soares*[1,2]*

[1] Centro de Tecnologia, Instituto de Macromoléculas, Universidade Federal Do Rio de Janeiro, Rio de Janeiro, Brazil,
[2] Departamento de Engenharia Metalúrgica e de Materiais, Centro de Tecnologia, Universidade Federal Do Rio de Janeiro, Rio de Janeiro, Brazil

In this work, immiscible poly(lactic acid) (PLA)/poly(ethylene vinyl acetate) (EVA) composites with 1 phr of multi-walled carbon nanotube (CNT) and different concentration of protonic—based imidazolium ionic liquid (mimbSO$_3$H·Cl) were prepared. The protonic ionic liquid (IL) was able to act as dispersing agent for CNT and as compatibilizing agent for the PLA/EVA blend. The multicomponent nanocomposites from the mixture of PLA and EVA containing CNT functionalized with ionic liquid, IL (CNT/ILSO$_3$H) were characterized by mechanical and dynamic–mechanical (DMA) tests, electrical conductivity analyses, differential scanning calorimetry (DSC), X-ray diffraction analysis and rheological measurements, as well as chromatographic gel permeation (GPC), and scanning electron microscopy (SEM). The non-covalent functionalization CNT resulted in composites with outstanding electrical and dielectric properties. The high dispersion of CNT promoted by the IL resulted in the formation of a physical networked structure, which was responsible for the higher electrical conductivity and higher melt viscosity. The crystallization process of PLA phase was improved with the presence of CNT/ILSO$_3$H. The degradation process during the transesterification reaction did not significantly affect the mechanical properties. The present work highlights the dual role of the IL as compatibilizing and dispersing agent and opens new perspectives for developing new conducting systems with low percolation threshold based on the good dispersion of CNT and the confinement of the filler within a phase of a multiphasic polymeric system.

Keywords: poly (lactic acid), ethylene-vinyl acetate copolymer, ionic liquid, carbon nanotube, conducting composite, electric conductivity

OPEN ACCESS

Edited by:
Andrea Dorigato,
University of Trento, Italy

Reviewed by:
Arup R. Bhattacharyya,
Indian Institute of Technology Bombay, India
Luca Fambri,
University of Trento, Italy
Rafael Guntzel Arenhart,
Federal University of Santa Catarina, Brazil

***Correspondence:**
Elaine Cristina Lopes Pereira
nanequimica@gmail.com
Bluma Guenther Soares
bluma@metalmat.ufrj.br

Specialty section:
This article was submitted to Polymeric and Composite Materials, a section of the journal Frontiers in Materials

Received: *16 April 2019*
Accepted: *09 September 2019*
Published: *27 September 2019*

Citation:
Lopes Pereira EC, da Silva MECF, Pontes K and Soares BG (2019) Influence of Protonic Ionic Liquid on the Dispersion of Carbon Nanotube in PLA/EVA Blends and Blend Compatibilization. Front. Mater. 6:234. doi: 10.3389/fmats.2019.00234

INTRODUCTION

Due to the widespread use of plastics in the packaging industry, there is a growing interest in the use of biodegradable polymers as a substitute for conventional polymers to reduce the environmental impact of plastic waste. Poly lactic acid (PLA) is a good example of these materials obtained from renewable resources (Lim et al., 2008; Nampoothiri et al., 2010). Besides being biodegradable and biocompatible, PLA also presents good processability when compared with other biodegradable polymers. However, it is quite rigid and brittle,

presents low moisture resistance and slow crystallization rate, which in turn limit its applications. Therefore, blending PLA with soft materials is a good strategy for overcoming these drawbacks. The appropriate choice of non-biodegradable polymers as component for PLA-based blends should reduce the biodegradation rate, cost and improve some mechanical properties. In these cases, the PLA phase undergoes a gradual degradation process, known as biodisintegration, resulting in very small pieces of the non-biodegradable polymer (Sarasa et al., 2009). A promising partner for blending with PLA is ethylene-vinyl acetate copolymer (EVA) due to its availability, low cost and versatility of applications, as it can present rubber or thermoplastic characteristics by changing the vinyl acetate (VA) content in the copolymer. Several papers have used EVA with different vinyl acetate content for the preparation of PLA/EVA blends for different purposes (Yoon et al., 1999; Li et al., 2011; Moura et al., 2011, 2012; Ma et al., 2012, 2015; Aghjeh et al., 2015, 2016; Sangeetha et al., 2016, 2018; Wang et al., 2016; Zhang and Lu, 2016; Lopes Pereira et al., 2017).

Blending conducting fillers as carbon nanotube (CNT) expands the field of applications of these semi-biodegradable composite as antistatic, dielectric and microwave absorbing materials for utilization in electronic packaging. Most of the studies involving CNT-based PLA/EVA composites focused on the improvement of mechanical properties and toughness of the blends (Shi et al., 2011, 2012; Wang et al., 2015, 2016; Liu et al., 2016). Studies related with the electrical properties of PLA/EVA blends loaded with CNT was reported by Shi et al. (2013). They used a master batch of PLA to prepare PLA/EVA (60:40 wt%) composites with different amounts of CNT. Resistivity values around 10^7 Ω·cm were obtained by adding 1 wt% of CNT. Higher amount of CNT did not affect the resistivity values.

A good distribution/dispersion of CNT within a thermoplastic matrix by melt mixing process is not an easy task due to the strong tendency to filler agglomeration caused by the highly conjugated structure and the Van der Waals interactions of CNT. To improve the dispersion of CNT in a polymer matrix, two strategies have been recently adopted: covalent and non-covalent surface functionalization. Covalent functionalization is based on chemical reactions on the surface of the CNT to introduce functional groups capable of reacting or interacting with the polymer matrix (Spitalsky et al., 2010). This methodology greatly facilitates the dispersion of CNT in polymer matrices, but destroys the π conjugation at the CNT surface, which is essential for good electrical conductivity. Therefore, the non-covalent functionalization is preferred because it does not destroy the conjugation at the CNT surface, besides being environmentally friendly because no chemical reactions with strong acids followed by purification are involved during the procedure. In this context, ionic liquid (IL) proved to be an excellent surface modifier for CNT since it efficiently interacts with the π cloud of the CNT, thus promoting a disaggregation of the CNT bundles and ropes (Fukushima et al., 2003).

Recently, several works in the literature reported the efficiency of the non-covalent functionalization of CNT with ILs to improve the dispersion of the filler within polymeric matrices consisted of epoxy resin (Lopes Pereira and Soares, 2016; Alves et al., 2018; Soares, 2018), thermoplastics (Zhao et al., 2012; Soares da Silva et al., 2017; Fang et al., 2018), elastomers (Subramaniam et al., 2013; Abraham et al., 2017; Hassouneh et al., 2017), as well as heterogeneous polymer blends (Bose et al., 2008; Soares et al., 2018; Lopes Pereira et al., 2019). Usually the presence of IL significantly increases the conductivity of the system.

Based on the importance of the theme for the electro-electronic, automobile and packaging industries, the aim of the present study is to investigate the efficiency of the protonic IL based on imidazolium cation as a dispersing agent for CNT in PLA/EVA blends and how the IL-CNT combination should affect the compatibility, morphology, electrical conductivity, mechanical and rheological properties. This protonic IL was recently reported as compatibilizing agent for PLA/EVA blends through a transesterification process (Lopes Pereira et al., 2017). To the best of our knowledge, no studies involving the functionalization of CNT with protonic IL and its use in polymer blends have been reported in the accessible literature. For this study, EVA containing 19 wt% of vinyl acetate (VA) was employed due to its great availability. PLA/EVA18 blend composition corresponding to 60:40 wt% was chosen for this study in order to increase the toughness of PLA while maintaining the biodegradability of the PLA matrix.

EXPERIMENTAL SECTION

Materials

Multiwalled CNT (pristine CNT–pCNT) (NC7000) was supplied by Nanocyl (Sambreville, Belgium) (average diameter = 59.5 nm; average length = 51.5 mm; surface area = 5,250–300 m^2/g). Ethylene vinyl acetate (EVA) copolymer with melt flow index = 2.5 g/10 min at 190°C/2.16 kg; vinyl acetate content = 19 wt%; density = 0.95 g/cm^3; melting temperature, Tm = 90°C and glass transition temperature, Tg = −14°C (Yamaki et al., 2002) was purchased from Braskem (São Paulo, Brazil). Poly (lactic acid) (PLA) designed for injection molding applications (trade name Ingeo™ Biopolymer 3251D; Mn = 80,000–90,000 $g{\cdot}mol^{-1}$; D isomer content = 4%; melt flow index = 35 g/10 min at 190°C/2.16 kg; density = 1.24 g/cm^3; glass transition temperature, Tg = 55–60°C; Tm = 155–170°C) was purchased by Nature Works LLC. N-methyl-imidazole and 1,4-butane sultone used for the synthesis of the protonic IL were supplied by Sigma-Aldrich.

Preparation of Sulfonic Acid–Based Ionic Liquid

The 1-methyl-imidazolium-3-butylsulfonic acid chloride [mimbSO_3H·Cl] ionic liquid was synthesized by reacting N-methyl-imidazole and butane-sultone, followed by a treatment with hydrochloric acid, according to the literature (Lopes Pereira et al., 2017). The structure of the ionic liquid, mimbSO_3H·Cl, is illustrated in **Figure 1** (yield = 75–85%; melting point = −59°C) and was confirmed by ^{1}H NMR spectrum (300 MHz, CDCl3) δ 1.85 (t, 2H), 2.17 (t, 2H), 3.05 (t, 2H), 4.05 (s, 3H), 4.4 (t,2H), 7.6 (d, 2H), 8.82 (s, 1H).

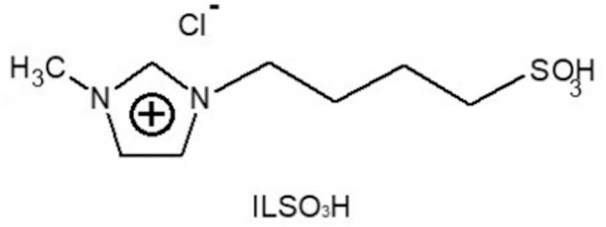

FIGURE 1 | Structure of the ionic liquid 1-methyl-imidazolium-3-butylsulfonic acid chloride [mimbSO$_3$H·Cl].

SAMPLE PREPARATION

The blend composition was fixed as PLA/EVA = 60:40 wt% to improve toughness while maintaining the biodegradability of the PLA. The polymers were first vacuum-dried overnight at 60°C before blending to eliminate water that should affect the processing and properties. Then, PLA and EVA were dry blended and introduced into the chamber of a Brabender plastograph equipped with a W50 EHT internal mixer (volume of 55 cm^3) and roller rotors at a temperature of 180°C and a rotating speed of 60 rpm. The total mixing time was 5 min. This time was enough to achieve the stable torque while decreasing the chance for the polymer degradation. For CNT modified with the IL mimbSO$_3$H·Cl (CNT/ILSO$_3$H), the pristine CNT (pCNT) was previously dispersed with IL in a proportion CNT/ILSO$_3$H = 1:2.5 and 1:5 wt/wt by grinding both components in a mortar for about 15 min. After that, the resulting CNT/ILSO$_3$H was blended with PLA and EVA using similar mixing protocol.

Before molding steps (injection or compression molding), the samples were milled and put in a vacuum oven at 60°C to dry the samples. The samples for mechanical and dynamic-mechanical analysis were injection molded in a Haake miniJet model, using the following parameters: barrel temperature = 180°C; injection pressure = 450 bar; mold temperature = 20°C; holding pressure: 250 bar, injection time: 10 s, holding time: 5 s. The total cycle time corresponded to 15 s. The samples for conductivity and rheological properties were compression-molded into disks of 20 mm diameter and 1 mm thickness in a hydraulic press at 180°C and pressure around 7 MPa for 3 min, followed by a cooling process at the same pressure using another hydraulic press at 20°C for 5 min.

CHARACTERIZATION

The molar mass of the PLA phase in the blends was determined by size exclusion chromatography (SEC) using a Shimadzu GPC, 803 equipped with 20A column (Column Phenomenex linear 300 × 7.8 mm, pore 5 μ) and a refractometer detector RID. Chloroform was used as eluent with a flow rate of 1 mL/min and at 22°C. The calibration curve was previously obtained with polystyrene standards in the range of 510–1,390,000 g/mol. For the SEC analysis, the PLA phase was extracted with chloroform, as follows: 2 g of the blend was stirred with 20 mL of chloroform during 48 h to extracted the PLA phase. Then, the solution was filtered and casting into Petri dish to evaporate the solvent at room temperature.

The rheological measurements were performed in a Discovery HR1 Hybrid rheometer from TA Instrument Inc., at 170°C, using parallel plate geometry (25 mm) with a distance of 1.0 mm between the plates. The measurements were performed in an oscillatory mode at a strain range from 0.1 to 100% under constant frequency of 1 Hz, which is within the linear viscoelastic regime. The testing temperature was fixed at 170°C to avoid excessive flow of the material out of the geometry and keep the fixed gap, since PLA used in this work has a high MFI and the testing cannot be performed at higher temperatures. This temperature was also employed in other studies involving PLA/EVA blends (Shi et al., 2013; Wang et al., 2016).

X-ray diffraction (XRD) measurements were performed on a Rigaku Ultima IV X-ray diffractometer (Cu Kα irradiation, 40 kV, 20 mA), in the range of 2θ from 1 to 40°.

Differential scanning calorimetry (DSC) of the blend and composites were performed on DSC Q20 from TA Instruments Inc. in dynamic mode under nitrogen flow of 50 mL·min^{-1}. The samples were submitted to the following protocol: first heating from 20 to 200°C at a rate of 10°C·min^{-1}; cooling up to 20°C at a rate of 10°C·min^{-1} and a second heating scan until 200°C at a rate of 10°C·min^{-1}.

Dynamic mechanical analysis (DMA) measurements were performed using a DMA Q800 TA Instruments at a fixed frequency of 1 Hz, strain of 0.1% and a heating rate of 3°C min^{-1}. The measurements were performed from −65 to 150°C, using single-cantilever clamp and rectangular samples with 17 × 12.7 × 3.2 mm dimensions, obtained by injection molding.

The morphology of the samples was observed through scanning electron microscopy (SEM) on a VEGA III from TESCAN operating at 15 kV. The injected samples were cryogenically fractured in liquid nitrogen and immersed into toluene at 50°C for 4 h to remove the EVA component. Then, the surface was washed with fresh toluene and alcohol with the aid of ultrasonic bath, according to the procedure reported by Bhattacharyya et al. (2005). The samples were dried and coated with gold for SEM examination.

The tensile properties were measured in a MTS Tytron 250 tensile tester at a crosshead speed of 5 mm·min^{-1}. The samples were injection molded into dimensions of the dumbbell-shaped tensile bars, according to the ASTM D-638-5 method.

The dielectric properties, including AC conductivity, were measured with an impedance analyzer Solartron SI 1260 gain phase analyzer equipped with a Solartron 1296 dielectric interface. The measurements were carried out at 25°C from 0.1 to 10^6 Hz with 0.1 V oscillating voltage with electrodes of 25 mm in diameter. The samples with 25 mm in diameter and 1 mm thickness were previously coated with a thin layer of gold in order to improve the contact.

RESULTS AND DISCUSSION

Rheological Behavior

The melt viscosity of the polymer components in a blend and the presence of filler exert strong influence on the rheological

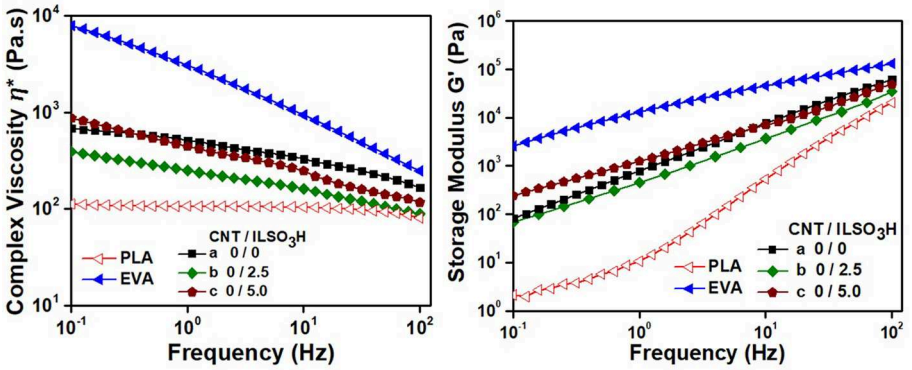

FIGURE 2 | Rheological parameters of PLA, EVA, and PLA/EVA blends loaded with CNT/$ILSO_3H$ in a proportion corresponding to (a) 0:0; (b) 0:2.5; and (c) 0:5.0 phr.

parameters and morphology of the final product. Therefore, it is important to investigate the effect of CNT and CNT/$ILSO_3H$ on the rheological parameters of the PLA/EVA blends. **Figures 2**, **3** illustrate the complex viscosity, η*, and storage modulus, G′, vs. frequency for the composites containing different proportions of IL or CNT/$ILSO_3H$, respectively. The rheological parameters of the pure components were also included for comparison. The η* and G′ values of PLA were significantly lower than those corresponding to the EVA component, mainly in the low frequency range. PLA also presented a Newtonian behavior at frequencies up to around 20 Hz, whereas EVA displayed a typical pseudo-plastic characteristic, with a significant decrease of η* as increasing the frequency. PLA grade with lower viscosity than EVA was chosen for this study to make easier the processability of the composites as the addition of CNT usually increases the melt viscosity of the system. Moreover, the lower viscosity of PLA associated with the higher proportion of this component ensures that this biodegradable polymer constitutes the matrix, which is interesting for biodegradability purpose.

The neat blend presented intermediary η* and G′ values and a less pseudo-plastic characteristic. The η* of the blend was lower than that reported by Li, et al. for PLA/EVA blends with PLA grade of higher molar mass, due to the lower molar mass of the PLA used in the present system (Li et al., 2011).

The presence of 2.5 phr of IL resulted in a decrease of η* and a slight decrease of G′, due to a plasticizing effect of the IL, a low molar compound. This plasticizing effect was also observed in the literature for other thermoplastic containing IL (Scott et al., 2002, 2003). However, an opposite effect was observed when the IL content was increased to 5 phr, that is, both η* and G′ increased when compared to the neat PLA/EVA blend. Moreover, a more pronounced pseudo-plastic behavior was observed for this mixture. This phenomenon may be related to the formation of graft copolymers between PLA and EVA through the transesterification reaction between the ester groups of both components promoted by IL that acts as a catalyst, as discussed in previous paper (Lopes Pereira et al., 2017). These reactions contribute for the compatibilization between the blend components. As the η* of EVA component is significantly higher than that of PLA, the EVA chemically attached to the PLA chains contributed for an increase of η* and G′, in spite of the presence of higher amount of IL, which usually acts as plasticizing. Also the interaction between IL and the blend component should contribute for an increase in viscosity, as stated by other authors (Yousfi et al., 2014).

The rheological parameters of the composites containing CNT modified with different amounts of IL are illustrated in **Figure 3**. The addition of 1 phr of CNT resulted in a significant increase of η* and G′ in the low frequency range. Moreover, the G′ vs. frequency slope at low frequencies decreased significantly. These features indicate that the CNT dispersed within the PLA/EVA matrix started to present a certain degree of interconnectivity, thus forming a physical networked structure. This characteristic was more pronounced for the composite loaded with CNT/$ILSO_3H$ in a proportion corresponding to 1:5. In this case, a more accentuated shear-thinning effect in the profile of the η* vs. frequency curve, as well as a higher G′ value at lower frequency range and a low G′ vs. frequency slope in the low frequency range were observed. All these features indicate that non-covalently functionalized CNT with the IL is more dispersed within the polymeric matrix, thus forming a more effective networked structure, which also was responsible for the higher electrical conductivity, as it will be discussed in the next sections. The IL at the surface of the CNT can favor the debundling of the aggregated hopes and bundles of CNT. This phenomenon was not so evident when lower amount of IL was employed. In fact, the composite containing CNT/$ILSO_3H$ (1:2.5) presented lower viscosity and G′ values than the composite containing only CNT, confirming the plasticizing/lubricating effect of this IL. The increase of melt viscosity with the addition of 1 wt% of CNT non-covalently functionalized with IL was also reported in our previous studies involving PP/PA12 blends (Lopes Pereira et al., 2019) or PP/PLA blends (Soares et al., 2019).

Morphology

Figure 4 illustrates the SEM micrographs of PLA/EVA (60:40 wt%) blend and the corresponding composites containing 1 phr of pristine CNT (pCNT) or CNT modified with IL (CNT/$ILSO_3H$). The images in the left side correspond to the micrographs obtained from non-etched surface samples and

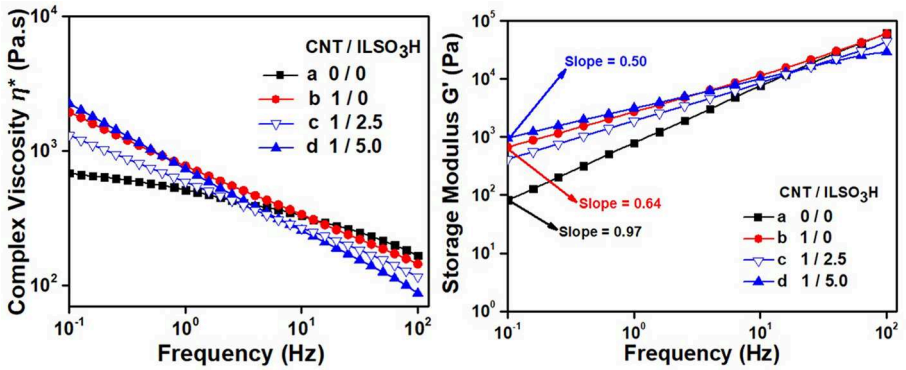

FIGURE 3 | Rheological parameters of PLA/EVA containing CNT/$ILSO_3H$ in a proportion of (a) 0:0; (b) 1:0; (c) 1:2.5; and (d) 1:5 phr.

those presented in the right side are related to the micrographs obtained from the etched surface samples in hot toluene. Then, the holes observed in these micrographs refer to the EVA phase that was removed after the treatment with toluene. The neat blend displayed a typical gross-separated and sea-island morphology with large EVA domains (**Figure 4a**). The extracted surface also presented large and non-homogeneous holes, confirming that the blend is incompatible/immiscible (**Figure 4a′**). The large domains were attributed to the great difference in viscosity between the blend components, being EVA much more viscous than PLA. When the viscosity of the dispersed phase is higher than the matrix, the morphology tends to present large domain size (Huang, 2011). The presence of pCNT exerted some influence on the blend morphology. Both non-extracted (**Figure 4b**) and extracted surface (**Figure 4b′**) displayed EVA domains with smaller size, as it was also observed in other heterogeneous blend loaded with CNT (Liebscher et al., 2013; Soares et al., 2018). The micrograph of the composite loaded with CNT/$ILSO_3H$ (1:5) also presented a more refined morphology. It is difficult to distinguish the EVA domains in the non-extracted surface (**Figure 4c**). However, it is possible to observe the presence of smaller holes formed from the extracted EVA phase (**Figure 4c′**). This behavior indicates that the IL at the CNT surface was able to improve the PLA/EVA compatibilization. The effect of IL on the morphology of the PLA/EVA blend is also presented in **Figures 4d,d′**. This blend also presents sea-island type morphology with relatively large EVA domains. However, the micrograph taken from non-etched surface suggests some kind of interfacial adhesion between matrix and dispersed phase, since the presence of cavities in the interface is not so evident. As discussed in our previous work (Lopes Pereira et al., 2017), the Bronsted acidic ionic liquid acts as catalyst for the transesterification between the ester groups of the EVA and PLA phase, enhancing the anchorage between them.

The changes in morphology of heterogeneous blends with the addition of CNT may be attributed to the increase of the shear forces due to the higher viscosity of the system imparted by the CNT and also some change in the viscosity ratio of the blend components, due to the preferential localization of CNT in one phase. According to thermodynamic calculation of the interfacial tension and wetting coefficient predicted in the literature, CNT presents a tendency to be located in the PLA phase (Shi et al., 2013). In our system, this should be also favored by the lower viscosity of the PLA phase. In order to estimate the localization of CNT, the CNT-loaded composites were submitted to a treatment with dichloromethane, which selectively extracted the PLA phase, and hot toluene, which extracts the EVA phase. After extraction, both chloroform and toluene appeared dark, indicating the presence of CNT in both phases. Although CNT has more affinity for the PLA phase as suggested by Shi et al. (2011) and also due to its lower viscosity, some amount of the filler was also located in EVA phase.

SEC Analysis

It was stated by several researchers in the literature that the transesterification reaction used for the reactive compatibilization of PLA-based blends may also provoke a decrease of the molar mass of the PLA phase due to the random cleavage of the ester groups along the PLA chain (Moura et al., 2012; Lins et al., 2015; Lopes Pereira et al., 2017). The magnitude of this phenomenon depends on the nature of the catalyst used during the reaction process. In our previous study, the use of 1 phr of the protonic ionic liquid, mimbSO_3H·Cl, as the catalyst for the compatibilization of PLA/EVA blend promoted a slight increase of the molar mass of the PLA phase, indicating that the degradation process was minimized by using this catalyst (Lopes Pereira et al., 2017). Therefore, the effect of the IL and CNT in different proportions on the molar mass of the PLA phase was investigated by SEC. **Table 1** summarizes the molar mass of PLA phase after submitting the blends to different treatment: mixing, mixing/injection molding and mixing/compression molding. The PLA extracted from the neat blend displayed significant decrease of the molar mass, when compared to the virgin PLA, indicating degradation process during the melt blending, as also observed in our previous study (Lopes Pereira et al., 2017) and by other authors (Park and Xanthos, 2009). The presence of EVA in the blend minimized the degradation process, since the molar mass of the PLA phase was higher than that of the neat

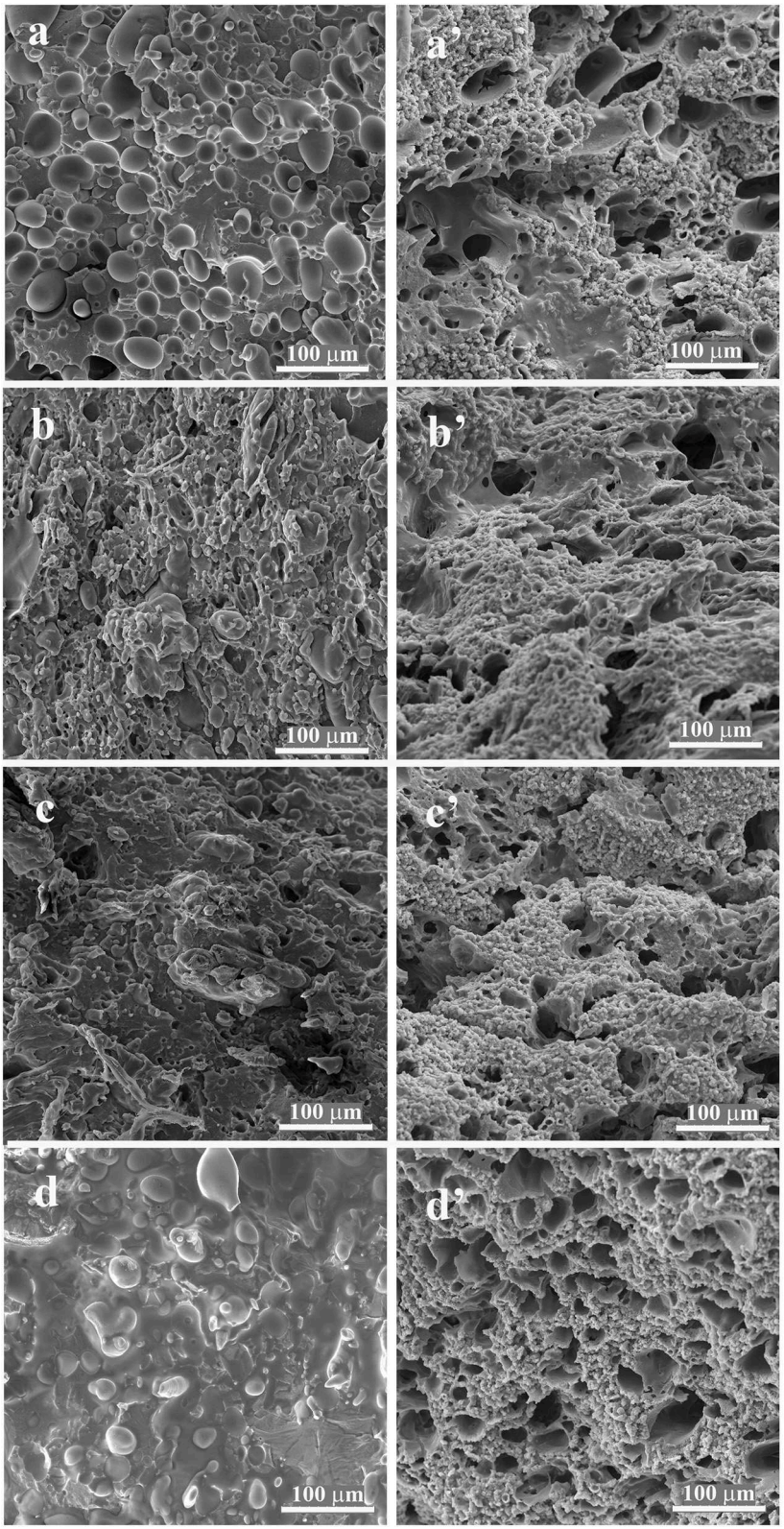

FIGURE 4 | SEM micrographs of non-etched surface of **(a)** PLA/EVA (60:40 wt%) blend and the composites containing **(b)** 1 phr of pCNT, **(c)** 6 phr of CNT/$ILSO_3H$ (1:5), and **(d)** 5 phr of $ILSO_3H$ (6 phr of CNT/$ILSO_3H$ corresponds to 1 phr of CNT in the system); and etched surface of the corresponding blend and composites **(a'-d')**.

TABLE 1 | Molar mass of PLA phase extracted from PLA/EVA (60:40 wt%) blends as a function of the processing conditions.

Filler content (phr)		Molar mass after mixing (Kg/mol)			Molar mass after mixing/injection molding (Kg/mol)			Molar mass after mixing/compression molding (Kg/mol)		
CNT	IL	Mw	Mn	PI	Mw	Mn	PI	Mw	Mn	PI
0[a]	0[a]	66	37	1.8	57	33	1.7	55	33	1.7
0	0	84	44	1.9	66	36	1.9	69	42	1.6
0	2.5	75	44	1.7	63	34	1.8	67	37	1.8
0	5.0	86	41	2.1	71	43	1.7	70	41	1.7
1	0	73	37	1.7	70	40	1.7	54	29	1.9
1	2.5	83	51	1.6	61	35	1.7	56	29	1.9
1	5.0	73	37	1.7	60	30	2.0	51	29	1.7

Unprocessed PLA; Mw = 124 Kg/mol; Mn = 80 Kg/mol; polydispersion index (PDI) = 1.5.

[a]*Values of neat PLA after processing.*

PLA after processing. The addition of the IL (2.5 phr) resulted in a decrease of Mw probably due to a cleavage of PLA chains promoted by the transesterification reaction. Increasing the amount of the IL (5 phr) resulted in a slight increase of Mw and a decrease of Mn. This behavior may be attributed to the transesterification reaction, which may occur between PLA and EVA chains or also between PLA chains. The last event should result in cleavage and combination of PLA chains. The presence of CNT promoted a degradation process of the PLA chains as indicated by a significant decrease of the molar mass. It is interesting to observe that the functionalization of CNT with the IL in a proportion CNT/ILSO_3H = 1:2.5 by mass promoted an increase of the PLA molar mass, when compared to the neat blend and that loaded with 1 phr of pCNT. This behavior suggests that the IL localized at the CNT surface minimized the deleterious degradation action of the CNT and helps on the compatibilization of the blend. Increasing the amount of IL to 5 phr resulted in a decreasing of the molar mass of PLA phase because the chain cleavage by transesterification reaction became more effective. The molding process also contributes for the degradation of PLA. In this context, PLA and the blends after submitting to the injection molding process resulted in additional decrease of MW, which may be explained by the high shear forces during the injection process. The molar mass of the blends without CNT did not present significant variation when submitted to injection or compression molding process. However, those loaded with CNT samples presented lower Mw and Mn values when submitted to compression molding when compared to those of the samples submitted to injection molding. This behavior may be attributed to the exposition of the samples to longer period at high temperature during the compression molding.

Crystallinity Behavior

The effect of CNT and CNT/ILSO_3H on the crystallinity behavior was investigated by X-ray diffraction (XRD) and DSC analysis. **Figure 5** presents the XRD patterns of PLA, EVA and the PLA/EVA blend and composites as a function of the processing parameters. Pure PLA submitted to compression molding process presented a broad amorphous halo over the entire 2θ range, indicating the amorphous nature of this sample. The injection molding induced some crystallinity to PLA, as the amorphous halo appeared together with a diffraction peak at $2\theta = 16.4^{\circ}$. This peak is related to the (200)/(110) plane of α-phase crystal of PLA (Zhang and Zhang, 2016). Pure EVA, both injection or compression molded, also presented an amorphous halo together with two diffraction peaks at $2\theta = 21$ and 23°, corresponding to the diffractions of (110) and (200) planes of EVA phase (Li et al., 2011). All PLA/EVA blend and composites displayed the characteristic diffraction peaks of the EVA component. However, no peak related to the PLA phase was observed, indicating that the PLA phase in the blend was completely amorphous regardless the processing conditions.

Differential scanning calorimetry (DSC) thermograms of PLA, EVA and their composites with EVA obtained during first heating scan and during the cooling process are illustrated in

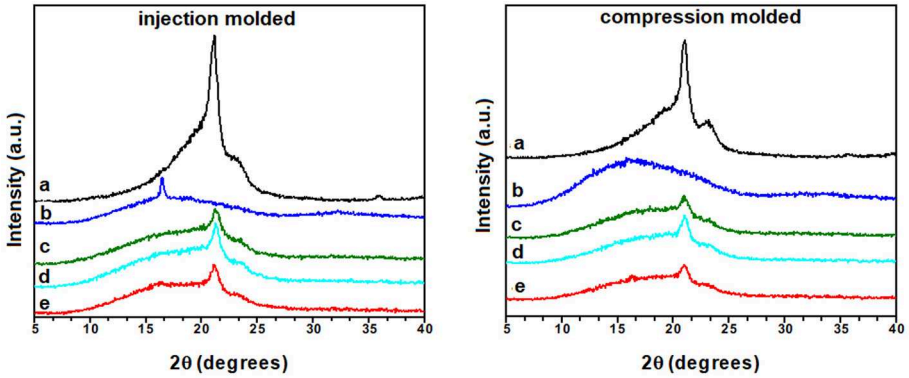

FIGURE 5 | XRD patterns of (a) EVA, (b) PLA, and the PLA/EVA (60:40 wt%) blends loaded with CNT/IL·SO_3H in the proportion of (c) 0:0; (d) 1:0; and (e) 1:5 phr.

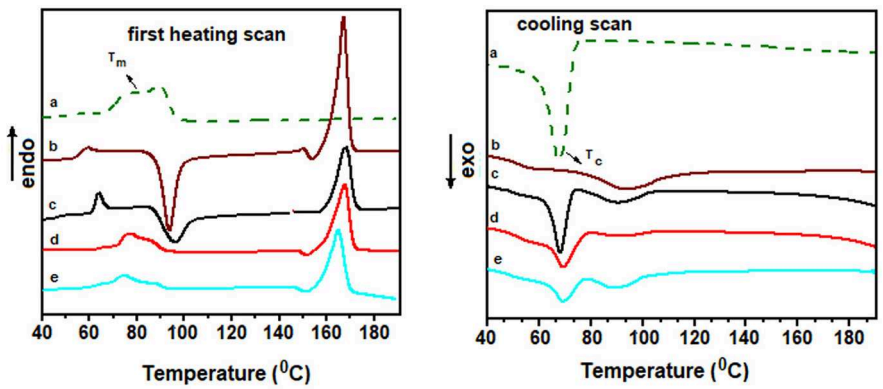

FIGURE 6 | First heating scan and cooling scan curves obtained from DSC thermograms of (a) EVA; (b) PLA; and the PLA/EVA (60:40 wt%) blends loaded with CNT/IL.SO_3H in the proportion of (c) 0:0; (d) 1:0; and (e) 1:5 phr.

Figure 6. The samples were obtained directly from the injection-molded specimens. **Table S1** presented in supplementary section summarizes the main data of the first and second heating scan, as well as, the cooling scan. Also **Figure S1** in the supplementary section illustrates the second heating scan curves. Pure PLA presented an endothermic transition at around 56°C, related to the glass transition temperature (T_g), an exothermic peak at around 94°C due to the cold crystallization temperature (T_{cc}) and an endothermic peak at around 167°C ascribed to the melting temperature (T_m). The prominent T_{cc} peak in the PLA sample is due to the slow crystallization process of PLA during processing. Pure EVA presented two broad endothermic peaks in the range of 76–90°C, which correspond to the T_m. This transition appeared close to the T_{cc} peak related to PLA. Blending with EVA did not exert great influence on the T_m of PLA, but resulted in a slight increase of T_{cc} from 94 to 97°C, suggesting that the EVA affected the crystallization process of PLA, as also found by other authors (Aghjeh et al., 2016; Agrawal et al., 2019). Nevertheless, by adding CNT of CNT/IL to the blend, the T_{cc} peak related to the PLA phase was suppressed, indicating that CNT and the CNT/IL exhibited great nucleating effect for the PLA crystallization, as also stated by other authors (Villmow et al., 2008).

The cooling scan curves presented clear exothermic peak at around 67–69°C, ascribed to the crystallization process of EVA component. The PLA phase displayed broad exothermic peak with very low intensity even for pure PLA sample, indicating slow crystallization process of PLA at this conditions. This feature is responsible for the appearance of the T_{cc} peaks in all blend and composites, during the second scan process (see **Figure S1** in the supplementary section). During the second scan, the presence of EVA did not affect the T_{cc} of PLA phase. However, the addition of CNT in the blend caused a slight increase of T_{cc}. Blend containing CNT/ILSO_3H = 1:5 presented a slight decreased of T_{cc} but a significant decrease of T_m, indicating that the CNT/IL system acts as nucleating agent favoring the crystallization of the PLA phase. This may be attributed to the interaction between IL and the PLA phase, which is increased due to the increase of the interfacial area due to the better CNT dispersion.

Mechanical and Dynamic-Mechanical Properties

Table 2 summarizes the tensile properties of PLA/EVA composites loaded with 1 phr of CNT modified with different IL proportions. The stress-strain curves are also illustrated in

TABLE 2 | Tensile properties of PLA/EVA (60:40 wt%) composites.

Filler content (phr)		Young modulus (MPa)	σ_B (MPa)	ϵ_B (%)
CNT	IL			
0[a]	0[a]	1,390 ± 55	41 ± 2.8	3.4 ± 0.7
0	0	690 ± 40	21 ± 3.0	9.0 ± 2.0
1.0	0	650 ± 30	21 ± 2.1	6.0 ± 0.5
1.0	2.5	660 ± 20	24 ± 3.0	8.0 ± 1.5
1.0	5.0	610 ± 25	21 ± 1.0	5.0 ± 0.3

[a] *Tensile properties of neat PLA; σ_B, tensile strength; ε_B, elongation at break.*

Figure S2 in supplementary section. PLA/EVA blend displayed a decrease of tensile strength and modulus when compared to neat PLA, but an increase of elongation at break (ϵ_B), due to flexible nature of EVA. The addition of pure CNT or that functionalized with IL did not exert significant influence on the tensile strength but decreased elongation at break. Similar behavior was also reported by Wang et al., for systems employing EVA50 and PLA/EVA with a composition of 80:20 (Wang et al., 2016). A slight improvement of ultimate tensile strength was observed when CNT/ILSO$_3$H (1:2.5) was used, probably due to some interfacial adhesion promoted by the compatibilization. In spite of some interfacial adhesion suggested by SEM micrograph and rheological measurements, the systems loaded with IL in higher proportion presented poorer mechanical properties. This behavior may be attributed to an increasing of a degradation process of PLA component through transesterification reaction involving ester groups in the middle of the PLA chain, as indicated by SEC analysis.

The dynamic mechanical properties of the composites are illustrated in **Figure 7** in terms of storage modulus (E′), loss factor (tan delta) and loss modulus (E″) as a function of the temperature. Also the main dynamic-mechanical parameters of the neat polymers are also summarized in **Table 3**. The storage modulus in the glassy region for the PLA/EVA blend increased with the addition of CNT, indicating a stiffness of the material due to the addition of the rigid filler. The composite loaded with CNT/ILSO$_3$H (1:2.5) resulted in an additional improvement of the modulus, probably due to a better dispersion of the CNT imparted by the presence of the IL at the surface. Increasing the amount of IL decreased the modulus when compared with those containing CNT probably due to a plasticizing effect of IL. These results suggest that the plasticizing effect of the low molar mass IL is effective in the solid state. In the melt state, as suggested by rheological measurements, the higher amount of IL resulted in an increase of the viscosity due to the better dispersion of the CNT and the formation of the physical networked structure. After around 50°C, E′ decreased due to the increase in chain mobility. The increase of the modulus at higher temperature is due to the cold crystallization phenomenon (Song et al., 2012; Agrawal et al., 2019). This characteristic is very common in PLA-based systems, due to its slow crystallization rate. The modulus in the rubbery region (at around 85°C) significantly increased for PLA/EVA blend when compared with the neat PLA. This phenomenon suggests that EVA exerts some reinforcing effect on

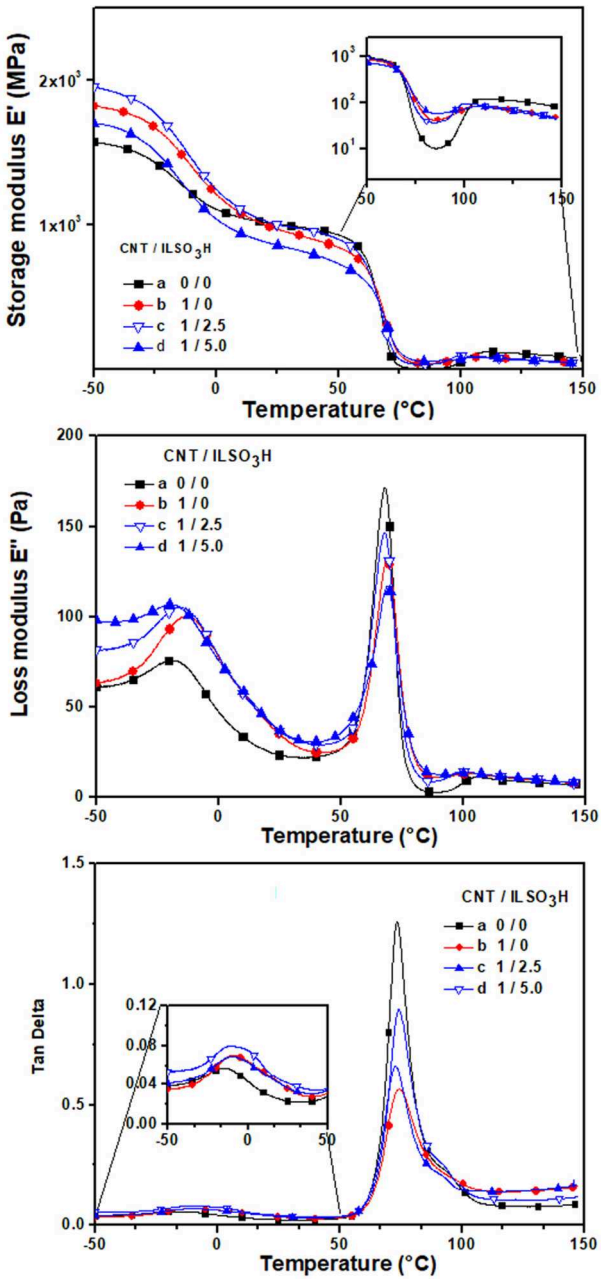

FIGURE 7 | Dynamic mechanical parameters as a function of the temperature for PLA/EVA blend containing CNT/ILSO$_3$H in a proportion of (a) 0:0; (b) 1:0; (c) 1:1.25; and (d) 1:5 phr.

the system probably due to an improvement of the crystallization process of PLA. The addition of CNT resulted in additional increase of E′ in the glassy region due to a reinforcing action of the filler. The use of CNT/ILSO$_3$H (1:2.5) also contributed for an additional increase of modulus, confirming the better dispersion state of the functionalized CNT with the IL and the formation of the networked structure in higher extent.

Another interesting feature observed in this region is the difference between the E′ values in the rubbery region and after

TABLE 3 | Dynamic mechanical properties of PLA, EVA, and PLA/EVA (60:40 wt%) composites.

Matrix (wt%)		Filler (phr)		E′ at −40°C (GPa)	E′ at 25°C (GPa)	E′ at 85°C (GPa)	Tg_{EVA} (°C)	Tg_{PLA} (°C)	I_{R-EVA}	I_{R-PLA}
PLA	EVA	CNT	IL							
100	0	0	0	2.1	2.0	0.005		69	–	–
0	100	0	0	1.7	0.1	–	−4		–	–
60	40	0	0	1.5	1.0	0.01	−14	73	0.29	5.73
60	40	1.0	0	1.8	1.0	0.04	−9	74	0.49	3.23
60	40	1.0	2.5	1.9	1.0	0.03	−9	73	0.40	2.98
60	40	1.0	5.0	1.7	0.9	0.06	−9	74	0.40	2.42

Tg from the maximum of Tan delta curves; I_R, integral area under the loss factor (tan delta).

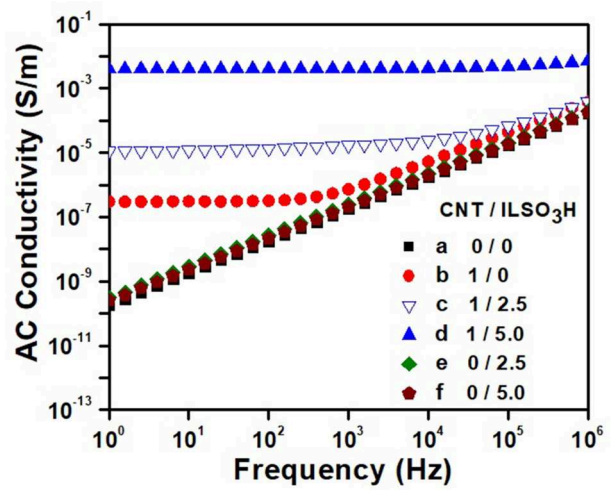

FIGURE 8 | AC electrical conductivity against frequency for PLA/EVA blends and composites containing CNT/$ILSO_3H$ in a proportion of (a) 0:0; (b) 1:0; (c) 1:1.25; (d) 1:5; (e) 0:2.5; and (f) 0:5.0 phr.

the cold crystallization phenomenon. This difference is smaller in the composite loaded with CNT than in neat polymer blend. This behavior may be related to the reinforcing action of CNT and also to the efficiency of CNT as nucleating agent, thus accelerating the crystallization process of PLA, as also reported in other studies Villmow et al. (2008). The presence of CNT/$ILSO_3H$ (1:5) decreased substantially this difference, that is, the cold crystallization phenomenon was almost absent, as observed from the DSC measurements during the first heating scan (see **Figure 6**). This behavior is also attributed to the better dispersion of CNT, thus increasing the interaction between the matrix and filler. Thus, the accelerating effect of the crystallization process was enhanced.

The effect of the CNT on the glass transition temperature of both PLA and EVA phases is also illustrated in **Figure 7** in terms of loss modulus and tan delta against temperature. The T_g values presented in **Table 3** were taken from the maximum of the tan delta curves. The T_g value of the EVA component in the blend is lower than that observed for the pure EVA, which may be attributed to an increase of the free volume at the interface due to the incompatibility between the blend component, as indicated by the SEM micrograph. The presence of CNT or CNT/IL did not exert significant influence on the T_g of the PLA phase, whose values stayed around 73–74°C. The Tg of the EVA phase slightly shifted toward higher temperature with the presence of CNT, which means a decreasing of the free volume in this phase. Moreover, some interaction between EVA phase and CNT may be responsible for this slight displacement of T_g. Similar features were also observed by Wang et al. (2016). According to the literature, the integral area (I_R) under the loss factor (tan delta) may be related to the total energy dissipated due to viscoelastic relaxation of the polymer chains (Jafari and Gupta, 2000; Wang et al., 2016). Thus, the I_R values can give an idea about the fracture toughness of polymers. **Table 3** presents the I_R values related to EVA and PLA relaxations in the composites. The presence of CNT in the blends resulted in higher I_{R-EVA} compared with neat blend. This behavior suggests an improvement of the toughness of the material (Wang et al., 2016). In the case of PLA component, the presence of CNT resulted in a decrease of the I_{R-PLA} values. This phenomenon may be related to an increase of stiffness of the PLA phase, caused by the presence of the rigid particle. It is interesting to point out that the non-covalent functionalization of CNT with ionic liquid promotes additional stiffness, indicated by lower I_R values for these samples. This result highlights the better dispersion of CNT promoted by the IL, thus forming a more effective physical network constituted by the dispersed CNT.

Electrical and Dielectric Properties

The dependence of the AC electrical conductivity with frequency for the PLA/EVA composites loaded with 1 phr CNT is illustrated in **Figure 8** as a function of the IL content. The blends containing only IL were also shown for comparison. The neat PLA/EVA blend and those containing only IL (2.5 or 5.0 phr—curves *e* and *f*) presented a linear dependence of the conductivity with the frequency, which is typical of insulating materials. The addition of 1 phr of pCNT (curve *b*) (without modification) resulted in composite with conductivity around 4×10^{-7} S/m in low frequency range and also a DC electrical conductivity plateau until a frequency of around 400 Hz. Beyond this frequency, known as critical frequency (f_c), the conductivity increased linearly with the frequency, obeying the Jonscher's universal power law for the frequency dependent conductivity of solids (Jonscher, 1977). This phenomenon arises from the presence of

trapped dipoles and charge carriers that cannot move at low frequencies but at higher frequencies, they have more chance to move due to the higher energy, thus displaying a typical non-ohmic conduction mechanism (frequency dependent) through tunneling/hopping effect (Min et al., 2013; Ram et al., 2017). Shi, et al. reached values around 10^{-5} S/m for PLA/EVA blend loaded with 1 wt% of CNT (Shi et al., 2013). However, it is difficult to compare the results as they used a master batch approach where CNT was previously dispersed in the PLA an also EVA component with 40% of vinyl acetate, whereas the processing conditions used in the present work involve only one processing step.

The functionalization of the CNT with the IL resulted in a significant increase of the conductivity. Moreover, the DC conductivity plateau is shifted toward higher frequency, indicating the formation of physical network of CNT in larger extent. The composite loaded with CNT/ILSO$_3$H (1:5) displayed conductivity value around 3.7×10^{-3} S/m (four order of magnitude higher than the blend containing pCNT) and frequency independent for all frequency range studied, characterizing a conductive material. Considering that no ionic conductivity was observed for the blends containing only IL, the outstanding electrical conductivity found for the composites containing CNT/ILSO$_3$H may be due to a better dispersion of the filler within the matrix imparted by the IL at the CNT surface. The IL contributes for a disaggregation of the CNT bundles and favors the formation of the conducting pathway in larger extent.

To investigate the effect of CNT and IL on the conduction mechanism that occurs in the PLA/EVA -based composites, the charge transport properties were estimated from the following power law equation (Jonscher, 1977):

$$\sigma_{AC} = \sigma_{DC} + k.f^n \quad (1)$$

where σ_{AC} is the AC electrical conductivity, σ_{DC} is the DC electrical conductivity, k is a constant dependent on temperature, f is the frequency and n is an exponent which provides an indication of the charge transport mechanism (Bose et al., 2008). The PLA/EVA composite loaded with 1 phr of CNT presented n value close to 0.96, indicating a charge transfer mechanism through hopping/tunneling, according to the literature (Bose et al., 2008). The composite loaded with CNT/ILSO$_3$H (1:2.5) displayed n value of 0.76, which characterizes a charge transfer mechanism through polarization effects, as stated by Bose et al. (2008). As also observed by Bose et al. (2008), the presence of IL facilitates the debundling of CNT and the contact between the conductive particles.

Table 4 compares the electrical conductivity of some thermoplastic matrices loaded with CNT/ionic liquid. As expected, the conductivity strongly depends on the nature of polymer matrix, nature and amount of IL used and processing conditions. However, it is possible to emphasize the significant increase in conductivity with the use of IL as dispersing agent for CNT. Some composites, including that reported in the present work, displayed an increase of conductivity by around four orders of magnitude.

Figure 9 shows the dependence of real permittivity (ϵ') and imaginary permittivity (ϵ'') of the composites with different CNT/ILSO$_3$H proportions with the frequency at room temperature. Both ϵ' and ϵ'' were independent of frequency in all measured frequency range, for the neat blend. The presence of pure IL (2.5 and 5.0 phr) did not significantly influence on the values of these properties and their dependence with frequency. Composite containing 1 phr of pCNT displayed very low ϵ' values but relatively high ϵ'' value, mainly in the low frequency range. This behavior suggests that the current leakage due to the movement of the mobile charge carrier throughout the materials is more important than the energy phenomenon storage.

The combination of CNT with the IL resulted in a significant increase of the ϵ' values for the corresponding composites, mainly in the low frequency region. The increase of ϵ' in the low frequency is related to the interfacial polarization, which usually occurs in heterogeneous systems with different dielectric constant, due to the accumulation of charge carriers at the interface between two materials (Jiang et al., 2009; Abraham et al., 2017). In this case, the ionic liquid at the CNT surface significantly contributes for the increasing of dielectric constant. This phenomenon cannot be only related to the contribution of the CNT and IL to the dielectric constant since these compounds, separately added to the blend, did not exert great influence on this

TABLE 4 | Electrical conductivity of heterogeneous polymer blends loaded with 1% of CNT-IL filler.

Matrix	Ionic liquid type	Conductivity (S/m)		References
		Without IL	With IL	
PMMA	Hmim·PF_6	10^{-9}	10^{-1}	Fang et al., 2018
PS	Alkyl-phosphonium-TFSI	10^{-4}	10^{-1}	Soares da Silva et al., 2017
PMMA	bmim·PF_6	10^{-11}	10^{-4}	Zhao et al., 2012
PC/PVDF	Aminopropyl-imidazol	10^{-5}	10^{-4}	Biswas et al., 2015
PVDF/ABS	Amino-terminated imidazol	10^{-3}	10^{-2}	Kar et al., 2015
PS/EVA	Alkyl-phosphonium-TFSI	5×10^{-1}	25×10^{-1}	Soares et al., 2018
PP/PA12	Alkyl-phosphonium-TFSI	3×10^{-7}	2×10^{-4}	Lopes Pereira et al., 2019
PP/PLA	Alkyl-phosphonium-TFSI	2×10^{-3}	10	Soares et al., 2019
PLA/EVA	mimbSO_3H·Cl	4×10^{-7}	3.7×10^{-3}	This work

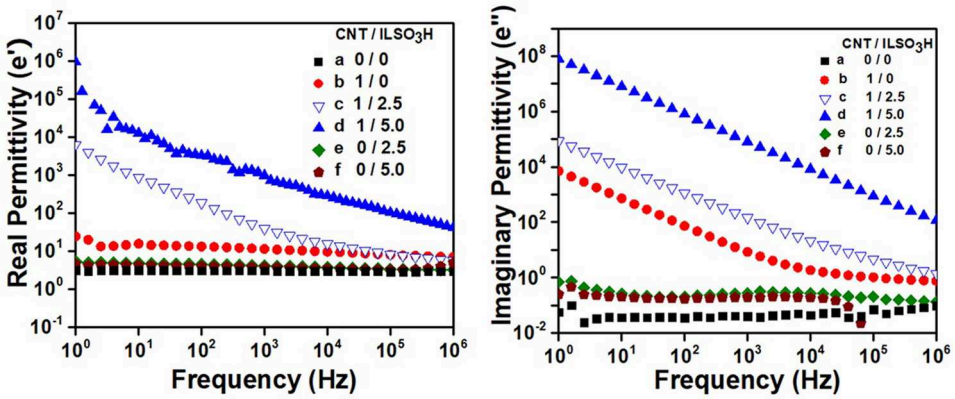

FIGURE 9 | Dielectric properties of PLA/EVA blends containing CNT/ILSO$_3$H in a proportion of (a) 0:0; (b) 1:0; (c) 1:2.5; (d) 1:5; (e) 0:2.5; and (f) 0:5 phr.

property. In fact, the IL at the surface of CNT forms a thin layer between the polymer matrix and the filler that acts as numerous micro-capacitors. Increasing the amount of IL in these hybrid CNT/ILSO$_3$H systems, increases the ϵ' values due to an increase of the interphase.

The imaginary permittivity (ϵ'') is mainly related to the energy dissipation within a dielectric. The increase of IL in the CNT/ILSO$_3$H complex also resulted in a significant increase of ϵ'' of the corresponding PLA/EVA composites. This property is related to the conductivity and agrees with increased AC conductivity values found for these samples.

CONCLUSION

Conductive composites based on PLA/EVA loaded with CNT or CNT non-covalently functionalized with two different amounts of mimbSO$_3$H·Cl as the protonic ionic liquid were prepared by melt mixing. The presence of CNT/ILSO$_3$H provided higher conductivity values to the composites when compared to that loaded with pristine CNT. The CNT/ILSO$_3$H proportion corresponding to 1:5 by weight resulted in higher electrical conductivity, which was attributed to a better dispersion of CNT within the polymer matrix and the formation of a conducting pathway in larger extent. This feature was confirmed by rheological parameters in the melt state. Thus, higher viscosity and higher storage modulus were achieved using this CNT/ILSO$_3$H proportion in the composite. Besides assisting the dispersion and debundling of the CNT during the melt processing, the IL also acted as interfacial agent between PLA and EVA phase, thus promoting a good interfacial adhesion. The compatibilization was suggested from SEM micrograph and also rheological properties. In fact, the presence of 5 phr of the mimbSO$_3$H·Cl resulted in an increase of the melt viscosity of the PLA/EVA blend. The results presented in this work highlight the dual effect of protonic ionic liquid as dispersing agent for CNT and also compatibilizing agent for PLA/EVA blends, and may considered a promising alternative for the development of semi-biodegradable conducting composites for antistatic packaging and other important applications in several fields of the electro-electronic industry.

DATA AVAILABILITY STATEMENT

All datasets generated for this study are included in the manuscript/**Supplementary Files**.

AUTHOR CONTRIBUTIONS

EL was responsible for the preparation of the samples and the management of their characterization. MS was responsible of the blends preparation and characterization. KP was involved in the main characterizations. BS was responsible for the general idea and was involved in the mains discussions of the results.

FUNDING

This work was sponsored in part by Coordenação de Aperfeiçoamento de Pessoal de Nível Superior–Brasil (CAPES)–(Grant number: 88887.333972/2019-00), Conselho Nacional de Desenvolvimento Científico e Tecnológico–CNPq (Grant number 303457/2013-9), and Fundação de Amparo à Pesquisa do Estado do Rio de Janeiro–FAPERJ (Grant number E-26/201.183/2014).

SUPPLEMENTARY MATERIAL

The Supplementary Material for this article can be found online at: https://www.frontiersin.org/articles/10.3389/fmats.2019.00234/full#supplementary-material

REFERENCES

Abraham, J., P, M. A., Xavier, P., Bose, S., George, S. C., Kalarikkal, N., et al. (2017). Investigation into dielectric behaviour and electromagnetic interference shielding effectiveness of conducting styrene butadiene rubber composites containing ionic liquid modified MWCNT. *Polymer* 112, 102–115. doi: 10.1016/j.polymer.2017.01.078

Aghjeh, M. R., Asadi, V., Mehdijabbar, P., Khonakdar, H. A., and Jafari, S. H. (2016). Application of linear rheology in determination of nanoclay localization in PLA/EVA/Clay nanocomposites: correlation with microstructure and thermal properties. *Compos. B Eng.* 86, 273–284. doi: 10.1016/j.compositesb.2015.09.064

Aghjeh, M. R., Nazari, M., Khonakdar, H. A., Jafari, S. H., Wagenknecht, U., and Heinrich, G. (2015). In depth analysis of micro-mechanism of mechanical property alternations in PLA/EVA/clay nanocomposites: a combined theoretical and experimental approach. *Mater. Des.* 88, 1277–1289. doi: 10.1016/j.matdes.2015.09.081

Agrawal, P., Araujo, A. P. M., Lima, J. C. C., Cavalcanti, S. N., Freitas, D. M. G., Farias, G. M. G., et al. (2019). Rheology, mechanical properties and morphology of poly(lactic acid)/ethylene vinyl acetate blends. *J. Polym. Environ*. 27, 1439–1448. doi: 10.1007/s10924-019-01445-8

Alves, F. F., Silva, A. A., and Soares, B. G. (2018). Epoxy—MWCNT composites prepared from master batch and powder dilution: effect of ionic liquid on dispersion and multifunctional properties. *Polym Eng. Sci*. 58:1689. doi: 10.1002/pen.24759

Bhattacharyya, A. R., Ghosh, A. K., Misra, A., and Eichhorn, K. J. (2005). Reactively compatibilized polyamide 6/ethylene-co-vinyl acetate blends: mechanical properties and morphology. *Polymer* 46, 1661–1674. doi: 10.1016/j.polymer.2004.12.012

Biswas, S., Kar, G. P., and Bose, S. (2015). Tailor-made distribution of nanoparticles in blend structure toward outstanding electromagnetic interference shielding. *ACS Appl. Mater. Interfaces* 7, 25448–25463. doi: 10.1021/acsami.5b08333

Bose, S., Bhattacharyya, A. R., Khare, R. A., Kulkarni, A. R., Patro, T. U., and Sivaraman, P. (2008). Tuning the dispersion of multiwall carbon nanotubes in co-continuous polymer blends: a generic approach. *Nanotechnology* 19:335704. doi: 10.1088/0957-4484/19/33/335704

Fang, D., Zhou, C., Liu, G; Luo, G., Gong, P., Yang, Q., et al. (2018). Effects of ionic liquids and thermal annealing on the rheological behavior and electrical properties of poly (methyl methacrylate)/carbon nanotubes composites. *Polymer* 148, 68–78. doi: 10.1016/j.polymer.2018.05.051

Fukushima, T., Kosaka, A., Ishimura, Y., Yamamoto, T., Takigawa, T., Ishii, N., et al. (2003). Molecular ordering of organic molten salts triggered by single-walled carbon nanotubes. *Science* 300, 2072–2074. doi: 10.1126/science.1082289

Hassouneh, S. S., Yu, L., Skov, L. A., and Daugaard., A. E. (2017). Soft and flexible conductive PDMS/MWCNT composites. *J Appl. Polym. Sci*. 134:44767. doi: 10.1002/app.44767

Huang, H. X. (2011). "Macro, micro and nanostructured morphologies of multiphase polymer systems," in *Chapter 6: Handbook of Multiphase Polymer, Systems, 1st Edn.*, eds A. Boudenne, L. Ibos, Y. Candau, and S. Thomas (John Wiley & Sons Ltd.), 161–249.

Jafari, S. H., and Gupta, A. H. (2000). Impact strength and dynamic mechanical properties correlation in elastomer-modified polypropylene. *J. Appl. Polym. Sci.* 78, 962–971. doi: 10.1002/1097-4628(20001031)78:5<962::AID-APP40>3.3.CO;2-X

Jiang, M. J., Dang, Z. M., Bozlar, M., Miomandre, F., and Bai, J. (2009). Broad-frequency dielectric behaviors in mulriwalled carbon nanotube/tuber nanocomposites. *J. Appl. Phys*. 106:084902. doi: 10.1063/1.3238306

Jonscher, A. K. (1977). The 'universal' dielectric response. *Nature* 267, 673–679. doi: 10.1038/267673a0

Kar, G. P., Biswas, S., Rohini, R., and Bose, S. (2015). Tailoring the dispersion of multiwall carbon nanotubes in co-continuous PVDF/ABS blends to design materials with enhanced electromagnetic interference shielding. *J. Mater. Chem. A* 3, 7974–7985. doi: 10.1039/C5TA01183C

Li, Y., Liu, L., Shi, Y., Xiang, F., Huang, T., Wang, Y., et al. (2011). Morphology, rheological, crystallization behavior and mechanical properties of poly (L-lactide)/ethylene-co-vinyl acetate blends with different VA contents. *J. Appl. Polym. Sci*. 121, 2688–2698. doi: 10.1002/app.33581

Liebscher, M., Tzounis, L., Pötschke, P., and Heinrich, G. (2013). Influence of the viscosity ratio in PC/SAN blends filled with MWCNTs on the morphological, electrical and melt rheological properties. *Polymer* 54, 6801–6808. doi: 10.1016/j.polymer.2013.10.040

Lim, L. T., Auras, R., and Rubino, M. (2008). Processing technology for poly(lactic acid). *Prog. Polymer Sci*. 33, 820–852. doi: 10.1016/j.progpolymsci.2008.05.004

Lins, L., Livi, S., Duchet-Rumeau, J., and Gerard, J. F. (2015). Phosphonium ionic liquids as new compatibilizing agents of biopolymer blends composed of poly(butylene-adipate-*co*-terephtalate)/poly(lactic acid) (PBAT/PLA). *RSC Adv*. 5:59082. doi: 10.1039/C5RA10241C

Liu, C. M., MA, F. F., Zhang, Z. X., Wang, Y., and Zhou, Z. W. (2016). Enhanced tensile creep stability of immiscible poly(L-lactide)/poly(ethylene vinyl acetate) blends achieved by adding carbon nanotubes. *Compos. B Eng.* 107, 174–181. doi: 10.1016/j.compositesb.2016.09.082

Lopes Pereira, E. C., Silva, J. M. F., Jesus, R. B., and Soares, B. G., Livi, S. (2017). Bronsted acidic ionic liquids: new transesterification agents for the compatibilization of polylactide/ethylene-co-vinyl acetate blends. *Eur. Polym. J.* 97, 104–111. doi: 10.1016/j.eurpolymj.2017.10.003

Lopes Pereira, E. C., Soares, B, G., Silva, A. A., Farias, S. J. M., Barra, G. M. O., Livi, S. (2019). Conductive heterogeneous blend composites of PP/PA12 filled with ionic liquids treated-CNT. *Polym. Test*. 74, 187–195. doi: 10.1016/j.polymertesting.2019.01.003

Lopes Pereira, E. C., and Soares, B. G. (2016). Conducting epoxy networks modified with non-covalently functionalized multi-walled carbon nanotube with imidazolium based–ionic liquid. *J. Appl. Polym. Sci.* 133:43976. doi: 10.1002/app.43976

Ma, P., Hristova-Bogaerds, D. G., Goossens, J. G. P., Spoelstra, A. B., Zhang, Y., Lemstra, P. J. (2012). Toughening of poly (lactic acid) by ethylene-co-vinyl acetate copolymer with different vinyl acetate contents. *Eur. Polym. J*. 48, 146–154. doi: 10.1016/j.eurpolymj.2011.10.015

Ma, P., Xu, P., Liu, W., Zhai, Y., Dong, W., Zhang, Y., et al. (2015). Bio-based poly(lactide)/ethylene-co-vinyl acetate thermoplastic vulcanizates by dynamic crosslinking: structure vs. property. *RSC Adv*. 5, 15962–15968. doi: 10.1039/C4RA14194F

Min, C., Yu, D., Cao, J., Wang, G., and Feng, L. (2013). A graphite nanoplatelet/epoxy composite with high dielectric constant and high thermal conductivity. *Carbon* 55, 116–125. doi: 10.1016/j.carbon.2012.12.017

Moura, I., Nogueira, R., Bournor-Legare, V., and Machado, A. V. (2011). Biobased grafted polyesters prepared by *in situ* ring-opening polymerization. *React. Funct. Polym.* 71, 694–703. doi: 10.1016/j.reactfunctpolym.2011.03.012

Moura, I., Nogueira, R., Bournor-Legare, V., and Machado, A. V. (2012). Synthesis of EVA-g-PLA copolymers using transesterification reactions. *Mater Chem. Phys*. 134, 103–110. doi: 10.1016/j.matchemphys.2012.02.036

Nampoothiri, K. M., Nair, N. R., and John, R. P. (2010). An overview of the recent developments in polylactide (PLA) research. *Bioresour. Technol*. 101, 8493–8501. doi: 10.1016/j.biortech.2010.05.092

Park, K. I., and Xanthos, M. (2009). A study on the degradation of polylactic acid in the presence of phosphonium ionic liquids. *Polym. Degrad. Stability* 94, 834–844. doi: 10.1016/j.polymdegradstab.2009.01.030

Ram, R., Rahaman, M., Aldalbahi, A., and Khastgir, D. (2017). Determination of percolation threshold and electrical conductivity of polyvinylidene fluoride (PVDF)/short carbon fiber (SCF) composites: effect of SCF aspect ratio. *Polym. Int*. 66, 573–582. doi: 10.1002/pi.5294

Sangeetha, V. H., Valapa, R. B., Nayak, S. K., and Varguese, T. O. (2016). Super toughened renewable poly (lactic acid) based ternary blends system: effect of degree of hydrolysis of ethylene vinyl acetate on impact and thermal properties. *RSC Adv*. 6, 72681–72691. doi: 10.1039/C6RA13366E

Sangeetha, V. H., Valapa, R. B., Nayak, S. K., and Varguese, T. O. (2018). Investigation on the influence of EVA content on the mechanical and thermal characteristics of poly(lactic acid) blends. *J. Polym. Environ.* 26, 1–14. doi: 10.1007/s10924-016-0906-0

Sarasa, J., Gracia, J. M., and Javierre, C. (2009). Study of the biodisintegration of a bioplastic material waste. *Bioresour. Technol.* 100, 3764–3768. doi: 10.1016/j.biortech.2008.11.049

Scott, M. P., Brazel, C. S., Benton, M. G., Mays, J. W., Holbrey, J. D., and Rogers, R. D. (2002). Application of ionic liquids as plasticizers for poly(methyl methacrylate). *Chem. Commun*. 13, 1370–1371. doi: 10.1039/b204316p

Scott, M. P., Rahman, M., and Brazel, C. S. (2003). Application of ionic liquids as low-volatility plasticizers for PMMA. *Eur. Polym. Sci.* 39, 1947–1953. doi: 10.1016/S0014-3057(03)00129-0

Shi, Y., Li, Y., Wu, J., Huang, T., Chen, C., Peng, Y., et al. (2011). Toughening of poly(L-lactide)/multiwalled carbon nanotubes nanocomposites with ethylene-co-vinyl acetate. *J. Polym. Sci. B Polym. Phys.* 49, 267–276. doi: 10.1002/polb.22177

Shi, Y., Li, Y., Xiang, F., Huang, T., Chen, C., Peng, Y., et al. (2012). Carbon nanotubes induced microstructure and mechanical properties changes in cocontinous poly(L-lactide)/ethylene-co-vinyl acetate blends. *Polym. Adv. Technol.* 23, 783–790. doi: 10.1002/pat.1959

Shi, Y. Y., Yang, J. H., Huang, T., Zhang, N., Chen, C., and Wang, Y. (2013). Selective localization of carbon nanotubes at the interface of poly(L-lactide)/ethylene-co-vinyl acetate resulting in lowered electrical resistivity. *Compos. B Eng.* 55, 463–469. doi: 10.1016/j.compositesb.2013.07.012

Soares da Silva, J. P., Soares, B. G., Livi, S., and Barra, G. M. O. (2017). Phosphonium–based ionic liquid as dispersing agent for MWCNT in melt-mixing polystyrene blends: rheology, electrical properties and EMI shielding effectiveness. *Mater Phys. Chem.* 189, 162–168. doi: 10.1016/j.matchemphys.2016.12.073

Soares, B. G. (2018). Ionic liquid: a smart approach for developing conducting polymer composites: a review. *J. Mol. Liquids* 262, 8–18. doi: 10.1016/j.molliq.2018.04.049

Soares, B. G., Calheiros, L. F., Silva, A. A., Indrusiak, T., Barra, G. M. O., and Livi, S. (2018). Conducting melt blending of polystyrene and EVA copolymer with carbon nanotube assisted by phosphonium-based ionic liquid. *J. Appl. Polym. Sci.* 135:45564. doi: 10.1002/app.45564

Soares, B. G., Cordeiro, E., Maia, J., Lopes Pereira, E. C., and Silva, A. A. (2019). The effect of the non-covalent functionalization of CNT by ionic liquid on electrical conductivity and electromagnetic interference shielding effectiveness of semi-biodegradable polypropylene/poly(lactic acid) composites. *Polym. Compos.* doi: 10.1002/pc.25347. [Epub ahead of print].

Song, P., Chen, G., Wei, Z., Chang, Y., Zhang, W., and Liang, J. (2012). Rapid crystallization of poly(l-lactic acid) induced by a nanoscaled zinc citrate complex as nucleating agent. *Polymer* 53, 4300–4309. doi: 10.1016/j.polymer.2012.07.032

Spitalsky, Z., Tasis, D., Papagelis, K., and Galiotis, C. (2010). Carbon nanotube-polymer composites: chemistry, processing, mechanical and electrical properties. *Prog. Polym. Sci.* 35, 357–401. doi: 10.1016/j.progpolymsci.2009.09.003

Subramaniam, K., Das, A., Simon, F., Heinrich, G. (2013). Networking of ionic liquid modified CNTs in SSBR. *Eur. Polym. J.* 49, 345–352. doi: 10.1016/j.eurpolymj.2012.10.023

Villmow, T., Pötschke, P., Pegel, S., Häussler, L., and Kretzschmar, B. (2008). Influence of twin-screw extrusion conditions on the dispersion of multi-walled carbon nanotubes in a poly (lactic acid) matrix. *Polymer* 49, 3500–3509. doi: 10.1016/j.polymer.2008.06.010

Wang, X., Zhang, Z., Li, J., Yang, J., Wang, Y., and Zhang, J. (2015). Largely improved fracture toughness of an immiscible poly(L-lactide)/ethylene-co-vinyl acetate blend achieved by adding carbon nanotubes. *RSC Adv.* 5, 69522–69533. doi: 10.1039/C5RA11192G

Wang, X. F., He, Z. Z., Yang, J. H., Zhang, N., Huang, T., Wang, Y., et al. (2016). Super toughened immiscible poly(L-lactide)/poly(ethylene vinyl acetate) (PLLA/EVA) blend achieved by *in situ* cross-linking reaction and carbon nanotubes. *Compos. A Appl. Sci. Manuf.* 91, 105–116. doi: 10.1016/j.compositesa.2016.09.020

Yamaki, S. B., Prado, E. A., and Atvars, T. D. Z. (2002). Phase transitions and relaxation processes in ethylene-vinyl acetate copolymers probed by fluorescence spectroscopy. *Eur. Polym. J.* 38, 1811–1826. doi: 10.1016/S0014-3057(02)00067-8

Yoon, J. S., Oh, S. H., Kim, M. N., Chin, I. J., and Kim, Y. H. (1999). Thermal and mechanical properties of poly (L-lactic acid)–poly (ethylene-co-vinyl acetate) blends. *Polymer* 40, 2303–2312. doi: 10.1016/S0032-3861(98)00463-7

Yousfi, M., Livi, S., and Duchet-Rumeau, J. (2014). Ionic liquids: a new way for the compatibilization of thermoplastic blends. *Chem. Eng. J.* 255, 513–524. doi: 10.1016/j.cej.2014.06.080

Zhang, N., and Lu, X. (2016). Morphology and properties of super-toughened bio-based poly(lactic acid)/poly(ethylene-co-vinyl acetate) blends by peroxide-induced dynamic vulcanization and interfacial compatibilization. *Polym. Test.* 56, 354–363. doi: 10.1016/j.polymertesting.2016.11.003

Zhang, X., and Zhang, Y. (2016). Reinforcement effect of poly(butylene succinate) (PBS)-grafted cellulose nanocrystal on toughened PBS/polylactic acid blends. *Carbohydr. Polym.* 140, 374–382. doi: 10.1016/j.carbpol.2015.12.073

Zhao, L., Li, Y., Cao, X., You, J., and Dong, W. (2012). Multifunctional role of an ionic liquid in melt-blended poly (methyl methacrylate)/multi-walled carbon nanotube nanocomposites. *Nanotechnology* 23:255702. doi: 10.1088/0957-4484/23/25/255702

Conflict of Interest: The authors declare that the research was conducted in the absence of any commercial or financial relationships that could be construed as a potential conflict of interest.

Copyright © 2019 Lopes Pereira, da Silva, Pontes and Soares. This is an open-access article distributed under the terms of the Creative Commons Attribution License (CC BY). The use, distribution or reproduction in other forums is permitted, provided the original author(s) and the copyright owner(s) are credited and that the original publication in this journal is cited, in accordance with accepted academic practice. No use, distribution or reproduction is permitted which does not comply with these terms.

frontiers in Materials

ORIGINAL RESEARCH
published: 31 October 2019
doi: 10.3389/fmats.2019.00265

Comparison of Electrical Conductivity in Compounds of Carbon Black With Natural and Butadiene Rubbers

Erol Sancaktar[1]* *and Satilmis Basan*[2]

[1] Department of Polymer Engineering, University of Akron, Akron, OH, United States, [2] Department of Chemical Engineering, Hittite University, Corum, Turkey

Carbon black (CB) filled butadiene (BR) (Cis-1,4-polybutadiene) and natural (NR) (Cis-1,4-polyisoprene) rubber compounds containing CB in 60–100 per hundred (phr) proportions were investigated for their pressure/time-dependent electrical conductivity. Due to their high deformability, the percolation thresholds for CB–BR and CB-NR compounds were functions of pressures (compression loads) applied. Resistivity of such compounds decreased with time and compressive load levels. Storage moduli, G', as well as the loss moduli, G" and the dynamic viscosities, η^* of the compounds were evaluated to assess viscoelastic response of the compounds' conductivities under pressure. The storage and loss moduli values for both the CB-BR and the CB-NR compounds decreased with increasing strain levels, indicating that the rate of increase in conductivity is expected to increase at higher compressive loads. The storage moduli increased with increasing frequency (rate), indicating that the rate of increase in conductivity should be lower at higher rates of compressive load application. Comparison of variations in conductivity between the CB–BR and CB-NR compounds as functions of time and pressure, however, revealed that, overall, the conductivity levels are also strongly dependent on the nature of the molecular structure of these rubber materials and their initial interactions with CB during compounding, and the resulting dispersion levels of CB. Once such dispersion structure is established, the overall difference in conductivity levels for the CB–BR and CB-NR compounds remain approximately unchanged for given time and pressure conditions for the cases where high CB fill levels (~90 phr) are used and asymptotic conductivity values are reached. The experimental results revealed that because of the presence of higher number (~2-fold) of hydrogen side atoms on the linear BR chains, CB–BR compound forms more physical crosslinks (mostly due to hydrogen bonding) in comparison to the CB-NR compound resulting in more effective CB dispersion and higher conductivity. Such higher efficiency in CB dispersion and percolation in BR is further implied by higher conductivities despite higher G' and η^* values for the CB–BR compound in comparison to the CB-NR compound.

Keywords: electrical conductivity, Cis-1,4-polybutadiene/carbon black rubber compound, Cis-1,4-polyisoprene/carbon black rubber compound, natural rubber, pressure dependent electrical conduction, percolation, carbon black dispersion, storage modulus—viscosity—electrical conduction relationships

OPEN ACCESS

Edited by:
Guilherme Mariz de Oliveira Barra, Federal University of Santa Catarina, Brazil

Reviewed by:
Gordana Markovic, Tigar A.D., Serbia
Claudia Merlini, Federal University of Santa Catarina, Brazil
Debora Pereira Schmitz, Federal University of Santa Catarina, Brazil

***Correspondence:**
Erol Sancaktar
erol@uakron.edu

Specialty section:
This article was submitted to Polymeric and Composite Materials, a section of the journal Frontiers in Materials

Received: *12 March 2019*
Accepted: *11 October 2019*
Published: *31 October 2019*

Citation:
Sancaktar E and Basan S (2019) Comparison of Electrical Conductivity in Compounds of Carbon Black With Natural and Butadiene Rubbers. Front. Mater. 6:265. doi: 10.3389/fmats.2019.00265

INTRODUCTION

Electrically conducting fillers are commonly used to induce conductivity in polymer-based composites, if added above their percolation threshold to form interconnected particle network. The percolation phenomenon is well-known and typically illustrated by either local inflection or terminal asymptotes in decreasing variation of resistivity. Sancaktar and Wei (1996), Wei and Sancaktar (1996), Sancaktar and Dilsiz (1999a,b), and Sancaktar and Bai (2011) reported on electrically conductive adhesives as a subset of polymer-based conductive composites. Sancaktar and Wei (Sancaktar and Wei, 1996; Wei and Sancaktar, 1996) developed a model for evaluating the relation between contact pressure and conductivity. This model used Holm's contact resistance theory (Holm, 1967) with conductive spherical powder fillers. The interparticle contact resistance among these fillers was modeled by adding the constriction resistance based on Hertz's contact stress equation (Timoshenko and Goodier, 1970) to the tunneling resistance. Experimental data by Sancaktar and Wei (1996) proved that powders' electrical resistance was dependent on the pressure applied on them. Applicability of Hertz's theory in their work proved that fillers' material properties, as well as their shape and size should also affect the constriction resistance. The tunneling resistance, however, is affected by presence of non-contact space as well as oxide layer on particle surfaces. The non-contact space is expected to decrease due to the deformations at particle contact points when compressive forces are applied on them. Thus, we expect the tunneling resistance to decrease and approach an asymptotic level (due to the presence of oxide layer and other non-conductive impurities) when compressive forces are applied.

Electrically conductive nanoparticles such as carbon black (CB) have large specific surface area which enhances interconnecting network formation as well as improving the mechanical properties of composites in which they are used as fillers and/or reinforcement agents (Sancaktar et al., 1996).

Unvulcanized butadiene (BR) (Cis-1,4-polybutadiene) and natural (NR) (Cis-1,4-polyisoprene) rubbers are tough linear polymers exhibiting large area under their stress-strain curves at room temperature. They flow plastically at higher temperatures (182–204°C). These rubbers are mixed with vulcanizing agents such as sulfur or peroxides at temperatures $\geq$100°C to crosslink them into molecular network which typically has one crosslink for every few hundred atoms of a polymer molecule. In the undeformed state, randomly coiled polymer molecules exist between the crosslinks. The Young's modulus for natural and synthetic rubbers range from 10^2 to 10^4 kPa. Vulcanized rubbers can be reversibly stretched more than 200% (Morton, 1987; White, 1995).

Basan and Sancaktar (2016) studied pressure-time dependent electrical resistivity/conductivity behavior of silicon rubber (SR) containing 40–100 phr (parts per hundred units of rubber) CB. Due to the high deformability of silicon rubber, the percolation thresholds for CB–SR compounds were functions of the applied pressure (compression load). Resistivity of such compounds decreased with time and compressive load levels. Storage moduli, G', as well as the loss moduli, G" and the dynamic viscosities, η^* of the compounds were evaluated to assess viscoelastic response of the compounds' conductivities under pressure. The storage and loss moduli values for the CB-SR compounds decreased with increasing strain levels, indicating that the rate of increase in conductivity is expected to increase at higher compressive loads. The storage moduli increased with increasing frequency (rate) (Basan and Sancaktar, 2016), indicating that the rate of increase in conductivity should be lower at higher rates of compressive load application. Work by Basan and Sancaktar was performed using a single rubber compound, namely CB-SR, and as such, did not provide insight on the effects of the molecular structure of the rubber matrix on the conductivity behavior of the compound.

In this work, pressure-time dependent electrical resistivity/conductivity behavior of Carbon black (CB) filled butadiene (BR) (Cis-1,4-polybutadiene) and natural (NR) (Cis-1,4-polyisoprene) rubber compounds containing 60–100 phr CB are investigated. Storage moduli, G', as well as the loss moduli, G" and the dynamic viscosities, η^* of the compounds are evaluated to assess viscoelastic response of the compounds' conductivities under pressure and at different rates. Variations in conductivity of the CB–BR and CB-NR compounds as functions of time and pressure are compared to assess whether the conductivity levels are also dependent on the nature of the molecular structure of these rubber materials, their initial interactions with CB during compounding, and the resulting dispersion levels of CB.

MATERIALS AND METHODS

Preparation of Composite Materials

The CB filled BR (Cis-1,4-polybutadiene, 96% Cis[1]) and NR (Cis-1,4-polyisoprene) rubber composites we tested were prepared using Diene 645 high cis BR (now Diene 645S, Firestone Polymers, Akron, OH), and SMR-CV60 NR (Akrochem, Akron, OH[2]). N330 CB was utilized in 40, 60, 70, 80, 90 ve 100 phr (per hundred rubber) proportions as the conductive component (Basan and Sancaktar, 2016). CB-BR and CB-NR composites were compounded using the recipe shown in **Table 1** for 50 phr CB. A Brabender compounder (C.W. Brabender Instruments Inc., South Hackensack, NJ) was employed using the compounding procedures shown in **Table 2**. The six different compounds obtained in this manner were press-cured into 2 mm thick sheets using 28 MPa pressure at 100°C over a 35 min period (Basan and Sancaktar, 2016). A hydraulic press (Carver Model 3912; Wabash, IN) was used for this purpose (Basan and Sancaktar, 2016).

Measurement of Electrical Conductivity

Twenty millimeter diameter, 2 mm thick circular samples were punch-cut (Basan and Sancaktar, 2016) using the composite

[1]https://na01.safelinks.protection.outlook.com/?url=http%3A%2F%2Fwww.firestonepolymers.com%2Fdiene_rubber.aspandamp;data=02%7C01%7Cerol%40uakron.edu%7C92e1aafc4d5e4e1dd29708d663b4aca8%7Ce8575dedd7f94ecea4aa0b32991aeedd%7C1%7C0%7C636806025988764877andamp;sdata$=$rqPc0DEVAATs%2BkNEa8H1bUNKYAvs9hgGJ702htfLQfc%3Dandamp;reserved=0

[2]http://www.akrochem.com/pdf/technical_data_sheet/elastomers/smr_cv60-smr-l_smr-gp.pdf

TABLE 1 | Compound recipes.

Function	Item-Grade	phr	Density (g/cm^3)	Weight (g)	Volume (cm^3)
Unvulcanized Rubber	Diene 645 high cis BR, or	100	0.90	174.42	193.80
	SMR-CV60 NR	100	0.92	174.42	189.59
Reinforcing filler	Carbon Black-N330	50	1.7∼1.9	87.21	48.45
Activator	Zinc Oxide-FP-H	5	5.6	8.72	1.56
Accelerator	Sulfenamides-CBTS	0.5	1.3	0.87	0.67
Vulcanizer	Sulfur:Rubbermakers-Regular	2.5	2.07	4.36	2.11
Activator	Stearic Acid-Rubber Grade	2	0.85	3.49	4.10
Antioxidants	Non-staining phenolic-Antioxidant 33	2	1.09	3.49	3.20
Plasticizer	Naphthenic process oil-Plasticizer-LN	5	0.9045	8.72	9.64
		172	1.116 or 1.136	291.28	263.53 or 259.32

TABLE 2 | Compounding procedures.

Number of pass	Item	Temp (°C)	Temp (°F)	Speed (rpm)	Time (min)
1st (Non-Productive)	Rubber+CB+Oil+Antioxidant	90	194	30	10
2nd (Productive)	+ Zinc Oxide +Stearic Acid + Sulfur +CBTS	70	158	20	10

sheets prepared as described in section Preparation of Composite Materials. These samples were placed in an insulating hollow cylinder fitted with conducting solid aluminum rods to apply compressive force to the samples (Sancaktar and Wei, 1996) and to measure the change in their resistivity with increasing pressure. A digital multimeter (Goldstar; DM-7241) was used to measure sample resistances (R) in kΩ.

The resistivity, ρ (Ω·cm) values for the composites were calculated using the equation:

$$\rho = \mathrm{R}\frac{A}{L} \tag{1}$$

where, A (cm^2) represents the cross sectional area, and L (cm) the linear dimension (specimen thickness) in the direction of current flow (Basan and Sancaktar, 2016).

The specimen thickness is reduced due to the pressure applied on the specimen. The relationship between the specimen thickness and the applied pressure was assumed to be linear, with the proportionality constant, α:

$$\alpha = \frac{L - L_o}{t} \tag{2}$$

where, L_o and L represent initial and final thicknesses during the loading cycle, t. Therefore, the final length can be calculated using the relation (Basan and Sancaktar, 2016):

$$\mathrm{L} = \mathrm{L_o} - \alpha t. \tag{3}$$

The conductivity, σ (S·cm^{-1}), is defined as the inverse of resistivity:

$$\sigma = \frac{1}{\rho} \tag{4}$$

The resistance values were measured over a period of 60 min using eight different pressures (0, 50, 100, 150, 250, 375, 500, and 750 kPa) (Basan and Sancaktar, 2016).

Rheological Measurements

5 × 5 cm CB-rubber composite samples weighing ∼5 g were prepared using the procedure described in section Preparation of Composite Materials and placed in between two PET (Mylar) film sheets for measurements of storage (G') and loss (G") moduli, as well as the dynamic viscosity (η*) (Basan and Sancaktar, 2016). A Torque Rheometer (RPA 2000; Alpha Technologies, Hudson, OH) was used for this purpose. 0.5–100% strain sweep (0.03–7° rotation) was done at 60°C using 10.5 rad/s (1.67 Hz) frequency. 0.3–157 rad/s frequency sweep (0.5–25 Hz) at 60°C using 4.2% strain level (0.29° rotation) (Basan and Sancaktar, 2016).

RESULTS AND DISCUSSION

Variation of Composite Resistivity With CB Fraction, Pressure, and Time

Figures 1A,B show the reductions in resistivity for CB–BR composites when the CB fill levels are increased from 70 to 100 phr. Such reductions in resistivity at 1 min pressure application is shown in **Figure 1A** and the same for 60 min pressure application is shown in **Figure 1B**. Locally asymptotic resistivity level appears to commence at ∼90 phr CB fill level for the Ω-cm resistivity range depicted. Reductions in resistivity levels are clearly observed when the pressure levels are increased up to 750 kPa at constant CB phr levels less than ∼90 phr.

Figures 2A,B show the reductions in resistivity for CB–NR composites when the CB fill levels are increased from 60 to 70 phr, indicating the formation of percolated network. Such reductions in resistivity at 1 min pressure application are shown in **Figure 2A** and the same for 60 min pressure application are

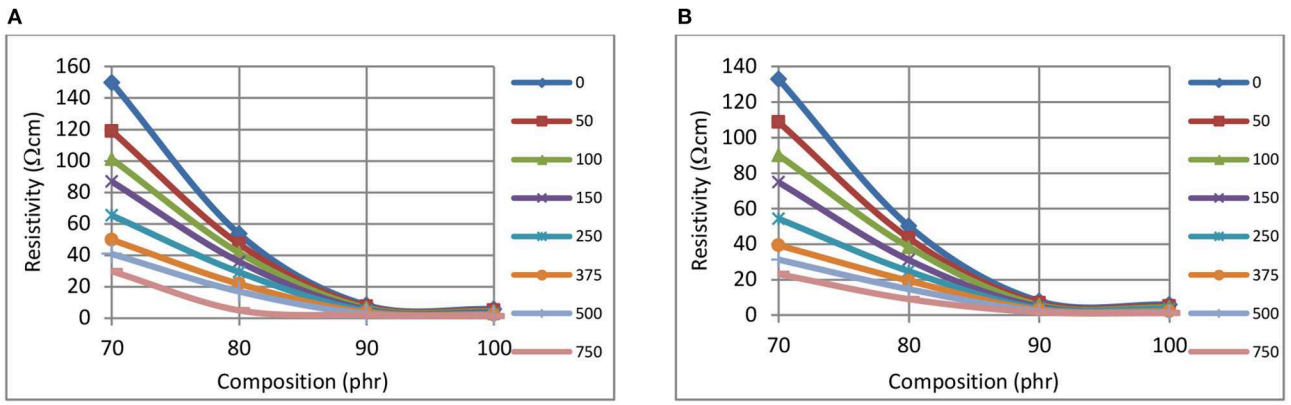

FIGURE 1 | The variation of resistivity, at 1 min **(A)**, and 60 min **(B)**, with composition, for CB-BR composites using different pressures (kPa, inset right).

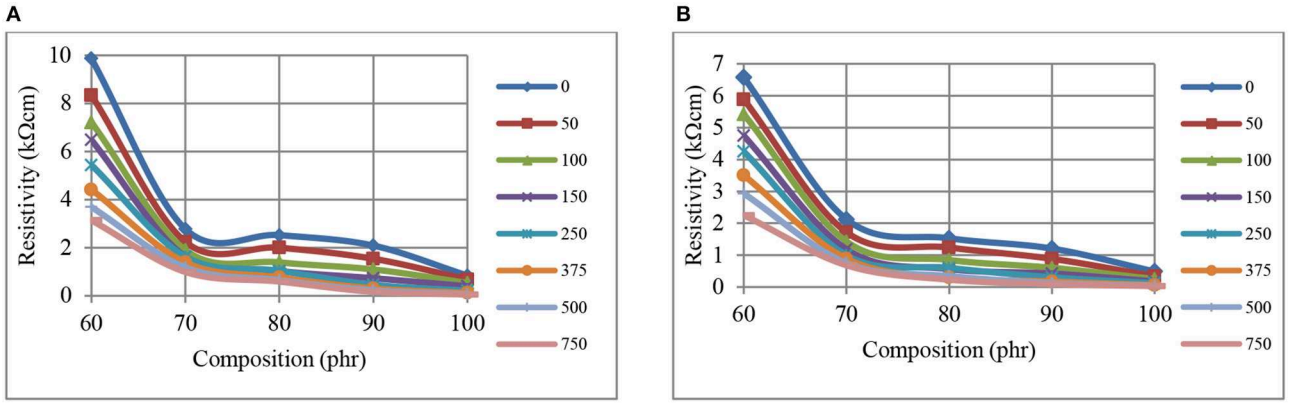

FIGURE 2 | The variation of resistivity, at 1 min **(A)**, and 60 min **(B)**, with composition, for CB-NR composites using different pressures (kPa, inset right).

shown in **Figure 2B**. Examination of **Figure 2** reveals that locally asymptotic resistivity level appears to commence at ∼70 phr for the kΩ-cm range depicted even though some local fluctuations are observed. Reductions in resistivity levels are clearly observed when the pressure levels are increased up to 750 kPa at constant CB phr levels. Furthermore, the percolation transition is more clearly observed at lower pressures with the variation of resistivity with composition approaching linearity as the pressure level is increased.

Figures 3(**A**- 1 min) and (**B**- 60 min) show the time dependent decrease in CB–BR composite resistivity levels beyond 70 phr CB level (at the initiation of percolated structure) when 0–750 kPa pressure levels are used. Asymptotic resistivity levels are reached at ∼90 phr CB when using either pressure, with this level at 750 kPa being ∼25% of that at 0 kPa (**Figure 3**).

Figures 4A,B illustrate a stronger time dependence for the CB–NR composite resistivity levels, within the kΩ-cm range depicted, when compared with **Figure 3** (CB-BR). We note that **Figure 4** presents resistivity data for CB levels ≥70 phr, the range which appears to have reached approximately asymptotic levels for resistivity in **Figure 2**. It is interesting to note that within the Ω-cm range corresponding to the higher pressure application (750 kPa) part (b) of **Figure 4**, another asymptotic level appears to have been reached at 90 phr CB.

Comparison of Conductivity Levels for the CB–BR and CB-NR Compounds

Changes in conductivity with pressure and time, for BR (a), and NR (b) composites containing 70 phr CB are shown in **Figures 5**, **6**, respectively. Increases in conductivity with pressure (**Figure 5**) and time (**Figure 6**) are clearly observed. **Figure 5** reveals that the effect of pressure on conductivity increases at higher pressures where the time dependent conductivity curves diverge for both CB-BR and CB-NR composites. This increase becomes more or less constant beginning at 5 min pressure application time (t) (**Figure 6**). In other words, the slopes of conductivity vs. pressure curves are approximately constant for $t \geq 5$ min. In comparison, the slopes of conductivity vs. pressure curves at 1 min pressure application time become relatively smaller. This may be attributed to viscoelastic behavior by the composites not being accurately represented in Equations (2) and (3) which are used to calculate the effective specimen length under pressure.

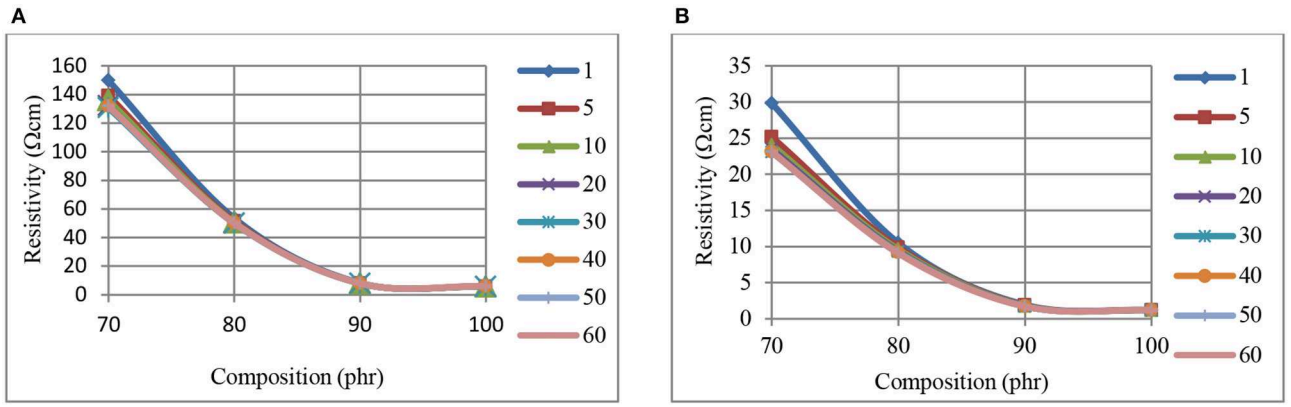

FIGURE 3 | The variation of resistivity, at 0 kPa **(A)**, and 750 kPa **(B)** pressure, with composition, for CB-BR composites measured at different times (min, inset right).

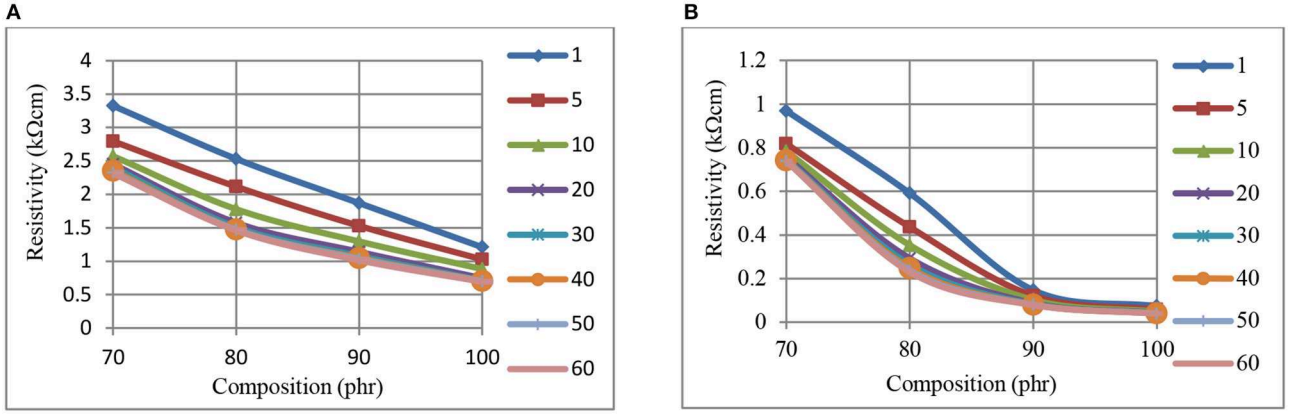

FIGURE 4 | The variation of resistivity, at 0 kPa **(A)**, and 750 kPa **(B)** pressure, with composition, for CB-NR composites measured at different times (min, inset right).

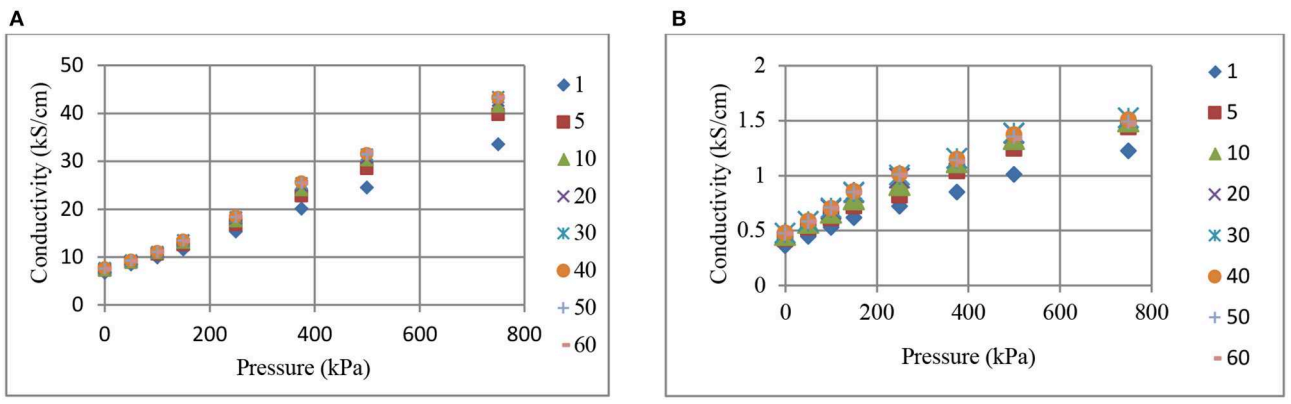

FIGURE 5 | The change in conductivity with pressure and time (min, inset right), for BR **(A)**, and NR **(B)** composites containing 70 phr CB.

Following initial high rate compressive load application, the specimen length after 1 min may be relatively higher than what is predicted by Equation (3).

Figure 6 reveals that the conductivity levels for both the CB-BR and CB-NR composites containing 70 phr CB remain relatively constant after about 20 min even if a high level of

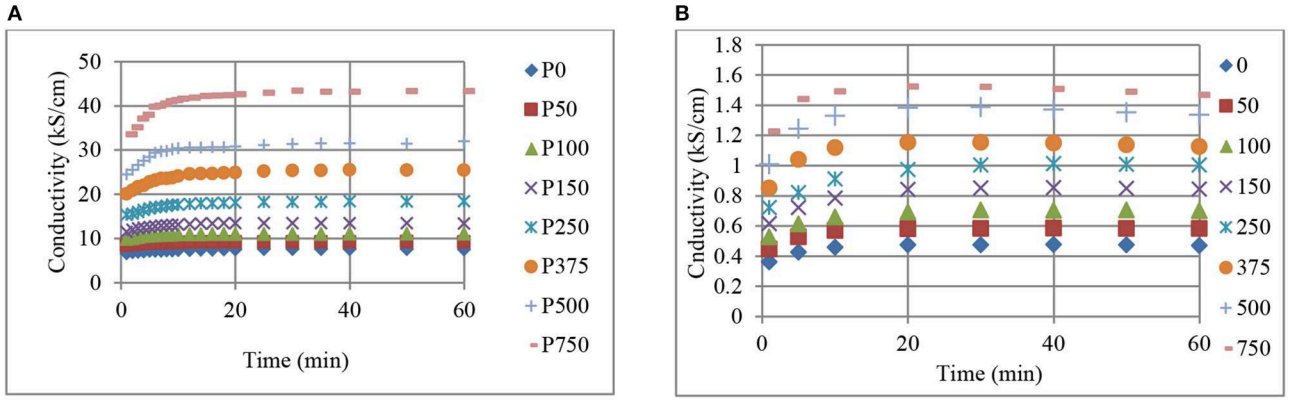

FIGURE 6 | The change in conductivity with time and pressure (kPa, inset right), for BR **(A)**, and NR **(B)** composites containing 70 phr CB.

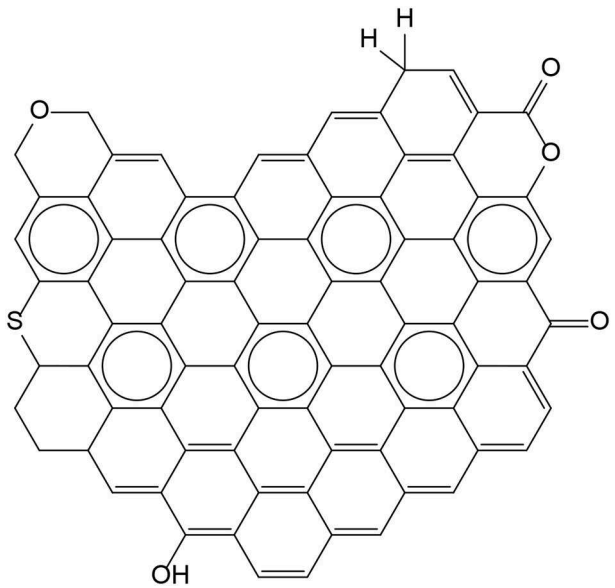

FIGURE 7 | Possible chemical functionalities of carbon black surface.

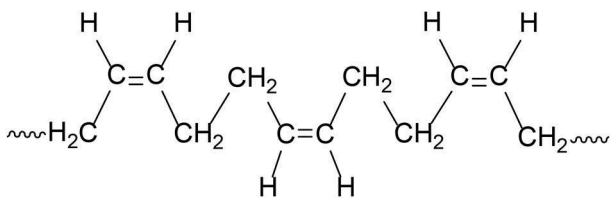

FIGURE 8 | Cis-1,4-polybutadiene.

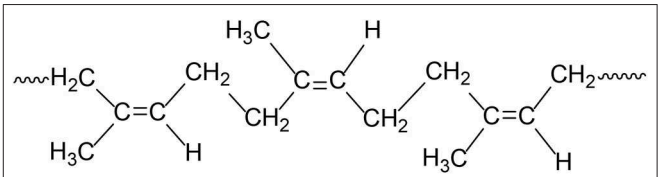

FIGURE 9 | Cis-1,4-polyisoprene.

pressure (750 kPa) is applied. The incremental increase in conductivity with pressure seems to be relatively constant with CB-NR for different time values (**Figure 6B**), while it seems to remain relatively constant for pressure values between 150 to 500 kPa for the CB-BR composite (**Figure 6A**).

Comparison of **Figures 1–6** reveal that, for the CB fill levels, pressures applied and their durations used, CB-BR compounds provide much higher electrical conductivity (σ) in comparison to the CB-NR compounds. The ratio of $\sigma_{CB-BR}/\sigma_{CB-NR}$ seemed to vary in the range of ∼18–28 when comparing different time and pressure conditions for 70 phr CB loading. This ratio was as high as ∼50 for specimens filled at 90 phr level and pressurized to 750 kPa. The overall difference in conductivity levels for the CB–BR and CB-NR compounds remain approximately unchanged for given time and pressure conditions for the cases where such high CB fill levels (∼90 phr) under high pressures (750 kPa) are used and asymptotic conductivity values are reached. These observations on conductivity variations between the CB–BR and CB-NR compounds as functions of time and pressure indicate that, overall, the conductivity levels are strongly dependent on the nature of the molecular structure of these rubber materials and their initial interactions with CB during compounding and the resulting dispersion levels of CB. Once such dispersion structure is established, a relatively constant conductivity ratio is obtained at high levels of CB fill and pressure as indicated by the $\sigma_{CB-BR}/\sigma_{CB-NR}$ ratio of ∼50 with 90 phr CB at 750 kPa. This ratio changes at lower CB fill levels and pressures ($\sigma_{CB-BR}/\sigma_{CB-NR} \cong 18$ to $\cong 28$) but the fact that $\sigma_{CB-BR} > \sigma_{CB-NR}$ remains valid.

There are a large number of reactive double bonds as well as O and OH on surfaces of carbon black fillers as shown in **Figure 7**.

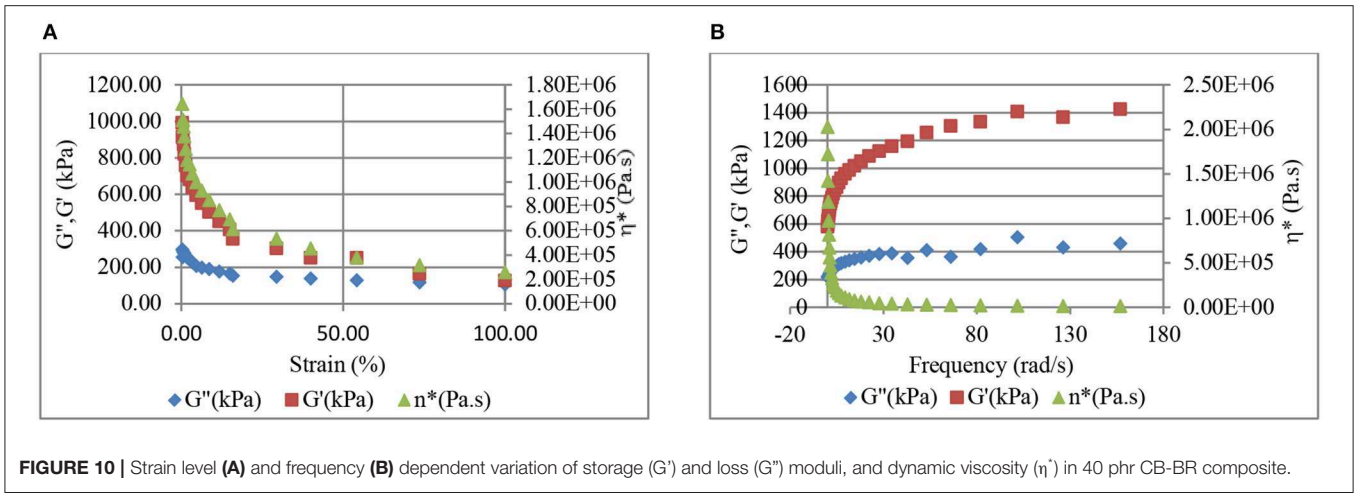

FIGURE 10 | Strain level **(A)** and frequency **(B)** dependent variation of storage (G') and loss (G") moduli, and dynamic viscosity (η^*) in 40 phr CB-BR composite.

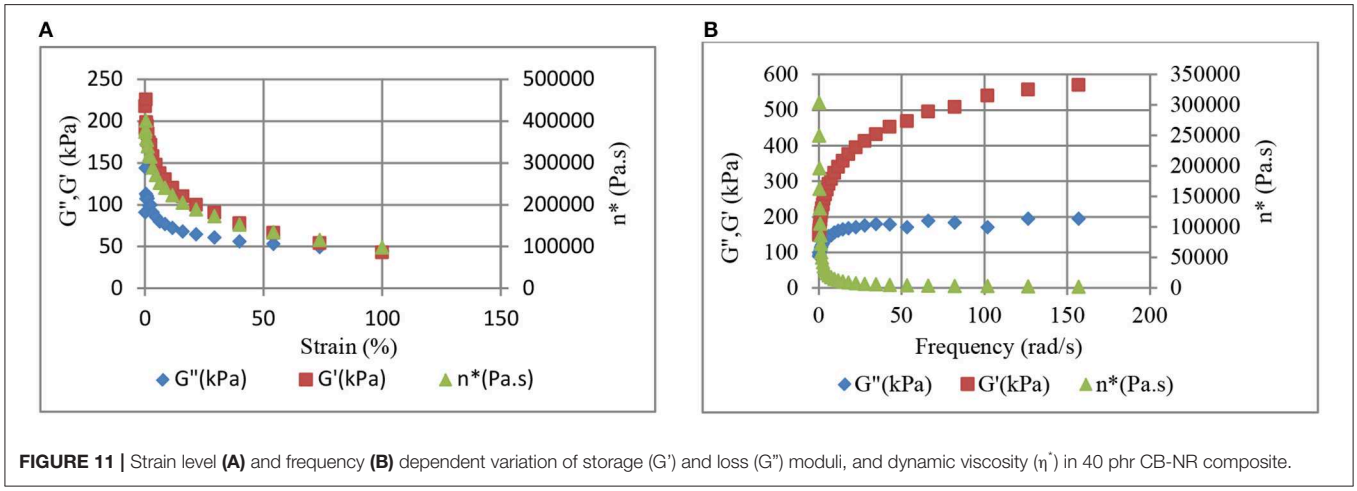

FIGURE 11 | Strain level **(A)** and frequency **(B)** dependent variation of storage (G') and loss (G") moduli, and dynamic viscosity (η^*) in 40 phr CB-NR composite.

The presence of sulfur, olefins, and radicals typically lead to the formation of covalent bonds between the CB surface and the rubber via these double bonds. O and OH sites provide hydrogen bonding. The hydrogen content built up in this manner correlates to reinforcement by carbon black (Papireb et al., 1969).

Based on our experimental results and due to the presence of higher number (∼2-fold) of hydrogen side atoms on the linear BR chains (Cis-1,4-polybutadiene, **Figure 8**), we believe that CB–BR compound forms more physical crosslinks (mostly due to hydrogen bonding) in comparison to the CB-NR (Cis-1,4-polyisoprene, **Figure 9**) compound resulting in more effective CB dispersion and higher conductivity. We note that for both Cis configurations, possible rotations about the C C bonds in CH_2 groups allow the molecules to coil upon themselves, thus resulting in disordered molecular conformations for both types of rubber materials; however, the CB particles are able to establish more effective conductive network when used with Cis-1,4-polybutadiene due to the formation of more physical crosslinks between these particles and the Cis-1,4-polybutadiene molecules as inferred based on the comparison of our rheological experiments for the CB–BR and CB–NR compounds reported in the section Correlation of Conductivity Levels with Rheological Properties for the CB–BR and CB-NR Compounds.

Correlation of Conductivity Levels With Rheological Properties for the CB–BR and CB-NR Compounds

Comparison of **Figures 10**, **11** reveals higher G' and η^* values for the CB–BR compound in comparison to the CB-NR compound. 40 phr CB was used in making this comparison. **Figures 10A**, **11A** reveal that the stiffnesses (storage moduli) for the CB-BR and CB-NR composites decrease at higher strain levels. Based on this result, we expect increases in the rate of increase in conductivity at higher pressure levels as observed in **Figure 5** for 70 phr CB and inferred from **Figures 1**, **2**. The storage modulus increases with increasing frequency (rate) for both CB-BR and CB-NR composites, as observed in **Figures 10B**, **11B**, respectively. Thus, lower rates of conductivity increase should be observed when compressive forces are applied at higher rates. These observations lead to the conclusion that the magnitude and the rate of applied pressure control

the conductive filler-induced resistivity/conductivity levels in rubber-based conductive devices.

Comparison of **Figures 10A**, **11A** reveal that the ratio of stiffnesses (storage modulus, G') for the CB-BR and CB-NR composites is $G'_{CB\text{-}BR}/G'_{CB-NR} \cong 4$ at 100% strain, indicating that the CB-BR composites should have lower conductivity in comparison to the CB-NR composites at higher pressure levels if all other effects are ignored; but, our experimental results have shown that not to be the case with $\sigma_{CB-BR}/\sigma_{CB-NR}$ ratio of ∼50 with 90 phr CB at 750 kPa. Thus, higher efficiency in CB dispersion and percolation in BR is further implied by higher conductivities despite higher G' and η^* values for the CB–BR compound in comparison to the CB-NR compound. Higher dynamic viscosities (η^*) obtained for the CB-BR composites (**Figure 10**) in comparison to the CB-NR composites (**Figure 11**) should also be considered evidence of better CB dispersion in CB-BR composites in comparison to the CB-NR composites.

CONCLUSIONS

Pressure-time dependent electrical resistivity/conductivity behavior of Carbon black (CB) filled butadiene (BR) (Cis-1,4-polybutadiene) and natural (NR) (Cis-1,4-polyisoprene) rubber compounds containing 60–100 phr CB were investigated in this work. Storage moduli, G', as well as the loss moduli, G" and the dynamic viscosities, η^* of the compounds were evaluated to assess viscoelastic response of the compounds' conductivities under pressure and at different rates. The storage and loss moduli values for both the CB-BR and the CB-NR compounds decreased with increasing strain levels, indicating that the rate of increase in conductivity is expected to increase at higher compressive loads. The storage moduli increased with increasing frequency (rate) indicating that the rate of increase in conductivity should be lower at higher rates of compressive load application. Variations in conductivities of the CB–BR and CB-NR compounds were compared as functions of time and pressure to assess whether the conductivity levels are dependent on the nature of the molecular structure of these rubber materials affecting initial rubber interactions with CB during compounding and the resulting dispersion levels of CB. Based on our experimental results, we inferred that the presence of higher number (∼2-fold) of hydrogen side atoms on the linear BR chains (Cis-1,4-polybutadiene) in comparison to NR chains (Cis-1,4-polyisoprene) helps CB–BR compound to form more physical crosslinks, mostly due to hydrogen bonding, resulting in more effective CB dispersion and higher conductivity.

Higher efficiency in CB dispersion and percolation in BR is further implied by higher conductivities of its CB compounds despite higher G' and η^* values for the CB–BR compound in comparison to the CB-NR compound. We also consider higher dynamic viscosities (η^*) obtained for the CB-BR composites in comparison to the CB-NR composites as additional evidence of better CB dispersion in CB-BR composites in comparison to the CB-NR composites.

Based on our experimental findings, we conclude that the molecular structure of the rubber, and thus the rubber type (i.e., BR vs. NR), as well as the magnitude and the rate of applied pressure control the conductive filler-induced resistivity/conductivity levels in rubber-based, pressure/time sensitive conductive devices.

DATA AVAILABILITY STATEMENT

All datasets generated for this study are included in the article/supplementary material.

AUTHOR CONTRIBUTIONS

ES conceived the theme and the investigative plan, wrote the entire manuscript, and constructed the final versions of figures and tables. SB performed the experiments, processed, and plotted the data.

REFERENCES

Basan, S., and Sancaktar, E. (2016). Electrical conductivity of carbon black - silicon rubber nanocomposites: effects of strain, load and loading rate. *Curr. Nanomater.* 1, 195–200. doi: 10.2174/2468187306666160418164202

Holm, R. (1967). *Electric Contact*. New York, NY: Springer-Verlag. doi: 10.1007/978-3-662-06688-1

Morton, M. (1987). *Rubber Technology*. New York, NY: Von Nostrand Reinhold. doi: 10.1007/978-1-4615-7823-9

Papireb, E., Voet, A., and Given, P. H. (1969). Transfer of labeled hydrogen between elastomers and carbon black. *Rubber Chem Technol* 41, 1200–1208. doi: 10.5254/1.3539290

Sancaktar, E., and Bai, L. (2011). Electrically conductive epoxy adhesives. *Polymers* 3, 427–466. doi: 10.3390/polym3010427

Sancaktar, E., and Dilsiz, N. (1999a). Pressure dependent conduction behavior of various particles for conductive adhesive applications. *J. Adhes. Sci. Technol.* 13, 679–693. doi: 10.1163/156856199X00938

Sancaktar, E., and Dilsiz, N. (1999b). Thickness dependent conduction behavior of various particles for conductive adhesive applications. *J. Adhes. Sci. Technol.* 13, 763–771. doi: 10.1163/156856199X00992

Sancaktar, E., and Wei, Y. (1996). The effect of pressure on the initial establishment of conductive paths in electronically conductive adhesives. *J. Adhes. Sci. Technol.* 10, 1221–1235. doi: 10.1163/156856196X00201

Sancaktar, E., Wei, Y., and Gaynes, M. A. (1996). Conduction efficiency and strength of electronically conductive adhesive joints. *J. Adhes.* 56, 229–246. doi: 10.1080/00218469608010510

Timoshenko, S. P., and Goodier, J. N. (1970). *Theory of Elasticity*. New York, NY: McGraw-Hill.

Wei, Y., and Sancaktar, E. (1996). Dependence of electric conduction on film thickness of conductive adhesives: modeling, computer simulation, and experiment. *J. Adhes. Sci. Technol.* 10, 1199–1219. doi: 10.1163/156856196X00193

White, J. L. (1995). *Rubber Processing*. New York, NY: Hanser.

Conflict of Interest: The authors declare that the research was conducted in the absence of any commercial or financial relationships that could be construed as a potential conflict of interest.

Copyright © 2019 Sancaktar and Basan. This is an open-access article distributed under the terms of the Creative Commons Attribution License (CC BY). The use, distribution or reproduction in other forums is permitted, provided the original author(s) and the copyright owner(s) are credited and that the original publication in this journal is cited, in accordance with accepted academic practice. No use, distribution or reproduction is permitted which does not comply with these terms.

frontiers in Materials

ORIGINAL RESEARCH
published: 04 February 2020
doi: 10.3389/fmats.2020.00012

Fused Filament Fabrication of Piezoresistive Carbon Nanotubes Nanocomposites for Strain Monitoring

*Sithiprumnea Dul, Alessandro Pegoretti and Luca Fambri**

Department of Industrial Engineering and INSTM Research Unit, University of Trento, Trento, Italy

Conductive carbon nanotubes (CNT)/acrylonitrile butadiene styrene (ABS) nanocomposites parts were easily and successfully manufactured by fused filament fabrication (FFF) starting from composite filaments properly extruded at a laboratory scale. Specific specimens for strain monitoring application were properly evaluated in both short term and long term mechanical testing. In particular, samples of ABS filled with 6 wt.% of CNT were additively manufactured in two different infill patterns: HC (0°/0°) and H45 (−45°/+45°). The piezoresistivity behavior was investigated under various loading conditions such as ramp tensile tests at different rate and extension, and also creep and cyclic loading at room temperature. Experimental work revealed that the resistance changes in the conductive samples were properly detectable during stress or strain modification, as consequence of damage and/or reassembling of the percolation network. The measurement of the gauge factor in various testing conditions evidenced an initial higher sensitivity of the 3D-built parts within H45 pattern in comparison to the correspondent HC counterparts. The CNT conductive network path in the investigated samples seems to be reformed during creep and cycling experiments, showing a progressive reduction of gauge factor that seems to stabilize at about 2.5 for both HC and H45 samples after long term testing. These findings suggest that conductive CNT/ABS nanocomposites at 6 wt.% of loading can be successfully processed by FFF to produce stable strain sensors in the range −25° and +60°C, as confirmed by the constancy of resistivity in these temperatures.

Keywords: strain sensor, conductive composites, carbon nanotubes, fused filament fabrication, gauge factor, 3D printing

OPEN ACCESS

Edited by:
Sébastien Livi, Institut National des Sciences Appliquées de Lyon (INSA Lyon), France

Reviewed by:
Jean-Marie Raquez, University of Mons, Belgium
Mariana Amorim Fraga, Federal University of São Paulo, Brazil

****Correspondence:***
Luca Fambri
luca.fambri@unitn.it

Specialty section:
This article was submitted to Polymeric and Composite Materials, a section of the journal Frontiers in Materials

Received: *19 April 2019*
Accepted: *14 January 2020*
Published: *04 February 2020*

Citation:
Dul S, Pegoretti A and Fambri L (2020) Fused Filament Fabrication of Piezoresistive Carbon Nanotubes Nanocomposites for Strain Monitoring. Front. Mater. 7:12. doi: 10.3389/fmats.2020.00012

INTRODUCTION

Polymer composites with carbonaceous micro and nano-scale reinforcement have been extensively investigated due to their outstanding mechanical, electrical, and thermal properties. In particular, nanocomposites not only have remarkable properties that can be tailored for broad application in many fields, but their processability is also simple. Nanocomposites could help the development of light-weight structural materials and functional materials (Park and Seo, 2012; Mittal et al., 2015; Chen et al., 2018; Mohan et al., 2018). One interesting possibility offered by functional nanocomposites is to exploit their piezoelectric response for structural health monitoring (SHM) (Pegoretti, 2019). Sensing internal strain/stress can allow the detection of damage within a

structural member during their lifetime (Georgousis et al., 2015; Moriche et al., 2016b; Saleh et al., 2019). This self-sensing with functional materials in fact, is a cost-effective method in comparison to other SHM methods such as acoustic emission or sonic infrared imaging.

Strain sensing with electrical conductive nanocomposites is based on the electrical resistance changes induced by deformation (piezoresistivity) and damages (loss of continuity) under loading conditions. The piezoresistivity behavior in nanocomposites is induced by the destruction of the conductive networks of nanofiller, the modification of tunneling resistance change in neighboring nanoparticles because of change of distance between them, and changes in piezoresistive of nanofillers themselves during applied deformation. Among these three factors, the first two are most likely the most influential on the electrical resistance upon mechanical deformation (Georgousis et al., 2015). The common matrices used for strain sensor materials can be thermosetting (Ku-Herrera and Avilés, 2012; Moriche et al., 2016b; Sanli et al., 2016), thermoplastics (Georgousis et al., 2015; Bautista-Quijano et al., 2016; Dawoud et al., 2018), and elastomers (Bautista-Quijano et al., 2010, 2013; Oliva-Avilés et al., 2011; Alsharari et al., 2018; Christ et al., 2019; Kim et al., 2019).

In recent years, increasing interest has focused on the producing of sensors through 3D printing technology or embedding 3D-printed components to traditional sensors. The main applicative areas are represented by electronics, force, motion, hearing, optics, etc… (Xu et al., 2017). 3D printing sensors have been achieved by several methods such as fused filament fabrication (FFF) (Alsharari et al., 2018; Dawoud et al., 2018), direct ink writing (DIW) (Muth et al., 2014), stereolithography (SLA) (Lee et al., 2015), laminated object manufacturing (LOM) (Park et al., 2012), selective laser sintering (SLS) (Ambrosi et al., 2016), photopolymer jetting (Polyjet) (Laszczak et al., 2015), and binder jetting (3DP) (Rivadeneyra et al., 2015). The frequently used conductive fillers for strain sensing applications are metal nanoparticles [e.g., silver (Lee et al., 2015), copper (Credi et al., 2016; Saleh et al., 2019), and Ti/Au (Cho et al., 2015)] and carbon-based fillers [e.g., carbon nanotubes (CNT) (Czyżewski et al., 2009; Bautista-Quijano et al., 2010; Oliva-Avilés et al., 2011; Pedrazzoli et al., 2012a; Zhao et al., 2013; Georgousis et al., 2015), carbon nanofibre (Pedrazzoli et al., 2012a), graphene (Moriche et al., 2016a,b; Alsharari et al., 2018), and carbon black (Dawoud et al., 2018; Zhao et al., 2018)]. In particular, however, only few reports are available on piezoresistive materials obtained through FFF technique, which is the dominated technique in 3D printing of polymers. Highly stretchable materials consisting of the blend of graphene-based polylactic acid (PLA) with thermoplastic polyurethane (TPU) were produced through the FFF process (Alsharari et al., 2018). The behavior of the obtained 3D-printed conductive composites was reversible until strain levels as high as 50%. Strain sensing of carbon black (CB) filled acrylonitrile butadiene styrene (ABS) nanocomposites was also investigated (Dawoud et al., 2018). The 3D-printed parts were produced with different raster angles and air gap parameters. PLA-carbon based nanocomposites derived from 3D printing have been also investigated on electrical and/or thermal conductivity (Guo et al., 2019; Ivanov et al., 2019). In order to produce strain sensor by using PLA conductive composites (Maurizi et al., 2019), the dependence of piezoresistive behavior on temperature should be properly considered. In particular taking into consideration the Tg of PLA matrix, a specific approach to compensate the temperature effect on resistivity of PLA conductive sample in the range 20–50°C has been discussed (Daniel et al., 2018; Coleman et al., 2019). The crucial effect of heating and distorsion in PLA conductive composites after voltage application has been recently detailed in dependence on the various process factors (extrusion and additive manufacturing); the authors compared the role of conductive filler (carbon black, carbon nanotubes, and nano copper wires) on resistivity in view of application for thermal sensors and piezo-resistive sensors (Watschke et al., 2019). Commercial graphene-PLA filaments with resistivity of 0.6 Ω.cm, are designed to be used for room-temperature operation, due to the low softening temperature (50°C), and for low-voltage and low-current only (lower than 12 volts and 100 mA, respectively)[1]. The use of low-cost conductive composite (Carbomorph) based on polycaprolactone with resistivity of 9–12 Ω.cm is also limited for piezoresistive sensors at room temperature, or at lower temperature, due to melting temperature of polymer matrix (65°C) (Leigh et al., 2012). In order to enlarge the application fields with high performance properties, especially for high temperature, a different approach was recently proposed with the processing and 3D printing up to 380°C of thermoplastic polyimide (TPI) filled with CNT; the change of resistance under cyclic bending deformation were properly studied and considered for aerospace application (Ye et al., 2019). A commercial filament Proto-Pasta PLA filled with carbon black was 3D printed as a strain sensor (Munasinghe et al., 2019). The authors determined a nearly linear relationship between the electrical resistance (up to 6.05%) and the strain; in the same time, they concluded that a long term suitability of sensor materials for creep loading and a better understanding of their viscoelastic behavior would be object of future research.

In our previous works, highly conductive ABS/CNT nanocomposites with 6 wt.% of nanofillers were successfully 3D-printed through FFF process and their extensive characterization including tensile, thermal and electrical properties was reported (Dul et al., 2018a). The composition percentage of 6 wt.% of CNT was properly selected in the tested range 2–8% wt.%, as an adequate compromise between the improvement of some properties after addition of the filler, and the correspondent reduction of composite processability, as evidenced by the critical decrease of melt flow (Dul et al., 2018b) and melt viscosity (Ecco et al., 2018). Electrical and magnetic properties of both graphene and CNT nanocomposites were studied and compared in view of EMI-SE applications (Ecco et al., 2018). Moreover their hybrid 6 wt.% nanocomposites with composition of graphene and CNT were also considered, in order to define suitable composites with relatively easy flowability for low CNT content, and adequate

[1]BlackMagic3D® PLA-Graphene conductive filaments from https://www.blackmagic3d.com/Conductive-p/grphn-pla.htm. (accessed on 14th September 2019).

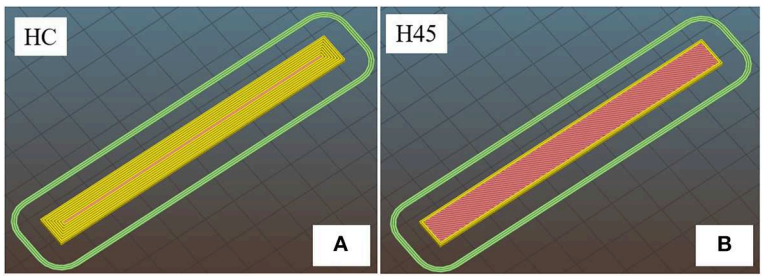

FIGURE 1 | Schematic of 3D-printed parallelepiped: **(A)** horizontal concentric (HC) and **(B)** horizontal 45°angle (H45).

electrical and magnetic properties for high CNT content (Dul et al., 2020). Another recent work reported about piezoresistivity of ABS filled with 5% CNT nanocomposites through 3D printing with resistivity of about 100 Ω.cm. The authors studied and compared a balanced effect of filler content and process on the fracture properties and on the samples conductivity (Thaler et al., 2019). On the other hand, a much lower resistivity in the range of about 29 and 0.9 Ω.cm was obtained for CNT/ABS plates with composition between 2 and 8 wt.% of nanofiller, respectively (Dul et al., 2018b).

Therefore, in the actual scenario of the additive manufacturing for the fabrication of conductive and functional parts, the present work has been also devoted for a specific evaluation of various effects, such as temperature, applied strain rate and loading/unloading cycles. In particular, the strain monitoring of ABS nanocomposites at 6 wt.% of CNT prepared by FFF technique has been investigated. Two different raster angles and different testing conditions cyclic test were evaluated and compared to test the piezoresistive behavior of 3D-printed parts, not only in short term testing (i.e., temperature effect, fracture test, and applied strain rate), but also in long term testing such as creep experiments and cycling test, for the evaluation and evolution of gauge factor.

EXPERIMENTAL

Materials

Carbon nanotube (CNT) (tradename NC7000™ multi-walled carbon nanotubes) were provided by Nanocyl S.A. Sambreville, Belgium). The technical data sheet[2] reports an average length of 1.5 μm, a diameter of 9.5 nm and a surface area of 250–300 m^2/g. TEM analysis is reported in literature (Dul et al., 2018b).

Acrylonitrile-butadiene-styrene (ABS) with tradename Sinkral®F322, used in this study as polymer matrix, was kindly provided by Versalis S.p.A. (Mantova, Italy). According to the producer's technical data sheet[3], the polymer is characterized by a melt volume rate of 14 cm^3/10 min (220°C/10 kg) and a density of 1.04 g/cm^3. Before processing, ABS chips were dried under vacuum at 80°C for at least 2 h.

Materials Processing and Sample Preparations

Production of Filament Nanocomposites

An selected composition (Dul et al., 2018b; Ecco et al., 2018) of 6 wt.% of CNT were first melt blended with ABS matrix through a Thermo-Haake Polylab Rheomix counter-rotating internal mixer at a temperature of 190°C and rotor speed of 90 rpm for 15 min. The resulting material was granulated in a Piovan grinder Model RN 166 and grinded pieces with average size of 2.1 ± 0.6 mm) were used to feed a Thermo Haake PTW16 intermeshing co-rotating twin screw extruder (screw diameter = 16 mm; L/D ratio = 25; nozzle die diameter 1.80 mm). The temperature profile was set in the range 180–215°C along the extruder and 220°C at the nozzle. The working parameters of extrusion were set for the production of filaments with a standard diameter of about 1.70 ± 0.05 mm.

3D-Printed Samples Preparation

3D-printed specimens were manufactured by feeding a Sharebot HT Next Generation desktop (Sharebot NG, Italy) prototype machine for high-temperatures with the filaments obtained as described in the previous paragraph. As schematically depicted in **Figure 1**, dumbbell and parallelepiped specimens were built-up along different orientations: (a) horizontal concentric (HC), and (b) horizontal 45°angle (H45). All samples were produced according to the following printing parameters: object infill 100%; nozzle diameter 0.40 mm; nozzle temperature 280°C; bed temperature 110°C, layer height 0.20 mm; infill speed 40 mm/s; raster angle of [0°/0°] and [−45°/+45°], respectively.

Testing Techniques

Transmission Electron Microscopy

Morphology of nanocomposite filament was observed through transmission electron microscopy (TEM), using a Philips® EM 400 T (Philips, Amsterdam, The Netherlands) transmission electron microscope. Ultrathin specimen was cut into thin slices with dimensions of about 200 × 150 μm perpendicular and parallel to the flow direction by using a Leica EM UC7 ultramicrotome equipped with a diamond knife. Specimens were

[2]Nanocyl®NC7000TM (2016) Multiwall Carbon Nanotubes Product Data from http://www.nanocyl.com/wp-content/uploads/2016/07/DM-TI-02-TDS-NC7000-V08.pdfXG (accessed on 15th April 2019).

[3]Versalis S.p.A SINKRAL® F 322- ABS Product Data from https://www.materialdatacenter.com/ms/en/Sinkral/Versalis+S%252Ep%252EA/SINKRAL%C2%AE+F+332/c6da6726/1895 (accessed on 15th April 2019).

deposited on a copper grid mesh covered by amorphous holey carbon film.

Electrical Resistance (Effect of Temperature)

The electrical resistance at various temperatures of 3D-printed sheets (100 × 10 × 1.4 mm) was measured by a two probes method by using ISO-TECH IDM 67 Pocket Multimeter electrometer in fridge (at −25 and +4°C) and in oven (at +60°C). HC and H45 specimens were conditioned at the selected temperature for at least 30 min before testing.

Dynamic Mechanical Thermal Analysis (DMTA)

Dynamic mechanical thermal analysis (DMTA) tests were carried out under tensile mode by a TA Instruments DMA Q800 device, in the range from −100 to 150°C at a heating rate of 3°C/min applying a dynamic maximum strain of 0.05% at a frequency of 1 Hz. Storage modulus (E') and loss tangent (tanδ) as a function of the temperature were reported. 3D-printed specimen sizes were detailed in the reference (Dul et al., 2018a). One HC specimen and one H45 specimen were tested.

Strain Monitoring

The monitoring of the change of electrical resistance upon the application of mechanical strain was performed on the conductive composites specimens in short term and long term experiments. The results represent the average of at least three specimens. 3D-printed sheets of 100 × 10 × 1.4 mm were tested by using an Instron®5969 electromechanical testing machine with the distance between the grips kept at 50 mm under quasi-static ramp tensile tests up to fracture, sinusoidal cyclic loading and creep tests. The ramp tests up to fracture were performed at a strain rate of 1%/min. Stress and strain at break are reported as average of three specimens (**Supplementary Table S-2**). For ramp strain, creep and cyclic test, the strain was measured by using the extensometer Instron® model 2620-601 with a gauge length of 12.5 mm with various strain rate (i.e., 0.3, 1, 3, and 10%/min). The results represent the average of five specimens (**Supplementary Table S-3**). The creep tests were performed by using the same equipment on specimens at a constant stress of 20 MPa at room temperature up to 3,600 s. A two probes setup was employed for the electrical resistance measurement at a very low voltage of 0.1 V. To ensure good electrical contact, a silver paste was applied on the surface of the conductive samples at a distance of 30 mm (see **Figure 2A**), and the electrical resistance was measured using a Keithley 6517A high-resistance meter as shown in **Figure 2.**

A gauge factor (K) was calculated by using the following equation:

$$K = \frac{\Delta R/R_0}{\varepsilon}$$

where R_0 is the initial electrical resistance, ΔR is the variation of electrical resistance, and ε is the applied or measured strain. Gauge factor has been evaluated in both short term (quasi static) test, as average values of at least three specimens, and in long term test, such as creep and cycling measurements. See representative details of the slope of best fit line of experimental $\Delta R/R_0$ in figures; tables with data of each specimen are reported in **Supplementary Materials**.

RESULTS AND DISCUSSIONS

Before studying the piezoelectrical behavior, morphological analysis of filaments, conductivity/resistivity measurements at various temperature and dynamical mechanical thermal analysis of 3D printed specimens were preliminarly considered.

An initial morphological analysis was performed on composite filament as extruded by twin screw extruder. **Figure 3** shows TEM microanalysis of parallel surface of CNT/ABS 6 wt.%, and various carbon nanotubes appear almost randomly dispersed with some point of contact, with evidence of a

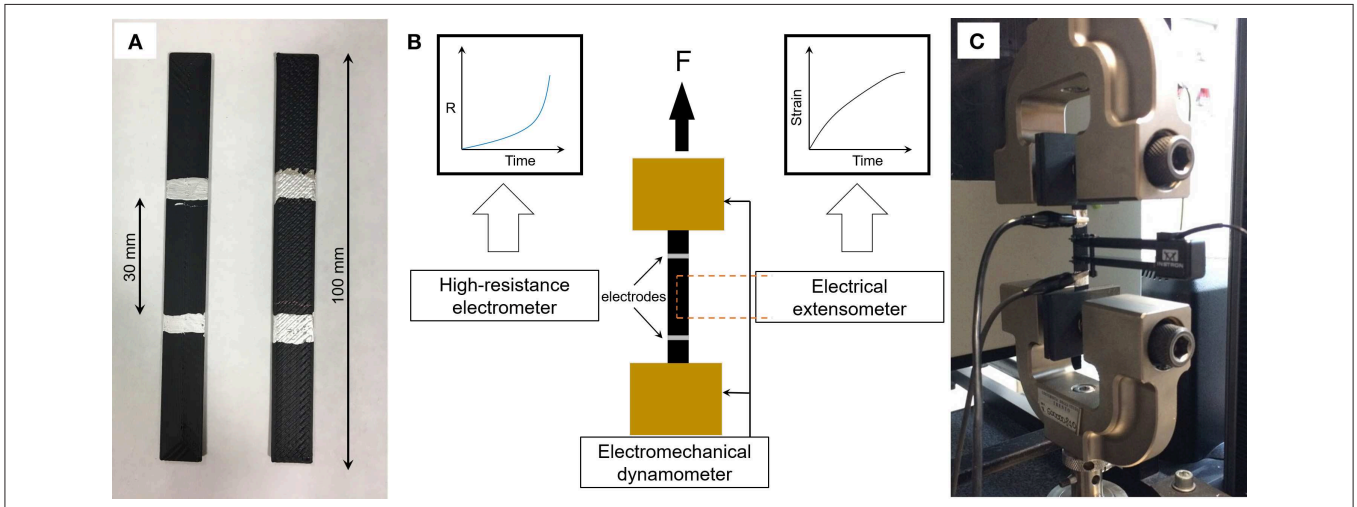

FIGURE 2 | Experimental setup for the strain monitoring: **(A)** Specimens after conductive paint; **(B)** Schematic of experimental setup; and **(C)** Actual setup in tensile test.

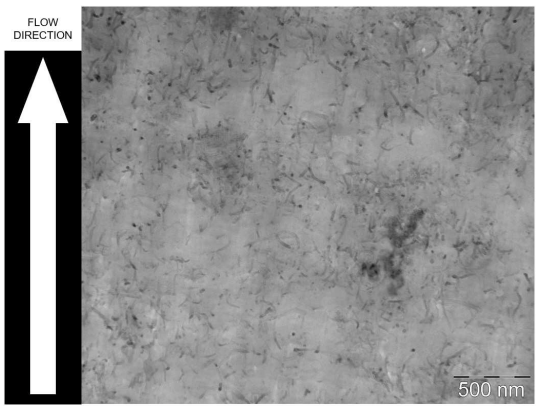

FIGURE 3 | TEM micrograph of ABS/CNT nanocomposite filament in parallel section.

connective path. **Supplementary Figures** are also showing the distribution and connection of CNT in both perpendicular and parallel cross-section. It should be noted that the percolation threshold of CNT in ABS has been determined at 0.42 vol.% and no electrical conductivity has been observed for CNT content lower than 2 %wt. (Dul et al., 2018b).

Then, in order to confirm the conductivity of 3D-printed samples, their electrical resistivity was assessed at values of 17.2 ± 1.5 and 31.2 ± 4.9 Ω.cm for HC and H45 items, respectively. As expected these values are higher than the values previously determined on compression molded plates (1.5 Ω.cm) (Dul et al., 2018b), and on the extruded filaments (4.1 Ω.cm) (Dul et al., 2018a). The increase of resistivity of extruded specimens could be attributed to the higher level of anisotropy and alignment in nanocomposite filaments, with respect to the molded plates where conversely CNT are isotropically distributed, as documented in literature (Georgousis et al., 2015; Sanli et al., 2016; Dul et al., 2018b). Moreover, the processing effect is further evidenced in 3D printed specimens and it is directly attributed to the internal structure of FFF samples. In fact, the resistance R_0 of 3D-printed samples has been found to be dependent on the manufacturing infill pattern, as summarized in **Table 1**. In particular, significant different average resistances were observed, being 387 ± 34 Ω for HC and 671 ± 106 Ω for H45 samples, respectively. The relatively low standard deviation confirms the quality and the good homogeneity and reproducibility of the manufacturing process.

Moreover, in order to better understand the performances at various temperatures, the results of dynamic mechanical analysis on 3D-printed specimens is briefly presented and discussed. The storage modulus and loss factor values of ABS/CNT nanocomposites as a function of temperature are reported in **Figure 4**. Two transitions can be observed as loss tangent peaks which can be attributed to the glass transition of butadiene phase (B-phase; $T_{g1} = -84°C$) and the glass transition of styrene–acrylonitrile phase (SAN phase; $T_{g2} = 125°C$), respectively. This means that at room temperature, the behavior of ABS is depending on the concurrent effects of

TABLE 1 | Summary of initial resistance values (R_0) at room temperature of the 3D-printed samples produced in HC and H45 configuration.

Type test	R_0 (Ω)	
	HC	H45
Temperature effect	321	685
Tensile fracture	403, 336, 402	498, 601, 786
Ramp strain (0.3–10%/min)	352, 406, 389, 423, 413	791, 626, 857 681, 582
Cyclic strain	407	603
Creep mode	402	669
Average	387 ± 34	671 ± 106

The type of testing is indicated for each specimen.

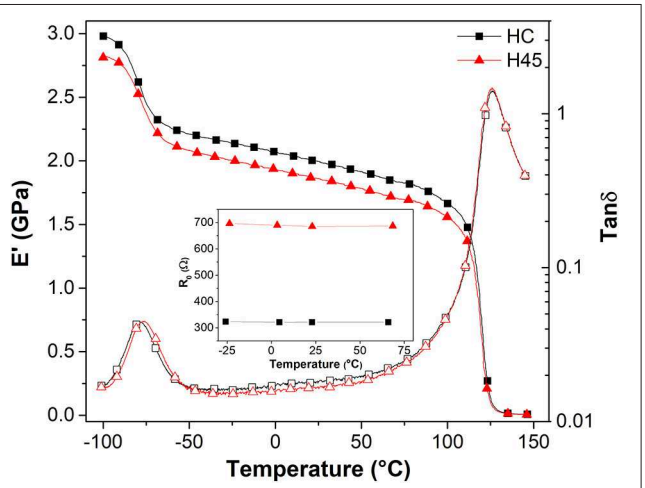

FIGURE 4 | DMA analysis of samples for evidencing the main viscoelastic properties of samples at a different temperature, and resistance of HC and H45 3D-printed parts in the range −20 and +60°C.

two different phases, rubbery and glassy, respectively. DMTA thermogram reveals that in the range −45/+75°C between two main transitions both storage modulus and loss factor evidence only a slight linear dependence without any other secondary transition. Consequently, taking also into account that the maximum using temperature is 83°C (determined by HDT at 1.8 MPa according to technical data sheet), precautionally the interval −25–60°C evidenced in **Figure 4** has been selected for investigating electrical resistance and mechanical response.

Two parallelepiped specimens built-up along different orientations, HC and H45 with resistance of 321 and 685 Ω, respectively, were selected for monitoring their electrical behavior in various isothermal conditions. The results are showed in the inset of **Figure 4**. No significant change in resistance was observed at 60°C; and only a very low variation of resistance of about +0.7 and +1.6% for HC and H45 samples, respectively, were evidenced at the lowest temperature. This behavior suggested that the performance of samples is stable in the selected range of temperature in direct dependence on the absence of transitions, as indicated by DMTA analysis.

On the other hand conductive PLA devices evidenced significant variations of resistivity with temperature and some specific corrections have been properly suggested for analysis up to 50°C (Daniel et al., 2018). For these findings, ABS conductive nanocomposites appears more suitable for application at least up to 60°C, being the polymer matrix in the glassy state until about 90°C.

Short Term Testing Ramp Tensile Tests Up to Fracture and at Various Strain Rates

In order to investigate the effect of applied strain on the conductivity behavior, the 3D-printed nanocomposite samples (HC and H45) were tested in various mechanical loading modes; their resistivity and the initial absolute resistance were simultaneously monitored by two probe contact method. Stress-strain behavior and relative electrical resistance variation ($\Delta R/R_0$) during quasi-static tensile tests on HC and H45 samples are reported in **Figure 5**. Gauge factor of each test was calculated as the slope of best fit line of $\Delta R/R_0$ (coefficient of correlation R^2 is reported). Due to internal alignments of deposited filaments in 3D samples, the strength of HC is slightly higher than that of H45 sample. Furthermore, tensile stress applied to 3D-printed nanocomposites causes a linear increment of the relative change of electrical resistance ($\Delta R/R_0$) until the fracture point for both samples. This behavior could be explained by the destruction of percolating paths forming the conducting network (Georgousis et al., 2015). It is important to note that H45 is more sensitive to strain change than HC due to the different infill pattern. For example, for strain of 2%, $\Delta R/R_0$ for the sample with HC is about 5.3% and for the sample with H45 is about 8.8%. The results are reported in **Table 2**, as average of three specimens at applied strain levels of 1, 2, and 3%. The gauge factor was found to slightly decrease with the applied strain for all the specimens (the values of each single test are reported in **Supplementary Materials**). Reduction of gauge factor from 2.8 to 2.4 for HC, and reduction from 4.5 to 3.2 for H45 samples were measured. Failure of the nanocomposites was detected as a pronounced increased of the electrical resistance in correspondence to the breakage of the specimen. These findings suggest potential application of this strain monitoring approach where detection of the level of damage is requested.

The relative change of electrical resistance ($\Delta R/R_0$) of 3D-printed samples under ramp strain measured by an electrical extensometer up to 1% at different applied strain rate (e.g., 0.3, 1, 3, and 10%/min) has been investigated and the results reported in **Figure 6**. No evident variations of $\Delta R/R_0$ with the strain rate have been observed. **Figures 7A,B** depicts representative curves of the relative resistance change of $\Delta R/R_0$ during stress/strain test performed at 0.3%/min. Gauge factor of each test was calculated as the slope of best fit line of $\Delta R/R_0$ (coefficient of correlation

TABLE 2 | Gauge factor (K) of ABS/CNT 3D-printed samples produced in HC and H45 configuration.

	HC	H45
MAX STRAIN (%)		
1	2.7 ± 0.4	4.5 ± 0.2
2	2.5 ± 0.1	3.5 ± 0.5
3	2.4 ± 0.2	3.5 ± 0.8
STRAIN RATE (%/MIN)		
0.3	5.4 ± 1.0	7.8 ± 1.4
1	6.0 ± 1.2	9.7 ± 2.6
3	4.0 ± 1.3	7.8 ± 3.2
10	4.4 ± 1.4	6.4 ± 0.8

The results represent the average values of at least three specimens from short term measurements at different strain (ε) up to fracture without estensometer, and at different strain rate (0.3–10%/min) up to 1% with estensometer. The results of each specimen are reported in ***Supplementary Materials*** *with the value of R^2, calculated from the average of three specimens for Max Strain (either HC or H45) and average of five specimens for Strain rate (either HC or H45) measurements.*

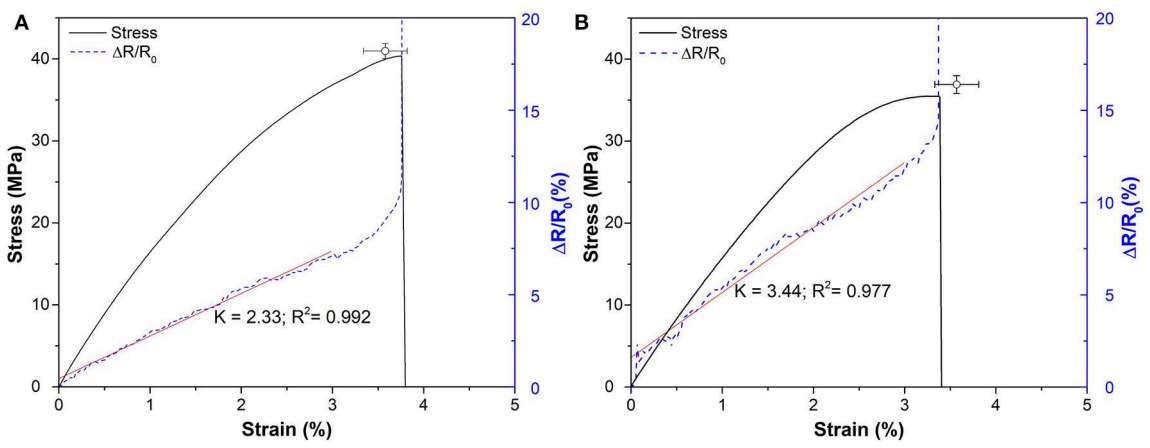

FIGURE 5 | Representative stress/strain curve and correspondent electrical resistivity change ($\Delta R/R_0$) of 3D-printed ABS/CNT nanocomposites under applied strain up to fracture: HC **(A)** and H45 **(B)**. Symbol indicates the average stress-strain at break of the three tested specimens. Gauge Factor is determined by the slope of the best fitting line.

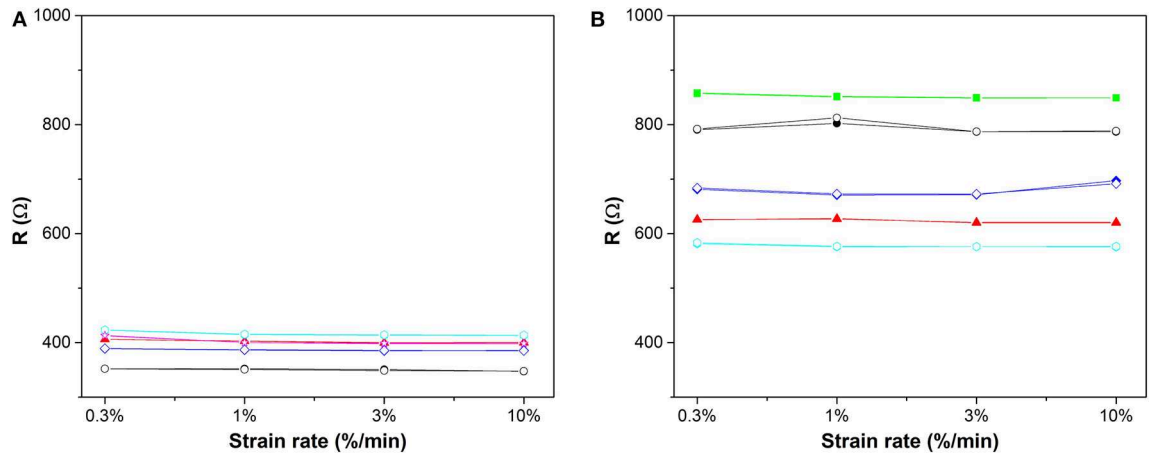

FIGURE 6 | Resistance of 3D-printed parts before (open symbol) and after (closed symbol) applied mechanical strain at different strain rate tests: HC **(A)** and H45 **(B)**. The error is lower than about 1%.

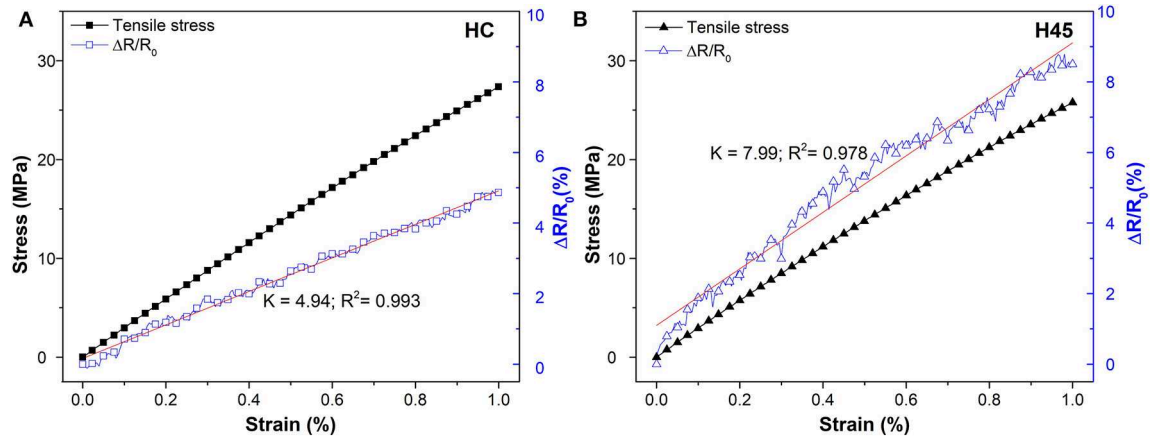

FIGURE 7 | Representative curves of mechanical and electrical ($\Delta R/R_0$) response of 3D-printed ABS/CNT nanocomposites HC **(A)** and H45 **(B)** during tensile test at 0.3%/min. Gauge Factor is determined by the slope of the best fitting line.

R^2 is reported). All single data with R^2 in the range 0.95–0.99 and their average are reported in **Supplementary Materials**. The higher the applied stress, the higher the resistance change, with an almost linear dependence for both the pattern specimens. However, it is well evident the different effect of the resistance variation of HC with respect to H45 sample, due to higher reduction of the conductivity in this latter case. It is worthwhile to note for a comparative evaluation, that the gauge factor, K, has been determined for each pattern configuration according to the formula ($K = (\Delta R/R_0)/\varepsilon$) as an average value of five specimens. The results reported in **Table 2** indicate a higher piezo-resistivity for H45 3D-printed parts. In particular, the high sensitivity of the $\Delta R/R_0$ curve even at low deformation levels should be underlined. The effect of strain rate of 0.3–10%/min has no significant influence on gauge factor which remains almost constant about 5.0 and 7.0 for HC and H45, respectively. These results are consistent with those reported in different studies by Georgousis et al. (2015), Oliva-Avilés et al. (2011), Bautista-Quijano et al. (2010), and Moriche et al. (2016b).

Long Term Testing. Creep and Cyclic Loading

Specific comparative tests have been modulated by measuring piezoresistivity of different specimens in a relatively long period with a continuous stress or cyclic loading at low level of deformation, in order to collect more information on the potentiality of strain monitoring applications of CNT/ABS nanocomposites. The performance of the samples under constant stress has been characterized during a creep test at room temperature for 3,600 s. The same stress of 20 MPa corresponding to about 50% of the stress at break has been selected for both samples. It should be noted that 20 MPa are reached at about 1.3% (**Figure 5**) and at about 0.7% of strain (**Figure 7**) at deformation rate of 1 and 0.3%/min, respectively. A creep strain of about 0.7 and 0.9% has been obtained after about

10 min of stress application for HC and H45 samples, respectively (see **Supplementary Figure S-2**). Moreover, it is worth noting an apparent stationary deformation for HC sample, and a slight progressive increase of creep deformation in the case H45 sample, as direct dependence on the different built-in angle (45° vs. 0°) and on the possibility of reorientation/extension of extruded filaments. And correspondingly the creep compliance, D(t), of HC sample is lower than that of H45, as shown in **Figures 8A,B**. In the same time the relative electrical resistance variation during creep experiments, after an initial sudden increase induced by the load application, the resistance $\Delta R/R_0$ appears to progressively decrease for both HC and H45 samples. This trend has been also previously observed in creep experiment of epoxy nanocomposites filled with carbon black (CB) and carbon nanofibers (Pedrazzoli et al., 2012b) and for epoxy/glass composites modified with a CB/CNF combination (Pedrazzoli et al., 2012a), and it could be attributed to the orientation and partial reformation of the conductive network path of the filler (Pedrazzoli et al., 2012a). Correspondingly the calculated Gauge Factor shows the tendency to decrease during creep time **Figure 8C**. In the initial step after 10 min, average values of 4.6 ± 0.1 and 6.5 ± 0.2 were calculated for HC and H45, respectively, quite similar to those measured in short term test at the higher strain rate (**Table 2**). Then an apparent stabilization was observed after 30 min (3.9 ± 0.2 for HC and 6.0 ± 0.2 for H45), and a slight further reduction in the last 15 min of creep experiments was determined with average values of 3.6 ± 0.3 for HC and 5.5 ± 0.3 for H45.

The resistivity decrease could be interpreted as a process of filler reorganization, similar to the case of NR and SBR, where the application of load determined the formation of new electrical path derived from alignment of CB domain (Yamaguchi et al., 2003). The same was observed for CNT in TPU (Zhang et al., 2013).

For sensor application various authors performed cycling test on conductive nanocomposites. **Table 3** summarized some selected data of resistivity, gauge factor and long term testing on different polymeric matrix, such as crosslinked materials (epoxy and vinyl ester resins, silicon rubber SR) and thermoplastics polymers (PSO, TPU, PVDF, PP, PC, PLA, PI, and ABS) that have considered for applications related to the piezoelectrical behaviors. The results depend on the type of carbonaceous filler (mainly MWCNT), its content and the type of process. Long time testing with cycling has been performed following 3–10 cycles, and different effects have been observed comparing carbon black and carbon nanotube (Zhang et al., 2013; Zhao et al., 2013). A higher number of cycles was performed for glassy crosslinked system (50 cycles for graphene/epoxy) and semicrystalline matrix with rubbery phase (80 cycles for MWCNT/TPU), showing interesting information related to the variation of resistivity and gauge factor.

For these reason and following the observed tendency of gauge factor of CNT/ABS to reduce during creep experiment, the authors decided to monitor the variation of electrical resistance during 50 cycles in the strain range of $0.1\% < \varepsilon < 0.5\%$ for both HC and H45 samples. The results are summarized in **Figures 9**, **10**, respectively. The resistance difference decreases with number of cycle, as derived from a dynamic mechanical effect on the nanocomposite 3D structure. It is in fact evident that piezoresistivity progressively decreases in cyclic strain for both samples. Results could be

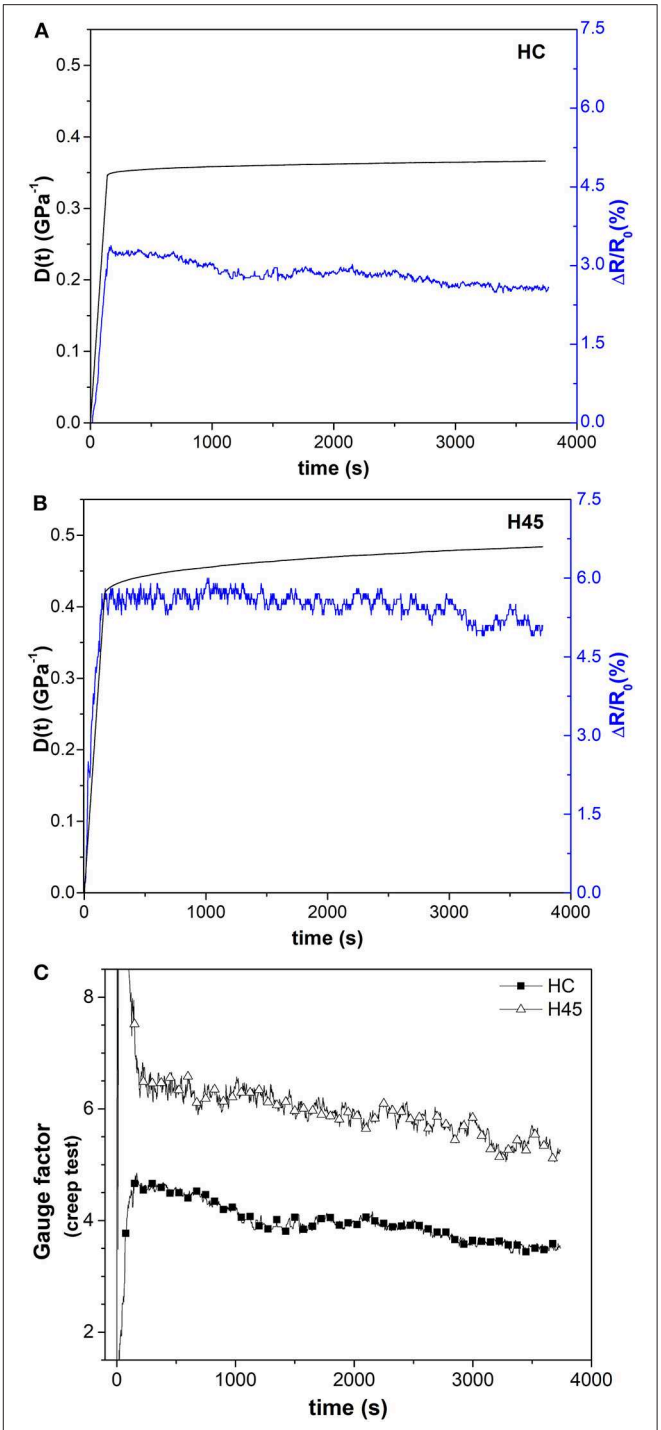

FIGURE 8 | Creep compliance at a constant stress of 20 MPa and ΔR/R0 for different infill samples: **(A)** HC and **(B)** H45. Gauge factor evolution during creep test **(C)**.

TABLE 3 | Comparison of resistivity and piezoelectric behavior of polymer composites filled with carbon nanostructures and produced with different matrix and process.

Filler (max content) /matrix	Processing method	ρ (Ω.cm)	Gauge factor	Long term testing	Applications	References
GNP (5 wt.%) /Epoxy	Solution casting	$\sim 4 \times 10^4$	∼4 (at 2% strain)	50 cycles	Reversible sensor	Moriche et al., 2016a,b
MWCNT (1 wt.%) /Epoxy	Solution casting	//	2.86	5 cycles	Strain sensors	Sanli et al., 2016
MWCNT (0.15 vol.%) /Epoxy	Solution casting	$\sim 10^5$	0.5–0.8	10 cycles	Strain sensing applications	Cao et al., 2017
MWCNT (0.3 wt.%) /VER	Solution casting	5×10^3	2.6 ± 0.1	10 cycles	Smart sensing and structural health monitoring	Ku-Herrera and Avilés, 2012
MWCNT (0.5%) /PSO	Solution casting	$\sim 10^4$	0.74	3 cycles	Strain-sensing nanostructured materials	Bautista-Quijano et al., 2010
MWCNT (0.5%) /PSO	Solution casting	$\sim 10^3$	2.8 ± 0.4	10 cycles	Strain-sensing nanostructured materials	Oliva-Avilés et al., 2011
CB (5 wt.%) /SR	Solution casting	$\sim 10^4$-10^5	//	10 cycles	Pressure sensors—piezo resistive sensor	Zhou et al., 2017
MWCNT (6 wt.%) /TPU	Solution casting	$\sim 10^3$	0.09–2.64	No	Highly stretchable sensor	Bautista-Quijano et al., 2013
MWCNT (6 wt.%) /TPU	Solution casting	$\sim 10^3$	from 4 to 0.8 (at 5% strain)	80 cycles	Flexible sensor film	Zhang et al., 2013
MWCNT (5 wt.%) /TPU	Extrusion/3D printing	$\sim 10^4$	//	200 cycles	Highly stretchable sensor	Kim et al., 2019
MWCNT (3 wt.%) /TPU	Extrusion/3D printing	//	//	20 cycles	Strain sensor (wearable glove)	Christ et al., 2019
MWCNT (8 wt.%) /PVDF	Compounding/ compression molding	∼10	∼1 (at 2% strain)	No	Structural health monitoring	Georgousis et al., 2015
CB-PPy (6 wt.%) /PVDF	Compounding/ compression molding	5.5	//	//	In progress	Bertolini et al. unpublished data
MWCNT (3.4 wt.%) /PP	Compounding/ compression molding	$\sim 10^3$	∼0.02 (at 2–3% strain)	10 cycles	Strain sensing device	Zhao et al., 2013
MWCNT (3.5 wt.%) /PC	Melt spinning	$\sim 10^4$	16	No	Health monitoring in robotics	Bautista-Quijano et al., 2016
CNT (1.0–1.6 wt.%) /PLA	Solution blending/ compression molding	4.2×10^5-1.6×10^3	from 0.02 to 0.013 (at 3% strain)	10 cycles	Strain sensing device	Hu et al., 2017
Graphene (%) /PLA/TPU	Extrusion/ 3D printing	//	//	10 cycles	Highly stretchable sensor	Alsharari et al., 2018
MWCNT (9%) /PI	Extrusion/ 3D printing	3.1×10^2	//	7–9 cycles	Aerospace and industrial fields	Ye et al., 2019
CB (26.4%) /ABS	Extrusion/ 3D printing	//	∼10 (at 2% strain)	No	Health monitoring purposes	Dawoud et al., 2018
CB/ABS	Extrusion/ 3D printing	30–115	∼1.4	1 cycle	Structural health monitoring	Munasinghe et al., 2019
MWCNT (6 wt.%) /ABS	Extrusion/ 3D printing	17 and 31	from 9.7 to 2.4 (at 0.5–3% strain)	50 cycles/creep test	Structural health monitoring	Dul et al., 2020

VER, vinyl ester resin; PSO, polysulphone; SR, silicon rubber; TPU, thermoplastic polyurethane; PVDF, polyvinylidene fluoride; PP, polypropylene; PC, polycarbonate; PLA, polylactide; PI, thermoplastic polyimide; CB-PPy, carbon black doped with polypyrrole.

attributed to the reorganization in conductive paths, due to possible rearrangement, rotations, and reorientation, of 1D nanoparticles forming the electrical network, as reported by Bautista-Quijano et al. (2010). Different is the case observed for 2D reinforcement, such as graphene 2D nanoparticles, for which the initial electrical resistance was maintained after each cycle (Moriche et al., 2016b). An apparent stabilization of the resistance decay (electrical resistance change) has been observed in the last 10 cycles, as shown in **Figures 9B**, **10B** for HC and H45, respectively. With the aim to evaluate the stability of strain monitoring, the effect of cyclic strain in a relatively low extent of deformation has been followed at each

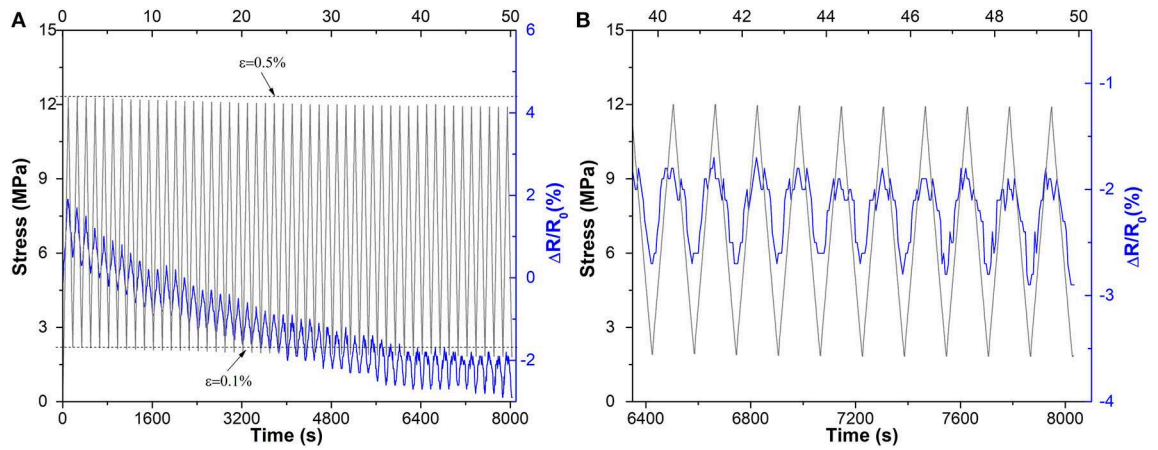

FIGURE 9 | Piezoresistivity of the HC samples in reversible mode **(A)** 50 strain cycles under tensile loading and **(B)** detail of the last 10 cycles.

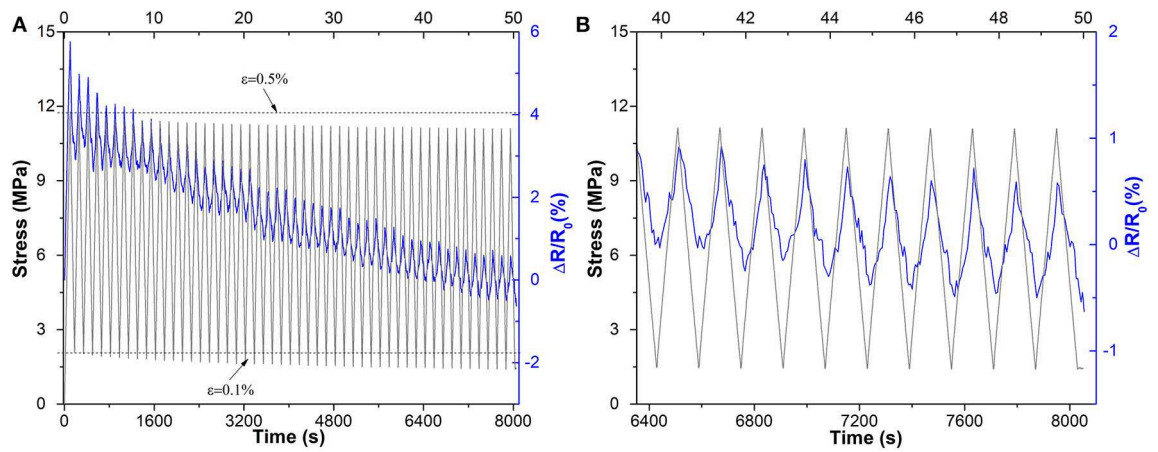

FIGURE 10 | Piezoresistivity of the H45 samples in reversible mode **(A)** 50 strain cycles under tensile loading and **(B)** detail of the last 10 cycles.

step of the cycle by the evaluation of a gauge factor (K_i) calculated as:

$$K_i = \frac{((R_{i+1} - R_i)/R_i)}{\varepsilon}$$

The evolution of the calculated value of gauge factor in each cycle is reported in **Figure 11**. It is well evident a progressive reduction of gauge factor especially for H45 samples in the first 10–15 cycles, followed by almost stationary values after 20 cycles. The average gauge factor in the first 10 cycles is about 2.8 ± 0.5 and 3.8 ± 0.6 for HC and H45, respectively; while K reaches a stable value of about 2.5 ± 0.2 for both samples after 30 cycles. These results suggest a pre-mechanical conditioning of 3D products by specific cyclic loading at controlled strain in dependence on the required applications (controlled max strain and/or max stress). The same comments were presented by various authors (Zhang et al., 2013; Zhao et al., 2013; Cao et al., 2017) with the indication of stabilization of piezoelectrical behavior during cycling loading, due to a competitive disruption and reformation of new electrical paths. In this case it is crucial the role of CNT because they can be partially realigned and they cab form some more contacts that reduce the resistivity.

Finally, it is interesting to note the effect of stress reduction during the 50 cycles of controlled strain deformation. In particular, the ratio between the maximum and the minimum stress reduced from 12.3/2.2 MPa/MPa of the first loading cycle to 11.9/1.8 MPa/MPa in the last cycle for HC sample (stress reduction of about 0.4 MPa. In the case of H45 sample, a higher stress reduction of about 0.7 MPa was observed, resulting in a max/min stress ratio of 11.8/2.1 and 11.1/1.4 MPa/MPa in the 1st and in the 50th cycle, respectively. This effect could be attributed to the viscoelastic effect of stress relaxation accompanied by thermal heating due to a mild Joule effect. During cycling deformation the progressive reduction of resistance is attributed to extension–retraction cycles, that gradually form a better conductive network, due to the partial mobility of the polymeric matrix, as previously observed for PP, PLA, TPU, and epoxy (Zhang et al., 2013; Zhao et al., 2013; Moriche et al., 2016b; Cao et al., 2017).

Representative optical pictures of HC and H45 samples before and after cyclic testing are depicted in **Figure 12**. After 50 cycles under tensile loading, no evidence of damage can be observed in any sample. Finally, it is worth noting a relatively low reduction of gauge factor from 3.8–4.9 to 2.5 (about 40%) for CNT/ABS, much lower than decrease gauge factor observed for MWCNT/TPU from 4 to about 0.8 after 60 cycles (Zhang et al., 2013). Hence these studied conductive nanocomposite based on MWCNT/ABS appear more suitable for strain monitoring, not only for the resistivity values, but also for relatively easy FFF processing. It should be noted however, that the maximum strain could cautiously fixed at 2% for strain monitoring device produced by FFF of CNT/ABS, whereas it is much higher in the case CNT/TPU with thermoplastic elastomer process by solution casting.

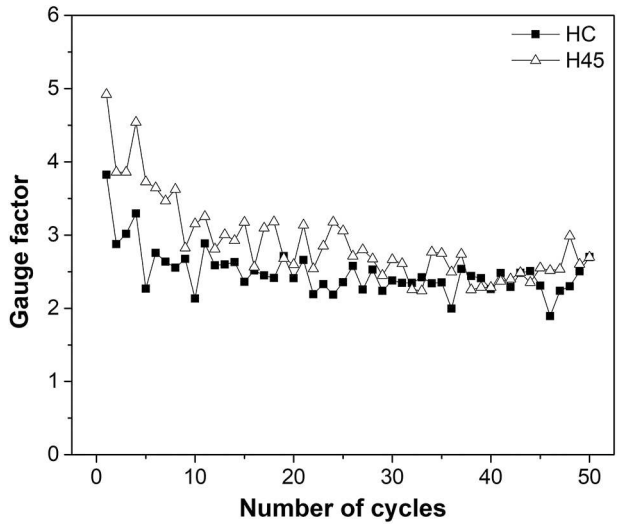

FIGURE 11 | Gauge factor of the 6 wt.% CNT 3D-printed nanocomposite samples along a number of cycle strain of HC and H45.

CONCLUSIONS

This work shed more light on the application of conductive nanocomposites for strain monitoring, evidencing the potential of piezoresistive behavior of 3D-printed CNT/ABS composites in short term and long term testing. In particular the strain sensing capabilities of electrically conducting samples of ABS containing 6 wt.% of CNT produced by FFF with two different infill patterns (HC and H45) were evaluated. The electrical resistance of the 3D-printed specimens was observed to be dependent on the manufacturing design and to maintain almost constant values in the temperature range between −25 and 60°C. Electrical resistance changes were also monitored during short mechanical testing under different loading conditions. An initial gauge factor has been determined for each 3D printed item, and it was found directly dependent on the infill pattern. In particular, the higher sensitivity of the 3D-part within H45 pattern in comparison to HC, according to the measurement of the gauge factor. A change of the strain rate in the range of 0.3–10%/min has no significant effect on gauge factor, which is about 5.0 for HC and 7.0 for H45 part. An abrupt variation of resistance of the specimens was detected at higher deformation when damage starts to develop approaching the failure of specimen. Long time testing of conductive behavior of thermoplastic glassy polymers has been also presented for the first time, according to the authors'

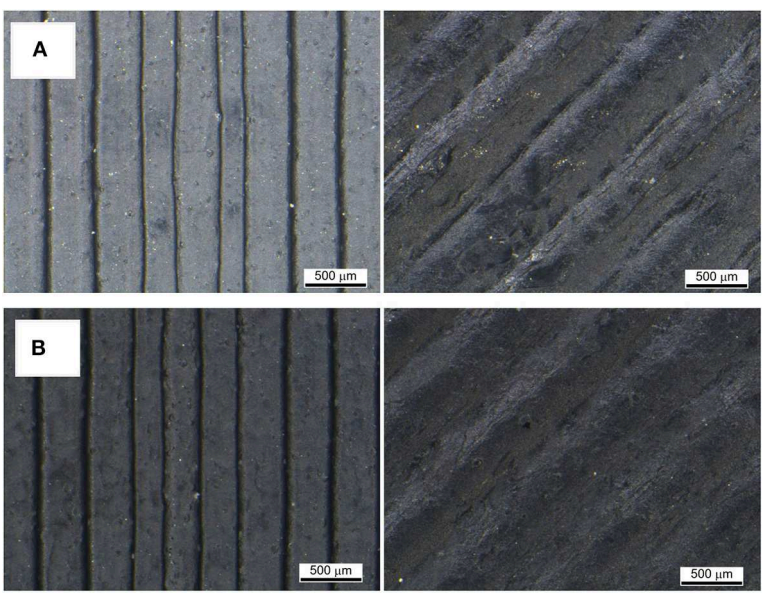

FIGURE 12 | Optical micrographs of HC (right) and H45 (left) samples: **(A)** before, and **(B)** after 50 cycles under tensile loading.

knowledge. Both creep experiments and cycling tests evidence the reduction of resistivity and gauge factor. The CNT conductive network path seems to be reformed during creep and fatigue test with a progressive reduction of gauge factor till an almost constant of about 2.5 for all samples. This behavior indicates a sort of rearrangement of the composite material, independently on the infill pattern, and directly related to the CNT content. In conclusion, the selection of material composition and the manufacturing of products confirmed the positive results in terms of potential applications in the field of strain monitoring.

In particular ABS conductive systems evidence a much larger interval of temperature application, with respect to commercial type composites based on PLA matrix. Moreover the composition of 6 wt.% of CNT in ABS can be relatively easy processed in quite common conditions, much more convenient with respect to high performance conductive products, such as thermoplastics polyimide, that require very high processing temperature and specific equipments for production, and in the same time guarantee a high temp application conditions.

The limits of the tested 3D printed for strain monitoring applications are the maximum using temperature (no more than 80°C) and the maximum deformation of strain 2–3%.

Each manufactured item requires to be properly calibrated and tested for the determination of its intrinsic gauge factor, and to evaluate any stabilization level depending on time and/or temperature. Some further research developments could be devoted to the long time aging up to 1–3 years, and to the evaluation of accelerated temperature aging.

DATA AVAILABILITY STATEMENT

The raw data supporting the conclusions of this article will be made available by the authors, without undue reservation, to any qualified researcher.

AUTHOR CONTRIBUTIONS

SD, AP, and LF conceived and designed the research work, analyzed the data, and wrote the paper. SD performed the experiments.

ACKNOWLEDGMENTS

Authors wish to thank Versalis S.p.A. (Mantova, Italy) for donating ABS pellet polymer for this work. Authors are also thankful Sharebot S.r.l. (Nibionno-LC, Italy) for providing Next Generation desktop 3D-printer. Moreover, Mr. Francesco Montagnaro is warmly acknowledged for performing some of the experiments. SD is grateful to AREAS+ EU Project of Erasmus Mundus Action 2 Programme for financial support.

SUPPLEMENTARY MATERIAL

The Supplementary Material for this article can be found online at: https://www.frontiersin.org/articles/10.3389/fmats.2020.00012/full#supplementary-material

REFERENCES

Alsharari, M., Chen, B., and Shu, W. (2018). 3D printing of highly stretchable and sensitive strain sensors using graphene based composites. *Proceedings* 2:792. doi: 10.3390/proceedings2130792

Ambrosi, A., Moo, J. G. S., and Pumera, M. (2016). Helical 3D-printed metal electrodes as custom-shaped 3D platform for electrochemical devices. *Adv. Funct. Mater.* 26, 698–703. doi: 10.1002/adfm.201503902

Bautista-Quijano, J. R., Avilés, F., Aguilar, J. O., and Tapia, A. (2010). Strain sensing capabilities of a piezoresistive MWCNT-polysulfone film. *Sensors Actuat. A: Phys.* 159, 135–140. doi: 10.1016/j.sna.2010.03.005

Bautista-Quijano, J. R., Avilés, F., and Cauich-Rodriguez, J. V. (2013). Sensing of large strain using multiwall carbon nanotube/segmented polyurethane composites. *J. Appl. Polym. Sci.* 130, 375–382. doi: 10.1002/app.39177

Bautista-Quijano, J. R., Pötschke, P., Brünig, H., and Heinrich, G. (2016). Strain sensing, electrical and mechanical properties of polycarbonate/multiwall carbon nanotube monofilament fibers fabricated by melt spinning. *Polymer* 82, 181–189. doi: 10.1016/j.polymer.2015.11.030

Cao, X., Wei, X., Li, G., Hu, C., Dai, K., Guo, J., et al. (2017). Strain sensing behaviors of epoxy nanocomposites with carbon nanotubes under cyclic deformation. *Polymer* 112, 1–9. doi: 10.1016/j.polymer.2017.01.068

Chen, J., Liu, B., Gao, X., and Xu, D. (2018). A review of the interfacial characteristics of polymer nanocomposites containing carbon nanotubes. *RSC Adv.* 8, 28048–28085. doi: 10.1039/C8RA04205E

Cho, S., Nam, T., Choi, S., Kim, M., and Kim, S. (2015). "3D printed multi-channel EEG sensors for zebrafish," in *Proceedings of 2015 IEEE Sensors* (Busan), 1–3. doi: 10.1109/ICSENS.2015.7370544

Christ, J. F., Aliheidari, N., Pötschke, P., and Ameli, A. (2019). Bidirectional and stretchable piezoresistive sensors enabled by multimaterial 3D printing of carbon nanotube/thermoplastic polyurethane nanocomposites. *Polymers* 11:11. doi: 10.3390/polym11010011

Coleman, D., Al-Rubaiai, M., and Tan, X. (2019). "Temperature-compensation of 3D-printed polymer-based strain gauge," in *Proceedings SPIE 10968, Behavior and Mechanics of Multifunctional Materials XIII, 109680M* (Denver, CO).

Credi, C., Fiorese, A., Tironi, M., Bernasconi, R., Magagnin, L., Levi, M., et al. (2016). 3D printing of cantilever-type microstructures by stereolithography of ferromagnetic photopolymers. *ACS Appl. Mater. Interfaces* 8, 26332–26342. doi: 10.1021/acsami.6b08880

Czyżewski, J., Burzyński, P., Gaweł, K., and Meisner, J. (2009). Rapid prototyping of electrically conductive components using 3D printing technology. *J. Mater. Process. Technol.* 209, 5281–5285. doi: 10.1016/j.jmatprotec.2009.03.015

Daniel, F., Patoary, N. H., Moore, A. L., Weiss, L., and Radadia, A. D. (2018). Temperature-dependent. electrical resistance of conductive polylactic acid filament for fused deposition modeling. *Int. J. Adv. Manuf. Technol.* 99, 1215–1224. doi: 10.1007/s00170-018-2490-z

Dawoud, M., Taha, I., and Ebeid, S. J. (2018). Strain sensing behaviour of 3D printed carbon black filled ABS. *J. Manuf. Process.* 35, 337–342. doi: 10.1016/j.jmapro.2018.08.012

Dul, S., Ecco, L. G., Pegoretti, A., and Fambri, L. (2020). Graphene/carbon nanotubes hybrid nanocomposites: effect of compression moulding and fused filament fabrication on properties. *Polymers* 12:101. doi: 10.3390/polym12010101

Dul, S., Fambri, L., and Pegoretti, A. (2018a). Filaments production and fused deposition modelling of ABS/carbon nanotubes composites. *Nanomaterials* 8:49. doi: 10.3390/nano8010049

Dul, S., Pegoretti, A., and Fambri, L. (2018b). Effects of the nanofillers on physical properties of acrylonitrile-butadiene-styrene nanocomposites: comparison of graphene nanoplatelets and multiwall carbon nanotubes. *Nanomaterials* 8:674. doi: 10.3390/nano8090674

Ecco, L., Dul, S., Schmitz, D., Barra, G., Soares, B., Fambri, L., et al. (2018). Rapid prototyping of efficient electromagnetic interference shielding

polymer composites via fused deposition modeling. *Appl. Sci.* 9:37. doi: 10.3390/app9010037

Georgousis, G., Pandis, C., Kalamiotis, A., Georgiopoulos, P., Kyritsis, A., Kontou, E., et al. (2015). Strain sensing in polymer/carbon nanotube composites by electrical resistance measurement. *Compos. Part B Eng.* 68(Suppl. C), 162–169. doi: 10.1016/j.compositesb.2014.08.027

Guo, R., Ren, Z., Bi, H., Xu, M., and Cai, L. (2019). Electrical and thermal conductivity of polylactic Acid (PLA)-based biocomposites by incorporation of nano-graphite fabricated with Fused Deposition Modeling. *Polymers* 11:549. doi: 10.3390/polym11030549

Hu, C., Li, Z., Wang, Y., Gao, J., Dai, K., Zheng, G., et al. (2017). Comparative assessment of the strain-sensing behaviors of polylactic acid nanocomposites: reduced graphene oxide or carbon nanotubes. *J. Mater. Chem. C* 5:2318. doi: 10.1039/C6TC05261D

Ivanov, E., Kotsilkova, R., Xia, H., Chen, Y., Donato, R. K., Donato, K., et al. (2019). PLA/Graphene/MWCNT composites with improved electrical and thermal properties suitable for FDM 3D printing applications. *Appl. Sci.* 9:1209. doi: 10.3390/app9061209

Kim, M., Jung, J., Jung, S., Moon, Y. H., Kim, D.-H., and Kim, J. H. (2019). Piezoresistive behaviour of additively manufactured multi-walled carbon nanotube/thermoplastic polyurethane nanocomposites. *Materials* 12:2613. doi: 10.3390/ma12162613

Ku-Herrera, J. J., and Avilés, F. (2012). Cyclic tension and compression piezoresistivity of carbon nanotube/vinyl ester composites in the elastic and plastic regimes. *Carbon N. Y.* 50, 2592–2598. doi: 10.1016/j.carbon.2012.02.018

Laszczak, P., Jiang, L., Bader, D. L., Moser, D., and Zahedi, S. (2015). Development and validation of a 3D-printed interfacial stress sensor for prosthetic applications. *Med. Eng. Phys.* 37, 132–137. doi: 10.1016/j.medengphy.2014.10.002

Lee, J. S., Han, C. M., Kim, J. H., and Park, K. S. (2015). Reverse-curve-arch-shaped dry EEG electrode for increased skin–electrode contact area on hairy scalps. *Electron. Lett.* 51, 1643–1645. doi: 10.1049/el.2015.1873

Leigh, S. J., Bradley, R. J., Purssell, C. P., Billson, D. R., and Hutchins, D. A. (2012). A simple, low-cost conductive composite material for 3D printing of electronic sensors. *PLoS ONE* 7:e49365. doi: 10.1371/journal.pone.0049365

Maurizi, M., Slavič, J., Cianetti, F., Jerman, M., Valentinčič, J., Lebar, A., et al. (2019). Dynamic measurements using FDM 3D-printed embedded strain sensors. *Sensors* 19:2661. doi: 10.3390/s19122661

Mittal, G., Dhand, V., Rhee, K. Y., Park, S.-J., and Lee, W. R. (2015). A review on carbon nanotubes and graphene as fillers in reinforced polymer nanocomposites. *J. Indus. Eng. Chem.* 21, 11–25. doi: 10.1016/j.jiec.2014.03.022

Mohan, V. B., Lau, K.-T., Hui, D., and Bhattacharyya, D. (2018). Graphene-based materials and their composites: a review on production, applications and product limitations. *Compos. Part B Eng.* 142, 200–220. doi: 10.1016/j.compositesb.2018.01.013

Moriche, R., Sánchez, M., Jiménez-Suárez, A., Prolongo, S. G., and Ureña, A. (2016a). Strain monitoring mechanisms of sensors based on the addition of graphene nanoplatelets into an epoxy matrix. *Compos. Sci. Technol.* 123, 65–70. doi: 10.1016/j.compscitech.2015.12.002

Moriche, R., Sánchez, M., Prolongo, S. G., Jiménez-Suárez, A., and Ureña, A. (2016b). Reversible phenomena and failure localization in self-monitoring GNP/epoxy nanocomposites. *Compos. Struct.* 136(Suppl. C), 101–105. doi: 10.1016/j.compstruct.2015.10.006

Munasinghe, N., Woods, M., Milesy, L., and Paul, G. (2019). "3-D printed strain sensor for structural health monitoring," in *2019 IEEE*, 1–6. Available online at: https://opus.lib.uts.edu.au/handle/10453/136992

Muth, J. T., Vogt, D. M., Truby, R. L., Mengüç, Y., Kolesky, D. B., Wood, R. J., et al. (2014). Embedded 3D printing of strain sensors within highly stretchable elastomers. *Adv. Mater.* 26, 6307–6312. doi: 10.1002/adma.201400334

Oliva-Avilés, A. I., Avilés, F., and Sosa, V. (2011). Electrical and piezoresistive properties of multi-walled carbon nanotube/polymer composite films aligned by an electric field. *Carbon N. Y.* 49, 2989–2997. doi: 10.1016/j.carbon.2011.03.017

Park, S. J., and Seo, M. K. (2012). "Carbon fiber-reinforced polymer composites: preparation, properties, and applications," in *Polymer Composites*, eds P. D. S. Thomas, P. D. J. Kuruvilla, D. S. K. Malhotra, P. K. Goda, and D. M. S. Sreekala (Weinheim: Wiley-VCH Verlag GmbH & Co. KGaA) 135–183.

Park, Y., Chen, B., and Wood, R. J. (2012). Design and fabrication of soft artificial skin using embedded microchannels and liquid conductors. *IEEE Sens. J.* 12, 2711–2718. doi: 10.1109/JSEN.2012.2200790

Pedrazzoli, D., Dorigato, A., and Pegoretti, A. (2012a). Monitoring the mechanical behavior under ramp and creep conditions of electrically conductive polymer composites. *Compos. Part A Appl. Sci. Manuf.* 43, 1285–1292. doi: 10.1016/j.compositesa.2012.03.019

Pedrazzoli, D., Dorigato, A., and Pegoretti, A. (2012b). Monitoring the mechanical behaviour of electrically conductive polymer nanocomposites under ramp and creep conditions. *J. Nanosci. Nanotechnol.* 12, 4093–4102. doi: 10.1166/jnn.2012.6219

Pegoretti, A. (2019). *Structural Health Monitoring: Current State and Future Trends*. Warrendale, PA: SAE International.

Rivadeneyra, A., Fernández-Salmerón, J., Agudo-Acemel, M., López-Villanueva, J. A., Capitan-Vallvey, L. F., and Palma, A. J. (2015). Improved manufacturing process for printed cantilevers by using water removable sacrificial substrate. *Sensors Actuat. A Phys.* 235, 171–181. doi: 10.1016/j.sna.2015.10.019

Saleh, M. A., Kempers, R., and Melenka, G. W. (2019) 3D printed continuous wire polymer composites strain sensors for structural health monitoring. *Smart Mater Struct.* 28:105041. doi: 10.1088/1361-665X/aafdef

Sanli, A., Müller, C., Kanoun, O., Elibol, C., and Wagner, M. F. X. (2016). Piezoresistive characterization of multi-walled carbon nanotube-epoxy based flexible strain sensitive films by impedance spectroscopy. *Compos. Sci. Technol.* 122, 18–26. doi: 10.1016/j.compscitech.2015.11.012

Thaler, D., Aliheidari, N., and Ameli, A. (2019). Mechanical, electrical, and piezoresistivity behaviors of additively manufactured acrylonitrile butadiene styrene/carbon nanotube nanocomposites. *Smart Mater. Struct.* 28:084004–084015. doi: 10.1088/1361-665X/ab256e

Watschke, H., Hilbig, K., and Vietor, T. (2019). Design and characterization of electrically conductive structures additively manufactured by material extrusion. *Appl. Sci.* 9:779. doi: 10.3390/app9040779

Xu, Y., Wu, X., Guo, X., Kong, B., Zhang, M., Qian, X., et al. (2017). The boom in 3D-printed sensor technology. *Sensors* 17:1166. doi: 10.3390/s17051166

Yamaguchi, K., Busfield, J. J. C., and Thomas, A. G. (2003). Electrical and mechanical behavior of filled elastomers. I. The effect of strain. *J. Polym. Sci. Part B Polym. Phys.* 41, 2079–2089. doi: 10.1002/polb.10571

Ye, W., Wu, W., Hu, X., Lin, G., Guo, J., Qu, H., et al. (2019). 3D printing of carbon nanotubes reinforced thermoplastic polyimide composites with controllable mechanical and electrical performance. *Compos. Sci. Technol.* 182:107671–107679. doi: 10.1016/j.compscitech.2019.05.028

Zhang, R., Deng, H., Valenca, R., Jin, J., Qiang, F., Bilotti, E., et al. (2013). Strain sensing behaviour of elastomeric composite films containing carbon nanotubes under cyclic loading. *Compos. Sci. Technol.* 74, 1–5. doi: 10.1016/j.compscitech.2012.09.016

Zhao, J., Dai, K., Liu, C., Zheng, G., Wang, B., Liu, C., et al. (2013). A comparison between strain sensing behaviors of carbon black/polypropylene and carbon nanotubes/polypropylene electrically conductive composites. *Compos. Part A Appl. Sci. Manuf.* 48, 129–136. doi: 10.1016/j.compositesa.2013.01.004

Zhao, S., Lou, D., Li, G., Zheng, Y., Zheng, G., Dai, K., et al. (2018). Bridging the segregated structure in conductive polypropylene composites: an effective strategy to balance the sensitivity and stability of strain sensing performances. *Compos. Sci. Technol.* 163, 18–25. doi: 10.1016/j.compscitech.2018.05.006

Zhou, Y., Zhou, Y., Deng, H., and Fu, Q. (2017). A novel route towards tunable piezoresistive behavior in conductive polymer composites: addition of insulating filler with different size and surface characteristics composites. *Compos. Part A Appl. Sci. Manuf.* 96, 99–109. doi: 10.1016/j.compositesa.2017.02.002

Conflict of Interest: The authors declare that the research was conducted in the absence of any commercial or financial relationships that could be construed as a potential conflict of interest.

Copyright © 2020 Dul, Pegoretti and Fambri. This is an open-access article distributed under the terms of the Creative Commons Attribution License (CC BY). The use, distribution or reproduction in other forums is permitted, provided the original author(s) and the copyright owner(s) are credited and that the original publication in this journal is cited, in accordance with accepted academic practice. No use, distribution or reproduction is permitted which does not comply with these terms.

frontiers in Materials

ORIGINAL RESEARCH
published: 03 March 2020
doi: 10.3389/fmats.2020.00045

Polypyrrole Modified E-Coat Paint for Corrosion Protection of Aluminum AA1200

Giseli Contri[1], Camila Aparecida Zimmermann[1], Sílvia Daniela Araújo Da Silva Ramoa[1], Débora Pereira Schmitz[1], Luiz Gustavo Ecco[1], Guilherme Mariz de Oliveira Barra[1] and Michele Fedel[2]*

[1] Department of Mechanical Engineering, Federal University of Santa Catarina, Florianópolis, Brazil, [2] Department of Industrial Engineering, University of Trento, Trento, Italy

This article reports the potential use of Polypyrrole (PPy) particles as anticorrosive additive on an epoxy water-based paint to increase the corrosion protective property of aluminum-coated panels. AA1200 aluminum panels were painted using the electrophoretic deposition method and the coatings with different concentrations of PPy particles were tested. PPy particles were synthetized by oxidative polymerization of pyrrole (Py) with iron (III) chloride hexahydrate ($FeCl_3.6H_2O$) in the presence of dodecylbenzenesulfonic acid (DBSA). Electrically conducting PPy particles (6.5 S cm^{-1}) were obtained with a size average of 154 nm. The as-prepared PPy particles were added into a water-based epoxy paint and AA1200 panels were coated via electrophoretic deposition method. The corrosion protective properties of e-coated AA1200 panels were evaluated by means of electrochemical impedance spectroscopy over prolonged exposure time in neutral non-aerated 0.1 M sodium chloride NaCl electrolyte. In particular, the addition of 0.4% by weight PPy has improved the coating corrosion protective property with respect to epoxy clearcoat and exhibited the highest value of impedance modulus at low frequency among the studied coatings.

Keywords: conductive polymers, electrophoretic deposition, organic coatings, EIS, Polypyrrole

OPEN ACCESS

Edited by:
Rani Elhajjar, University of Wisconsin–Milwaukee, United States

Reviewed by:
Elaine Armelin, Universitat Politecnica de Catalunya, Spain
Azman Hassan, University of Technology, Malaysia, Malaysia
Issam Qamhia, University of Illinois at Urbana–Champaign, United States

****Correspondence:***
Giseli Contri
giselicontri2@gmail.com

Specialty section:
This article was submitted to Polymeric and Composite Materials, a section of the journal Frontiers in Materials

Received: *22 August 2019*
Accepted: *12 February 2020*
Published: *03 March 2020*

Citation:
Contri G, Zimmermann CA, Ramoa SDADS, Schmitz DP, Ecco LG, Barra GMO and Fedel M (2020) Polypyrrole Modified E-Coat Paint for Corrosion Protection of Aluminum AA1200. Front. Mater. 7:45. doi: 10.3389/fmats.2020.00045

INTRODUCTION

Cathodic electrodeposition of paints, also known as e-coat or cathodic painting, denotes an application paint method used to coat metals with organic coatings. In cathodic electrodeposition, water is used as dispersive medium and the formulations are heavy-metals free (Romano et al., 2011; Chimenti et al., 2017; Fedel, 2017). The water-based formulations, constituted of polymer and stabilized additives are deposited onto the surface of the cathode, i.e., metal to be coated, under the application of an electric field (Wicks et al., 1999). A variety of metals including aluminum alloys can be used as cathodes (Dalmoro et al., 2015). The cathodes are coated with a homogeneous highly adherent layer whose composition and dry film thickness are precisely controlled (usually within 10–30 μm) and with excellent resistance to corrosion (Bodo and Poth, 2012). In industry, cathodic electrodeposition has advantages of ease of automation therefore it is a cost-effective method of applying organic coatings in addition of being environmentally friendly (Krylova, 2001; García and Suay, 2009; Fedel et al., 2010; Rossi et al., 2017). The automotive industry is the biggest successful

example of cathodic electrodeposition application. The cathodic painting has been used to coat automobile bodyworks since its implementation in the 70′s and still remains widely used nowadays due to the advantages previously described (Bodo and Poth, 2012; Bučko et al., 2015). Recent studies in the use of cathodic electrodeposition have dealt with the incorporation of ceria oxide nanoparticles (Živković et al., 2014), graphene (Rossi and Calovi, 2018), SiO_2 (Abd El-Lateef and Khalaf, 2019) into the paint formulation as attempts to improve their anticorrosion properties (Bodo and Poth, 2012).

In recent years, intrinsically conducting polymers (I) have attracted attention of research groups for anticorrosion applications (Hosseini et al., 2011; Gurunathan et al., 2013; Ecco, 2014; Kamaraj et al., 2015; Aravindan and Sangaranarayanan, 2016; Qiu et al., 2017; Contri et al., 2018; Chen et al., 2019). Among them, the polypyrrole (PPy) stands out mainly because of its properties, such as: ease of synthesis, low cost, control of electrical conductivity, and high stability in environmental conditions, compared to other polymers of the same class (Ramôa et al., 2014). In addition, the PPy has the ability to change its oxidation state, depending on the characteristics of the medium. This behavior allows to create a passive layer on the surface of the metal, reduce the corrosion reaction rate and improve the corrosion protection of the metal (Castagno et al., 2011; Gergely et al., 2011; González and Saidman, 2012; Qi et al., 2015; Jiang et al., 2019). The PPy can be obtained by several techniques and one of the most used is the chemical oxidation of the pyrrole in the presence of stabilizers for the production of an aqueous dispersion (Ramôa et al., 2014). Thus, an aqueous dispersion modified epoxy resin system based on PPy in aqueous dispersion can be employed on a cathodic electrodeposition to produce a polymeric coating on a metal surface.

Many studies reported in the open literature have shown the potentiality of PPy-filled epoxy coatings in preventing for corrosion of aluminum alloys (Arenas et al., 2008; Qi et al., 2008; Yan et al., 2010; Castagno et al., 2011; Jadhav et al., 2013). Good adhesiveness on metallic substrate, suitable chemical and mechanical properties, environmental stability, excellent corrosion resistance for metallic materials and non-toxicity are among the strengths of PPy-filled epoxy coatings (Gupta et al., 2013). Jadhav et al. (2013) noted the effectiveness of PPy-filled-epoxy systems on the corrosion inhibition onto AA 2024-T3 aluminum alloy surface. They concluded that these coatings containing epoxy resin and conducting polymer present comparable electrochemical properties to hexavalent chromates. Therefore, they are promising candidates for chromates replacement (Jadhav et al., 2013). Moreover, Hosseini et al. (2011) have formulated "smart" corrosion protective PPy/Epoxy coatings on AA5000 aluminum alloy panels. These authors also demonstrated the importance of the secondary dopant for corrosion mechanism (Hosseini et al., 2011). In this work, anionic surfactant DBSA was used as the secondary dopant to improve pigment dispersibility by improving pigment wetting characteristics, preventing reaggregation, and increasing the stability of the dispersion (Tracton, 2007). DBSA also is used in the PPy synthesis acting as co-dopant improving it's electrical conductivity (Ramôa et al., 2015; Contri et al., 2018; Vargas et al., 2018). To advance knowledge on the corrosion inhibition effect of PPy as well as the viability of using PPy as anticorrosive additive for e-coat water-based formulations, this paper presents the potential of PPy particles to be used as anticorrosive additive on an epoxy water-based paint in order to increase the corrosion protective property of aluminum-coated panels. The scientific and technological contribution of this study is related to three main aspects: (i) obtaining a stable cataphoretic bath containing PPy particles; (ii) deposition of a thin film on the surface of a metal substrate by cataphoresis technique and (iii) development of a coating for corrosion protection of AA1200 H14 aluminum alloy. The obtained results are expected to provide understandings on the potential of PPy for Al corrosion inhibition as well as on the application of PPy particles as anticorrosive additive for E-coat water-based formulations.

EXPERIMENTAL

Synthesis of PPy

The used materials were: Pyrrole (Py) 98% and dodecylbenzene sulfonic acid (DBSA) purchased from Sigma Aldrich. Iron (III) chloride hexahydrate ($FeCl_3.6H_2O$) analytical grade purchased from Vetec Química Fina, Brazil. Before use, the Py has been double distilled for impurities removal and stored at 4°C while DBSA and $FeCl_3.6H_2O$ were used as received.

In a typical preparation route to obtain PPy (Ramôa et al., 2014), two aqueous solutions of 2.5 g DBSA and 0.25 mol of $FeCl_3.6H_2O$ were prepared in distilled water under mechanical stirring. $FeCl_3.6H_2O$ was selected as reaction initiator and DBSA acted as surfactant and dopant agent. The solution containing $FeCl_3.6H_2O$ was poured onto the DBSA solution under mechanical stirring. The mixture was kept under agitation for 10 min. After that, an aqueous solution of 0.11 mol of Py was poured dropwise on the previous prepared mixture under agitation. The reaction was carried out for 24 h under agitation at room temperature, 22°C. The obtained PPy particles were vacuum filtered, abundantly washed using distilled water and dried under reduced pressure at 60°C for 24 h.

PPy Particles Characterization

The mean volumetric size and size distribution of the PPy particles were evaluated using Dynamic Light Scattering (DLS) at 180° with 780 nm laser using a NANO-flex equipment from MICROTRAC EUROPE. Due to the pasty appearance of the PPy dispersion, was necessary dilute with deionized water to 6 mg mL^{-1}, to conduct the analysis. The analysis was conducted at a temperature of 21 ± 2°C, using as parameters spherical and absorptive particles in the Microtrac software 11.1.1.0.3. Readings were reported as the average of three consecutive readings calculated by the software.

The PPy particles surface zeta potential measurements, were evaluated using Microtrac Stabino® equipment from MICROTRAC EUROPE. The zeta potential obtained was directly

calculated by Stabino Particle Metrix 2.00.27.02 software. The PPy dispersion was diluted with deionized water to 6 mg. mL^{-1} at pH 5, equal to the pH of the cataphoretic bath, and the analysis conducted at a temperature of 21 ± 2°C.

Scanning electron microscopy (SEM) was used to observe the PPy particles morphology using a JEOL equipment model JSM-6390LV (JEOL, United States). Prior to the analysis, PPy powder particles were gold-coated. An accelerating voltage of 15 keV was used.

Electrical conductivity of PPy measurements were taken at room temperature using a four-probe apparatus. The electrical current was applied with a Keithley 6220 (United States) current source and the resulting voltage was registered by a Keithley Model 6517A (United States) electrometer. For sample preparation, first the powder was oven dried, and then molded to a 13 mm diameter pastille by compression molding. A Bovenau hydraulic press, model P15 ST, was used. The average of five measurements for each sample was calculated for results expression.

Aluminum alloy AA1200 panels (dimension of 75 × 35 × 1 mm) were used as substrates. **Table 1** reports the alloy composition. Before the experimental tests, the panels were immersed in acetone for 10 min in an ultrasonic bath, followed by rinsing with distilled water, soaking in 5% by weight NaOH for 6 min, rinsed again with water and let dry using compressed air. All steps were conducted at room temperature.

Coatings Preparation

The epoxy paints deposition on AA1200 substrates was conducted by electrophoretic deposition method using an epoxy-based binder supplied by Arsonsisi, Lainate, MI, Italy (Arsonkote 212). The coatings were prepared by diluting the epoxy-based binder with distilled water under mechanical stirring. The final volume was adjusted to 0.5 L. The produced and studied specimens were the epoxy clearcoat and epoxy loaded with PPy particles at 0.4%, 0.8%, and 1.2% by weight, as described in **Table 2**. The incorporation of as-prepared PPy particles was calculated considering the dissolved epoxy-based binder final weight. The epoxy clearcoat was used as the reference specimen and the variable under investigation was the concentration of PPy particles in the coating formulation. The deposition bath presented pH of 5.7, total solids content of 15.2% by weight and ionic conductivity near 1.14 mS cm^{-1}. The pH and the ionic conductivity did not change by adding the PPy particles in the cataphoretic bath.

Aluminum alloy AA1200 panels of 75 × 35 × 1 mm prepared as mentioned in the item 2.2. were used as cathodes and one AISI 316 stainless steel panel was used as the anode during coatings deposition. The ratio between the electrodes areas was 1:1. The electrodeposition on the cathodes was carried out applying 150 Volts for 120 s with a Pulsed DC Generator MKS, model RDPG 50 5KW (United States). The cataphoretic bath temperature was kept at 28°C. After the depositions, the coated aluminum panels were put at 180°C for 30 min in vacuum oven for crosslinking. The time, temperature, voltage, and pH values used during the coating procedure and crosslinking, are in accordance with the epoxy-based binder supplier's data sheet. Thickness measurements of dry film coatings were taken with an AKSO equipment, model AK157 following the ASTM D6132-13 standard (**Table 2**). **Table 2** lists the coatings identification, amount of added PPy particles and samples dry film thickness.

TABLE 1 | AA1200 H14 composition alloy as informed by the supplier.

Element	Si + Fe	Cu	Mn	Mg	Zn	Ti	Others	Al
%	0.74	0.01	0.02	0.01	0.01	0.02	0.03	99.18

TABLE 2 | Coatings identification (labels), fillings of each sample and their dry film thickness.

Label	Material	PPy into E-coat formulation (% by weight)	Dry film thickness (μm)
E-coat	Dissolved epoxy-based binder (Arsonkote 212)	–	10.7 ± 0.4
E-coat/PPy 0.4	Dissolved epoxy-based binder + PPy particles	0.4	12.4 ± 1.5
E-coat/PPy 0.8		0.8	17.0 ± 1.1
E-coat/PPy 1.2		1.2	20.0 ± 1.0

Characterization of the Coatings

The obtained coatings were evaluated by fourier-transform infrared spectroscopy (FTIR) in the range from 4000 up to 600 cm^{-1} with a step-size of 4 cm^{-1}. An infrared spectrometer Bruker Tensor 27 (Bruker, United States) with attenuated total reflection (ATR) accessory were used for spectra acquisition.

Adhesion of e-coat films was assessed via cross-cut test according to ISO 2409:2007 using Scotch fibrous tape #880 (purchased from 3M) before immersion tests. The spacing of the cuts were 2 mm. The tape was placed parallel to one cutting direction on the e-coat film, pressed for air removal and after 5 min it was pulled off. The appearance of the cross-cut site was evaluated based on coating detachment amount and classified according to the ISO 2409.

Electrochemical impedance spectroscopy (EIS) was carried out to evaluate the coatings protective properties. Single-sine EIS measurements were performed using a potentiostat combined with a frequency response analyzer (FRA) module (Autolab Metrohm PGSTAT302N). A single sine perturbation of 10 mV of amplitude (peak-to-peak) was applied on the samples based on the average open circuit potential (OCP), within the frequency range of 10^5 up to 10^{-2} Hz. An OCP reading time of 5 min and potential stabilization of dE/dt lower than 1 mV/s were set before EIS data acquisition. In a typical three-electrode arrangement, the coated AA1200 panels were used as the working electrodes with an Ag| AgCl reference electrode (+205 mV vs. SHE) and a stainless-steel ring counter electrode (21 cm^2). The coating area in contact with the electrolyte was 1 cm^2. All the measurements were conducted at 23°C using a non-aerated 0.1 M NaCl (sodium chloride) solution at a pH of 6.0 ± 0.2 as electrolyte.

RESULTS AND DISCUSSION

Characterization of PPy Particles

Figure 1 depicts the relative frequency distribution by volumetric size of PPy particles in water. A bimodal distribution is observed and can be related to the difficulty of maintaining a homogeneous PPy dispersion. The mean size of PPy particles was found to be near 154.1 nm. The zeta potential of the PPy dispersion at pH 5 was verified to be near −35 mV. This can be attributed to the presence of the DBSA's SO_3^- counter ions as the negative charge source in the diffuse layer of the particles.

Scanning electron microscopy micrograph of PPy particles is shown in **Figure 2**. The PPy in dry powder form is composed of agglomerates particles of different sizes and irregular shapes (Saremi and Yeganeh, 2014; Mert, 2016). Some aggregates are observed, probably responsible by the larger size particles detected in the particle size analysis. The observed particles are not perfectly spherical, due to the not formation of micelles surrounded by monomer during pyrrole polymerization (Aldissi and Armes, 1991; Boeva and Sergeyev, 2014; Vargas et al., 2018).

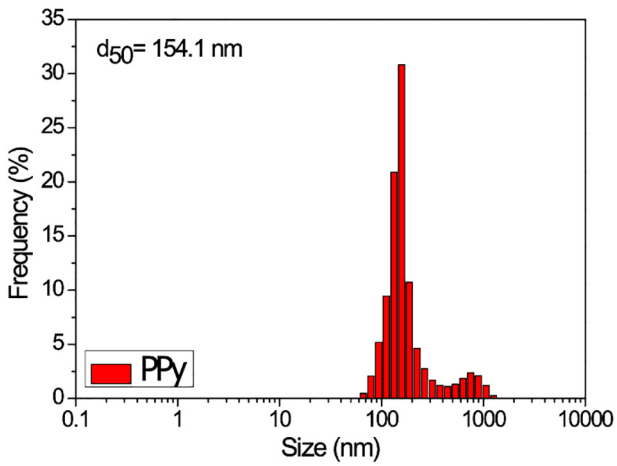

FIGURE 1 | Particle size distribution of PPy.

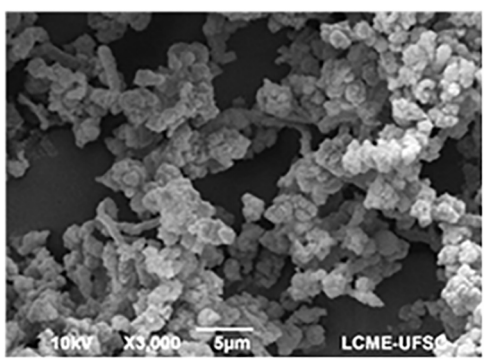

FIGURE 2 | SEM micrograph of PPy.

The PPy particles showed d.c. electrical conductivity average of 6.5 S cm^{-1}.

Characterization of the Coatings

The infrared spectra of neat e-coat, e-coat/PPy filled with 0.4%, 0.8%, and 1.2% by weight of conductive filler are depicted in **Figure 3**. The absorption band of neat e-coat in 3697 cm^{-1} is assigned to the N-H group of the primary amide of polyurethane present in the epoxy-based coating formulation, according to the product technical data sheet. The absorption band at 3361 cm^{-1} can be attributed to the hydroxyl/amine group of hydrogen bonds. Absorption bands at 2975, 2934, and 2855 cm^{-1} are attributed to the C-H stretch of aliphatic chain. In addition, the stretching vibrations of the carbonyl group urethane are observed in the absorption band at 1724 cm^{-1}. The bands at 1646 and 1609 cm^{-1} are assigned to the NH_2 group while at 1507 cm^{-1} the NH stretch of the benzene rings. The absorption band at 1226 cm^{-1} is attributed to the elongation of the vibrations of the group = C-O-C, at 913 cm^{-1} is attributed to the absorption band of the epoxy ring. And the absorption at 824 cm^{-1} attributed to the CH bonds of the aromatic ring. Similar e-coat spectra were obtained by Almeida et al. (2003), Reichinger et al. (2017) and confirm the epoxy nature of the cataphoretic coating. The spectra of coatings containing conductive additive show absorption bands overlapping on the neat e-coat.

The band at 3361 cm^{-1}, **Figure 4A**, is related to the bonded OH or NH group, a displacement to 3324 cm^{-1} for e-coat/PPy 0.4% by weight and to 3294 cm^{-1} for e-coat/PPy 0.8% and 1.2% by weight. According to Petrovic and Ferguson (1991), the frequency of hydrogen bonds changes with the strength of bonds, stronger bonds are displaced to larger wave numbers. Possibly, the observed displacements are due to the intermolecular interactions (H bonds) between the PPy additive and the neat e-coat matrix.

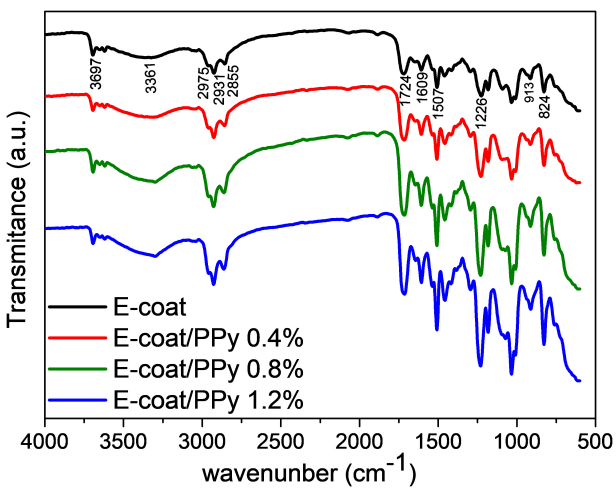

FIGURE 3 | FTIR-ATR spectrum of panels of AA1200 coated with neat e-coat and e-coat/PPy 0.4%, 0.8%, and 1.2% by weight.

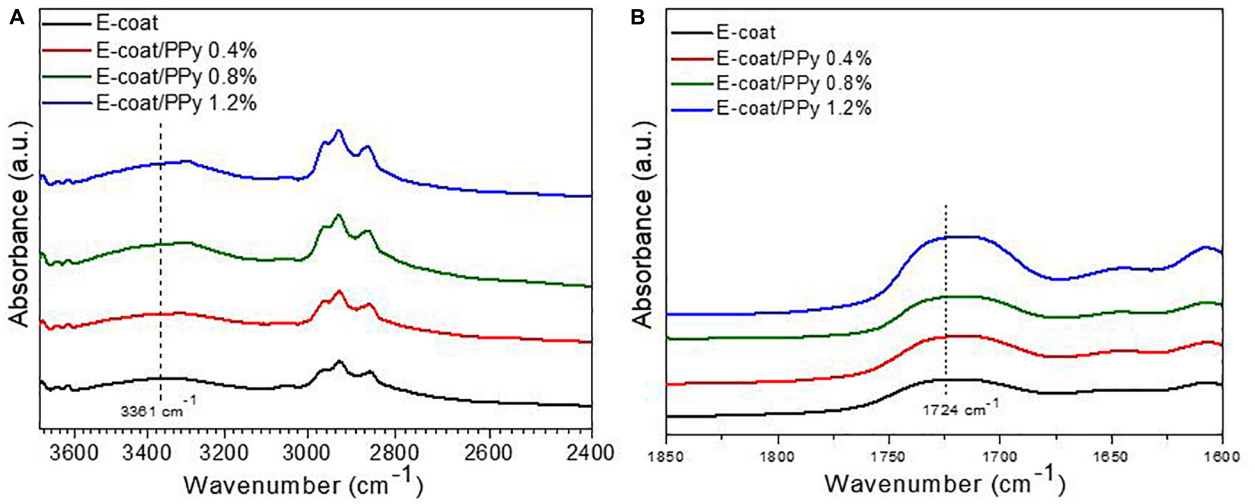

FIGURE 4 | Infrared spectra for the neat e-coat and e-coat containing 0.4%, 0.8%, and 1.2% by weight of PPy in the stretched region of the bound OH or NH **(A)** and the carbonyl stretching region **(B)**.

From **Figure 4B**, a shift in the absorption bands associated with the hydrogen bonded carbonyl group at 1724 cm^{-1} of the neat e-coat is observed for smaller values (1720, 1722, and 1721 cm^{-1}), with the addition of PPy, at respective concentrations of 0.4%, 0.8%, 1.2% by weight. This result indicates the occurrence of a higher number of hydrogen bonds between the C = O and the -NH of the urethane and/or -NH of the PPy.

Adhesion Test

The adhesion of neat e-coat and e-coats containing 0.4%, 0.8%, and 1.2% by weight of PPy was assessed using a tape peel-test, according to ISO 2409:2007, before immersion tests. All coatings were classified as grade 0 according to the ISO standard due to the absence of coating detachment as depicted in **Figure 5**. The excellent coating adhesion on AA1200 H14 aluminum alloy, implies that the coating-substrate interface presents good mechanical stability. These results indicate a proper substrate surface preparation and that the addition of different conductive additive contents in the e-coat formulation did not affect the coating adhesion on the metal substrate.

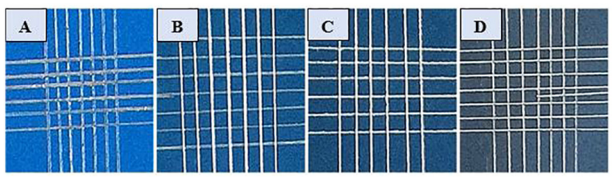

FIGURE 5 | Aspect of the samples submitted to the adhesion test of the coatings of neat e-coat **(A)**, e-coat/PPy 0.4% by weight **(B)**, 0.8% by weight **(C)**, 1.2% by weight **(D)**.

Electrochemical Tests of Coatings

Dry layer thickness is one of the most important measures for inspection and quality control of anti-corrosion coatings, which relates the barrier effect to the durability of the coating (Olajire, 2018). According to the **Table 2**, with increasing PPy concentration in the neat e-coat, the coating thickness and electrolyte permeability in the coating| metal interface increased.

Figure 6 shows the Bode diagrams of EIS spectra of the samples with neat e-coat (a1, a2), e-coat/PPy 0.4% by weight (b1, b2), e-coat/PPy 0.8% by weight (c1, c2), and e-coat/PPy 1.2% by weight (d1, d2) during 672 h immersion in chloride rich solution. In the Bode phase plot for neat e-coat, **Figure 6A1**, partially overlapping peaks indicating two-time constants are noticed. One time constant is located in 10^4–10^2 Hz and the second one in 10^1–10^{-1} Hz regarding the substrate-coating interface and the dissipative phenomena occurring in the presence of the coating, respectively. The presence of two-time constants in the e-coat/PPy 0.4% by weight appeared just within 336–672 h of exposure, which suggests an improvement in the corrosion protection of the AA1200 H14 aluminum alloy panel at this PPy load for a prolonged length of time. While the e-coat/PPy 0.8% by weight, **Figure 6C1**, and the e-coat/PPy 1.2% by weight, **Figure 6D1**, behaved similarly, with two different segments of the high and low frequency regions. These results indicate that the corrosion protection at both PPy contents (0.8% and 1.2% by weight) was not improved, since they have phase angles near to the neat e-coat. Similar results to these described above were found for Jadhav et al. (2013), Živković et al. (2015), Mert (2016), Kumar et al. (2017).

The total impedance modulus of the neat e-coat at low frequency range ($|Z|_{0.01\ Hz}$) was 10^6 Ohm cm^2 within the first 24 h of exposure (**Figure 6A2**). After 24 h, $|Z|_{0.01\ Hz}$ decreased with exposure time indicating a gradual reduction of the coating barrier effect until reaching 10^5 Ohm cm^2 at 168 h of immersion and remaining in this impedance range up to the end of the test.

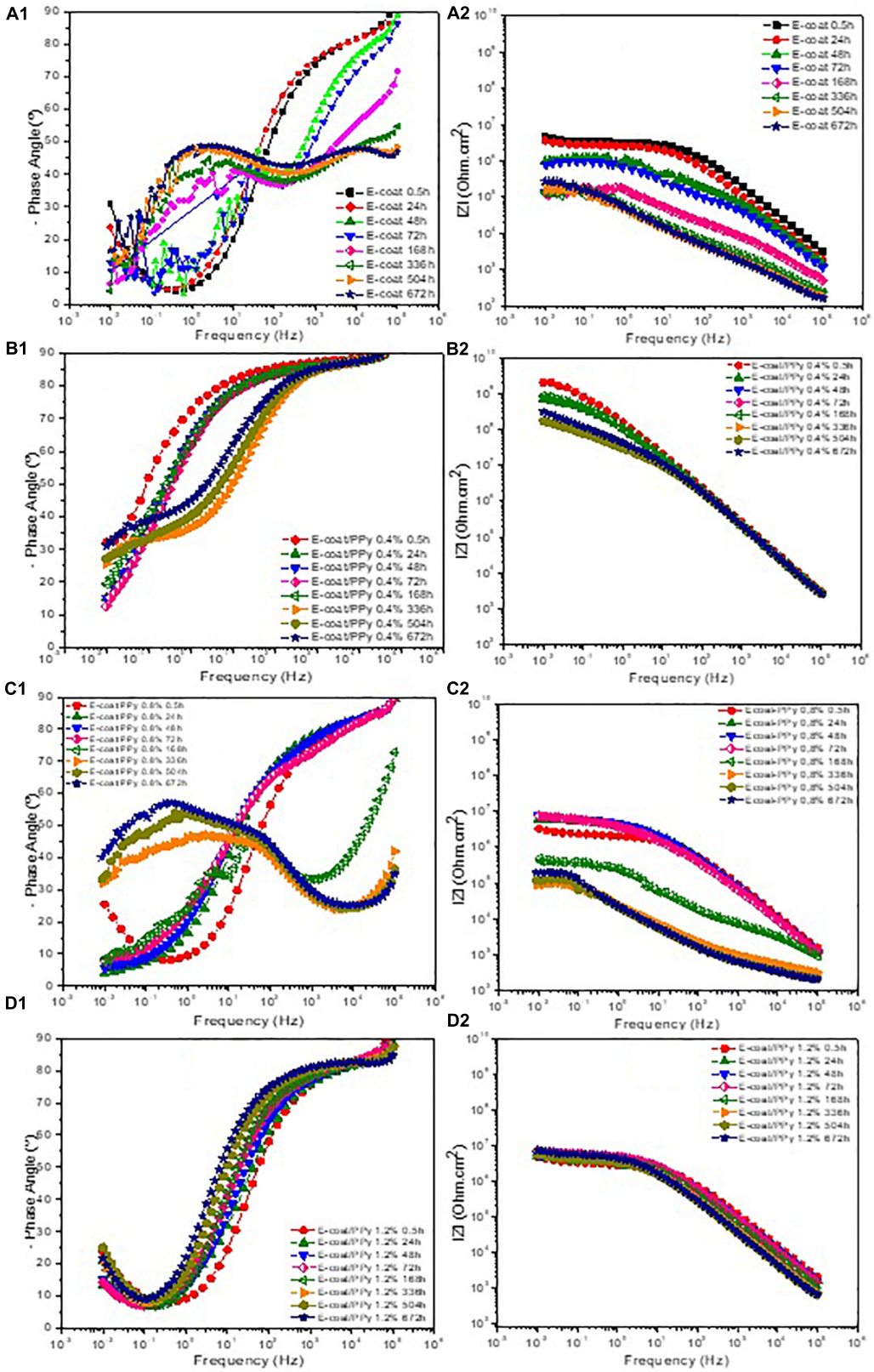

FIGURE 6 | Bode diagram for neat e-coat **(A1,A2)**, e-coat/PPy 0.4% by weight **(B1,B2)**, e-coat/PPy 0.8% by weight **(C1,C2)**, and e-coat/PPy 1.2% by weight **(D1,D2)** during 672 h exposure.

The e-coat/PPy 0.4% by weight, **Figure 6B2**, shown values of $|Z|_{0.01\ Hz}$ at 10^9 Ohm cm^2 in the first 24 h of immersion test decreasing up to 10^8 Ohm cm^2 at the end of exposure time to the electrolyte. Whereas the e-coat/PPy 0.8% by weight, **Figure 6C2**, behaved similarly to the neat e-coat. And the e-coat/PPy 1.2% by weight, **Figure 6D2**, increased by only one order of magnitude (10^7 Ohm cm^2) when compared to the neat e-coat, remaining in this impedance range without further protection improvement.

It can be concluded that the addition of PPy in the cataphoretic bath above an optimal concentration presented a detrimental effect. Instead of increasing the corrosion protection compared to the neat e-coat. This behavior can be attributed to an increased porosity allowing the free migration of the electrolyte through the coating (Bandeira et al., 2017). In this work the probable optimal concentration of PPy particles is below 0.8% by weight once the e-coat/PPy 0.4% by weight coating offered much higher impedance moduli compared to neat e-coat, that means an improved barrier effect (Huerta-Vilca et al., 2004; Contri et al., 2018).

The electrical parameters have been extracted after modeling the EIS data and the electrical equivalent circuit presented in **Figure 7**. In the equivalent circuit shown in **Figure 7A**, R_s is the electrolyte resistance, R_c the coating resistance and Q_c the constant phase element (CPE) of the coating, related to the coating capacitance. A CPE replaced the pure capacitance since the use of a CPE element with exponent *n* gives a better fitting of the spectra. The **Figure 7B** shows two-time phase constant, where R_{ct} is the resistance associated with the transfer of charges between the electrolyte and the surface of Al and the resistance associated with the passive film, Q_{dl} is the dielectric contribution of the electric double layer generated at the Al electrolyte/surface interface and the passive oxide film. Over immersion time, the electrolyte reaches the metal, resulting in two-time phase constants associated responses of oxides/hydroxides present in the metal/coating interface (Kumar et al., 2017).

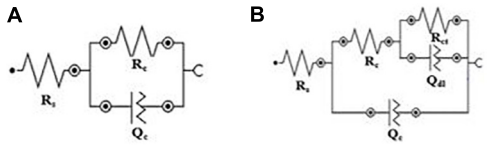

FIGURE 7 | Electrical circuits used for fitting the coatings electrical parameters. **(A)** One-time constant $R_s(Q_cR_c)$ and **(B)** two-time constants $R_s\{Q_c[R_c(Q_{dl}R_c)]\}$.

The stack plot given in **Figure 8** shows the evolution, as function of time, of the electrical parameters R_c as well as the pre-factor "Y_0" and the exponent "n" of the CPE labeled Q_{sl} + ox ($Z_{CPE} = [Y_0(\omega j)^n)]^{-1}$). R_c and Q_c values were taken into account to evaluate the level of defects in the obtained coatings (**Figures 8A,B**). The graph in **Figure 8A** shows a significant decrease in R_c value after 24 h of testing due to water absorption in the coating at the beginning of the test. Again, the sample e-coat/PPy 0.4% by weight shows a superior behavior, with resistance values always higher than 10^6 **Ω** cm^2. The other samples (neat e-coat, e-coat/PPy 0.8% and 1.2% by weight) presented a poorer performance attributed to a higher coating porosity due to conductive additive concentration bigger than an optimal content losing of the barrier effect.

The graph of **Figure 8B** shows the evolution of Q_c in the time of exposure. The pre-factor of the CPE showed a continuous reduction of its magnitudes during the period of testing. The behavior for e-coat/PPy 0.8% and 1.2% by weight were similar the neat e-coat. As a consequence, e-coat/PPy 0.8% and 1.2% by weight samples exhibited higher capacitance values by increasing the absorption of electroactive species with the time of exposure. However, it is observed for the e-coat/PPy 0.4% by weight that the capacitance values are smaller in comparison to the other coatings, indicating low water absorption by the film and presenting elevated barrier effect over time (Zanella et al., 2014).

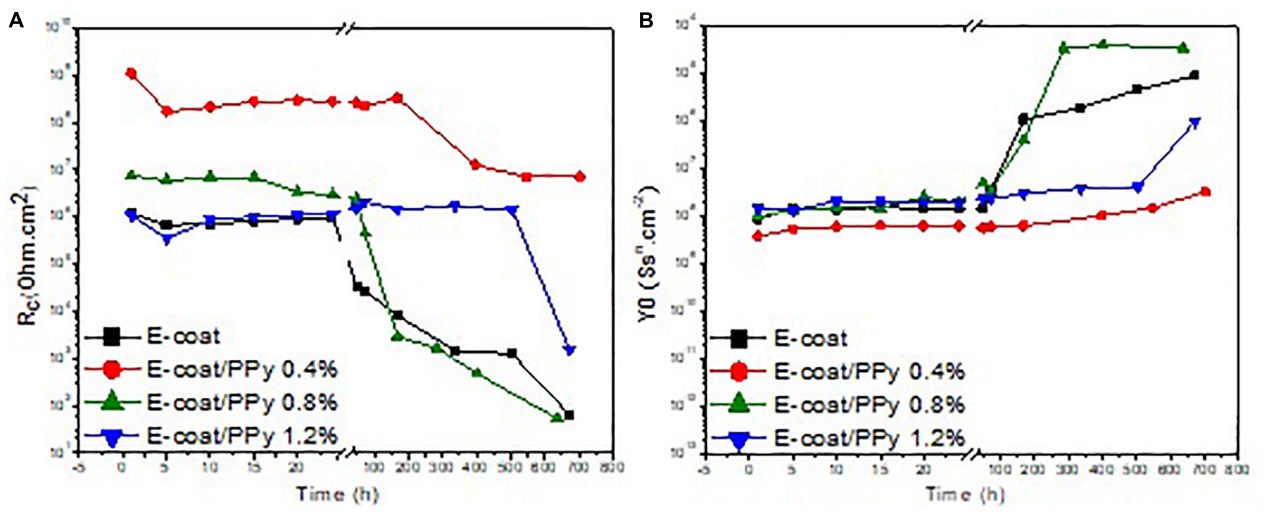

FIGURE 8 | Electrical parameters evolution **(A)** R_c and **(B)** Q_c over time for the AA1200 coated with neat e-coat and e-coat/PPy 0.4%, 0.8%, and 1.2% by weight.

CONCLUSION

In this study, a new coating for corrosion application of the AA1200 H14 aluminum alloy was successfully obtained from epoxy resin (e-coat) and PPy by the cataphoresis technique. According to the results presented in this work, it can be concluded that the e-coat/PPy 0.4%, 0.8%, and 1.2% by weight showed shifts to lower wavelengths for the absorption bands to the bonded OH and NH groups and to the carbonyl absorption bands of the urethane group, indicating that there was interaction between the PPy and the epoxy matrix. The electrodeposited coatings presented good adhesion on AA1200 H14 aluminum alloy panels, indicating that the addition of different conductive additive contents in the e-coat formulation did not affect coating performance on adhesion to the metal substrate. The electrochemical tests showed that e-coat/PPy 0.4% by weight coating provides higher impedance modulus values when compared to neat e-coat, e-coat/PPy 0.8% and e-coat/PPy 1.2% by weight.

Finally, this study showed that the coatings of e-coat/PPy are promising coatings with potential of corrosion protection for the AA1200 H14 aluminum alloy, in particular e-coat/PPy 0.4% by weight, which presented the highest anticorrosive performance during the exposure.

DATA AVAILABILITY STATEMENT

All datasets generated for this study are included in the article/supplementary material.

AUTHOR CONTRIBUTIONS

GC, CZ, LE, and SR performed the production of polymer composites composition and characterization. DS, LE, GB, and MF assisted in writing of the manuscript and discussion of the results. All authors reviewed the final manuscript.

FUNDING

This work was supported by the CNPq (Conselho Nacional de Desenvolvimento Científico e Tecnológico), the CAPES (Coordenação de Aperfeiçoamento de Pessoal de Ensino Superior), and the FAPESC (Fundação de Amparo à Pesquisa e Inovação do Estado de Santa Catarina). The Authors are grateful to Central Electronic Microscopy Laboratory (LCME-UFSC) for FESEM analyses, and Linden for particle size and zeta potential analyses.

REFERENCES

Abd El-Lateef, H. M., and Khalaf, M. M. (2019). Novel dispersed Tl_2O_3-SiO_2/polyaniline nanocomposites: in-situ polymerization, characterization and enforcement as a corrosion protective layer for carbon-steel in acidic chloride medium. *Colloids Surf. A Physicochem. Eng. Asp.* 573, 95–111. doi: 10.1016/j.colsurfa.2019.04.059

Aldissi, M., and Armes, S. P. (1991). Colloidal dispersions of conducting polymers. *Prog. Org. Coat.* 19, 21–58. doi: 10.1016/0033-0655(91)80009-8

Almeida, E., Alves, I., Brites, C., and Fedrizzi, L. (2003). Cataphoretic and autophoretic automotive primers: a comparative study. *Prog. Org. Coat.* 46, 8–20. doi: 10.1016/S0300-9440(02)00144-3

Aravindan, N., and Sangaranarayanan, M. V. (2016). Influence of solvent composition on the anti-corrosion performance of copper-polypyrrole (Cu-PPy) coated 304 stainless steel. *Prog. Org. Coat.* 95, 38–45. doi: 10.1016/j.porgcoat.2016.02.008

Arenas, M. A., Gónzalez, B. L., de Damborenea, J. J., and Ocón, P. (2008). Synthesis and electrochemical evaluation of polypyrrole coatings electrodeposited onto AA-2024 alloy. *Prog. Org. Coat.* 62, 79–86. doi: 10.1016/j.porgcoat.2007.09.019

Bandeira, R. M., Drunen, J. V., Garcia, A. C., and Tremiliosi, G. F. (2017). Influence of the thickness and roughness of polyaniline coatings on corrosion protection of AA7075 aluminum alloy. *Electrochim. Acta* 240, 215–224. doi: 10.1016/j.electacta.2017.04.083

Bodo, M., and Poth, U. (2012). *Coatings Formulation: An International Textbook*. Hanover: Vincentz Network, 288.

Boeva, Z. A., and Sergeyev, V. G. (2014). Polyaniline: synthesis, properties, and application. *Polym. Sci. Ser. C* 56, 144–153. doi: 10.1134/s1811238214010032

Bučko, M., Mišković-Stanković, V., Rogan, J., and Bajat, J. B. (2015). The protective properties of epoxy coating electrodeposited on Zn-Mn alloy substrate. *Prog. Org. Coat.* 79, 8–16. doi: 10.1016/j.porgcoat.2014.10.010

Castagno, K. R. L., Dalmoro, V., and Azambuja, D. S. (2011). Characterization and corrosion of polypyrrole/sodium dodecylbenzene sulfonate electropolymerised on aluminum alloy 1100. *Mater. Chem. Phys.* 130, 721–726. doi: 10.1016/j.matchemphys.2011.07.052

Chen, Z., Yang, W., Xu, B., Chen, Y., Qian, M., Su, X., et al. (2019). Corrosion protection of carbon steels by electrochemically synthesized V-TiO2/polypyrrole composite coatings in 0.1M HCl solution. *J. Alloys Compd.* 771, 857–868. doi: 10.1016/j.jallcom.2018.09.003

Chimenti, S., Vega, J. M., Aguirre, M., Lecina, E. G., Díez, J. A., Grande, H. J., et al. (2017). Effective Incorporation of ZnO nanoparticles by miniemulsion polymerization in waterborne binders for steel corrosion protection. *J. Coat. Technol. Res.* 14, 829–839. doi: 10.1007/s11998-017-9958-x

Contri, G., Barra, G. M. O., Ramoa, S. D. A. S., Merlini, C., Ecco, L. G., Souza, F. S., et al. (2018). Epoxy coating based on montmorillonite-polypyrrole: electrical properties and prospective application on corrosion protection of steel. *Prog. Org. Coat.* 114, 201–207. doi: 10.1016/j.porgcoat.2017.10.008

Dalmoro, V., Alemán, C. A. F., dos Santos, J. H. Z., Azambuja, D. S., Armelin, A., and Armelin, E. (2015). The influence of organophosphonic acid and conducting polymer on the adhesion and protection of epoxy coating on aluminium alloy. *Prog. Org. Coat.* 88, 181–190. doi: 10.1016/j.porgcoat.2015.07.004

Ecco, L. G. (2014). *Waterborne Paint System Based on CeO2 and Polyaniline Nanoparticles for Anticorrosion Protection of Steel*. Doctorals thesis. University of Trento, Italy.

Fedel, M. (2017). Effect of Sol–Gel layers obtained from GLYMO/MTES mixtures on the delamination of a cataphoretic paint on AA1050. *J. Coat. Technol. Res.* 14, 425–435. doi: 10.1007/s11998-016-9860-y

Fedel, M., Druart, M. E., Olivier, M., Poelman, M., Deflorian, F., and Rossi, S. (2010). Compatibility between cataphoretic electro-coating and silane surface layer for the corrosion protection of galvanized steel. *Prog. Org. Coat.* 69, 118–125. doi: 10.1016/j.porgcoat.2010.04.003

García, S. J., and Suay, J. (2009). Optimization of deposition voltage of cataphoretic automotive primers assessed by EIS and AC/DC/AC. *Prog. Org. Coat.* 66, 306–313. doi: 10.1016/j.porgcoat.2009.08.012

Gergely, A., Pfeifer, E., Bertóti, I., Török, T., and Kálmán, E. (2011). Corrosion protection of cold-rolled steel by zinc-rich epoxy paint coatings loaded with nano-size alumina supported polypyrrole. *Corros. Sci.* 53, 3486–3499. doi: 10.1016/j.corsci.2011.06.014

González, M. B., and Saidman, S. B. (2012). Properties of polypyrrole electropolymerized onto steel in the presence of salicylate. *Prog. Org. Coat.* 75, 178–183. doi: 10.1016/j.porgcoat.2012.04.015

Gupta, G., Birbilis, N., Cook, B., and Khanna, S. (2013). Polyaniline-lignosulfonate / epoxy coating for corrosion protection of AA2024-T3. *Corros. Sci.* 67, 256–267. doi: 10.1016/j.corsci.2012.10.022

Gurunathan, T., Chepuri, R. K. R., Narayan, R., and Raju, K. V. S. N. (2013). Synthesis, characterization and corrosion evaluation on new cationomeric polyurethane water dispersions and their polyaniline composites. *Prog. Org. Coat.* 76, 639–647. doi: 10.1016/j.porgcoat.2012.12.009

Hosseini, M. G., Jafari, M., and Najjar, R. (2011). Effect of polypyrrole-montmorillonite nanocomposite powders addition on corrosion performance of epoxy coatings on Al 5000. *Prog. Org. Coat.* 206, 280–286. doi: 10.1016/j.surfcoat.2011.07.012

Huerta-Vilca, D., de Moraes, S. R., and de Jesus Motheo, A. (2004). Anodic treatment of aluminum in nitric acid containing aniline, previous to deposition of polyaniline and its role on corrosion. *Synth. Met.* 140, 23–27. doi: 10.1016/s0379-6779(02)01314-0

Jadhav, N., Vetter, C. A., and Gelling, V. J. (2013). The effect of polymer morphology on the performance of a corrosion inhibiting polypyrrole/aluminum flake composite pigment. *Electrochim. Acta* 102, 28–43. doi: 10.1016/j.electacta.2013.03.128

Jiang, L., Syed, J. A., Lu, H., and Meng, X. (2019). In-situ electrodeposition of conductive polypyrrole-graphene oxide composite coating for corrosion protection of 304SS bipolar plates. *J. Alloys Compd.* 770, 35–47. doi: 10.1016/j.jallcom.2018.07.277

Kamaraj, K., Devarapalli, R., Siva, T., and Sathiyanarayanan, S. (2015). Self-healing electrosynthesied polyaniline film as primer coat for AA 2024-T3. *Mater. Chem. Phys.* 153, 256–265. doi: 10.1016/j.matchemphys.2015.01.012

Krylova, I. (2001). Painting by electrodeposition on the eve of the 21st century. *Prog. Org. Coat.* 42, 119–131. doi: 10.1016/S0300-9440(01)00146-1

Kumar, A. M., Babu, R. S., Ramakrishna, S., and de Barros, A. L. F. (2017). Electrochemical synthesis and surface protection of polypyrrole-CeO2 nanocomposite coatings on AA2024 alloy. *Synth. Met.* 234, 18–28. doi: 10.1016/j.synthmet.2017.10.003

Mert, B. D. (2016). Corrosion protection of aluminum by electrochemically synthesized composite organic coating. *Corros. Sci.* 103, 88–94. doi: 10.1016/j.corsci.2015.11.008

Olajire, A. A. (2018). Recent advances on organic coating system technologies for corrosion protection of offshore metallic structures. *J. Mol. Liq.* 269, 572–606. doi: 10.1016/j.molliq.2018.08.053

Petrovic, Z. S., and Ferguson, J. (1991). Polyurethane elastomers. *Prog. Polym. Sci.* 16, 695–836. doi: 10.1016/0079-6700(91)90011-9

Qi, K., Qiu, Y., Chen, Z., and Guo, X. (2015). Corrosion of conductive polypyrrole: galvanic interactions between polypyrrole and metal substrates. *Corros. Sci.* 91, 272–280. doi: 10.1016/j.corsci.2014.11.025

Qi, X., Vetter, C., Harper, A. C., and Gelling, V. J. (2008). Electrochemical investigations into polypyrrole/aluminum flake pigmented coatings. *Prog. Org. Coat.* 63, 345–351. doi: 10.1016/j.porgcoat.2007.12.003

Qiu, S., Chen, C., Zheng, W., Li, W., Zhao, H., and Wang, L. (2017). Long-term corrosion protection of mild steel by epoxy coating containing self-doped polyaniline nanofiber. *Synth. Met.* 229, 39–46. doi: 10.1016/j.synthmet.2017.05.004

Ramôa, S. D. A. S., Barra, G. M. O., Merlini, C., Schreiner, W. H., Livi, S., and Soares, B. G. (2015). Production of montmorillonite/polypyrrole nanocomposites through in situ oxidative polymerization of pyrrole: effect of anionic and cationic surfactants on structure and properties. *Appl. Clay Sci.* 104, 160–167. doi: 10.1016/j.clay.2014.11.026

Ramôa, S. D. A. S., Merlini, C., Barra, G. M. O., and Soares, B. G. (2014). Obtenção de nanocompósitos condutores de montmorilonita/polipirrol: efeito da incorporação do surfactante na estrutura e propriedades. *Polímeros Ciênc. Tecnol.* 24, 57–62. doi: 10.4322/polimeros.2014.051

Reichinger, M., Bremser, W., and Dornbusch, M. (2017). Interface and volume transport on technical cataphoretic painting: a comparison of steel. Hot-dip galvanised steel and aluminium alloy. *Electrochim. Acta* 231, 135–152. doi: 10.1016/j.electacta.2017.02.013

Romano, A. P., Fedel, M., Deflorian, F., and Olivier, M. G. (2011). Silane sol-gel film as pretreatment for improvement of barrier properties and filiform corrosion resistance of 6016 aluminium alloy covered by cataphoretic coating. *Prog. Org. Coat.* 72, 695–702. doi: 10.1016/j.porgcoat.2011.07.012

Rossi, S., and Calovi, M. (2018). Addition of graphene oxide plates in cataphoretic deposited organic coatings. *Prog. Org. Coat.* 125, 40–47. doi: 10.1016/j.porgcoat.2018.08.023

Rossi, S., Calovi, M., and Fedel, M. (2017). Corrosion protection of aluminum foams by cataphoretic deposition of organic coatings. *Prog. Org. Coat.* 109, 144–151. doi: 10.1016/j.porgcoat.2017.04.042

Saremi, M., and Yeganeh, M. (2014). Application of mesoporous silica nanocontainers as smart host of corrosion inhibitor in polypyrrole coatings. *Corros. Sci.* 86, 159–170. doi: 10.1016/j.corsci.2014.05.007

Tracton, A. A. (2007). *Coatings Materials and Surface Coatings*. New York, NY: CRC press, 528.

Trchová, M., and Stejskal, J. (2011). Polyaniline: the infrared spectroscopy of conducting polymer nanotubes (IUPAC Technical Report)*. *Pure Appl. Chem.* 83, 1803–1817. doi: 10.1351/pac-rep-10-02-01

Vargas, P. C., Merlini, C., Ramôa, S. D. A. S., Arenhart, R., Barra, G. M. O., and Soares, B. G. (2018). Conductive composites based on polyurethane and nanostructured conductive filler of montmorillonite/polypyrrole for electromagnetic shielding applications. *Mater. Res.* 21:e2018 0014.

Wicks, Z. W., Jones, F. N., and Pappas, S. P. (1999). *Organic Coatings: Science and Technology*. New York, NY: Wiley Interscience, 630.

Yan, M., Vetter, C. A., and Gelling, V. J. (2010). Electrochemical investigations of polypyrrole aluminum flake coupling. *Electrochim. Acta* 55, 5576–5583. doi: 10.1016/j.electacta.2010.04.077

Zanella, C., Pedrotti, A., Fedel, M., and Deflorian, F. (2014). Influence of the electrochemical behavior of metal substrates on the properties of cataphoretic clearcoat. *Prog. Org. Coat.* 77, 1987–1992. doi: 10.1016/j.porgcoat.2014.06.019

Živković, L. S., Bajat, J. B., Popić, J. P., Jegdić, B. V., Stevanović, S., and Mišković-Stanković, V. B. (2015). Protective properties of cataphoretic epoxy coating on aluminium alloy AA6060 modified with electrodeposited Ce-based coatings: effect of post-treatment. *Prog. Org. Coat.* 79, 43–52. doi: 10.1016/j.porgcoat.2014.10.014

Živković, L. S., Popić, J. P., Jegdić, B. V., Dohčević-Mitrović, Z., Bajat, J. B., and Mišković-Stanković, V. B. (2014). Corrosion study of ceria coatings on AA6060 aluminum alloy obtained by cathodic electrodeposition: effect of deposition potential. *Surf. Coat. Technol.* 240, 327–335. doi: 10.1016/j.surfcoat.2013.12.048

Conflict of Interest: The authors declare that the research was conducted in the absence of any commercial or financial relationships that could be construed as a potential conflict of interest.

Copyright © 2020 Contri, Zimmermann, Ramoa, Schmitz, Ecco, Barra and Fedel. This is an open-access article distributed under the terms of the Creative Commons Attribution License (CC BY). The use, distribution or reproduction in other forums is permitted, provided the original author(s) and the copyright owner(s) are credited and that the original publication in this journal is cited, in accordance with accepted academic practice. No use, distribution or reproduction is permitted which does not comply with these terms.

frontiers in Materials

ORIGINAL RESEARCH
published: 10 June 2020
doi: 10.3389/fmats.2020.00174

Hybrid Composites Based on Thermoplastic Polyurethane With a Mixture of Carbon Nanotubes and Carbon Black Modified With Polypyrrole for Electromagnetic Shielding

Mayara C. Bertolini[1], Sílvia D. A. S. Ramoa[1], Claudia Merlini[1,2], Guilherme M. O. Barra[1], Bluma G. Soares[3] and Alessandro Pegoretti[4]*

[1] Departamento de Engenharia Mecânica, Universidade Federal de Santa Catarina, Florianópolis, Brazil, [2] Departamento de Engenharia, Universidade Federal de Santa Catarina, Blumenau, Brazil, [3] Departamento de Engenharia Metalúrgica e de Materiais, Universidade Federal do Rio de Janeiro, Rio de Janeiro, Brazil, [4] Department of Industrial Engineering and INSTM Research Unit, University of Trento, Trento, Italy

OPEN ACCESS

Edited by:
Sher Bahadar Khan, King Abdulaziz University, Saudi Arabia

Reviewed by:
Serge Zhandarov, National Academy of Sciences of Belarus (MPRI), Belarus
Fabrizio Sarasini, Sapienza University of Rome, Italy

***Correspondence:**
Guilherme M. O. Barra
g.barra@ufsc.br

Specialty section:
This article was submitted to Polymeric and Composite Materials, a section of the journal Frontiers in Materials

Received: *18 April 2019*
Accepted: *12 May 2020*
Published: *10 June 2020*

Citation:
Bertolini MC, Ramoa SDAS, Merlini C, Barra GMO, Soares BG and Pegoretti A (2020) Hybrid Composites Based on Thermoplastic Polyurethane With a Mixture of Carbon Nanotubes and Carbon Black Modified With Polypyrrole for Electromagnetic Shielding. Front. Mater. 7:174. doi: 10.3389/fmats.2020.00174

Hybrid conducting composites comprising thermoplastic polyurethane (TPU) and mixtures of carbon black modified with polypyrrole (CB-PPy) and carbon nanotubes (CNT) were prepared by melt mixing process. The electrical conductivity, rheological properties and electromagnetic shielding effectiveness (EMI SE) of TPU/CB-PPy and TPU/CNT composites were also investigated those results observed for TPU/CB-PPy/CNT hybrid composites. TPU/CNT composites show a very sharp insulator-conductor transition and the electrical percolation threshold was about 1 wt% of CNT, which was lower than that found for TPU/CB-PPy (7 wt%). Moreover, EMI SE values of TPU/CNT composites were higher than those for TPU/CB-PPy due to the denser CNT conductive pathway into TPU matrix. In order to achieve the highest electrical conductivity and EMI SE values, mixtures of CB-PPy/CNT were added in the composites in different mass fractions. In fact, the electrical conductivity values increased by combining CB-PPy and CNT, resulting in hybrid composites of TPU/CB-PPy/CNT with higher EMI SE values when compared to TPU/CB-PPy composites. The present study demonstrates the potential use of hybrid polymer composites containing 5 or 8 wt% of CB-PPy/CNT at specific CB-PPy/CNT ratios with good processabilty and EMI SE values as high as −20 dB indicating the potential use of these materials for electromagnetic shielding application in the X-band frequency region.

Keywords: carbon black, polypyrrole, carbon nanotubes, thermoplastic polyurethane, electromagnetic shielding

INTRODUCTION

The production of electromagnetic shielding materials has been extensively studied due to the proliferation of electromagnetic interference (EMI) produced by high-performance electronic devices (Håkansson et al., 2007; Ramoa et al., 2013; Kausar, 2016). Metals are the most common materials to prevent EMI; however, these materials have some disadvantages such as high density, low corrosion resistance, high stiffness and processing difficulties (Mahapatra et al., 2008). In this context, the interest in developing electrically conductive polymer composites (CPC) comprising an insulating polymer matrix and a disperse phase of electrically conductive filler has increased because of their low weight, corrosion resistance and ease of processing. Moreover, the electrical properties and electromagnetic shielding effectiveness (EMI SE) of these materials can be modified by adding different amounts of conductive filler into insulating polymer matrix.

Several interesting works concerning the production of EMI shielding polymer composites with improved electrical conductivity and EMI SE values have been reported (Yavuz et al., 2005; Mahapatra et al., 2008; Sudha et al., 2009; Kim et al., 2011; Kaur et al., 2012; Zhang et al., 2012; Al-Saleh et al., 2013; Sharma et al., 2016; Kumar et al., 2017; Kuester et al., 2018; Kumar and Patro, 2018). The most commonly used conductive fillers are carbon fillers, such as carbon nanotubes (CNT) (Mahapatra et al., 2008; Socher et al., 2011; Kaur et al., 2012; Zhang et al., 2012; Al-Saleh et al., 2013; Kumar et al., 2017; Yu et al., 2018), expanded graphite (EG) (Piana and Pionteck, 2013; Kuester et al., 2016), carbon black (CB) (Sumfleth et al., 2009; Chen J. et al., 2013; Burmistrov et al., 2016; Pan et al., 2016; Jeddi and Katbab, 2017; Mondal et al., 2018), graphene (GE) (Al-Saleh, 2015; Sharma et al., 2016) and graphene nanoplateles (GnP) (Chu et al., 2012; Al-Saleh, 2016), and intrinsically conducting polymers (ICP), for instance, polypyrrole (PPy) (Yavuz et al., 2005; Taunk et al., 2008) and polyaniline (PAni) (Sudha et al., 2009; Kim et al., 2011; Oyharçabal et al., 2013). Their advantages are good thermal stability, lightweight, ease of processing, and compatibility with polymer matrices. Although significant progress in this field has been achieved, a great effort has been made to produce conductive polymer composites at lower conductive filler concentrations in order to maintain the rheological and mechanical properties of the insulating polymer matrix. There are several strategies available to reduce the electrical percolation threshold in CPC, including the adequate choice of the filler, polymer matrix, manufacturing method and the most suitable processing conditions.

The technique based on dispersion of two or more conductive fillers into an insulating polymer matrix has been used to improve the composite properties. In fact, some works in the open literature demonstrate better EMI SE results when conductive fillers with different geometries are combined into an insulating polymer matrix (Zhang et al., 2012, 2018; Szeluga et al., 2015; Jang et al., 2016; Kumar et al., 2017; Wu et al., 2017). For instance, Sharma et al. (2016) and Kuester et al. (2017) observed higher EMI SE values for hybrid composites containing CNT/GR and CNT/GnP, respectively, than those found for composites containing the individual fillers.

As previously mentioned, the selection of the polymer matrix is another important key to developing CPC for EMI shielding (Socher et al., 2011). Among insulating polymer matrices, thermoplastic polyurethane (TPU) is widely used due to its versatility. Besides its thermoplastic properties, TPU also has the elasticity of vulcanized rubbers without the need of the vulcanization process (Ramoa et al., 2013). In addition, TPU is composed of two-phase microstructure based on a soft polyester or polyether phase reinforced by a hard phase of aromatic diisocyanate extended with a short-chain diol. Moreover, several studies have reported the production of TPU/CNT composites using various manufacturing methods including solution and melt processing (Guo et al., 2008; Ramoa et al., 2013; Chen et al., 2015). Generally, CNT-filled polymer composites show a better EMI shielding effectiveness and electrical conductivity values at the same filler content when compared to the conductive carbon black (CB)-filled polymer composites. However, composites containing high amount of CNT are more expensive and difficult to process than CB-filled polymer composites. Based on this context, this work proposes the preparation of conductive hybrid composites composed of carbon black modified with polypyrrole (CB-PPy), CNT, and TPU matrix through melt mixing in order achieve the best relationship between electrical conductivity, EMI shielding effectiveness and processability. The microstructure, electrical conductivity, rheological properties and EMI SE of TPU/CB-PPy/CNT hybrid composites were evaluated and compared to those obtained for TPU/CB-PPy and TPU/CNT composites.

EXPERIMENTAL

Materials

The thermoplastic polyether-based polyurethane Elastollan® 1180 A10 used in this study was supplied by Basf –Brasil.

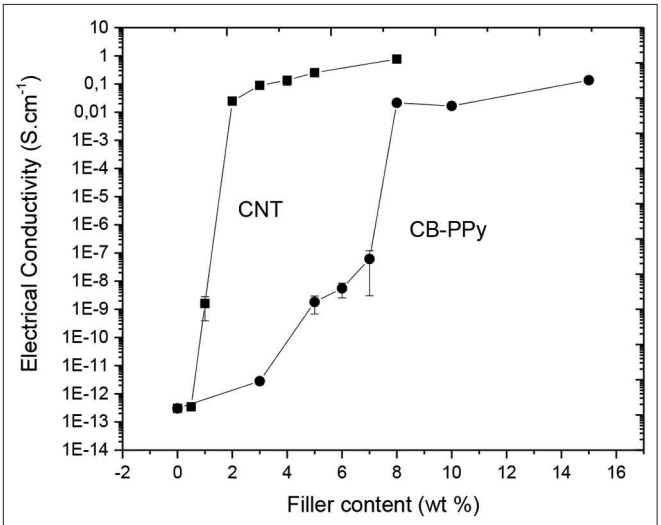

FIGURE 1 | Electrical conductivity of TPU/CNT and TPU/CB-PPy as function of filler content.

It was characterized by a specific gravity of 1.11 g.cm^{-3} and electrical conductivity of 10^{-13} S.cm^{-1}. The multi walled carbon nanotubes were provided by Nanocyl SA (NC 7000) with carbon purity of 90%, average diameter of 9.5 nm, average length of 1.5 μm and electrical conductivity of 10^{4} S.cm^{-1}. Carbon black/polypyrrole was purchased from Sigma Aldrich (80 wt% of carbon black) with electrical conductivity 3×10^{1} S.cm^{-1}.

Composites and Sample Preparation

The composites were prepared by melt blending with different amounts of carbon black/polypyrrole (from 0 to 15 wt%) and carbon nanotubes (from 0 to 8 wt%). Initially, the materials were dried overnight at 60°C. The hybrid composites were produced with 3, 5, and 8 wt% of total filler and the fraction of each filler was 25:75, 50:50, and 75:25. Then, the polymer and the fillers were mixed in a Thermo Haake Polylab Rheomix 600p internal mixer at a rotor speed of 60 rpm for 15 min and at 170°C. The mixed compounds were molded (in square plaques) by thermo-compression using a hydraulic press at 170°C for 5 min and under a 15 MPa pressure.

Methodology

The electrical conductivity of the high-conductive samples was measured using a four-probe standard method. The current source was a Keithley 6220 equipment and the voltage was measured by a Keithley electrometer Model 6517A. For the high-resistive samples a two-probe standard method was performed by a Keithley 6517A electrometer connected to a Keithley 8009 test fixture. The sample thickness was 0.5 mm and the measures were performed on both sides of three different films.

A field emission gun scanning electron microscope (FEG-SEM) Jeol model JSM-6701F was used to investigate the morphology and the filler dispersion. The samples were prepared using liquid nitrogen to break the films in a brittle manner and the fractured surface was sputtered with a gold layer. A tension of 10 kV was applied during the analyses. Different regions of a sample were analyzed.

The rheological properties of the composites in the molten state were measured by a dynamic oscillatory rheometer ThermoHaake MARS II with 20 mm plate–plate geometry at 170°C. The analysis was carried out under a nitrogen atmosphere and the frequency scanned from 0.01 to 100 Hz. Three specimens were analyzed and the thickness and the diameter of the samples were 1 mm and 25 mm, respectively.

The EMI SE analysis was performed by a N5230C Agilent Technology PNA series analyser in the X-band frequency range (8.2–12.4 GHz) connected to a waveguide used as the sample holder. The thickness of the samples was 2 mm and three specimens of each composition were analyzed. The contribution of reflection (SE_R) and absorption (SE_A) shielding on the total EMI SE values was determined using the experimental power data (incident (I), reflected (R) and transmitted (T) power) and equations (1)–(3):

$$SE_R = 10 \log \frac{I}{I - R} \quad (1)$$

$$SE_A = 10 \log \frac{I - R}{T} \quad (2)$$

$$EMI\ SE = 10 \log \frac{I}{T} \quad (3)$$

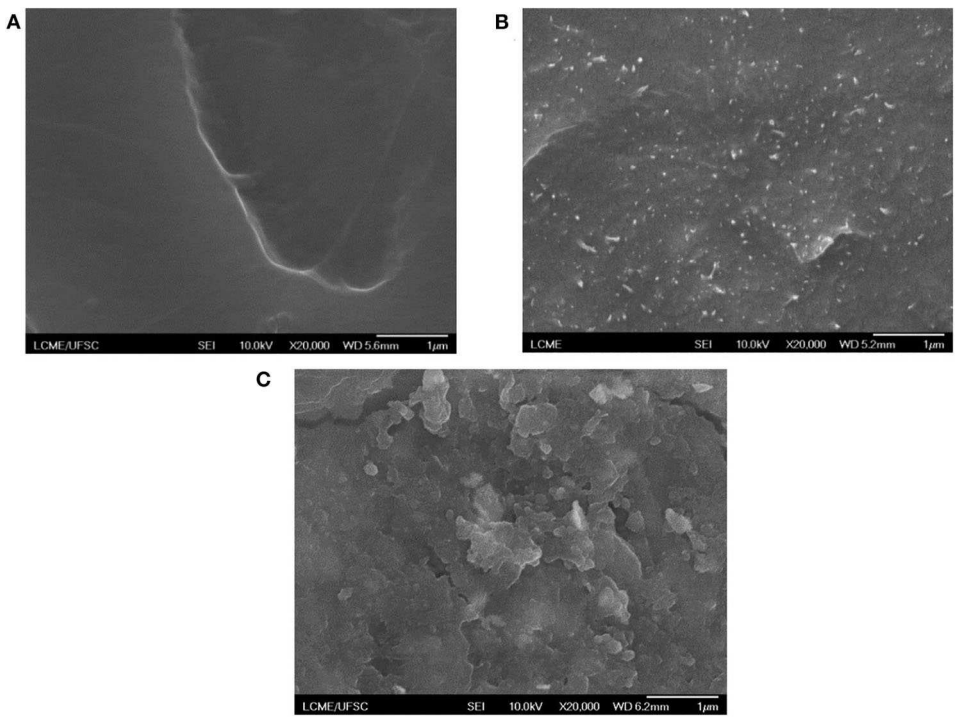

FIGURE 2 | FEG-SEM micrographs of cryogenically fractured surfaces of **(A)** neat TPU, **(B)** TPU/CNT, and **(C)** TPU/CB-PPy containing 8 wt% of conductive filler.

RESULTS AND DISCUSSION

In order to evaluate the effect of CB-PPy and CNT contents on the electrical conductivity of the TPU matrix, composites based on TPU/CB-PPy and TPU/CNT were produced. As shown in **Figure 1**, TPU/CNT composites exhibit a very sharp insulator-conductor transition and the electrical conductivity enhances significantly with increasing CNT content. The electrical conductivity of TPU/CNT composites containing 1 and 2 wt% of filler increased 10^4 and 10^{11} times, respectively, when compared to the neat TPU (10^{-13} S.cm^{-1}), reaching a maximum value of about 1 S.cm^{-1} at 8 wt% of CNT content. These values are quite similar to those observed by Ramoa et al. (2013) and Zhang et al. (2007), suggesting that a good dispersion of CNT into TPU matrix was achieved. On the other hand, a slight increase on the electrical conductivity with the increasing in CB-PPy content was observed. This behavior can be assigned to the higher aspect ratio and better distribution of CNT into the TPU matrix than those found for CB-PPy. In fact, the percolation threshold (f_p) and the critical exponent (t) determined by a power law equation (Equation 4) for TPU/CNT were 1 wt% and 2.4, respectively, while TPU/CB-PPy showed a higher percolation

TABLE 1 | Complex viscosity of TPU and composites composition.

Material	Composition (wt%)	Complex viscosity at 1 Hz (Pa.s)
TPU	100	2.1
TPU/CNT	97/3.0	82.4
TPU/CB-PPy	97/3.0	8.4
TPU/CNT	95/5.0	142.2
TPU/CB-PPy	95/5.0	14.8
TPU/CNT	92/8.0	358.9
TPU/CB-PPy	92/8.0	34.1

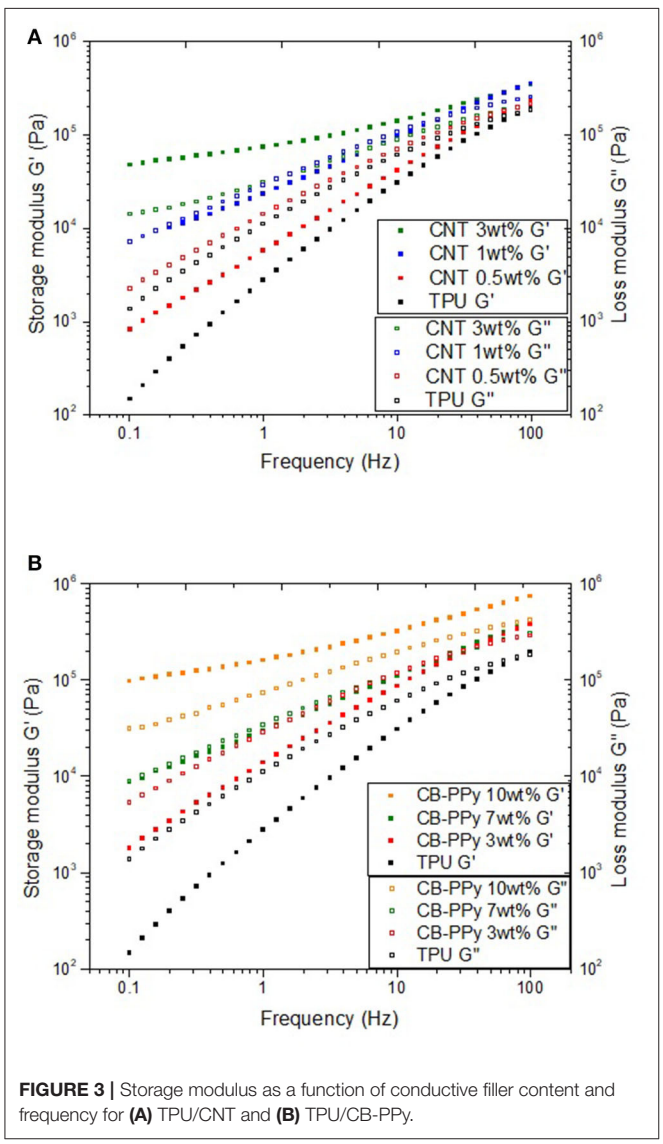

FIGURE 3 | Storage modulus as a function of conductive filler content and frequency for **(A)** TPU/CNT and **(B)** TPU/CB-PPy.

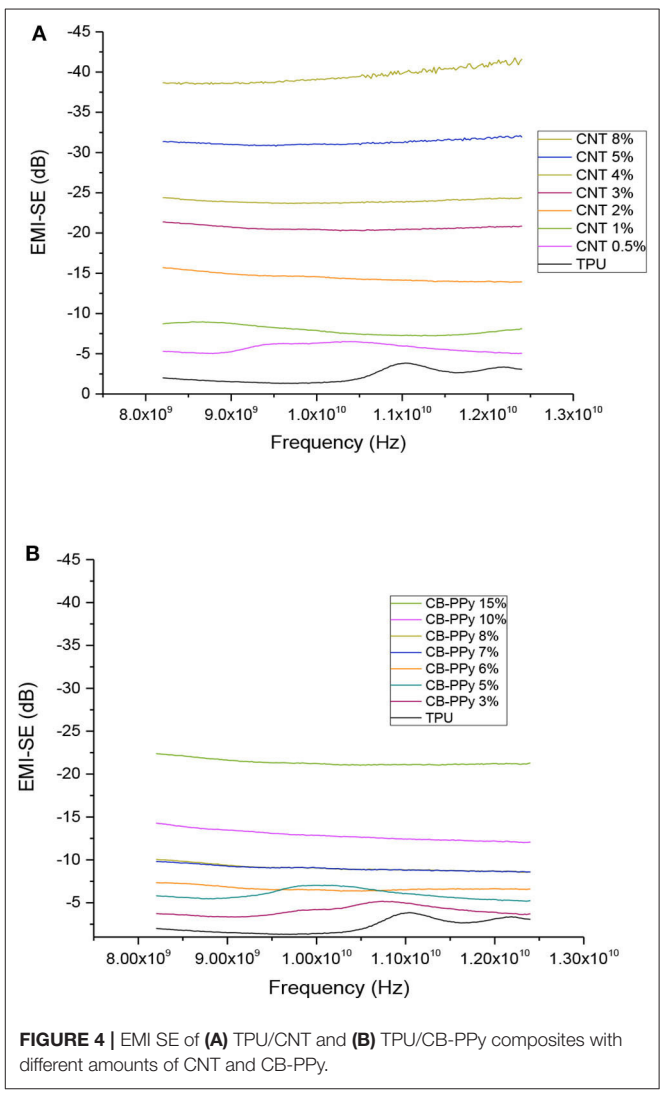

FIGURE 4 | EMI SE of **(A)** TPU/CNT and **(B)** TPU/CB-PPy composites with different amounts of CNT and CB-PPy.

threshold, 7 wt%, and lower t, 2.1. For both composites, the critical exponent was higher than 2, which implies multiple percolation or tunneling (Levon et al., 1993).

$$\sigma = c(f - f_p)^t \quad (4)$$

σ is the electrical conductivity of the composites, c is a constant, f is the filler weight content, f_p is the filler weight content at the percolation threshold and t is the critical exponent. The critical exponent t is related to the number of contacts between the fillers at the percolation threshold. The Equation 4 is used as an empirical approximation for mixtures with weight fraction compositions.

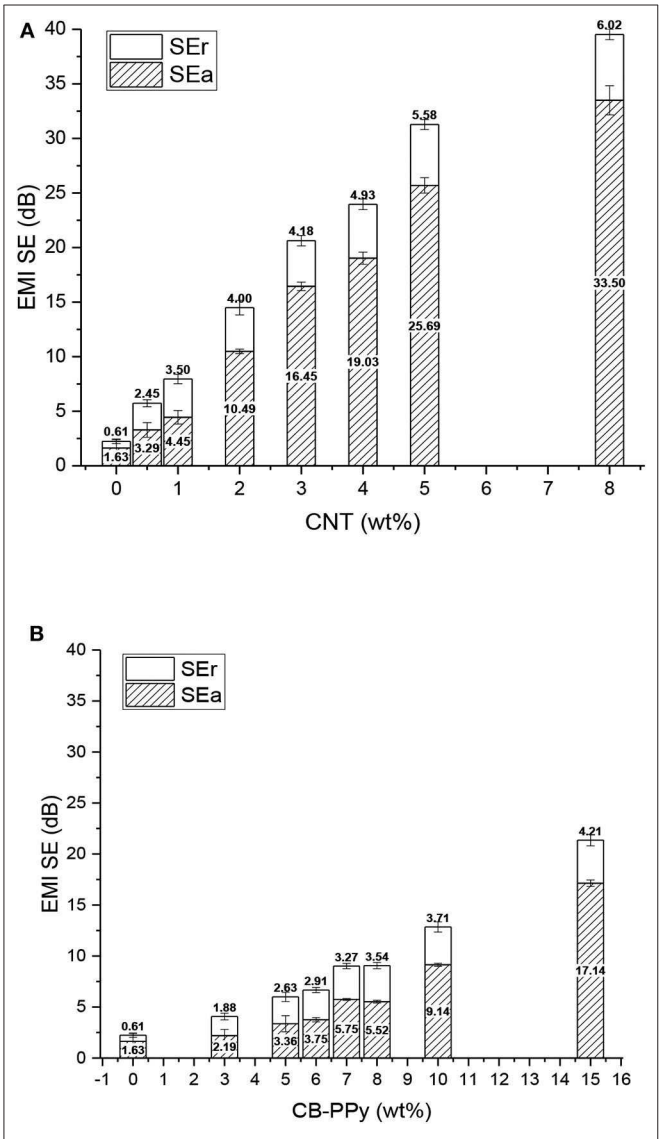

FIGURE 5 | Total EMI SE, SE_A and SE_R values of composites as a function **(A)** CNT and **(B)** CB-PPy content measured at 9 GHz.

FEG-SEM micrographs of cryogenically fractured surfaces of neat TPU, TPU/CNT, and TPU/CB-PPy composites containing 8 wt% of the conductive fillers are observed in **Figure 2**. The white points correspond to the disperse phase into TPU matrix. The microstructure of both composites shows a typical separation and the presence of conductive filler agglomerates well-dispersed contributing to the formation of a conducive pathway in the TPU matrix. As discussed on the above, CNT have high aspect ratio, therefore, small filler content is necessary to create a conductive network in the TPU matrix reducing the percolation threshold. On the other hand, carbon black-polypyrrole has spherical morphology with low aspect ratio and higher percolation threshold, which means a larger amount of this filler is necessary to form a conductive path.

The storage modulus (G′) and loss modulus (G″) as a function of the conductive filler and the frequency for both TPU/CNT and TPU/CB-PPy composites are shown in **Figure 3**. The neat TPU presents a liquid-like behavior ($G'' > G'$) and its transition from liquid to solid-like behavior ($G'' < G'$) is observed at a frequency of 64.8 Hz. For both composites, G′ and G″ increase significantly with the increasing in the conductive filler content into the TPU matrix, indicating that these systems exhibit a pseudo-solid-like behavior. TPU/CNT and TPU/CB-PPy composites with 0.5 and 3 wt% of filler content, respectively, exhibit a transition from liquid to solid-like behavior at the same frequency value found for the neat TPU, while the values for G′ and G″ become almost independent of the frequency at lower frequencies for composites containing 3 wt% of CNT and 10 wt% of CB-PPy. The origin of this behavior can be assigned to the formation of a percolate network, in which the number of interfaces between conductive fillers into the insulating polymer matrix is considered.

It is important to highlight that complex viscosity of TPU (2.1 Pa.s) increases abruptly with increasing the CNT content, as shown in **Table 1**. For example, the complex viscosity of

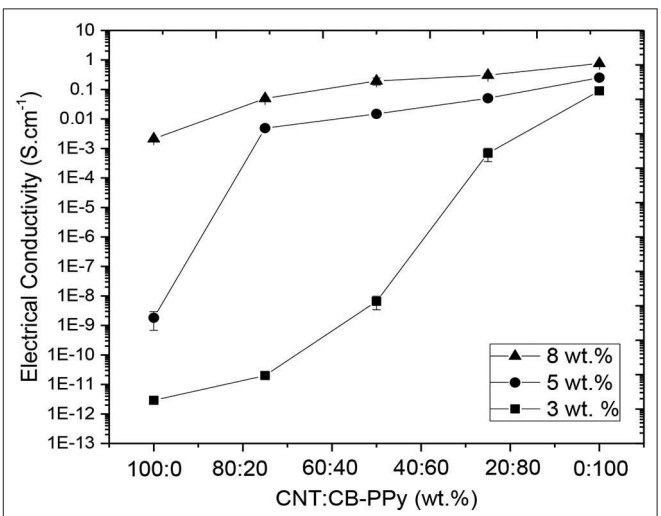

FIGURE 6 | Electrical conductivity of composites as a function of CNT/CB-PPy (wt%) ratio for hybrid composites containing a total filler amount of 3, 5, and 8 wt%.

neat TPU increased approximately 171- and 16-fold by adding 8 wt% of CNT and CB-PPy, respectively. Moreover, TPU/CNT composites was partially impaired for CNT filler concentration above 8 wt%. Therefore, conductive hybrid composites were produced to achieve the best relationship between electrical conductivity, EMI shielding effectiveness and processability at the same reducing the cost.

Figure 4 displays the effect of the conductive filler type and content on the EMI SE as a function of the frequency in the range of 8–12 GHz. TPU/CNT composites exhibit higher EMI SE at the same filler content in the whole frequency range when compared with TPU/CB-PPy due to the higher aspect ratio of CNT, what leads to the easier creation of the filler path and consequently, higher increase in the electrical conductivity. For example, composites with 3 wt% of CNT and CB-PPy show EMI SE values of −21.2 and −3.1 dB, respectively. These results are in good agreement with the electrical conductivity, rheological properties and microstructure analyses of TPU/CNT and TPU/CB-PPy composites, as discussed previously. The EMI SE values of TPU/CNT composites obtained in the present work are higher than those reported by Liu et al. (2007) and Ramoa et al. (2013).

In addition, the EMI SE of TPU/CB-PPy is quite similar to that presented by Ramoa et al. (2013) for TPU/CB composites. Furthermore, the EMI SE values found for TPU/CNT composites containing 3 to 8 wt% of filler are similar or quite higher than those results observed in composites containing different carbonaceous fillers (Al-Saleh et al., 2013; Jeddi and Katbab, 2017; Kumar et al., 2017; Kuester et al., 2018). According to the literature (Li et al., 2006), the desirable EMI SE is at least−20 dB for commercial application, which corresponds to 99% of radiation attenuation (Chen Z. et al., 2013; Ramoa et al., 2013). This value was reached for TPU composites containing 15 wt% of CB-PPy and 3 wt% of CNT.

Figure 5 illustrates the relationship between the conductive filler and the contribution on the EMI SE by reflection and

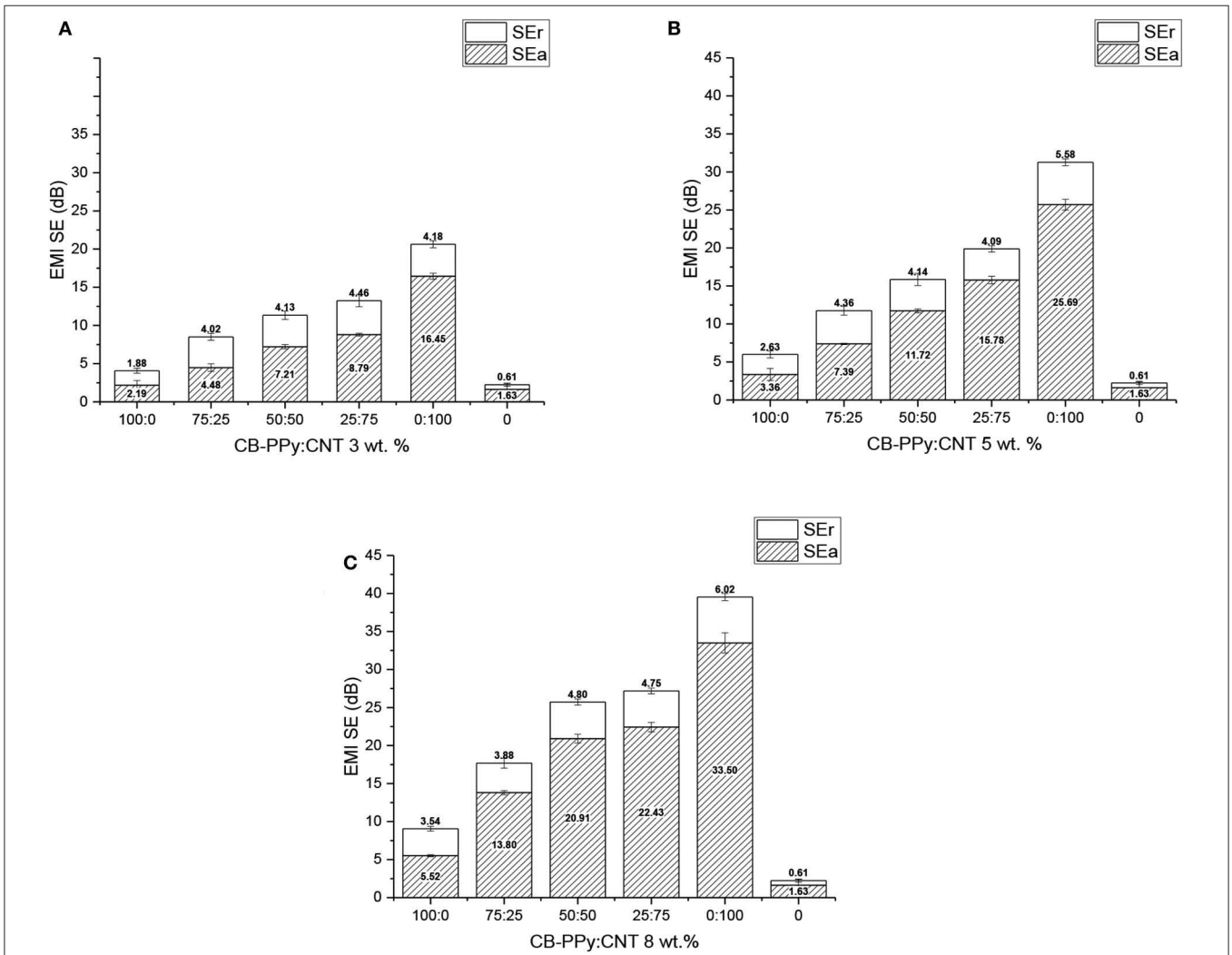

FIGURE 7 | (A–C) Total EMI SE, SEA and SER values of TPU/CB-PPy/CNT composites as a function of filler content.

TABLE 2 | Values of SE_A, SE_R and electrical conductivity for hybrids composites of TPU/CNT/CB-PPy measured at 10 GHz.

CB-PPy/CNT	5 wt%				8 wt%			
	SE_R	SE_A	SE_T	σ	SE_R	SE_A	SE_T	σ
100/0	2.63	3.36	5.99	1.82E-09	3.54	5.52	9.06	2.13E-03
75/25	4.36	7.39	11.75	4.87E-03	3.88	13.80	17.68	4.96E-02
50/50	4.14	11.72	15.86	1.48E-02	4.80	20.91	25.71	1.94E-01
25/75	4.09	15.78	19.87	5.05E-02	4.75	22.43	27.18	3.05E-01
0/100	5.58	25.69	31.27	2.51E-01	6.02	33.50	39.52	7.64E-01

absorption shielding. The SE_R and SE_A increase with the increasing in the conductive filler content for both composites. Moreover, the SE_A values for TPU/CNT at all compositions are higher than those found for TPU/CB-PPy composites, probably due to the higher aspect ratio, better distribution and better interaction between CNT and the electromagnetic radiation when compared to those observed for CB-PPy.

In order to reach a maximum EMI SE and electrical conductivity values at the lowest CB-PPy content, hybrid composites of TPU/CB-PPy/CNT were produced. The correlation between electrical conductivity and conductive filler fraction for (a) 3 wt%, (b) 5 wt%, and (c) 8 wt% of total filler content (CB-PPy/CNT) is illustrated in **Figure 6**. For composites with 3 wt% of total filler concentration having different filler ratios of CNT/CB-PPy = 0; 0.25; 0.5; 0.75; and 1, the electrical conductivity increases with decreasing CB-PPy content, indicating that CNT played an important role on the conductive network formation. On the other hand, the electrical conductivity for all hybrid composites containing 5 and 8 wt% of different filler ratio is quite similar probably due to the high amount of CNT concentration, which is higher than the percolation threshold for TPU/CNT composites.

Figure 7 illustrates the EMI SE of TPU/CB-PPy/CNT as a function of filler content. With increasing CNT content for the hybrid composites, the total EMI SE enhances and the main shielding mechanism is by absorption. For hybrid polymer composites containing 3 wt% of conductive filler, the EMI SE is lower than the desirable value for shielding material applications. As shown in **Table 2**, the EMI SE values are dependent on the electrical conductivity of the composites because of the conductive network formation. Therefore, polymer composites with electrical conductivity below 10^{-3} $S.cm^{-1}$ generally show EMI SE values lower than −20 dB. On the other hand, hybrid composites containing 5 wt% at CB-PPy/CNT ratio of 75:25 and 8 wt% at filler ratio of 75:25, 50:50, and 25:75 presented total EMI SE values higher than −20 dB, suggesting that those composites have a great potential as EMI shielding material.

CONCLUSION

Conducting polymer composites comprised of TPU/CB-PPy, TPU/CNT, and TPU/CB-PPy/CNT were successfully produced through melting mixing process. Electrical conductivity, rheological properties and EMI SE were significantly affected by the conductive network formation. Therefore, the increase of filler content resulted in the raise of the electrical conductivity and EMI SE values of both TPU composites. The electrical conductivity of composites with 3 wt% of CNT and 15 wt% of CB-PPy increases about 12 orders of magnitude when compared to that found for neat TPU. TPU/CNT exhibited the desired level of EMI SE, −20 dB, at a filler content higher than 3 wt% while 15 wt% of CB-PPy is required to reach this value. This behavior can be assigned to the higher aspect ratio and better distribution of CNT filler into TPU matrix when compared to the CB-PPy filler. On the other hand, TPU composites containing CNT are more difficult to be processed at the same conductive filler content than CB-PPy-filled TPU composites. TPU/CNT composites was partially impaired for CNT filler concentration above 8 wt%. Concerning the hybrid composites (TPU/CB-PPy/CNT), the CNT play an important role on the electrical conductivity, EMI and rheological properties. In fact, with increasing the CNT content in the TPU/CB-PPy/CNT these properties enhance significantly. A schematic drawing of the interaction between CNT/CB-PPy particles is shown in the **Supplementary Figure**. For hybrid polymer composites containing 3 wt% of conductive filler, the EMI SE is lower than the desirable value for shielding material applications. Moreover, hybrid composites with good processability at 5 wt% of CNT/CB-PPy ratio 75:25 and 8 wt% of filler ratio 75:25, 50:50, and 25:75 presented total EMI SE values higher than −20 dB, demonstrating the potential use of these materials for electromagnetic shielding applications.

DATA AVAILABILITY STATEMENT

All datasets generated for this study are included in the article/**Supplementary Material**.

AUTHOR CONTRIBUTIONS

MB and SR performed the production of polymer composites composition and characterization. CM, GB, BS, and AP assisted in writing of the manuscript and discussion of results. All authors reviewed the final manuscript.

ACKNOWLEDGMENTS

The authors gratefully acknowledge the financial support of the Conselho Nacional de Desenvolvimento Científico e Tecnológico (CNPq), the Coordenação de Aperfeiçoamento de Pessoal de Ensino Superior (CAPES), the Fundação de Amparo à Pesquisa E Inovação do Estado de Santa Catarina (FAPESC), and the Central Electron Microscopy Laboratory of the Universidade Federal de Santa Catarina (LCME-UFSC) for the FEG-SEM images.

SUPPLEMENTARY MATERIAL

The Supplementary Material for this article can be found online at: https://www.frontiersin.org/articles/10.3389/fmats.2020.00174/full#supplementary-material

REFERENCES

Al-Saleh, M. H. (2015). Electrical and mechanical properties of graphene/carbon nanotube hybrid nanocomposites. *Synth. Met.* 209, 41–46. doi: 10.1016/j.synthmet.2015.06.023

Al-Saleh, M. H. (2016). Electrical, EMI shielding and tensile properties of PP/PE blends filled with GNP:CNT hybrid nanofiller. *Synth. Met.* 217, 322–330. doi: 10.1016/j.synthmet.2016.04.023

Al-Saleh, M. H., Saadeh, W. H., and Sundararaj, U. (2013). EMI shielding effectiveness of carbon based nanostructured polymeric materials: a comparative study. *Carbon* 60, 146–156. doi: 10.1016/j.carbon.2013.04.008

Burmistrov, I., Gorshkov, N., Ilinykh, I., Muratov, D., Kolesnikov, E., Anshin, S., et al. (2016). Improvement of carbon black based polymer composite electrical conductivity with additions of MWCNT. *Compos. Sci. Technol.* 129, 79–85. doi: 10.1016/j.compscitech.2016.03.032

Chen, J., Du, X. C., Zhang, W. B., Yang, J. H., Zhang, N., Huang, T., et al. (2013). Synergistic effect of carbon nanotubes and carbon black on electrical conductivity of PA6/ABS blend. *Compos Sci Technol.* 81, 1–8. doi: 10.1016/j.compscitech.2013.03.014

Chen, J., Zhang, Z. X., Huang, W. B., Li, J. L., Yang, J. H., Wang, Y., et al. (2015). Carbon nanotube network structure induced strain sensitivity and shape memory behavior changes of thermoplastic polyurethane. *Mater. Design* 69, 105–113. doi: 10.1016/j.matdes.2014.12.054

Chen, Z., Xu, C., Ma, C., Ren, W., and Cheng, H. M. (2013). Lightweight and flexible graphene foam composites for high-performance electromagnetic interference shielding. *Adv. Mater.* 25, 1296–1300. doi: 10.1002/adma.201204196

Chu, K., Li, W. S., Jia, C. C., and Tang, F. L. (2012). Thermal conductivity of composites with hybrid carbon nanotubes and graphene nanoplatelets. *Appl. Phys. Lett.* 101, 211903–2119034. doi: 10.1063/1.4767899

Guo, S., Zhang, C., Wang, W., Liu, T., Tjiu, W. C., He, C., et al. (2008). Preparation and characterization of polyurethane/multiwalled carbon nanotube composites. *Polym. Polym. Comp.* 16, 501–507. doi: 10.1177/096739110801600803

Håkansson, E., Amiet, A., Nahavandi, S., and Kaynak, A. (2007). Electromagnetic interference shielding and radiation absorption in thin polypyrrole films. *Eur. Polymer J.* 43, 205–213. doi: 10.1016/j.eurpolymj.2006.10.001

Jang, M. G., Cho, C., and Kim, W. N. (2016). Synergistic effects of hybrid conductive fillers on the electrical properties of carbon fiber pultruded polypropylene/polycarbonate composites prepared by injection molding. *J. Comp. Mater.* 51, 1005–1017. doi: 10.1177/0021998316658536

Jeddi, J., and Katbab, A. A. (2017). The electrical conductivity and EMI shielding properties of polyurethane foam/silicone rubber/carbon black/nanographite hybrid composites. *Polym. Comp.* 39, 3452–3460. doi: 10.1002/pc.24363

Kaur, A., Ishpal, D., and Hawan, S. K. (2012). Tuning of EMI shielding properties of polypyrrole nanoparticles with surfactant concentration. *Synth. Metals* 162, 1471–1477. doi: 10.1016/j.synthmet.2012.05.012

Kausar, A. (2016). Electromagnetic interference shielding of polyaniline/poloxalene/carbon black composite. *Int. J. Mater. Chem.* 6, 6–11. doi: 10.5923/j.ijmc.20160601.02

Kim, B. R., Lee, H. K., Park, S. H., and Kim, H. K. (2011). Electromagnetic interference shielding characteristics and shielding effectiveness of polyaniline-coated films. *Thin Solid Films* 19, 3492–3496. doi: 10.1016/j.tsf.2011.01.093

Kuester, S., Barra, G. M. O., and Demarquette, N. R. (2018). Morphology, mechanical properties and electromagnetic shielding effectiveness of poly (styrene-b-ethylene-ran-butylene-b-styrene)/carbon nanotube nanocomposites: effects of maleic anhydride, carbon nanotube loading and processing method. *Polymer Int.* 67, 1229–1240. doi: 10.1002/pi.5630

Kuester, S., Demarquette, N. R., Ferreira, J. C., Soares, B. G., and Barra, G. M. O. (2017). Hybrid nanocomposites of thermoplastic elastomer and carbon nanoadditives for electromagnetic shielding. *Eur. Polym. J.* 88, 328–339. doi: 10.1016/j.eurpolymj.2017.01.023

Kuester, S., Merlini, C., Barra, G. M. O., Ferreira, J. C., Lucas, A., de Souza, A. C., et al. (2016). Processing and characterization of conductive composites based on poly(styrene-b-ethylene-ran-butylene-b-styrene) (SEBS) and carbon additives: a comparative study of expanded graphite and carbon black. *Comp. Part B Eng.* 84, 236–247. doi: 10.1016/j.compositesb.2015.09.001

Kumar, A., Kumar, V., Kumar, M., and Awasthi, K. (2017). Synthesis and characterization of hybrid PANI/MWCNT nanocomposites for EMI applications. *Polym. Comp.* 39, 3858–3868. doi: 10.1002/pc.24418

Kumar, G. S., and Patro, T. U. (2018). Efficient electromagnetic interference shielding and radar absorbing properties of ultrathin and flexible polymer-carbon nanotube composite films. *Mater. Res. Exp.* 5:115304. doi: 10.1088/2053-1591/aade39

Levon, K., Margolina, A., and Patashinsky, A. Z. (1993). Multiple percolation in conducting polymer blends. *Macromolecules* 26, 4061–4063. doi: 10.1021/ma00067a054

Li, N., Huang, Y., Du, F., He, X., Lin, X., Gao, H., et al. (2006). Electromagnetic interference (EMI) shielding of single-walled carbon nanotube epoxy composites. *Nano Lett.* 6, 1141–1145. doi: 10.1021/nl0602589

Liu, Z., Bai, G., Huang, Y., Ma, Y., Du, F., Li, F., et al. (2007). Reflection and absorption contributions to the electromagnetic interference shielding of single-walled carbon nanotube/polyurethane composites. *Carbon* 45, 821–827. doi: 10.1016/j.carbon.2006.11.020

Mahapatra, S. P., Sridhar, V., and Tripathy, D. K. (2008). Impedance analysis and electromagnetic interference shielding effectiveness of conductive carbon black reinforced microcellular EPDM rubber vulcanizates. *Polym. Comp.* 29, 465–472. doi: 10.1002/pc.20421

Mondal, S., Das, P., Ganguly, S., Ravindren, R., Remanan, S., Bhawal, P., et al. (2018). Thermal-air ageing treatment on mechanical, electrical, and electromagnetic interference shielding properties of lightweight carbon nanotube based polymer nanocomposites. *Compos. Part A.* 107, 447–460. doi: 10.1016/j.compositesa.2018.01.025

Oyharçabal, M., Olinga, T., Foulc, M. P., Lacomme, S., Gontier, E., and Vigneras, V. (2013). Influence of the morphology of polyaniline on the microwave absorption properties of epoxy polyaniline composites. *Compos. Sci. Technol.* 74, 107–112. doi: 10.1016/j.compscitech.2012.10.016

Pan, Y., Liu, X., Hao, X., Star,ý, Z., and Schubert, D. W. (2016). Enhancing the electrical conductivity of carbon black-filled immiscible polymer blends by tuning the morphology. *Eur. Polym. J.* 78:106–115. doi: 10.1016/j.eurpolymj.2016.03.019

Piana, F., and Pionteck, J. (2013). Effect of the melt processing conditions on the conductive paths formation in thermoplastic polyurethane/expanded graphite (TPU/EG) composites. *Comp. Sci. Technol.* 80, 39–46. doi: 10.1016/j.compscitech.2013.03.002

Ramoa, S. D. A. S., Barra, G. M. O., Oliveira, R. V. B., de Oliveira, M. G., Cossad, M., and Soares, B. G. (2013). Electrical, rheological and electromagnetic interference shielding properties of thermoplastic polyurethane/carbon nanotube composites. *Polym. Int.* 62, 1477–1484. doi: 10.1002/pi.4446

Sharma, S. K., Gupta, V., Tandon, R. P., and Sachdev, V. K. (2016). Synergic effect of graphene and MWCNT fillers on electromagnetic shielding properties of graphene–MWCNT/ABS nanocomposites. *RSC Adv.* 6, 18257–18265. doi: 10.1039/C5RA23418B

Socher, R., Krause, B., Boldt, R., Hermasch, S., Wursche, R., and Pötschke, P. (2011). Melt mixed nano composites of PA12 with MWNTs: influence of MWNT and matrix properties on macrodispersion and electrical properties. *Compos. Sci. Technol.* 71, 306–314. doi: 10.1016/j.compscitech.2010.11.015

Sudha, J. D., Sivakala, S., Prasanth, R., Reena, V. L., and Nair, P. R. (2009). Development of electromagnetic shielding materials from the conductive blends of polyaniline and polyaniline-clay nanocomposite-EVA: preparation and properties. *Comp. Sci. Technol.* 69, 358–364. doi: 10.1016/j.compscitech.2008.10.026

Sumfleth, J., Adroher, X. C., and Schulte, K. (2009). Synergistic effects in network formation and electrical properties of hybrid epoxy nanocomposites containing multi-wall carbon nanotubes and carbon black. *J. Mater. Sci.* 44, 3241–3247. doi: 10.1007/s10853-009-3434-7

Szeluga, U., Kumanek, B., and Trzebicka, B. (2015). Synergy in hybrid polymer/nanocarbon composites: a review. *Compos. Part A. Appl. Sci. Manuf.* 73, 204–231. doi: 10.1016/j.compositesa.2015.02.021

Taunk, M., Kapil, A., and Chand, S. (2008). Synthesis and electrical characterization of self-supported conducting polypyrrole-Poly(vinylidene fluoride) composite films. *Open Macromol. J.* 2, 74–79. doi: 10.2174/1874343900802010074

Wu, J., Ye, Z., Ge, H., Chen, J., Liu, W., and Liu, Z. (2017). Modified carbon fiber/magnetic graphene/epoxy composites with synergistic effect for electromagnetic interference shielding over broad frequency band. *J. Colloid Interf. Sci.* 506, 217–226. doi: 10.1016/j.jcis.2017.07.020

Yavuz, Ö., Ram, M. K., Aldissi, M., Poddar, P., and Srikanth, H. (2005). Polypyrrole composites for shielding applications. *Synth. Metals* 151, 211–217. doi: 10.1016/j.synthmet.2005.05.011

Yu, W. C., Wang, T., Zhang, G. Q., Wang, Z. G., Yin, H. M., Yan, D. X., et al. (2018). Largely enhanced mechanical property of segregated carbon nanotube/poly(vinylidene fluoride) composites with high electromagnetic interference shielding performance. *Compos. Sci. Technol.* 167:260–267. doi: 10.1016/j.compscitech.2018.08.013

Zhang, C. S., Fu, S. Y., Ni, Q. Q., and Kurashiki, K. (2007). Electromagnetic interference shielding effect of nanocomposites with carbon nanotube and shape memory polymer. *Compos. Sci. Technol.* 67, 2973–2980. doi: 10.1016/j.compscitech.2007.05.011

Zhang, H., Zhang, G., Tang, M., Zhou, L., Li, J., Fan, X., et al. (2018). *Synergistic effect of carbon nanotube and graphene nanoplates on the* mechanical, electrical and electromagnetic interference shielding properties of polymer composites and polymer composite foams. *Chem. Eng. J.* 353, 381–393. doi: 10.1016/j.cej.2018.07.144

Zhang, S. M., Lin, L., Deng, H., Gao, X., Bilotti, E., Peijs, A. A. J. M., et al. (2012). Synergistic effect in conductive networks constructed with carbon nanofillers in different dimensions. *Exp. Polym. Lett.* 6, 159–168. doi: 10.3144/expresspolymlett.2012.17

Conflict of Interest: The authors declare that the research was conducted in the absence of any commercial or financial relationships that could be construed as a potential conflict of interest.

Copyright © 2020 Bertolini, Ramoa, Merlini, Barra, Soares and Pegoretti. This is an open-access article distributed under the terms of the Creative Commons Attribution License (CC BY). The use, distribution or reproduction in other forums is permitted, provided the original author(s) and the copyright owner(s) are credited and that the original publication in this journal is cited, in accordance with accepted academic practice. No use, distribution or reproduction is permitted which does not comply with these terms.

Advantages of publishing in Frontiers

OPEN ACCESS
Articles are free to read for greatest visibility and readership

FAST PUBLICATION
Around 90 days from submission to decision

HIGH QUALITY PEER-REVIEW
Rigorous, collaborative, and constructive peer-review

TRANSPARENT PEER-REVIEW
Editors and reviewers acknowledged by name on published articles

Frontiers
Avenue du Tribunal-Fédéral 34
1005 Lausanne | Switzerland

Visit us: www.frontiersin.org
Contact us: info@frontiersin.org | +41 21 510 17 00

REPRODUCIBILITY OF RESEARCH
Support open data and methods to enhance research reproducibility

DIGITAL PUBLISHING
Articles designed for optimal readership across devices

FOLLOW US
@frontiersin

IMPACT METRICS
Advanced article metrics track visibility across digital media

EXTENSIVE PROMOTION
Marketing and promotion of impactful research

LOOP RESEARCH NETWORK
Our network increases your article's readership